Fabrication, Characterisation and Tuning of Micromechanical Resonators

by

Stefan Enderling

A thesis submitted for the degree of

Doctor of Philosophy

The University of Edinburgh

March 2006

to my parents and family

Abstract

Micromechanical resonators have many attractive properties, making them ideal components to provide frequency shaping and generation in future wireless transceivers. Their applicability in communication equipment depends on fabrication cost, impedance and the ability to tune their resonant frequency while maintaining a high Q-factor. This thesis characterises (i) CMP polysilicon polishing for the fabrication of micromechanical resonators and (ii) FIB platinum (Pt) and (iii) electrochemical silver (Ag) deposition for their tuning.

Both polysilicon bridge and cantilever beam resonators have been fabricated and characterised. In addition, a CMP planarisation based process has been used to demonstrate a fabrication platform for producing micromechanical resonators with submicron transducer gaps. This process requires one photolithographic step less than previously reported fabrication methods and does not suffer from transducer gap widening, which otherwise strongly affects the impedance of manufactured resonators. As part of this work, pattern dependent removal rates for polysilicon have been determined and design guidelines defined to optimise the yield of CMP fabricated resonators.

FIB Pt deposition on both bridge and cantilever beam resonators has been used to demonstrate frequency tuning (-15.6%). In contrast to competing technologies, such as laser trimming, FIB deposition does not cause device failure. Its advantage is that it is performed at room temperature and no power is consumed to maintain the trimmed frequency.

Real time electrochemical Ag deposition has been demonstrated to be capable of tuning polysilicon bridge resonators. It showed a location dependent bidirectional frequency change (-10% to +10.7%) using minimal power (200nW). This was implemented using an Ag deposition scheme consisting of a solid electrolyte, an Ag anode and Al contacts, and was integrated into bridge resonators using evaporation and shadow mask techniques. The advantage of this method over FIB Pt deposition is that it can provide dynamic in-situ simultaneous tuning of many resonators on the same chip.

Contents

Declaration of Originality

I hereby declare that the research recorded in this thesis is my own work, unaided except where otherwise acknowledged in the text, and the thesis itself was composed entirely by myself in the School of Engineering and Electronics at the University of Edinburgh. This work has not been submitted for any other degree or professional qualification.

Signed

22.05.2005

Date

Acknowledgements

Of course, I would have not been able to do this work without the help of others. Therefore, I would like to use the opportunity to thank those people who supported, helped and encouraged me to conduct my research over the past four years at the Scottish Microelectronics Centre (SMC). First of all I would like to sincerely thank my supervisor Prof. Anthony Walton for suggesting this work to me and guidance throughout this project. I also would like to thank many people at the SMC for their support, advice and encouragement, namely, Dr. Rebecca Cheung, Dr. Liudi Jiang, Dr. Tom Stevenson, Alan Gundlach, Dr. Andrew Bunting, Dr. William Parkes, Alan Ross, Dr. Camelia Dunare, Dr. Jon Terry, Dr. Stewart Smith, Sue Bond, Ann Cunningham, Alec Ruthven, Ewan McDonald, Gerry McDade, Andrew Brooks, Kevin Tierney, Jennifer McGregor and Joanna Venkov.

Most work reported work in this thesis was in collaboration with researchers from University of Newcastle, UK and Arizona State University, USA. I am indebted to Dr. John Hedely, Dr. Barry Gallacher, Prof. Jim Burdess and Dr. Alun Harris for their support, helpful technical discussions and access to their optical workstation, which was a vital equipment during my PhD project. I also would like to express my gratitude to Prof. Michael Kozicki, Charles Brown III, Murali Balakrishnan and Dr. Maria Mitkova from Arizona State University who were greatly involved in this project and spent considerable time providing me with test samples, helpful suggestions and knowledge about chalcogenide glasses.

I especially would like to thank those who provided the social environment at my work place in the SMC and being good friends, namely Dr. Martin Dicks, Dr. Natalie Plank, Louise Teo, Huamao Lin, Yifan Li, Petros Argyrakis and Keith Baldwin. I would like to thank Dr. Emily Hackett-Jones and Mark Sorrell for being our Edinburgh family.

Outside the University and the SMC, I would like to first thank my wife Katherine for her endless support and help during my PhD. I am deeply thankful to my parents and family to whom I have dedicated this thesis. Unfortunately, my grandfather died during the final stage of my PhD and was not able to see this work finished, but he was always interested and supported me whatever I was doing.

Publications

[1] S. Enderling, C.L. Brown III, S. Smith, M.H. Dicks, J.T.M. Stevenson, M. Mitkova, M.N. Kozicki, and A.J. Walton. Sheet resistance measurement of non-standard cleanroom materials using suspended Greek cross test structures. *IEEE Transactions on Semiconductor Manufacturing*, 19(1):2–9, 2006.

[2] Michael N. Kozicki, Anthony Walton, and Stefan Enderling. Microelectromechanical structures, devices including the structures, and methods of forming and tuning same, 2005. (US Patent: 20050225413).

[3] M.N. Kozicki, C.L. Brown III, M. Mitkova, S. Enderling, J. Hedley, and A.J. Walton. Application of Mass Transport in Solid Electrolyte Films in Tunable Microelectromechanical Resonators. In *Technical Proceedings of the 2005 NSTI Nanotechnology Conference and Trade Show*, pages 447–450, Anaheim, CA, USA, 2005.

[4] S. Enderling, C.L. Brown III, S.Smith, M.H. Dicks, J.T.M. Stevenson, A.W.S. Ross, M.Mitkova, M.N. Kozicki, and A.J. Walton. Suspended Greek cross test structures for measuring the sheet resistance of non-standard cleanroom materials. In *Proc. 18th International Conference on Microelectronic Test Structures*, pages 1–4, Leuven, Belgium, 2005.

[5] S. Enderling, C.L.Brown III, M. Balakrishnan, J. Hedley, J.T.M. Stevenson, S.Bond, C.C. Dunare, A.J. Harris, J.S. Burdess, M. Mitkova, M.N. Kozicki, and A.J. Walton. Integration of a novel electrochemical tuning scheme with MEMS surface micromachined resonators. In *Proc. 18th IEEE Int. Conf. on Micro Electro Mechanical Systems*, pages 159–162, Miami, USA, 2005.

[6] John Hedley, Jim S. Burdess, Alun J. Harris, Barry J. Gallacher, Calum J. McNeil, Peter J. Cumpson, and Stefan Enderling. An optical 'workstation' for characterization and modification of MEMS. In *Poceedings of SPIE 5458*, pages 244–252, Strasbourg, France, 2004.

[7] S. Enderling, M.H. Dicks, S.Smith, J.T.M. Stevenson, and A.J. Walton. Design Rules to Minimize the Effect of Joule Heating in Greek Cross Test Structures. *IEEE Transactions on Semiconductor Manufacturing*, 17(2):84–90, 2004.

[8] S. Enderling, L. Jiang, A.W.S. Ross, S. Bond, J. Hedley, A.J. Harris, J.S. Burdess, R. Cheung, C.A. Zorman, M. Mehregany, and A.J. Walton. MEMS resonator tuning using focused ion beam platinum deposition. In *Technical Proceedings of the 2004 Nanotechnology Conference and Trade Show*, volume 3, pages 421–424, Boston, USA, 2004.

[9] S. Enderling, M.H. Dicks, S.Smith, J.T.M. Stevenson, and A.J. Walton. Thermal Design Considerations for Greek Cross Test Structures. In *Proc. 16th International Conference on Microelectronic Test Structures*, pages 8–13, Monterey, USA, 2003.

List of Figures

List of Tables

Acronyms and abbreviations

AC	Alternating Current
AFM	Atomic Force Microscope/Microscopy
CCD	Coupled Charged Device
CMOS	Complementary Metal Oxide Semiconductor
CMP	Chemical Mechanical Polishing
CPD	Critical Point Drying
DC	Direct Current
DRIE	Deep Reactive Ion Etch
FED	Field Effect Devices
FIB	Focused Ion Beam
HF	Hydrofluoric Acid/ High Frequency
IC	Integrated Circuit
LF	Low Frequency
LMIS	Liquid Metal Ion Source
LNA	Low Noise Amplifier
LPCVD	Low Pressure Chemical Vapour Deposition
MEMS	Micro Electro Mechanical Systems
MESFET	MEtal Semiconductor Field Effect Transistor
MF	Medium Frequency
PA	Power Amplifier
PECVD	Plasma Enhanced Chemical Vapour Deposition
PIN	P-type, Intrinsic, N-type diode
RF	Radio Frequency
RIE	Reactive Ion Etch
SEM	Scanning Electron Microscope/Microscopy
SNR	Signal to Noise Ratio
SSD	Solid Source Diffusion
TEM	Transmission Electron Microscope
UV	Ultra Violet
VCO	Voltage Controlled Oscillator

Glossary

Bandwidth

The bandwidth of a resonator or filter refers to the difference in frequency between two points at 3dB attenuation of the maximum output amplitude.

Biaxial stress

A stress condition, in which two in-plane stress components are equal to each other without shear shear stress.

Insertion loss

The decrease in transmitted signal power resulting from the insertion of a device in a transmission line.

Mode shape

During vibration of a system with N degrees of freedom, the mode shape defines the relationship between all the coordinates of the system undergoing synchronous motion. In a N degree of freedom system, the synchronous motion can have N natural frequencies. A N degree of freedom system with N natural frequencies has N mode shapes.

Neutral line/axis

The position of neutral line/axis of a beam during bending is the location in the cross section with zero normal stresses.

Chapter 1

Introduction

This chapter introduces the reader to the field of Micro Electro Mechanical Systems (MEMS) and highlights the increasing importance of this technology in wireless communication systems. After motivating the work and presenting the objectives of the thesis, the chapter ends with a description of the thesis structure.

1.1 Background

Only a few discoveries have had such a strong impact on humanity as the transistor and the planar fabrication process, which have developed together over decades into a multi-billion pound semiconductor industry. Semiconductor research enabled the miniaturisation of electronics into Integrated Circuits (IC) and provided the foundation for inventions such as personal computers, mobile phones and ever increasing memory capacity. These products have influenced the daily life of modern societies and inspired new areas of research, which have borrowed processes and technology originally used for making ICs.

One of these areas of research is Micro Electro Mechanical Systems (MEMS) technology in which mechanical systems are miniaturised and integrated with transistor electronics. The MEMS industry has been growing continuously over the past two decades and uses fabrication processes adapted from the original IC planar process. It harnesses the same advantages of miniaturisation which transistors have experienced for decades, namely, faster speed, lower power consumption, lower cost and smaller size. Devices based on MEMS technology have a continuing impact on society and find commercial applications ranging from pressure sensors and accelerometers to gyroscopes.

1.2 Motivation

Communication systems such as wireless handsets have benefited from the development of MEMS technology. Thin film bulk acoustic resonators (FBAR), which are composed of deposited piezoelectric material sandwiched between metal electrodes, present an alternative to the off-chip passives that were formerly used. FBARs have been demonstrated that have operating frequencies well within the GHz range [156, 108] and sufficient quality (Q)-factors to be used as RF filters in front end transceivers of wireless handsets.

At the same time, advances in Radio Frequency (RF) micromechanical resonators have yielded miniature vibrating on-chip devices with Q-factors exceeding 10,000 and GHz resonant frequencies. Micromachined RF resonators can replace Surface Acoustic Wave (SAW) devices in the same way as FBARs, but they can also be interlinked to form "integrated micromechanical circuits", which can realise frequency mixing, shaping and generation in wireless transceivers [86].

Fig. 1.1 presents an example of a wafer-vacuum packaged MEMS surface micromachined resonator on top of an US one cent coin. The figure clearly shows the small size of the miniaturised resonator. Note that micromechanical resonators can be three times smaller in volume than FBARs [8].

Figure 1.1. Micromachined on-chip resonator on top of an US one cent coin. In future, multiple micromachined resonators will be able to be interlinked to form mixers, filters and oscillators on one single chip, providing a reduction in cost and size and an increase in functionality in multi-band wireless transceivers. (Picture courtesy: Discera Microcommunication Technologies) [124].

Despite the advantages of using micromechanical resonators in wireless communication equipment, their application has being hindered by their (i) high intrinsic impedances, (ii) complex fabrication processes and (iii) the lack of suitable post-fabrication tuning methods.

The fabrication of micromechanical resonators involves a combination of conformal multi-layer deposition and several photolithographic steps, typically followed by etching. As the number of fabrication steps increases, so do the manufacturing costs. In addition, current fabrication processes are not able to produce small enough transducer gaps in capacitive actuated resonators in order to to match their impedances to 50Ω macroscopic off-chip antennas and to improve the Signal-to-Noise-Ratio (SNR).

Every fabrication process involves tolerances that cause a change in the resonant frequency of micromechanical resonators (Ch. 3). Frequency tuning is required to correct

these changes and is categorised into passive and active tuning methods. Passive tuning methods are often used because of their superior accuracy, but in some cases they have a tendency to cause resonator device failure [1]. Hence, a passive tuning method is required, which does not cause failure of devices. Active tuning methods are able to perform tuning on several resonator devices simultaneously, but often the tuning voltage or power consumption is too high [6], which make them unsuitable for low power communication equipment. Therefore, active tuning methods are required, which can provide frequency changes in real time using minimal power consumption.

1.3 Scope and objective of the thesis

As described in the previous section, micromechanical resonators have many attractive characteristics. This thesis concentrates on their fabrication and tuning as these are areas where there is the potential to improve their performance.

In this work, a novel Chemical Mechanical Polishing (CMP) process is proposed, which reduces the number of fabrication steps and the transducer gaps of capacitive actuated resonators (Fig. 1.2). The process starts with patterning of polysilicon to form the resonator device structure. Subsequent thermal oxidation of the polysilicon sidewalls defines the resonator transducer gaps. After oxidation, polysilicon is deposited and CMP planarised to form electrodes for lateral vibration excitation. The removal of the sacrificial sidewall silicon dioxide (SiO_2) layer by chemical wet etching produces the capacitive transducer gaps.

Several fabrication methods have been developed to improve the fabrication and reduce the impedance of micromechanical resonators (Ch. 2). Most fabrication processes achieved low impedances by a reduction in transducer gap width, which is located between the electrode and resonator of capacitive actuated devices. In contrast to other methods, the advantage of the new process is that the resonator transducer gap width is independent of lithography resolution and issues associated with resist tapering [100]. Apart from the gap width definition, the sacrificial SiO_2 on top of the resonator provides a polish stop layer. Therefore, possible variation in thickness or even complete resonator removal after CMP polishing is not an issue using this process. The performed CMP planarisation patterns the electrodes without an additional photolithographic masking step. This simplifies the fabrication process and reduces

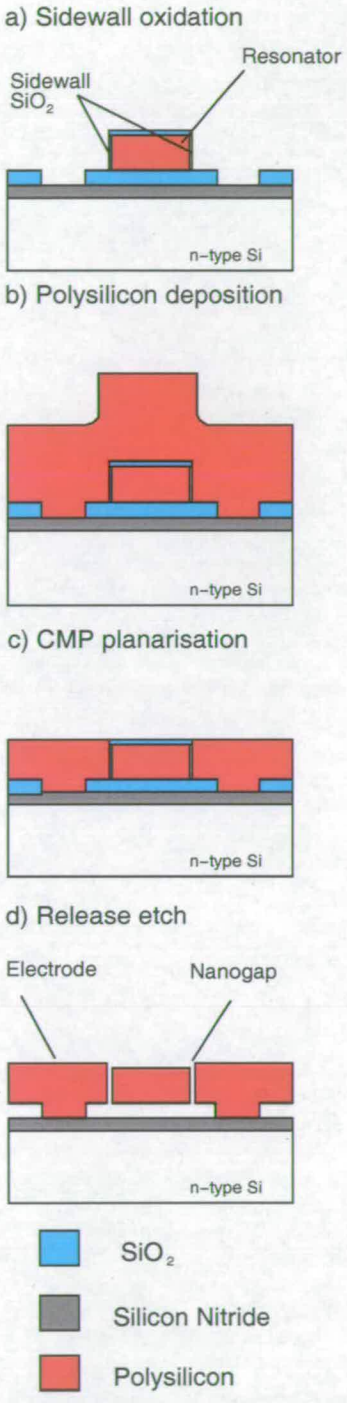

Figure 1.2. Proposed CMP resonator fabrication process. Cross sectional view of resonator beam CMP fabrication. The process proposed in this thesis employs conformal thermal sidewall oxidation to achieve submicron transducers gap widths. Transducer gap width variation from photoresist tapering was observed in other processes, which used lithographic gap definition. Photoresist tapering is not an issue in the presented process, since the oxidation rate is constant for the sidewalls of the resonator.

cost. Further, the proposed CMP process does not suffer from transducer gap widening after the release etch and the consequent increase in impedance after sacrificial layer etching [100].

After fabrication, the resonant frequency of resonators typically experiences changes, which need to be adjusted to maintain performance specifications. Focused Ion Beam (FIB) is used in the semiconductor industry for IC failure analysis and repair because it can make submicron and micron physical changes on metal tracks (Ch. 7). Its ability to make these physical changes (through deposition and sputtering) can be directly applied to micromechanical resonators to perform tuning.

One way to modify frequency is to selectively FIB deposit platinum (Pt) at the desired location onto the resonator (Fig. 1.3) [29]. The deposition of Pt alters the resonator mass and stiffness and modifies the resonant frequency. The advantage of FIB Pt deposited tuning is threefold. Firstly, it can alter the resonant frequency over a wide range due to its ability to deposit Pt in submicron and micron sizes. Secondly, the deposition process is performed at room temperature, preventing the development of residual stress as a result of different thermal expansion coefficients between the deposit and the resonator. Thirdly, deposited Pt does not require any energy to maintain tuning. This provides desperately needed power savings for future wireless communication equipment with ever increasing functionality.

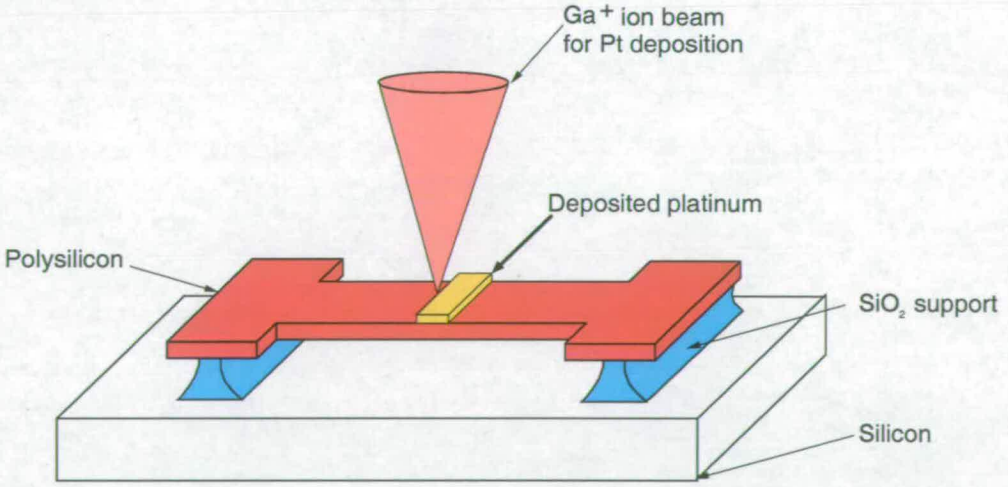

Figure 1.3. Frequency tuning of resonators by FIB Pt deposition. FIB selectively deposits Pt on the resonator, altering the mass and stiffness of the device. A change in mass generates a decrease, while a change in stiffness produces an increase in resonant frequency.

Recently, silver-germanium-selenium (Ag-Ge-Se) ternary materials have emerged in MEMS device applications, because of their high ion mobility and ability to transport Ag ions. These material systems have promising properties, being capable of moving significant amounts of Ag ions over several hundred microns via the combination of ion transport and electrodeposition/reduction [59]. The medium used to transport the Ag ions from their reservoir (an Ag anode) is a blanket deposited Ag doped chalcogenide glass film, which serves as a solid electrolyte. Ag ion migration in the solid electrolyte and subsequent deposition is induced by a DC voltage between an oxidizable Ag anode and an inert cathode (Fig. 1.4). Once Ag has been deposited, the stiffness and mass of the resonator is changed and the resonant frequency modified.

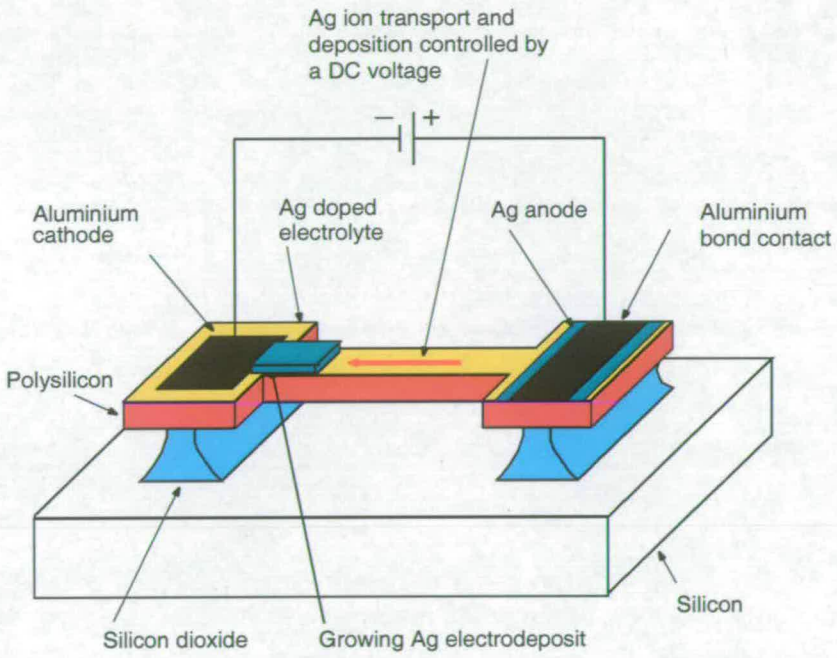

Figure 1.4. Schematic of Ag deposited frequency tuning. Application of a DC voltage between Ag anode and Al cathode results in Ag ion transport and subsequent deposition. Deposited Ag alters the stiffness and mass of the resonator and modifies the resonant frequency.

The advantage of this method is that Ag deposition can be electrically controlled in real time using low DC bias voltages (<5V) [26]. Low operating voltages and active control make this method ideal for filters in wireless transceivers, where a low supply voltage is used. Real time tuning allows correction of the resonant frequency during any stage of the resonator life time. This is particularly valuable when the resonant frequency is subject to changes caused by variations in humidity and temperature [57].

This thesis characterises a CMP polysilicon based polishing process for the fabrication of micromechanical resonators and FIB Pt and electrochemical Ag deposition for their tuning. The design and production of test structures is described and the characterisation of the CMP polishing and tuning are explained. The results are presented and then used to determine process issues and design rules for CMP fabricated resonators and evaluate the suitability of FIB Pt and electrochemical Ag deposited tuning for use in RF MEMS resonators.

1.4 Thesis plan

The thesis is divided into three parts. In the first part, Chapter 2 and Chapter 3 review the literature concerning various RF MEMS components, their fabrication processes and resonator tuning methods. In the second part, Chapter 5 to Chapter 8 report on the design and fabrication of test structures as well as the characterisation of CMP polishing and FIB Pt and electrochemical Ag deposited frequency tuning. In part three of the thesis, Chapter 9 draws conclusions about the research and gives details of possible future work.

Chapter 2: Review of RF MEMS: This chapter reviews RF MEMS components and circuits and compares their performance with their current macroscopic and solid-state counterparts. In the second part of the chapter, the geometrical design, a deposited tuning model, electrostatic actuation and fabrication methods of micromechanical resonators are reviewed and explained. At the end of the chapter, remaining resonator research issues are discussed.

Chapter 3: Frequency tuning methods for MEMS resonators: This chapter identifies the strength of frequency changes in micromechanical resonators and reviews and compares active and passive tuning methods.

Chapter 4: Characterisation of a CMP based polishing process: In this chapter, a test mask design is used to analyse a CMP based polysilicon polishing process for the fabrication of capacitive micromechanical resonators.

Chapter 5: Fabrication of MEMS resonators: Chapter 5 describes the fabrication of micromechanical cantilever beam and bridge test resonators intended for the characterisation of FIB Pt and electrochemical Ag deposited tuning. A solid electrolyte, Ag anodes and aluminium (Al) contacts are integrated with a set of micromachined polysilicon bridge resonators in order to analyse Ag deposited frequency tuning.

Chapter 6: Characterisation of micromachined MEMS resonators: This chapter briefly describes the optical workstation and the characterisation of fabricated MEMS test resonators.

Chapter 7: Characterisation of frequency tuning by FIB platinum deposition: Focused Ion beam platinum deposition is used to characterise frequency tuning of polysilicon and 3C SiC micromechanical cantilever beam and bridge test resonators. Simulation and vibration measurements are used to analyse the FIB deposition tuning. FIB deposition is investigated and a model and simulations are used to explain the observed tuning.

Chapter 8: Characterisation of frequency tuning by silver deposition: In Chapter 8, electrical and mechanical test structures are used to analyse the solid electrolyte. Polysilicon bridge resonators with integrated solid electrolyte, Ag anodes and aluminium (Al) contacts are used to analyse Ag deposited frequency tuning. A model and simulation are used to characterise the shifts in resonant frequency of micromechanical polysilicon bridge resonators.

Chapter 9: Conclusions and future work: The work of the thesis is reviewed and results discussed. Possible improvements and future work are derived from the obtained results.

Chapter 2

Review of RF MEMS

This chapter reviews different RF MEMS components and circuits with special emphasis on capacitive transduced resonators. Their mechanical geometrical design, capacitive transduction and fabrication are described and developed. At the end of the chapter, remaining resonator research issues are discussed and an outlook into the future is made.

2.1 Introduction

In the last decade large resources and research effort has been devoted to the field of Radio Frequency (RF) MEMS. The major impetus for these efforts were the provision of on-chip passive RF components to allow power savings and increased functionality in future multiband wireless communication equipment. Over the years, large numbers of publications have appeared, reporting on different RF MEMS components and their performance. A selection of these RF components and circuits are summarised in the following sections with particular emphasis on those, which find application in future multiband wireless transceivers, laptop computers and wristwatches. Note, the number of publications describing various RF components and circuits exceeds obviously significantly those referenced in this thesis as only representative examples are identified. Hence, other micromachined RF components and circuits such as antennas, transmission lines and phase shifters are not included in this review. For more information, the reader is referred to [134, 109, 85, 127, 150, 5, 71, 102].

2.2 RF MEMS components and circuits

2.2.1 Micromechanical Switches

Solid state switches such as PIN diodes and GaAs MEtal Semiconductor Field Effect Transistors (MESFET) currently used in wireless front end transceivers for signal routing purposes, have large insertion losses of up to 1-2dB per stage for frequencies beyond 1GHz and poor electrical isolation in the blocking state of -20 to -25 dB. Additionally, these devices consume about 100mW of power during actuation compared to their RF MEMS counterparts with 1mW [12]!

RF MEMS switches [39] by comparison are an attractive alternative to solid state devices because of insertion losses of 0.1dB at 1GHz and isolation of -35dB at 35GHz. They achieve such superior switching action of a freely movable member using electromagnetic [126], electrostatic [39] and electrothermal [144] actuation. Electrostatic switches provide in the up state of a metal electrode signal transfer, while in the down state, the RF signal is blocked (Fig. 2.1). Their superior linearity, low power consumption and integration compatibility with transistor circuits make them compelling for signal routing between receiving and transmitting paths in RF front ends, antenna switching and programmable low-loss filtering for multi-band transceivers. However,

issues such as short lifetimes, slow switching speed and high actuation voltages need to be resolved before these structures can use their full potential in wireless communication technology.

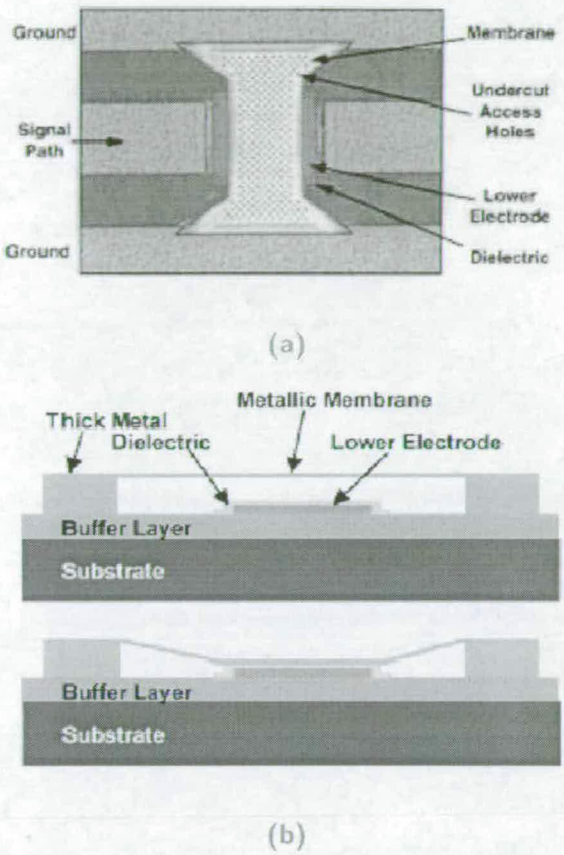

Figure 2.1. A capacitive coupled micromechanical shunt switch. (a) Micrograph and (b) a schematic representation of a capacitive coupling MEMS RF switch. In this design, two metal electrodes are separated by a dielectric film and an air gap. In the up state of the movable metal bridge electrodes, signal can pass through the signal line. In the down state, the RF signal is shorted and blocked through the switch structure to ground [39].

2.2.2 Tunable Capacitors

Tunable RF MEMS capacitors consist of a parallel plate capacitor with air as a dielectric between them. Capacitance in these devices is varied by the displacement of these plates in respect to each other by means of electrothermal [43], piezoelectric [92] and electrostatic [30] actuation. Most researchers have concentrated on the electrostatic

actuation, due to the zero DC power consumption and integration compatibility with transistor electronics.

MEMS electrostatic tunable capacitors adjust their capacitance by altering the electrode gap spacing or the electrode areas (Fig. 2.2). Both capacitors achieve a tuning ratio (defined as the relative capacitance swing for a given DC voltage) of around 3:1 and Q factor of up to 66 at 1GHz [30]. Paired together with medium-Q inductors, RF MEMS

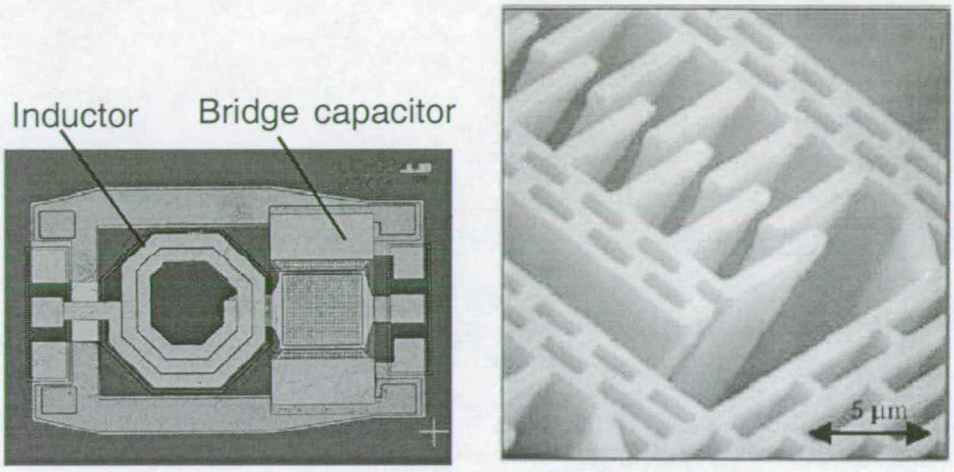

Figure 2.2. Photographs of two different RF MEMS tunable capacitors. (a) Tunable gap bridge capacitor with high-Q inductor [30] and (b) Comb-area tunable capacitor [152].

capacitors could enhanced the performance of voltage controlled oscillators (VCO); be employed in tunable RF filters and impedance matching circuits, where they would outperform currently used semiconductor Schottky varactor diodes due to their high linearity, low power consumption and high electric self resonance. However, the current research challenge is to achieve high tuning ratios using low DC voltages.

2.2.3 Medium-Q Inductors

Tunable micromechanical capacitors have to be paired with inductors with Qs > 20 to realise low noise VCOs or tunable RF front end filters. Conventional planar IC manufactured inductors have Qs not larger than 10 due to high series resistances and capacitive losses through the underlying Si substrate.

MEMS technology can provide inductors with thicker metal lines to reduce series resistance and suspend the inductor away from the substrate to limit capacitive loss through the substrate, which can produce Qs of up to 70 [17, 21]. Although demonstrated Qs are not high enough to serve in tunable RF front end filters, demonstrated Qs are sufficient to pair these inductors with tunable capacitors to allow the implementation of low noise VCOs with considerable lower power consumption than those fabricated with conventional IC manufacturing processes [157].

Figure 2.3. Curled spiral inductor. The inductor is bend away from the substrate as a result of the compressive stress in the device structure [17].

2.2.4 High-Q Micromechanical Resonators and circuits

Resonators find widespread applications in transceiver architectures such as frequency - controlling elements in reference oscillators, as tunable resonator tanks for Voltage Controlled Oscillators (VCOs) and as building blocks for filters [127].

Based on the principle of operation, resonator can be divided into (i) *electromagnetic wave* (EW) resonators, e.g. LC-type or transmission line resonators, and (ii) *electromechanical or electro-acoustic wave* (AW) such as mechanical, bulk acoustic wave (BAW) and surface acoustic wave (SAW) resonators. Acoustic wave resonators vibrate with

higher Qs than their electromagnetic counterparts, making them essential components for communication equipment [127].

MEMS technology has produced miniaturised versions of such electro-acoustic resonators and partly replaced bulky off-chip SAW filters in wireless communication equipment. Example of micromachined on-chip resonators with frequencies ranging from a few kHz to GHz are comb-drive [88], doubly clamped microbeam [6] and diamond disks resonators [140, 156].

The following section reviews different resonator transduction methods and presents the latest filter and oscillator circuits based on capacitive actuated resonators.

Resonator transduction

Three major transduction methods for micromechanical resonator can be classified into (i) piezoelectric [96], (ii) magnetomotive [105] and (iii) capacitive [140] actuation. The transduction method influences the impedance level of the resonator, the Q factor and their ability of integration with CMOS circuitry.

Piezoelectric transduced resonators such as *film bulk acoustic resonators* RFBARs consist of an aluminium nitride (AlN) piezoelectric layer sandwiched by two parallel metal electrodes. By the application of an AC voltage between the electrodes, a mechanical vibration is induced in the piezoelectric material, which is determined by vertical [156, 108] or lateral [96] dimensions of the resonator. In order to attain a high Q of 2,900 in air with demonstrated frequencies of 473MHz [96], the acoustic losses are minimised by removal of the underlying substrate material (Fig. 2.4). FBARs have been successfully implemented in mobile handsets as RF filters.

Magnetic actuation is less frequently studied than piezoelectric and electrostatic transduction, probably because of its fabrication complexity and difficulty to generate a strong magnetic field within a CMOS environment. However, in [149] flexural beam resonators were magnetically excited by exposing them to a strong magnetic field of 7T and passing an alternating current through the device. The combination of magnetic field and electric current generated an electrodynamic (Lorentz) force, which caused mechanical resonance at one of the intrinsic harmonics of the beam. The beam operated with a fundamental resonance frequency of 70 MHz with a Q of 20,000 under vacuum (Fig. 2.5).

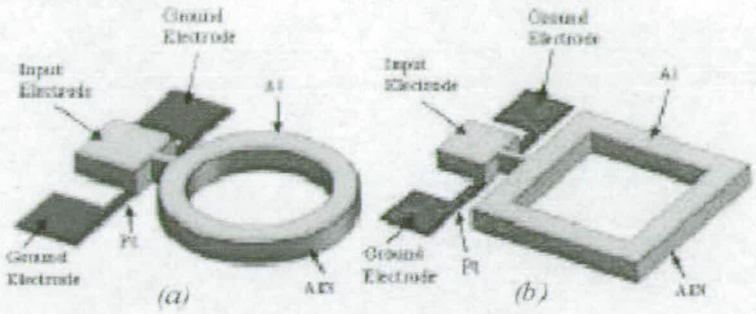

Figure 2.4. Lateral vibrating piezoelectric FBAR resonator. The resonator is piezoelectrically actuated and vibrates laterally. Resonant frequency is determined by lateral dimensions rather than by thickness [96].

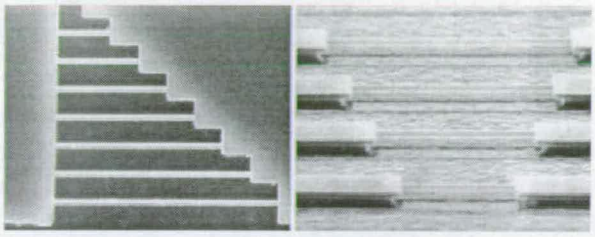

Figure 2.5. Submicron doubly clamped SiC bridges. Nanometer sized SiC bridges are actuated by exposing them to a strong magnetic field and passing an alternating current through the device. The resulting Lorentz force causes resonance at one of the bridge's intrinsic harmonics [149].

Capacitive actuated resonators consist of a suspended mechanically vibrating member, e.g. comb [88], beams [6] disks [140] and input and output transducer electrodes. The application of a Directed Current (DC) bias voltage and Alternating Current (AC) excitation signal between vibrating member, e.g.diamond disk [140] and input electrode produces mechanical resonance, which is determined by the lateral dimensions of the resonator (see Fig. 2.6). Mechanical vibration generates a motional current at the output electrode, which when plotted as function of frequency traces a sharp resonant peak transfer function with a maximum resonant frequency of 1.51GHz. To attain a high Q of 10,100 in air, acoustic losses to the underlying substrate were minimised using the acoustic wave reflection between the polysilicon support stem and the diamond disk. Such high Q-factors in air further reduce cost, because expensive vacuum encapsulation to remove air damping as in previous reported resonators becomes redundant.

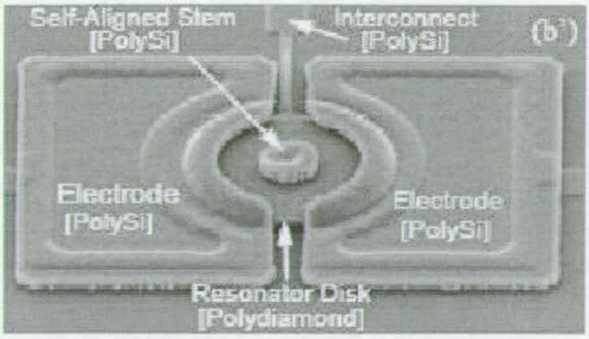

Figure 2.6. Capacitive actuated diamond disk resonator. The diamond disk is suspended by a polysilicon stem to reduce acoustic losses to the underlying substrate [140]. Vibration is generated by a DC bias and AC actuation signal between one of the electrodes and the disk resonator. The resonator operates at resonance when the frequency of the actuation signal equals one of the mechanical resonant frequencies of the disk.

Unlike piezoelectric actuated devices, capacitive resonator fabrication is compatible with CMOS manufacturing and devices do not require electrodes on top of the device to actuate and sense vibration. Electrodes on top of resonators add to the overall damping and reduce the mechanical Q-factor of the device. Additionally, the DC bias voltage used to charge up capacitive resonators can be employed to switch resonators on and off, which lowers the number of switches in front end transceivers and therefore reduces insertion loss and cost.

Inefficiency of capacitive resonators is caused by the low electromechanical coupling, which produces a high device impedance. This makes matching to macroscopic elements such antenna difficult, since these require impedances of 50Ω or 377Ω for maximum power transfer [85]. Piezoelectric transduction can achieve higher electro mechanical coupling and therefore lower impedances (80Ω [96]). Indeed piezoelectric resonators [96] can present a solution to the impedance problem.

However, capacitive lateral vibrating mechanical resonators have higher Qs, process simplicity and IC compatibility (lower cost), and built-in switchability [87]. Their biggest advantage, however, is that they can be interlinked to micromechanical circuits such as filters and oscillators.

Micromechanical filters and oscillators

The most attractive application of micromechanical resonators includes frequency selection (via micromechanical filters) and low power frequency generation (i.e oscillators) using a combination of resonators and transistor electronics [87].

A typical topology of a micromechanical bandpass filter consists of a number of resonator tanks connected with one another using coupling elements. Coupling between individual resonator tanks can be performed either capacitively or mechanically. For more information, the reader is referred to an excellent book [52], which gives a detailed description on different filter designs and concepts.

A recent published [23] composite mechanical filter (Fig. 2.7) consist of an array of mechanically coupled square micromechanical resonators. This design provides the designed filtering function with a centre frequency of 68.1MHz, insertion loss of 2.7dB and bandwidth of 0.28%. The advantage of the arraying approach is that the outputs the individual resonators are summed to a larger current for a given input voltage and hence a lower impedance and allowing matching to 50Ω.

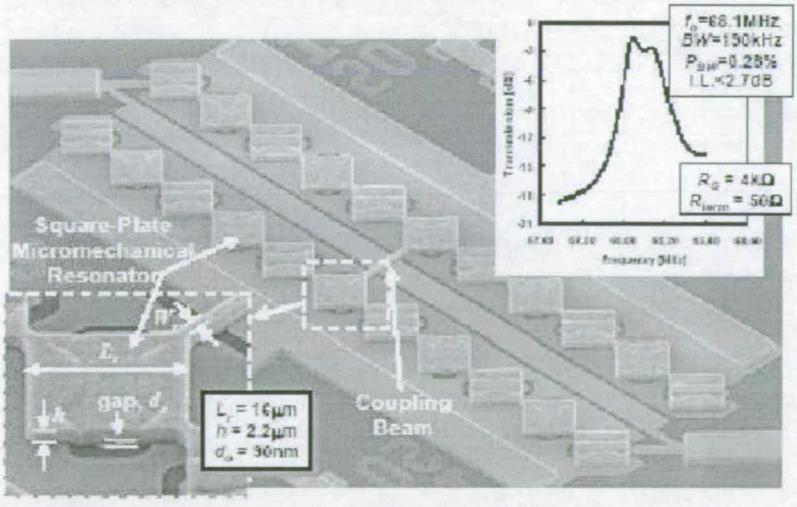

Figure 2.7. Array coupled 68.1 MHz micromechanical filter. SEM picture and transmission curve of a micromechanical bandpass filter comprised of 43 coupled square plate resonators [23].

However, such small impedances can only be achieved with a sufficient large number of coupled devices. A large number of coupled filters, however, are prone to mechanical shock, which can present a reliability issue of these devices. Therefore, alternative solution need to found to solve the impedance problem of capacitive resonators.

Apart from filtering functions, high micromechanical resonators can also be used as high-Q ultra stable local oscillators for frequency generation. Local oscillators in wireless transceiver require high-Q resonators with a high thermal stability to ensure a stable resonant frequency over time and low phase noise [83]. An example of a micromachined oscillator is shown in Fig. 2.8, depicting a 61MHz oscillator based on a micromechanical disk resonator with a power consumption of 950μW [69].

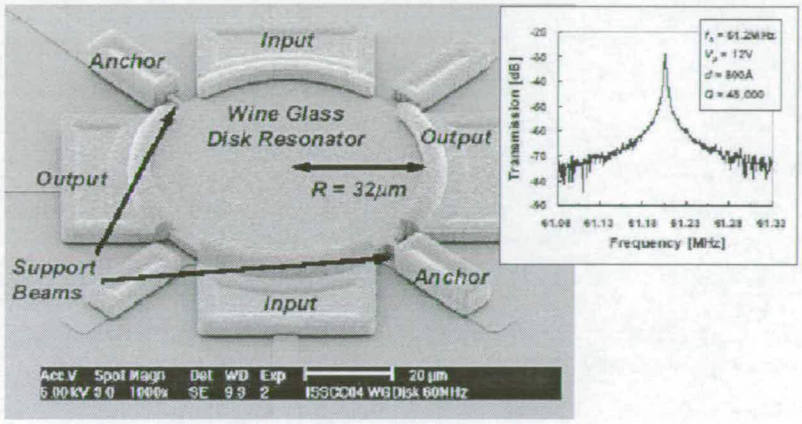

Figure 2.8. SEM picture of a 61MHz disk oscillator. The frequency setting element of this oscillator is a disk resonator operating at a resonant frequency of 61MHz with a Q-factor of 10,00 [69].

2.3 Micromechanical Resonators

Micromechanical resonators are building blocks for filters and ultra stable oscillators. Their manufacturing process provide devices with a variety of possible resonant frequencies largely dependent on the devices geometries and material.

In this section, micromechanical cantilever beam and bridge resonators will be reviewed in terms of their design, electrostatic actuation, fabrication and remaining research issues are discussed.

2.3.1 Geometrical Design

The simplest micromechanical resonators are the cantilever beam and bridge resonator as shown in Fig. 2.9. By applying the elementary theory of bending of beams [129],

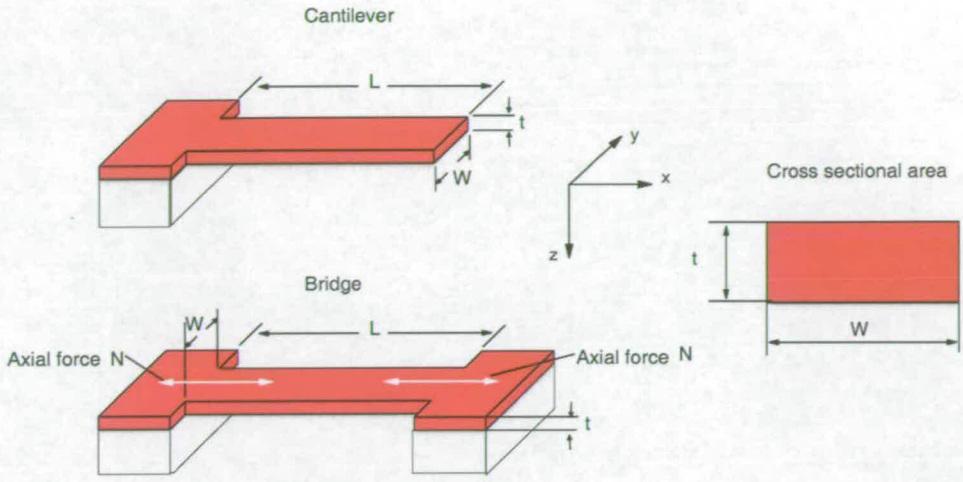

Figure 2.9. Schematic of a cantilever and bridge resonator. Both resonators are defined by their length L, width w and thickness t. Their resonant frequencies are determined by their geometry and material properties. Depending on the sign, the bridge resonant frequency is decreased for compressive and increased for a tensile force N acting along the length of the resonator. Cantilevers are not influenced by an axial force, since this is relieved through the free end of the device.

one can determine the fundamental natural frequency of a cantilever beam and bridge resonators of length L, width w and thickness t using the relationship:

$$f_0 = \frac{(k_n\, L)^2}{2\pi\, L^2}\sqrt{\frac{\hat{E}I}{\rho\, A}} \tag{2.1}$$

where k_n are the roots of the frequency equation for n modes of vibration. For the first mode of vibration, the root value for cantilever beams is (k_1=1.875) and for bridges (k_1=4.73), respectively.

Other variables in Eq. (2.1) such as I,$\hat{E}$, $A = w\ t$, ρ are the second moment of area, effective Young's modulus, cross sectional area and mass density, respectively.

For wide resonators ($w/t\ > 5$), the Young's modulus E is replaced with the *effective* Young's modulus $\hat{E} = E/(1-\eta^2)$ [130]. The second moment of area for a rectangular cross section is:

$$I = \frac{wt^3}{12}. \tag{2.2}$$

The mode shape for the first vibrational mode can be written as:

$$X(x) = \alpha\,(cos(kx) - cosh(kx)) + sin(kx) - sinh(kx) \tag{2.3}$$

for cantilevers with $k_1 = 1.875/L$, $\alpha_1 = -1.3623$ and for bridges with $k_1 = 4.730/L$, $\alpha_1 = -1.01781$, respectively [129]. Note, this equation assumes fixed boundary conditions for the cantilever and bridges with no etch undercut and no vibrational movement at their supports.

When an initially flat prismatic homogeneous bridge is subjected to an axial force N, the resonant frequency will differ from the stressless state (see Fig. 2.9).

In this case the expression for the resonant frequency ($f_n(N)$) for mode n can be found by applying the Rayleigh method and is given by [11, 128]:

$$f_n(N) = f_{0n}\sqrt{1 + \gamma_n \frac{NL^2}{12\hat{E}I}} \tag{2.4}$$

, where γ_n is a coefficient with a given value for the first vibrational mode $\gamma_1 = 0.295$ [128].

In case compressive axial forces exceed the buckling point, $N = -N_b = 4\pi^2 \frac{\hat{E}I}{L^2}$, a zero resonant frequency is found for the first vibrational mode. For compressive forces beyond this buckling point, the above model is not adequate [128]. Further, the effect of shear deformation, rotational inertia and squeeze film damping are omitted in the above analysis [11].

2.3.2 A model for composite beams

The following section describes the development of an analytical model to calculate the change in resonant frequency of bridge and cantilever beam resonators as a result of a film being deposited. The developed analytical model assumes that the cantilevers and bridge resonators as well as the deposited layer are stress free. The vibrational mode shape does not change with the deposited layer and any friction and sliding at the interface between the resonator and the deposited layer during flexural vibration are neglected. Damping effects in the resonator or in the deposited film are omitted from the analysis. Additionally, the resonator is considered stress free with fixed boundary conditions at their supports.

For the analysis, beam or bridge resonators are treated as spring-mass systems. In this case, the stiffness and the mass of the resonators at any point along their lengths are summarised into so called "equivalent" values. In this situation, the resonator spring-mass systems is made up of an equivalent stiffness k_{eq}, which resonates the equivalent mass m_{eq} at a given frequency f_0 [52].

$$f_0 = \frac{1}{2\pi}\sqrt{\frac{k_{eq}}{m_{eq}}} \tag{2.5}$$

, where the m_{eq} and k_{eq} are calculated as follows [34]:

$$m_{eq} = \rho w t \int_0^L (X(x))^2 dx \tag{2.6}$$

$$k_{eq} = \hat{E} I \int_0^L \left(\frac{d^2X(x)}{dx^2}\right)^2 dx \tag{2.7}$$

The function $X(x)$ is the mode shape of the resonators as defined in Eq. (2.3).

The neutral line (zero stress and bending moment) of the bridge/beam resonators shifts when a film is deposited. In order to determine the location of the new neutral line, the composite cross section is transformed by multiplying the width of deposited film (w_{film}) with the modular ratio [37]: $mr = \frac{\hat{E}_{film}}{\hat{E}_{beam}}$ (see Fig. 2.10(b)). The variables $\hat{E}$ and $\hat{E_{film}}$ are the effective Young's moduli of the resonator material and of the deposited film, respectively.

The new neutral line is:

$$\acute{Z} = \frac{w_{film}t_{film}\left(t + \frac{t_{film}}{2}\right) + wt\left(\frac{t}{2}\right)}{\left(w_{film}t_{film}\right)\left(wt\right)}. \tag{2.8}$$

The second moment of areas for both the resonator and the film are:

$$I_b = \frac{1}{12}(w)(t)^3 + (w)(t)(\acute{Z} - \frac{t}{2})^2 \tag{2.9}$$

$$I_{film} = \frac{1}{12}(w)(t_{film})^3 + (w)(t_{film})[(t + \frac{t_{film}}{2}) - \acute{Z}]^2 \tag{2.10}$$

The frequency f_{film} of deposited beams or bridges can be modelled by [34]:

$$f_{film} = \frac{1}{2\,\pi}\sqrt{\frac{k_{eq} + \Delta k}{m_{eq} + m_{film}}}. \tag{2.11}$$

where Δk and m_{film} are the added stiffness and mass to the resonator.

The added mass is calculated by:

$$m_{film} = \rho w t_{film} \int_0^{L_{film}} (X(x))^2 dx \tag{2.12}$$

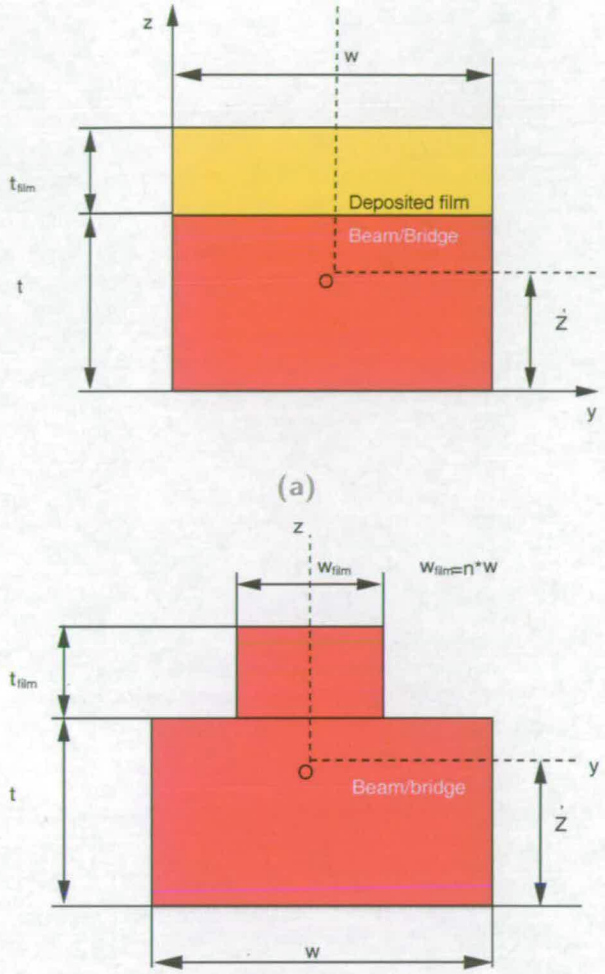

Figure 2.10. Composite beam/bridge resonator. (a) Cross section and (b) Transformed section.

The stiffness of the composite bridge or beam is:

$$k_c = \hat{E} I_b \int_0^L \left(\frac{d^2 X(x)}{dx^2} \right)^2 dx + \hat{E}_{film} I_{film} \int_0^{L_{film}} \left(\frac{d^2 X(x)}{dx^2} \right)^2 dx. \tag{2.13}$$

where the variable L_{film} is the length of the deposited film on the resonator.

The added stiffness Δk is calculated from k_c by:

$$\Delta k = k_c - k_{eq}. \tag{2.14}$$

The change in resonant frequency as result of a deposited layer is then:

$$\Delta f_0 = \frac{f_0 - f_{film}}{f_0} \tag{2.15}$$

In principle, this model can be extended to resonators with n layers. The resonant frequency of a resonator with n layer is:

$$f_{film}n = \frac{1}{2\,\pi}\sqrt{\frac{k_{eq} + \sum_{i=1}^{n} \Delta k_i}{m_{eq} + \sum_{i=1}^{n} \Delta m_{film}i}}. \tag{2.16}$$

In case the change in resonant frequency Δf_0 is a result added mass of a film m_{film} alone, one can write [111]:

$$\Delta f_0 = -\frac{1}{2}\left(\frac{m_{film}}{m_{eq}}\right) f_0 \tag{2.17}$$

In case both the stiffness Δk and mass are added, then the change in resonant frequency can be expressed by:

$$\Delta f_0 \cong \frac{1}{2}\left(\frac{\Delta k}{k_{eq}} - \frac{m_{film}}{m_{eq}}\right) f_0 \tag{2.18}$$

Note, Eq. (2.17) and Eq. (2.18) are only valid, if $m_{eq} \gg m_{film}$ and $k_{eq} \gg \Delta k$.

2.3.3 Quality Q-factor

The main advantage of MEMS resonators is their high quality (Q)-factor. A high-Q in RF filters is important, because it prevents interferences from neighbouring transmitters entering the signal path of a receiver unit [82]. As a result, signals with less noise are passed down the receiving path of the transceiver. These low noise signals reduce the power consumption in a transceivers, since amplification is not required any longer to lift the signal above the noise level. Hence, a high-Q factor provides an improvement in signal quality and power savings in wireless transceivers.

The mechanical Q-factor itself is the ratio of the energy stored to the energy dissipated during one vibrational cycle. The Q-factor can be extracted from the frequency spectrum of a micromechanical resonator by relating the resonant frequency to the bandwidth as depicted in Fig. 2.11.

The Q-factor of a resonator depends on several damping mechanism, such as viscous damping, Q_v, damping to imbalances, Q_s, damping resulting from internal material related losses, Q_i, and surface related losses,$Q_{surface}$. These factors can be related to the

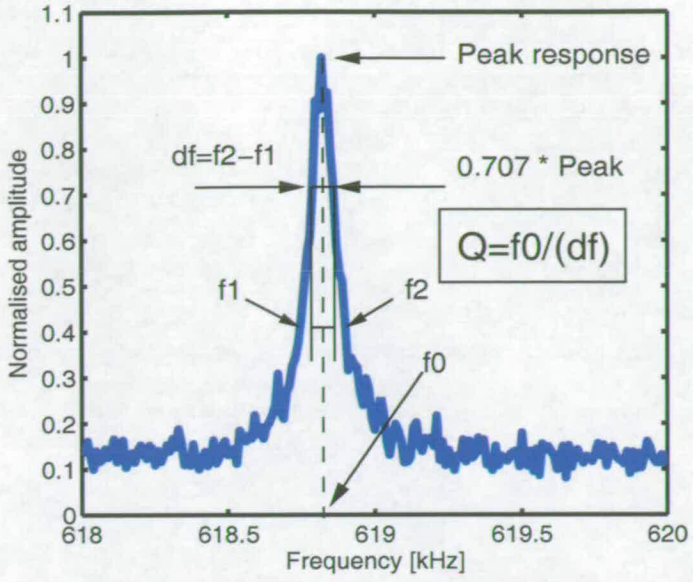

Figure 2.11. Measured frequency spectrum of a manufactured polysilicon bridge resonator. Measured frequency spectrum for a 619kHz polysilicon bridge resonator operated under vacuum (p=20μbar). The Q-factor of 10,314 was determined from the ratio of the resonant frequency and the bandwidth at $1/\sqrt{2}$ of the normalised amplitude [18].

overall Q-factor of a resonator as: $1/Q = 1/Q_v + 1/Q_s + 1/Q_i + 1/Q_{surface}$ [117, 154]. This relationship indicates that lowest Q-factor limits the total Q of a resonator.

Viscous damping arises when a resonator is operated in a fluid or gas. In a gas pressure strongly influences the Q-factor above 1mTorr [154]. In this regime, so called viscous elastic damping takes place, which can be divided into squeeze film damping for out-of-plane vibrating structures and Couette damping for lateral vibration [46]. In order to attain a high-Q factor, resonators are often operated in vacuum. However, recently demonstrated resonators [140, 67] achieved a Q as a high as 10,100 under atmospheric pressure mainly due to the small vibrational amplitude and reduced anchor losses.

When a resonator is operated in vacuum, the Q-factor is influenced by support losses through the anchor structure and internal material losses. Support losses arise when vibrational energy is transfered from the resonating structure into the underlying substrate. Support losses can be reduced using resonators with a balanced vibration movements, i.e. using triple bridge structure operating in antiphase mode [117].

Internal damping is dependent on the purity, dislocation and thermoelastic damping of the material being used. Thermoelastic damping is caused by irreversible heat flow across the thickness of the resonator as it oscillates [154].

During vibration the resonator material is constantly expanded and contracted. When the material contracts, it heats up and when it expands it cools. This process generates a temperature across the thickness of the resonator. Energy will flow from the hot side of the resonator to the cool, resulting in irreversible energy loss. The rate of energy dissipation depends on materials properties such as thermal conductivity, thermal expansion coefficient and heat capacity. It also is dependent on the resonant frequency [154].

Surface related losses arising from disruption of the atomic lattice and surface contamination. The surface layer in most cases does not substantially change the stored energy in a system, but can substantially enhance the dissipated energy [154] and reduce Q.

2.3.4 Capacitive Transduction

Vibration can be actuated and sensed using a number of methods, which were briefly discussed in Sec. 2.2.4. Capacitive actuation and detection is beneficial, because it is compatible with CMOS fabrication and has zero DC power consumption. This section briefly reviews capacitive actuation, which has been described in detail in [88], but is repeated for clarity and hightlights some of the issues that are of importance to the reported work in this thesis.

The earliest capacitively transduced resonators consisted of cantilevers [79] or clamped - clamped bridges, which were driven perpendicular to the substrate (Fig. 2.12). Other capacitive resonators include comb - structures and disks [88, 140] driven parallel to the substrate. For operation, the resonator is biased using a bias voltage $V_{PS} = V_P - V_S$ and excited by $v_d = V_d cos\omega_i t$. Resonance is created when the drive voltage frequency ω_d matches one of the several natural mechanical resonant frequencies of the resonator ($\omega_r = 2\pi\ f_0$) (Sec. 2.3.1). This periodical movement during vibration creates a time-varying capacitance between the resonator and electrodes. The generated motional current at the sense electrode is:

$$i_o = -V_{PS}\frac{\partial C}{\partial t} = -V_{PS}\frac{\partial C}{\partial z}\frac{\partial z}{\partial t} \tag{2.19}$$

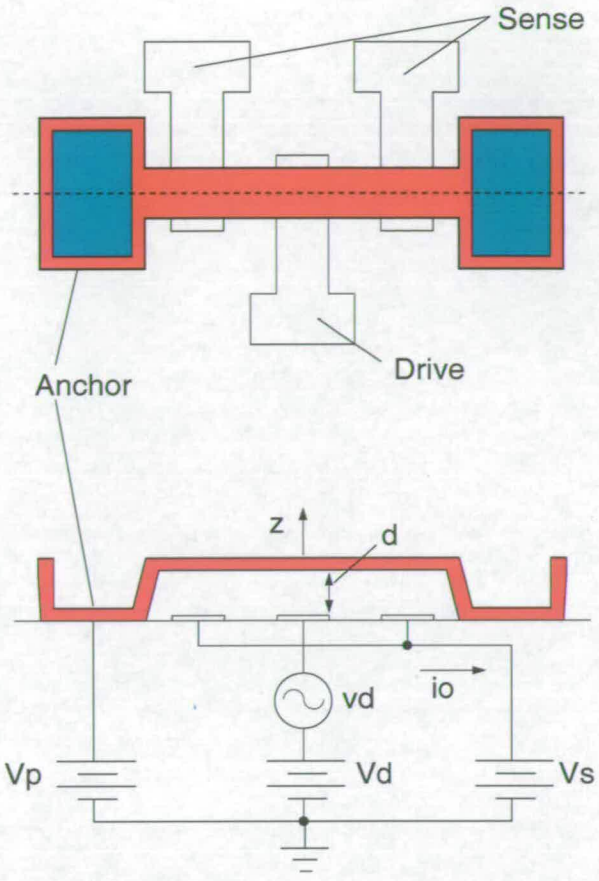

Figure 2.12. Schematic of a clamped-clamped electrostatic actuated resonator. Vertically capacitively driven microresonator with typical bias and excitation configuration.

where $\frac{\partial C}{\partial z}$ is the change of the sensing capacitance C per unit displacement z. Eq. (2.19) written in phasor form gives

$$I_o = -j\omega V_{PS} \frac{\partial C}{\partial z} Z. \tag{2.20}$$

Ignoring fringing fields and assuming a flat capacitor plate, the sense capacitance for a beam resonator as a function of displacement and is approximated by:

$$C(z) = \frac{\epsilon_o A_{overlap}}{(d+z)} = C_0 \left(1 + \frac{z}{d}\right)^{-1} \tag{2.21}$$

where $A_{overlap}$ is the overlap area and C_0 is the static capacitance between the resonator and the sense electrode. Differentiating Eq. (2.21) we obtain

$$\frac{\partial C}{\partial z} = -\frac{C_0}{d} \left(1 + \frac{z}{d}\right)^{-2} \tag{2.22}$$

Note, that with $V_{PS} = 0$, no motional current is generated. Hence, capacitively operated resonators can be switched on or off by means of their DC bias. This makes

the use of switches in transceivers redundant and improves power consumption and insertion loss figures.

The force F_d created by the drive electrode is

$$F_d = -\frac{1}{2}(V_{PS} + v_d cos\omega t)^2 \frac{\partial C}{\partial z} \tag{2.23}$$

After collecting terms of the same frequency as the drive, the resulting force at resonance is amplified by the mechanical quality factor Q and the DC bias voltage:

$$F_{\omega_0} = V_{PS} v_d Q \frac{\partial C}{\partial z} \tag{2.24}$$

According to Hooke's law, the spring restoring force during vibration is:

$$F = k_{eq} Z \tag{2.25}$$

where Z is the maximum displacement at resonance at the overlap area between the sense electrode and resonator.

The maximum resonator displacement Z at resonance is then given by:

$$Z = \frac{FQ}{k_{eq}} = \frac{QV_{PS} v_d}{k_{eq}} \frac{\partial C}{\partial z} \tag{2.26}$$

The motional current detected during vibration can be rewritten using Eq. (2.26) and Eq. (2.20):

$$I_o = \frac{V_{PS}^2 v_d Q}{k_{eq}} \left(\frac{\partial C}{\partial z}\right)^2 \tag{2.27}$$

The motional resistance of the resonator is defined as follows:

$$R_{eq} = \frac{v_d}{I_o} = \frac{k_{eq}}{\omega_0 Q \left[V_{PS}\left(\frac{\partial C}{\partial z}\right)\right]^2} = \frac{\sqrt{k_{eq} m_{eq}}}{Q\eta^2} \tag{2.28}$$

where

$$\eta = V_{PS}\left(\frac{\partial C}{\partial z}\right). \tag{2.29}$$

Apart from R_{eq}, other parameters such as equivalent inductance L_{eq} and C_{eq} can be derived. These three LCR parameters can be used to describe the behaviour of a resonator using an electrical circuit. This electromechanical analogy is beneficial when several coupled resonators (i.e. in a filter) have to be modelled. For more detailed information, the reader is referred to references [88, 4].

The series motional resistance R_{eq} is of most importance and is often referred as the impedance of the resonator. This parameter has to be small enough to match the impedances of antennas to avoid unwanted signal reflection from and to resonators. Additionally, the impedance determines the amount of output current for a given input voltage and the input-referred noise of a resonator. As smaller the impedance, the higher the output current and lower the generated noise level [80].

High-Q resonators for example, are accomplished with high R_{eq}, because of their relative high stiffness and mass [140]. One way of reducing the resonator impedance is to increase η, the electromechanical coupling, or alternatively the Q-factor of the resonator. The electromechanical coupling factor η strongly depends on the DC bias voltage V_{PS} and on $\frac{\partial C}{\partial z}$. The increase in DC bias is limited by the available supply voltage, which for handheld wireless communication equipment is in the order of 3-5V. The $\frac{\partial C}{\partial z}$ is directly proportional to the electrode-to-resonator overlap area $A_{overlap}$ and the electrode-to-resonator gap spacing d. The overlap area increase is limited by smaller and higher frequency resonators, while the gap distance can be defined by an oxide spacer thickness, and thus can be made very small in the range of hundreds Angstroms (10^{-10}m). Hence, increasing the electromechanical coupling and reducing R_{eq} by means of smaller gap spacing seems to be a reasonable approach.

2.3.5 Fabrication

Microfabrication technologies, which realise micromechanical RF MEMS structures, can be divided into (i) *surface* and (ii) *bulk* micromachining.

Bulk micromachining [58, 73] defines geometries photographically on a wafer and subsequently etches the *bulk* silicon (Si) using anisotropically or isotropically etching techniques to form three dimensional features. An example for bulk micromachining is a Si resonator [81]. The advantage of single crystal Si over its polysilicon counterparts is an order of magnitude higher Q-factor for resonators operating in the Medium Frequency (MF) range. However, Si bulk micromachining strongly restricts the use of arbitrary

device design, since resonators always have to be attached to the silicon substrate and so isolated anchor structures required for thermally stable comb-drive resonators are not feasible.

In contrast, surface micromachining [15, 73] uses a sequence of IC compatible layer deposition and patterning techniques to form mechanical components suspended over the Si substrate. Polysilicon is the material of choice for most of the micromechanical resonators, because it has a high intrinsic material Q factor and offers, in combination with a surface micromachining process, design flexibility to produce devices with arbitrary shape and anchors. In this case, resonator structures are often produced as a result of a single masking step and can be integrated with transistor electronics on the same die either before (pre-CMOS), during (Mixed-CMOS-MEMS) or after (post-CMOS) microresonator fabrication [88].

Howe and Muller demonstrated the first surface micromachined suspended Low Pressure Chemical Vapour Deposition (LPCVD) polysilicon beam resonator structures using silicon dioxide (SiO_2) as a sacrificial layer in the early 1980s [47]. This process sequence (with modification) is still used today and is shown in Fig. 2.13. The fabrication

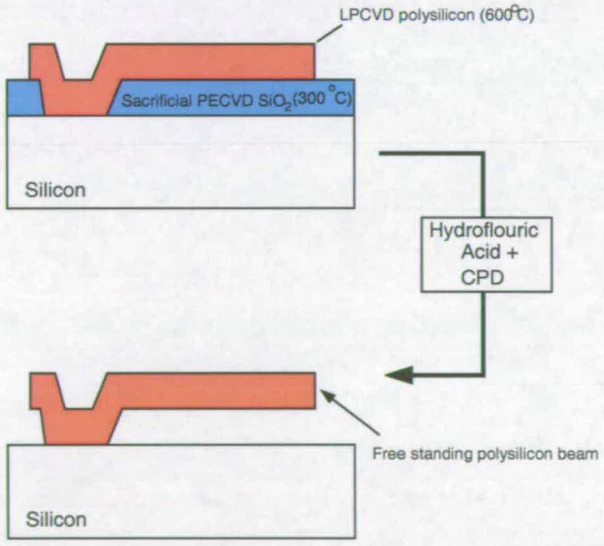

Figure 2.13. Surface micromachining process. The free standing structure is formed by a row of deposition, etching and final sacrificial SiO_2 removal. SiO_2 is followed by a Critical Point drying (CPD) using liquid carbon dioxide to prevent stiction of the micromechanical resonators.

relies on a thermally grown sacrificial silicon dioxide SiO_2 layer, which is used as support for the polysilicon during deposition, doping, annealing and dry etch patterning.

To form a free standing suspended microstructure, the sacrificial SiO_2 is subsequently removed via wet chemical etching in hydrofluoric acid (HF) and dried using critical point drying (CPD) in liquid carbon dioxide (CO_2). Polysilicon surface micromachining also inherently includes the possibility to produce different capacitively actuated microresonator designs such as comb-structures [123], clamped-clamped beams [81] and nowadays suspended rings and disks on the same die [67, 140].

The fabrication of a high-Q disk resonators involves the deposition, doping, photolithographically patterning and subsequent etching of a polysilicon layer to define the resonator disk (Fig. 2.14). After etching the polysilicon resonator disk is thermally oxidised to provide a thin sacrificial SiO_2 layer to later define the capacitive transducer gap width. After oxidation, another polysilicon layer is conformally deposited, doped and etched to form the transducer electrodes. The resonator structures are subsequently wet chemically released using HF.

The high number of fabrication steps in this process increase the cost of disk resonator devices and therefore of the overall transceiver unit. Additionally, during fabrication electrodes are produced, which partly overhang the resonator device. Such an electrode arrangement is likely to cause signal coupling between in and output transducer electrodes, especially when the resonant frequencies are high and disk diameters small. The removal of the sacrificial SiO_2 between the resonator and the electrodes is difficult, especially when smaller capacitive gaps and lower impedances are required. This consequently limits gap width and the reduction in impedance. However, lower impedances are required to keep up with the rising stiffness of resonators with increasing resonant frequencies (Eq. (2.28)).

The issue of electrostatic coupling between input and output electrodes and the difficulty of releasing sacrificial transducer gaps can be easily resolved by planarising resonator electrodes using Chemical Mechanical Polishing (CMP).

Global planarisation via CMP planarisation is a standard tool in semiconductor manufacturing to achieve submicron linewidths and multilevel interconnects. The reader is referred to [158] for a very detailed review on CMP in microelectronics.

CMP is relative new to the field of MEMS and it can produce flat mirror like surfaces for optical devices [136], is an alternative tool for material etching for Field Emission Devices [63], reduces the roughness for improve wafer bonding and enables planarised multilevel polysilicon devices such as microengines and pressure sensors [116].

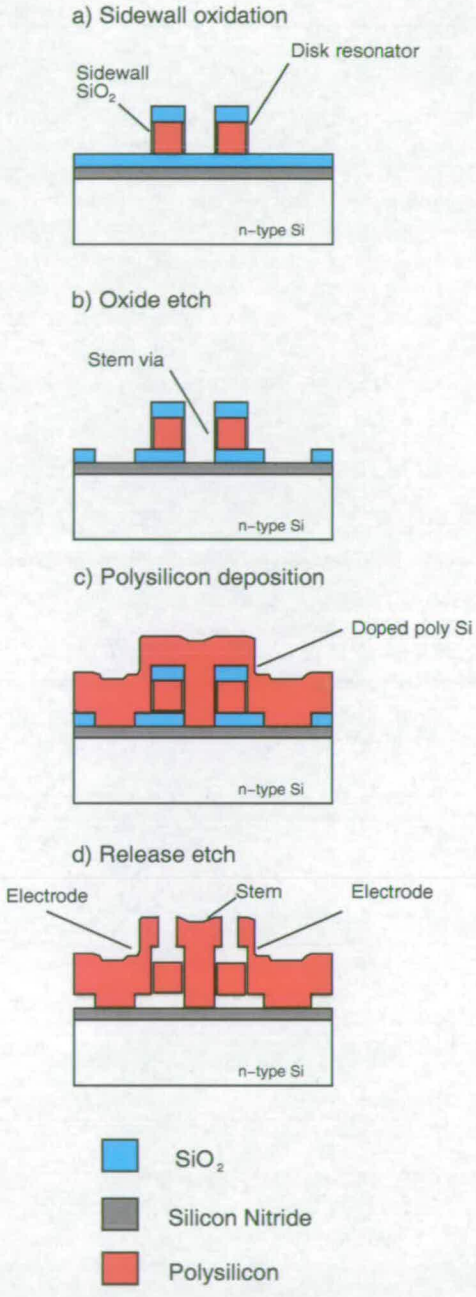

Figure 2.14. Fabrication process for a disk resonator. This process involves the deposition, doping, patterning and subsequent etching of two polysilicon layers to define the disk resonator and transducer electrodes. The thin capacitive transducer gap is produced by a nanometer thick sacrificial SiO_2 layer, which is wet chemically removed during the device release etch using HF [141].

During a CMP planarisation process (Fig. 2.15), the device wafer is pressed face down against a rotating polishing pad, while a a chemically and physically (abrasive) acting slurry planarises the wafer [158]. The amount of material removed R_{CMP} by the action

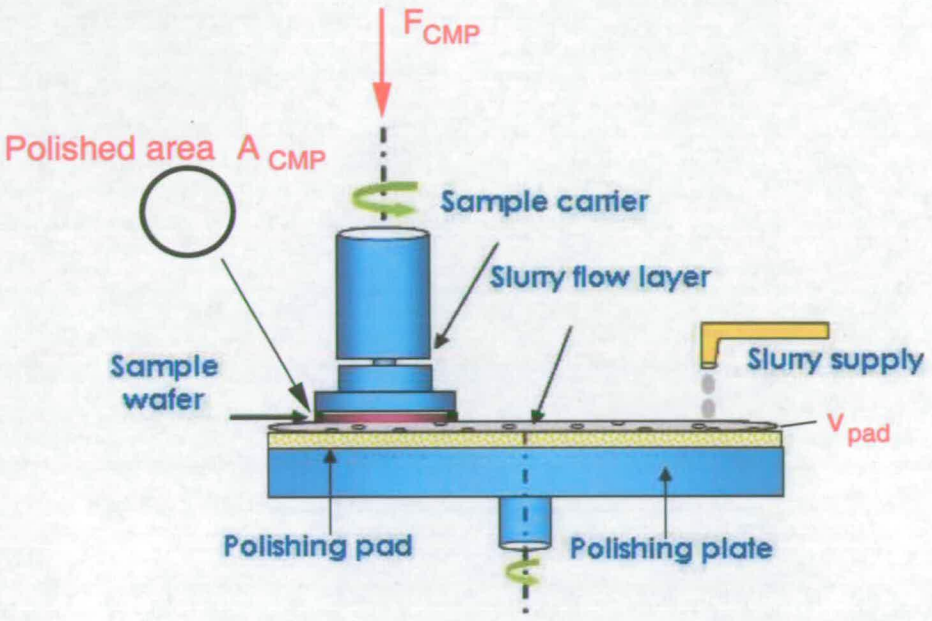

Figure 2.15. Representation of a CMP planarisation process. The layer on the wafer is planarised under pressure by pressing the a rotating wafer against a polishing pad in the presence of a slurry. (Picture courtesy: Korea University) [133].

of CMP is defined by Preston's law. This law states that the CMP removal rate depends on linearly on the polishing pad velocity v_{pad} and force F_{CMP} the wafer area A_{CMP} is pressed against the polishing pad [153]:

$$R_{CMP} \approx v_{pad} \frac{F_{CMP}}{A_{CMP}}. \tag{2.30}$$

The process shown in Fig. 2.16 uses CMP and greatly simplifies the fabrication of high-Q capacitive resonators. It uses a combination of photolithography and CMP to produce submicron transducer gaps (Ch. 2). To produce such gaps, photoresist is applied on top of sacrificial Germanium (Ge). The photoresist is patterned and critical line widths are further reduced by oxygen plasma treatment to the required submicron gap widths. PolySiGe is subsequently deposited and CMP planarised to produce the resonator and adjacent in and output electrodes. In the final step sacrificial Ge is wet chemically removed to produce submicron gaps and the movable micromechanical resonator.

This CMP fabrication process suffers from several disadvantages. One of them is tapering of the critical gap linewidth after photoresist oxygen plasma treatment. This inevitably increases the transducer gap width and causes a rise in resonator impedance. Another drawback of this process is that the device yield is considerable affected by the fragile photolithograhic defined sacrificial Ge blades and the absence of a CMP polishing stop layer (Fig. 2.16 a)-c)). The fragile Ge blades are easily destroyed during following fabrication, which results in resonators with missing transducer gaps. The absence of a polishing stop layer consequently produces resonators with a varying thickness and resonant frequency across the wafer. In extreme cases, all PolySiGe is completely removed. This would affect the device yield considerably. Additionally, reported poor etch selectivity between sacrificial Ge and PolySiGe widens the transducer gap, which affects the impedance even more [100].

2.3.6 Research issues and future outlook

Although micromechanical resonators can operate at GHz frequencies, have high-Q factors in air, zero DC power consumption and can be integrated with CMOS electronics; research issues for these devices remain. Apart from f_0 or Q, other important parameters of capacitive resonators that require further investigation are: temperature and aging stability, impedance and tuning.

Capacitive resonators have shown excellent thermal stabilities [48] comparable or even better than the AT-cut quartz crystal resonators commonly used for local oscillator applications in wireless transceiver technology. However, there is still the requirement for more comprehensive long term stability tests to be undertaken.

As indicated before, high intrinsic impedance is one of the reasons why micromechanical resonators are not employed by end users as filters in wireless transceivers. Impedance can be reduced by increasing the electrode-to-resonator area, decreasing the capacitive gap area or increasing the DC bias. Unfortunately, the bias voltage can not be made infinitely large due to supply voltage constraints of low power receivers. The electrode area reduces even further with high frequency and stiffer resonators. Hence, a decrease in resonator gap seems to be a reasonable approach to reduce the impedance of micromechanical resonators.

Although surface micromachined resonators vibrate with resonant frequencies in the GHz range, tolerances during the fabrication process and environmental factors such

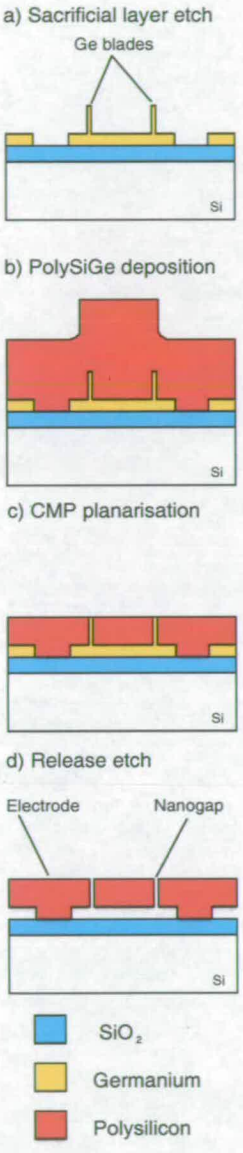

Figure 2.16. CMP resonator fabrication. The process published in [100] uses standard lithography and subsequent photoresist ashing to achieve the critical gap dimensions. Tapering of the resist profiles causes a variation in transducer gap width which inevitably increases impedance.

as temperature and contamination cause frequency deviations from their designed value. To apply these resonators in filters and oscillators, a suitable tuning method for micromechanical resonator has to be found. In this situation, it be would be advantageous if the resonant frequency could be tuned without device failure and in a real time manner during device operation.

Once the above issues have been solved, high-Q resonators and other RF components can be integrated into future multiband wireless front end transceivers and shown in Fig. 2.17 [85].

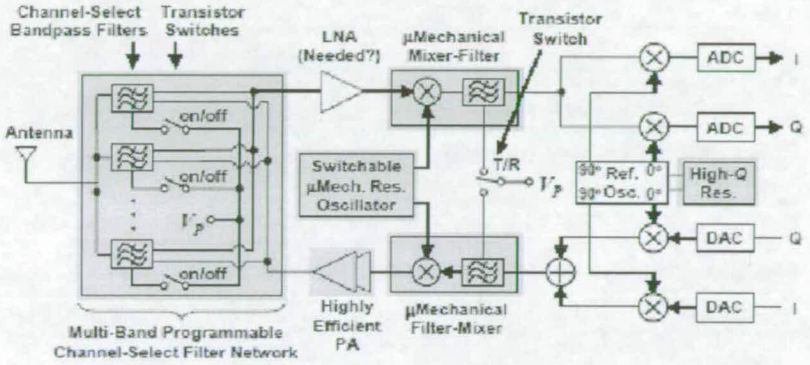

Figure 2.17. System-level block diagram of low power RF channel select transceiver architecture. Active solid-state and passive off-chip building blocks are replaced by passive-high-Q micromechanical building building blocks (shaded areas) to enhance robustness and power consumption of present-day wireless front-end transceivers [85].

The reasons for such architecture are power savings and robustness. Power savings are mainly achieved by the characteristic zero DC power consumption and high-Q RF components. High-Q factor in resonators makes Low Noise Amplifiers (LNA) after multi-band channel select filter network redundant, since amplification of the received signal against losses and noise is no longer required. Additionally, transistor switches to change between the transmitting or receiving path are no longer required due to the built in switchability of capacitive micromechanical filters. In all, the use of RF MEMS components will provide integrated, miniaturised low power wireless transceivers with an increased and improved functionality and battery life.

2.4 Conclusions

This chapter has reviewed and compared RF MEMS components and circuits with their solid state and macroscopic counterparts. This identified that RF MEMS devices have higher Q-values and enable future wireless transceivers with lower power consumption and increased functionality. However, current MEMS devices such as switches and resonators have to be further improved in areas such as aging, reliability and speed where their macroscopic and solid-state counterparts are still better. Capacitive transduced resonators in particular seem to be best suited for filter and oscillator applications due to their inherent IC compatibility and zero DC power consumption.

In the second part of this chapter, topics such as geometrical design, a deposited tuning model, capacitive transduction, fabrication and remaining research issues of polysilicon micromechanical resonators were developed and explained. It was pointed out that improvements in fabrication of high-Q resonators and post-fabrication tuning are issues that need to be addressed to reduce impedance, reduce cost and frequency variability of high-Q micromechanical resonators. Future trends in RF MEMS architecture were briefly addressed and their impact highlighted.

Chapter 3

Frequency tuning methods for MEMS resonators

This chapter quantifies the strength of frequency variations in resonators and reviews and compares published active and passive MEMS resonator frequency tuning methods.

3.1 Introduction

Micromechanical capacitive transduced resonators have favourable properties such as high Q, low power consumption and a small size. Their full potential lies in their ability to be interlinked with each other to make micromechanical circuits, which form highly selective bandpass filters and high precision oscillators. When such filters and oscillators are used in wireless transceivers, power consumption and cost is reduced and functionality increased. To ensure good performance, the resonant frequency of resonators in bandpass filters has to be held within 0:03% [84]. In oscillators, the frequency drifts should not be more than 4ppm per year [83].

However, the resonant frequency of micromechanical resonators is changed by various effects, including those originating from fabrication tolerances and variations in ambient environmental conditions. Depending on the strength of these effects, the resonant frequency can differ significantly from the designed value. In this situation, a tuning method has to be employed that can make both *fine* and *coarse* adjustments to individual resonators to match their frequencies to the designed values. For example, resonators in micromechanical filter with unmatched resonant frequencies cause passband distortions, which need to be corrected to ensure the designed filter response. Hence, a tuning method is required to correct and match the resonant frequency to the specified values.

This chapter first identifies and quantifies the strength of these resonant frequency variations found in micromechanical resonators and then reviews and categorises reported frequency tuning methods to correct them. In each category, tuning methods are described and compared with each other.

3.2 Frequency variations

The frequency stability of micromechanical resonators is influenced by fabrication tolerances and changes in ambient environmental conditions. Frequency changes caused by fabrication tolerances can be corrected after device manufacturing using one of the available tuning methods (Sec. 3.3). These changes alter the resonant frequency over a small period of time and influence the so called *short* term frequency stability of a resonator. Changes in environmental conditions, including temperature, pressure and contamination, alter the frequency after tuning during the whole lifetime of the device.

These effects influence the *long* term frequency stability of a resonator. This section addresses effects, which influence both the short and long term frequency stability of micromechanical resonators and quantifies the amount of tuning required to correct their impact on the resonant frequency.

The short term frequency stability of micromechanical resonators is influenced by fabrication related effects such as as layer non-uniformity, lateral device variations and biaxial stress. While the former have been reported to cause maximum frequency changes of up to 3% [88], the latter can alter the resonant frequency by several per cent. The amount of biaxial stress and tuning in those polysilicon resonators can be greatly reduced using a combination of doping and annealing techniques (Appendix B), but small residual stress (±20MPa) always remains and contributes to the resonator frequency variation. To illustrate this, Eq. (2.4) is rewritten to normalise the resonant frequency with $f_1(\sigma)$ and without f_0 biaxial stress $\sigma = \frac{N}{A}$ of out-of-plane vibrating polysilicon bridge resonators of length L, width w and thickness t

$$\frac{f_1(\sigma)}{f_0} = \sqrt{1 + \gamma_1 \frac{\sigma L^2}{\hat{E} t^2}} \tag{3.1}$$

with $\gamma_1 = 0.295$ for the first vibrational mode.

Fig. 3.1 shows the normalised resonant frequency as a function of residual biaxial stress for 2μm thick, 20μm wide polysilicon bridge resonators with different lengths ranging from 40μm-200μm. The graph shows the frequency dependence of micromechanical bridge resonators on biaxial stress. The resonant frequency of bridges increases for tensile and decreases for compressive biaxial stress. The graph also shows that a resonator's frequency change depends on the device length. Long bridges show large frequency changes (up to 46%) for tensile and tend to buckle for compressive biaxial stress. Short bridges also show a considerable amount of frequency change (2.2%) for both compressive and tensile biaxial stress, for example, those with the same length (40μm) used for temperature compensated micromechanical oscillators [48].

The simple mathematical model indicated that a tuning method is needed in the presence of relatively small biaxial stress to make *coarse* changes in frequency over several per cent in commonly used resonators.

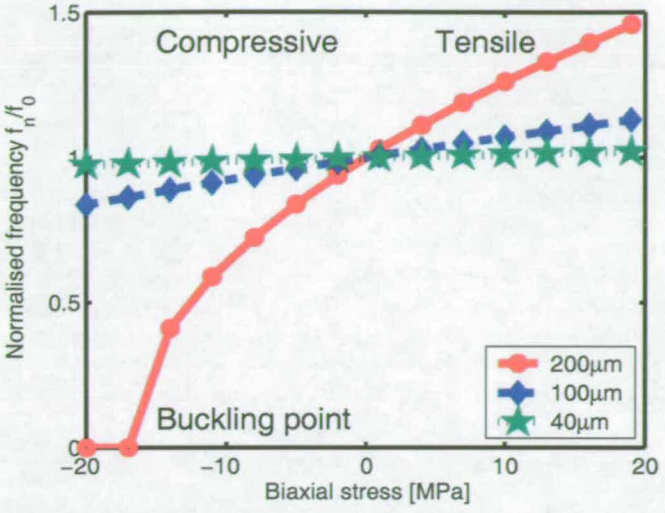

Figure 3.1. Normalised resonant frequency as a function of biaxial stress. This graph shows the normalised resonant frequency (first vibrational mode) as a function of compressive and tensile biaxial stress for polysilicon bridge resonators with various lengths. The resonant frequency of different sized resonators is altered by even small residual biaxial stress in the polysilicon. The resonant frequency of shorter bridges is less affected by the biaxial stress than that of longer ones. Longer resonators start to buckle even for relatively small amounts of stress, indicated by the zero resonant frequency of the 200μm long bridge. Hence, a frequency tuning methods needs to be used, which can perform *coarse* changes in resonant frequency over several per cent.

The long term frequency stability of micromechanical resonators is affected during their whole lifetime by changes in ambient environmental conditions and aging. Environmental conditions affecting the long term frequency stability include device contamination [155], temperature and humidity [57]. These effects have been reported to change the resonant frequency by tens parts per million (ppm) [57]. Aging, as another factor affecting the long term frequency stability of micromechanical resonators, has been reported to change the resonant frequency by up to 0.22% during an initial stabilisation phase [94]. After this stabilisation phase, which is often defined as the burn-in time, the resonant frequency changes by no more than 1ppm per year [55]. For some applications, such as ultra stable oscillators, those relatively small long term changes in resonant frequency are not acceptable. In this situation, a tuning scheme is required, which can make *fine* frequency changes (ppm range) throughout the whole life time of the device.

In summary, to ensure a stable resonant frequency of resonators in the short and long term, a tuning method needs to be made available, which can perform *coarse* and *fine* changes in resonant frequency. The following section reviews a selection of tuning methods capable of performing these changes.

3.3 Tuning methods

Published tuning methods can be divided into *active* and *passive* methods. Methods of both categories alter the resonant frequency by changing the equivalent stiffness (k_{eq}) or mass (m_{eq}) of resonators. Active tuning requires energy to maintain tuning and causes no damage to the resonators structure. Passive tuning requires no external energy source to maintain tuning, instead they produce time permanent changes to the resonator structure. This section reviews and compares published tuning methods for both categories, which can be used to correct the above frequency variations in micromechanical resonators.

3.3.1 Active frequency tuning

Published active tuning methods can be divided into electrostatic [6, 151, 2, 3, 64] and electrothermal [121, 103] tuning. Both methods alter the stiffness of the resonator. These methods are summarised in Table 3.1.

An example of electrothermal tuning is shown in Fig. 3.2. In this example, a DC current is passed through the straight tuning beam suspension of a 31kHz comb-resonator. The process generates compressive stress and lowers the resonant frequency. The resonant frequency can be tuned over a relative large range of -1% to -6.5% with a minimum resolution of 0.5%, making it suitable to perform the needed *coarse* changes in resonant frequency. The advantage of this method is that it is easy to integrate with CMOS electronics and the mechanical quality-(Q) factor is not affected by the tuning method. However, power consumption of up to 25mW can become an issue if several tens of resonators have to be tuned at once.

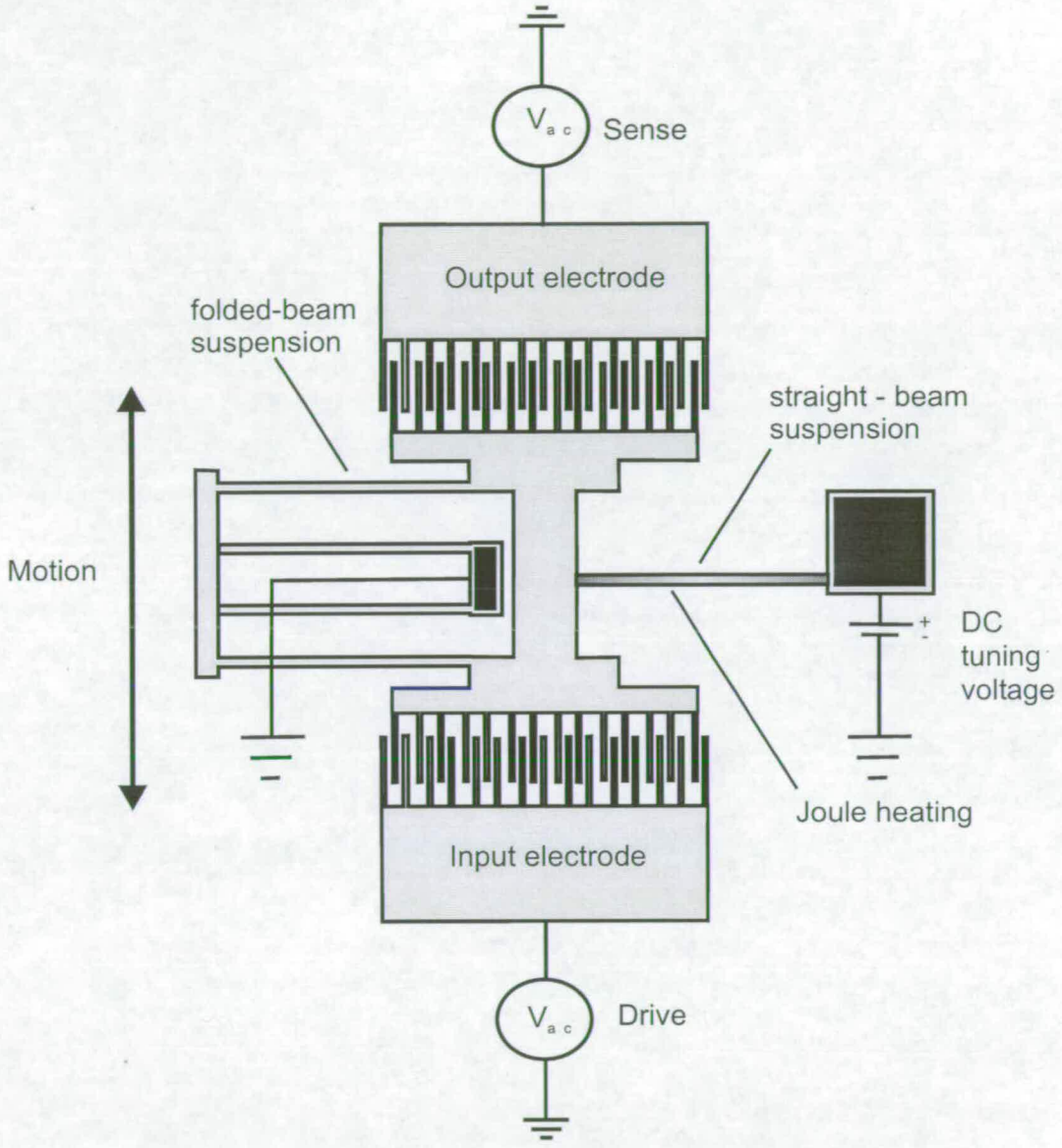

Figure 3.2. Example of the electrothermal frequency tuning of a comb-shaped micromechanical resonator. The comb-structure was modified by replacing one of the folded-beam suspensions with a straight suspension as the tuning beam. Tuning is achieved by passing a DC current through the straight-beam suspension of a comb-resonator. This generates compressive stress and lowers the resonant frequency of the resonator [103].

Method	Tuning range (accuracy)	Power consumption or Tuning voltage	Demonstrated frequency range (application)	Q-change	Ref.
Electrostatic	-9.4% - 0% (0.2%)	30V	7.8MHz (filters & oscillators)	no data available	[6]
Electrostatic	-6.25% - 0% (not specified)	35V	960kHz (sensors)	no data available	[151]
Electrostatic	-7% - 146% (not specified)	60V	21-23kHz (sensors)	no data available	[2]
Electrostatic	-55% - 0% (not specified)	150V	19kHz (sensors)	no data available	[64]
Electrothermal	-6.5% - 0% (0.5%)	25 mW	31kHz (sensors & resonators)	no change	[103]
Electrothermal	-25% - 50% (-2.5%/mW)	10mW	1-2kHz (sensors)	no data available	[121]

Table 3.1. Comparison of active MEMS tuning methods. Active frequency tuning can be controlled by an electronic circuit and is therefore amenable to integration with CMOS circuitry. Most tuning methods use electrothermal heating or an electrostatic force to change the resonator stiffness.

Electrostatic tuning (Fig. 3.3) uses a DC voltage to change the resonant frequency of capacitively actuated 7.8MHz resonators [6]. The DC tuning voltage imposes a transverse electrostatic force onto microresonators [6], which reduces the equivalent resonator stiffness. A reduction in equivalent stiffness decreases the resonant frequency over a relative wide range (-9.4%).

This method can be integrated with CMOS electronics and in contrast to electrothermal tuning dissipates virtually zero power. However, the large tuning voltage (35V) used to perform the required *coarse* frequency changes makes it difficult to use this method within low power wireless transceivers, where limited battery supply voltage (3V) is available. However, electrostatic frequency trimming is an alternative to ensure the long term frequency stability of micromechanical resonators. In this situations, *fine* (ppm range) rather than *coarse* changes in frequency and hence smaller DC bias voltages are required. In contrast, electrothermal tuning might be an option to perform large changes in frequency and ensure the short term stability of micromechanical resonators, but increased power consumption presents a bottleneck when several resonators in a filter arrangement need tuning.

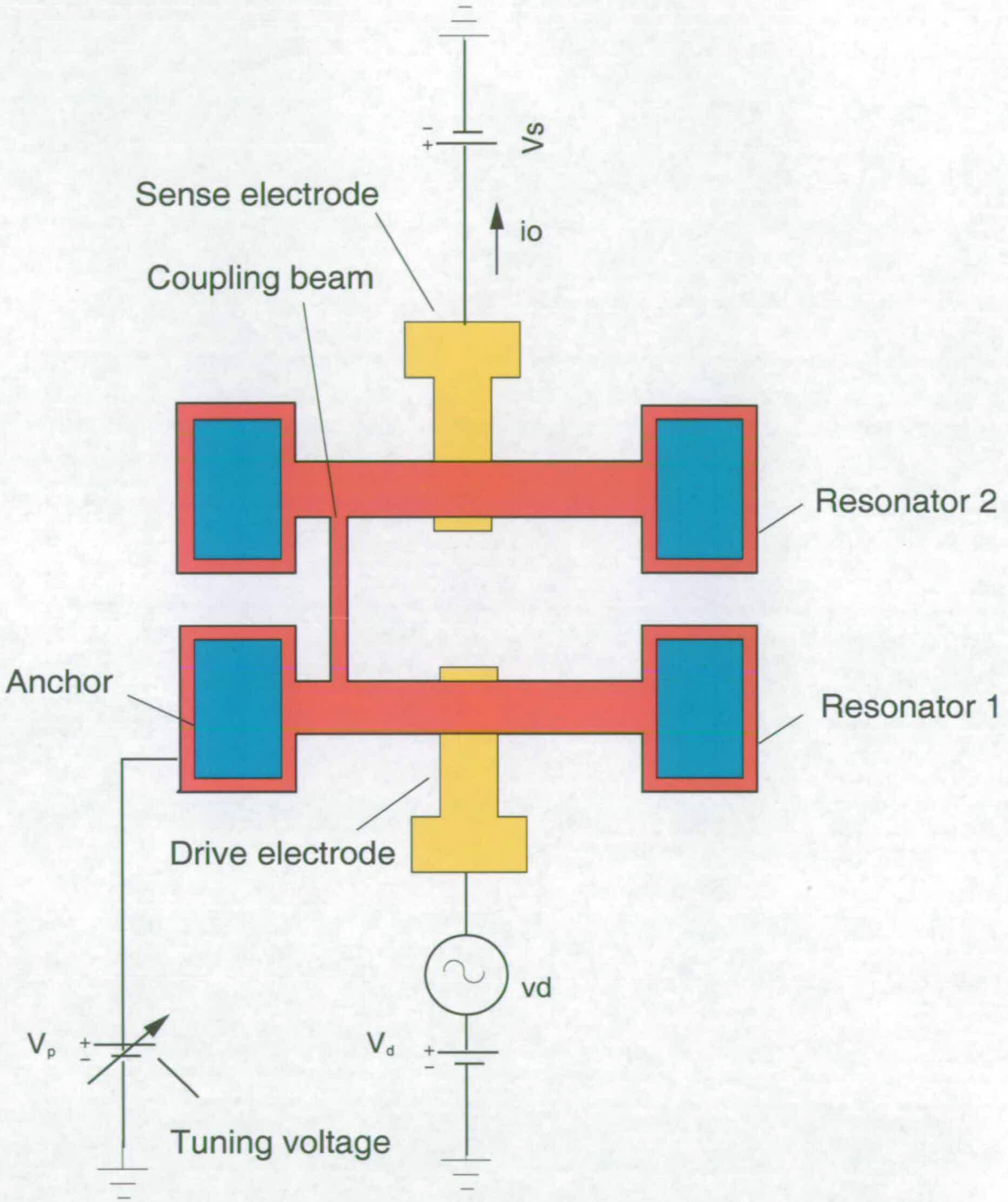

Figure 3.3. Example of the transverse DC tuning mechanism for a micromechanical filter. The application of a DC tuning voltage alters the electrostatic stiffness of resonator 1 until it matches the resonant frequency of resonator 2 [6].

3.3.2 Passive frequency tuning

Passive tuning methods (see Table 3.2.) cause permanent changes to the resonators *stiffness* and *mass*. These changes have been shown by other researchers using a laser [34, 1, 16], Focused Ion Beam (FIB) [122], Chemical Vapour Deposition (CVD) of polysilicon [51] and electrothermal annealing [142].

Method	Tuning range (accuracy)	Power consumption or Tuning voltage	Demonstrated frequency range (application)	Q-change	Ref.
CVD deposition	0.5%-1.96% (0.5%)	2.38mW	85kHz (resonators)	no data available	[51]
Laser deposition	0.5%-1.2% (0.5%)	587mJ/cm^2	12kHz (resonators & sensors)	no data available	[16]
FIB milling	-5%-0% (not specified)	-	650Hz (sensors)	no data available	[122]
Laser ablation	-0.06% - +0.003% (30ppm)	-	32kHz (sensors)	no data available	[34]
Laser ablation	±2.2% (21ppm)	-	9MHz-195MHz (filters & oscillators)	no data available	[1]
Electrothermal annealing	-3.3%-0% (16ppm)	no data available	455kHz (filters & oscillators)	+600%	[142]

Table 3.2. Comparison of passive MEMS tuning methods. This tables summarises demonstrated passive MEMS resonator tuning methods. Passive frequency tuning causes permanent changes to the microstructure.

Frequency tuning by laser deposition is shown in Fig. 3.4. In this case, a micromechanical comb-shaped resonator is covered with a pyrex glass wafer for laser deposited frequency tuning. A pulsed laser is used to locally vapourize a metal donor film (gold (Au), indium (In), aluminium (Al)) that has been pre-deposited on the glass cap. The vapourized metal deposits where the laser hits the shuttle of a comb-resonator. The resonant frequency of the comb-shape resonator reduces with the deposited metal.

Experimental results have shown that an increasing metal mass through multiple laser shots can reduce the resonant frequency of comb-drive resonators by up to -18%, which

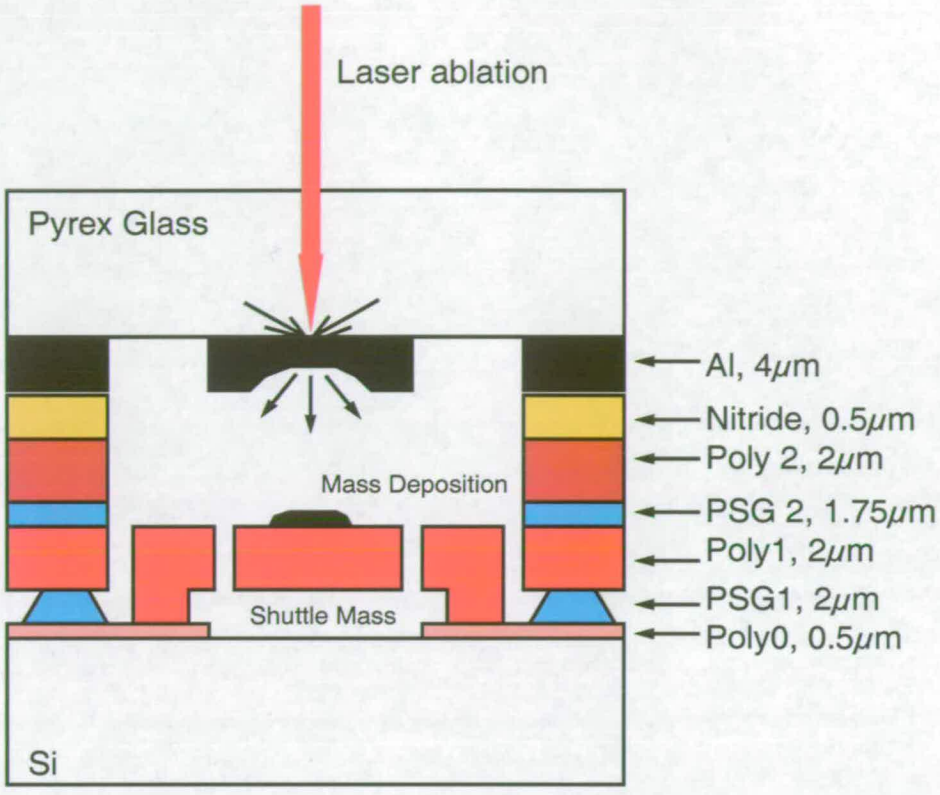

Figure 3.4. Schematic of post-packaging laser mass deposited frequency tuning. The comb-shaped resonator is packaged by bonding a pyrex glass cap onto the MEMS device wafer. A pre-deposited donor metal film on the glass gap is locally vapourized using laser pulses. The metal is re-deposited on the shuttle of the resonator and reduces the resonant frequency [16].

makes this method suitable to ensure the short term stability of micromechanical resonators. The demonstrated tuning resolution for resonators with 12kHz resonant frequency is 0.5% per laser shot. The tuning resolution is mainly determined by the $25 \times 25 \mu m^2$ laser beam spot size. This method can be used to deposit different donor films onto the resonator, but it has only been demonstrated for the relatively low frequencies, which are used for sensors. Further research is needed to extend it to higher filter frequencies and the influence of Q in the course of metal deposition needs investigation.

A second passive tuning method uses the sputtering mode of a Focused Ion Beam (FIB) system to lengthen the suspension of a comb-drive electrostatic microactuator [122]. The sputtering makes the suspension more compliant and causes a smaller reduction

in resonant frequency (5%) than in case of laser deposition. However, those changes are sufficient to make *coarse* frequency changes (see Fig. 3.5).

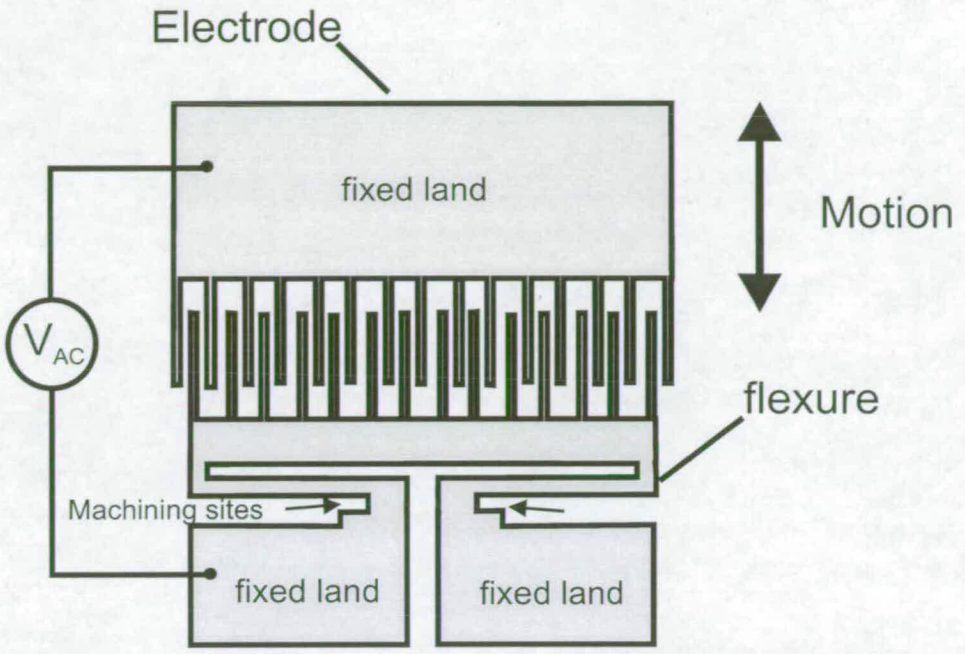

Figure 3.5. FIB trimming of the suspension of an in-plane vibrating comb-resonator. The lengthening of the suspension reduces the stiffness of the resonator and therefore the resonant frequency [122].

FIB systems are commonly used to make accurate micron and submicron modifications to integrated circuits. This makes them ideal for frequency trimming of micromechanical resonators, where relatively large and small changes in frequency are required. They operate at room temperatures where there is less chance of the development of thermal stresses [51], which can relief over time and alter the long term stability of resonators. High operation costs and low device throughput mean FIB systems are not seen as suitable for mass market application. However, high volume disc drive heads are FIB adjusted [104] and so, provided the trim time per device can be minimised, throughput may not be quite the issue it appears to be.

FIB is a promising tuning method, because it can perform frequency tuning over a large frequency range by sputtering material from submicron to micron sizes without any resonator device failure [122]. However, FIB has only been demonstrated for low frequency resonators [122], with frequencies commonly used for sensors. Hence, FIB tuning needs to be characterised on resonators with higher resonant frequencies. In fact, FIB is ideal suited for frequency tuning at high frequencies, because smaller

amounts of material have to be removed to achieve the required frequency changes than for low frequencies.

Laser [16] and CVD [51] deposited tuning deposit relatively large volumes of material and can, as well as FIB, make *coarse* changes in frequency. However, they both can not, in the present form, alter the resonant frequency of smaller (high frequency) resonators. Further research is needed to perform frequency tuning of devices operating at higher frequencies.

FIB is most attractive in terms of tuning range and accuracy, but it has compared to laser and CVD tuning high operating costs and perceived low device throughput. This makes this method more likely to be used in low volume applications, such as in military front end transceivers. A recently developed laser trimming method [1] can perform very accurate and fast changes in frequency and with lower operating costs than FIB. However multiple laser shots, which are required to adjust larger shifts in frequency, can cause device failure.

3.4 Conclusions

This chapter has identified the strength of frequency variation in micromechanical resonators and subsequently reviewed *active* and *passive* tuning methods. Active tuning methods alter the resonant frequency using Joule heating or electrostatic forces. The tuning of capacitively driven resonator by means of a DC voltage [6] has zero power consumption, is amenable to on-chip integration and has a high device throughput.

Active tuning methods are not suitable to make *coarse* frequency changes in low power communication equipment, because of their large DC tuning voltages and power consumption. However, their amenability to IC integration makes them favourable for on-chip *fine* frequency tuning over the life time of micromechanical resonators.

Passive tuning methods in contrast have successfully been proven to make *coarse* permanent changes in frequency [1]. Spring softening, after excessive laser milling, is an issue and needs to be addressed. Passive tuning methods are high in cost and low in device throughput. They are most likely to be used in post-fabrication tuning of micromechanical resonators, because of their ability to ensure the short term stability of micromechanical resonators without using high DC voltages and excessive on-chip power consumption.

In conclusion, a new non-destructive passive tuning method is needed to improve the short term stability and a low voltage active method to guarantee the long term stability of micromechanical resonators. In practise, a reasonable approach is to use a passive method to perform *coarse* postfabrication frequency correction and an active DC voltage scheme to *fine* tune resonant frequency throughout the life time of micromechanical resonators.

Chapter 4

Characterisation of a CMP based polishing process

This chapter describes the characterisation of a Chemical Mechanical Polishing (CMP) based polysilicon polishing process to demonstrate a novel fabrication platform for micromechanical resonators.

4.1 Introduction

Capacitively actuated micromechanical resonators have several advantages, which makes them favourable for future single chip transceivers. Their most important properties are zero DC power consumption, built in switching, amenability to integration with CMOS electronics and the ability of interconnection to form micromechanical circuits for signal shaping and generation [83]. Despite their advantages, limitation of capacitively actuated micromechanical resonators still remain, which need to be addressed before devices can be used in large quantities in filters and oscillators in wireless transceivers. Two of these limitations include their complex costly fabrication and high intrinsic impedance. Complex fabrication in current resonator manufacturing processes increases the cost of devices, while high intrinsic impedances cause signal reflection, signal losses and phase noise, which reduce the Signal-to-Noise Ratio (SNR) and signal quality of low power communication equipment. A novel Chemical Mechanical Polishing (CMP) fabrication process was proposed (Fig. 1.2), which reduces fabrication complexity and impedance at the same time. This chapter describes the design and fabrication of a test chip used to investigate and characterise this Chemical Mechanical Polishing (CMP) based polysilicon polishing process to overcome the impedance and cost issues associated with capacitively actuated micromechanical resonators.

4.2 Materials and Methods

A key process for the fabrication of in-plane vibrating micromechanical resonators with planarised in and output electrodes is CMP polishing (Fig. 1.2). This process can be applied to a variety of resonator geometries included in a test chips design presented in Appendix C. To ensure successful integration of CMP planarisation into different micromechanical resonators, the polysilicon polishing rate has to be characterised to provide high yield fabricated resonators with the same device performance across the Si wafer.

4.2.1 CMP test masks

To characterise CMP polysilicon polishing, a test mask is required which "simulates" the polishing of resonator features and their adjacent electrodes. In microelectronics,

other researchers have developed and used several test masks to determine the influence of the CMP polishing rate on the (i) area, (ii) pitch, (iii) density and (iv) aspect-ratio of a pattern in a damascene process [118] (see Fig. 4.1). From this selection of designs, the density mask is the most suitable choice, since it represents a large variation in pattern density typically found on resonator test chips. Previously, these four masks have been tested on 1.5μm thick SiO_2 for inter-level dielectric damascene CMP and it was found that the polishing rate is most affected by density and less by area, pitch and aspect-ratio [119]. However, in case of resonator fabrication, a thicker (3μm) layer has to be polished to form planarised transducer electrodes. The study of the polishing characteristics of such thick layers is of interest, since it evaluates the suitability of the proposed CMP process for MEMS resonator fabrication. In addition it provides guidelines for the MEMS test chip designs for uniform high yield CMP planarisation.

The density test mask itself is shown in Fig. 4.1(c). The pattern density (the ratio of etched Si area in each structure to the total area of each structure) on the mask was varied ranging from 4% in the lower left corner to 100% in the top right corner. The pitch of each structure was 250μm^2. The mask contained 25 structures each 2mm$\times$2mm arranged in a 5$\times$5 array. A 1mm wide buffer pattern surrounds the test pattern. This buffer reduces the interaction between neighbouring low and high density patterns of two adjacent dies on the wafer.

4.2.2 CMP density mask fabrication

The pattern on the mask is used to simulate the CMP fabrication of resonators with different sizes and spaces between them (Fig. 4.2). To do so, the density pattern is transfered into photoresist on six 76mm n-type $<$ 100 $>$ Si wafers. A STS DRIE ICP system is used to etch 2μm deep density patterns into the wafers in 1 minute. A 0.1μm thick thermal SiO_2 is subsequently grown at 950°C to act as a sacrificial SiO_2 to produce small gaps. The gap width equals the thickness of the SiO_2 and can be controlled within University facilities to thicknesses as small as 0.01μm. To provide CMP polysilicon for the polishing experiments, a 3μm thick LPCVD polysilicon layer is deposited at 585°C and subsequently doped via Solid Source Diffusion (SSD) for 90 minutes in a LPCVD furnace at 1000°C. Dopants are activated using annealing in a N_2 environment at 1100°C for one hour.

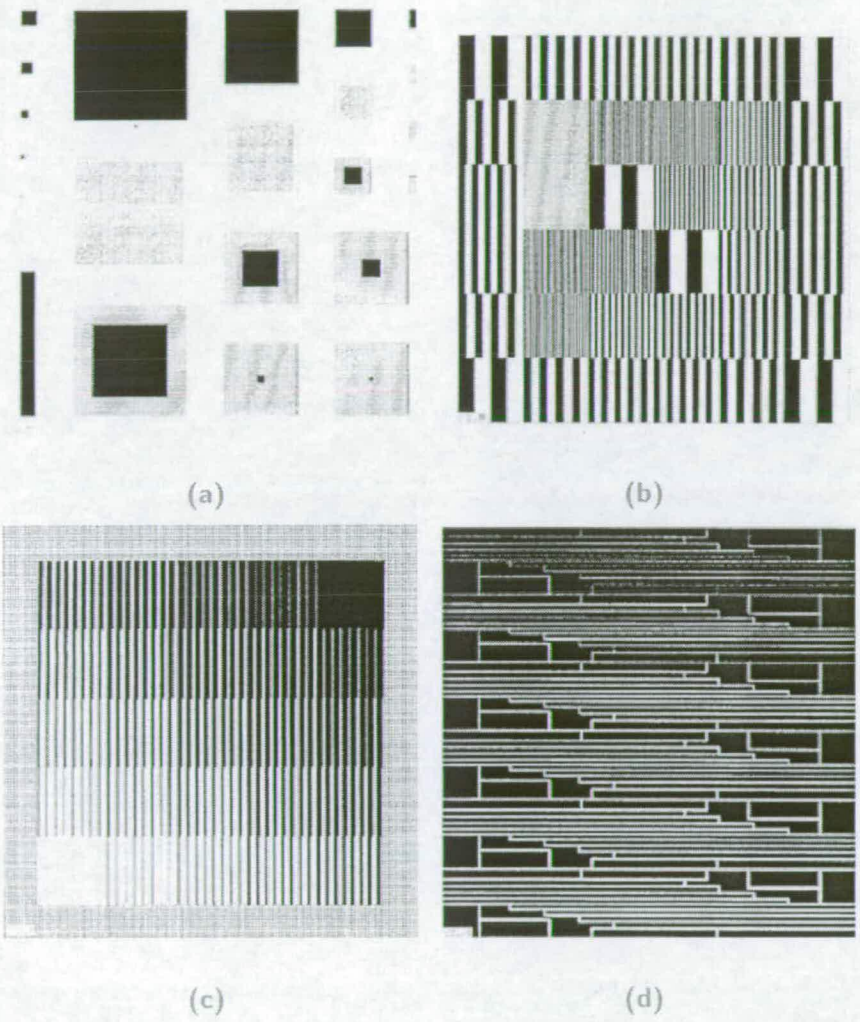

Figure 4.1. CMP characterisation test masks. (a) Area, (b) pitch, (c) density and (d) aspect ratio mask. Each die is 12mm×12mm. The density test mask is most suitable for analysing the polysilicon CMP polishing step, since it best represents the different feature size of resonators and varying spacing between them. The CMP density mask has a varying pattern density ranging from 4% to 100%. The test mask is surrounded by a buffer zone to reduce the influence of neighbouring dies during wafer polishing. The buffer zone has a pattern density of 25% [119].

To establish an estimate for the CMP polysilicon rate, two wafers with blanket deposited 3μm thick polysilicon are CMP polished using the recipe summarised in Table 4.1.

Parameter	Units	Stage 1	Stage 2	Stage 3	Stage 4
Slurry	-	PL1509-35	PL1509-35	DI	DI
Slurry dilution	-	-	-	-	-
Slurry feed rate	ml/min.	90	90	175	-
Chiller temperature	°C	10	10	10	10
Pad rotation	RPM	40	40	40	2
Holder rotation	RPM	40	40	40	2
Back pressure	bar	-	0.3	-	-
Head supply pressure	bar	0.25	0.6	0.25	0.15
Polish time	s	10	TBC	40	2

Table 4.1. CMP recipe for polysilicon planarisation. The presented CMP polish recipe consists of four stages. The first and last stage are used to apply slurry to the wafer and to prevent stiction of the wafer to the polishing pad. The second and third stage are utilised for the polishing and cleaning of the wafer substrate. Wafer cleaning during CMP is performed using a combination of Tetra-Methyl Ammonium Hydroxide (TMAH) and deionised (DI) water.

4.2.3 CMP polishing experiments

Wafers with blanket deposited polysilicon are polished for two minutes. The remaining thickness on the wafers is measured at five points (centre, top, bottom, left and right) with a spectrophotometer. An average polishing rate of 0.65μm/ minute is extracted from the thickness measurements. A CMP recipe with such a removal rate polishes a 3μm thick polysilicon layer in approximately 5 minutes. This polishing time is not too long to affect the condition of the polishing pad and therefore the polishing rate. In semiconductor manufacturing, polishing times are usually kept short. In regular time intervals, the polishing pad is conditioned to provide a constant polishing

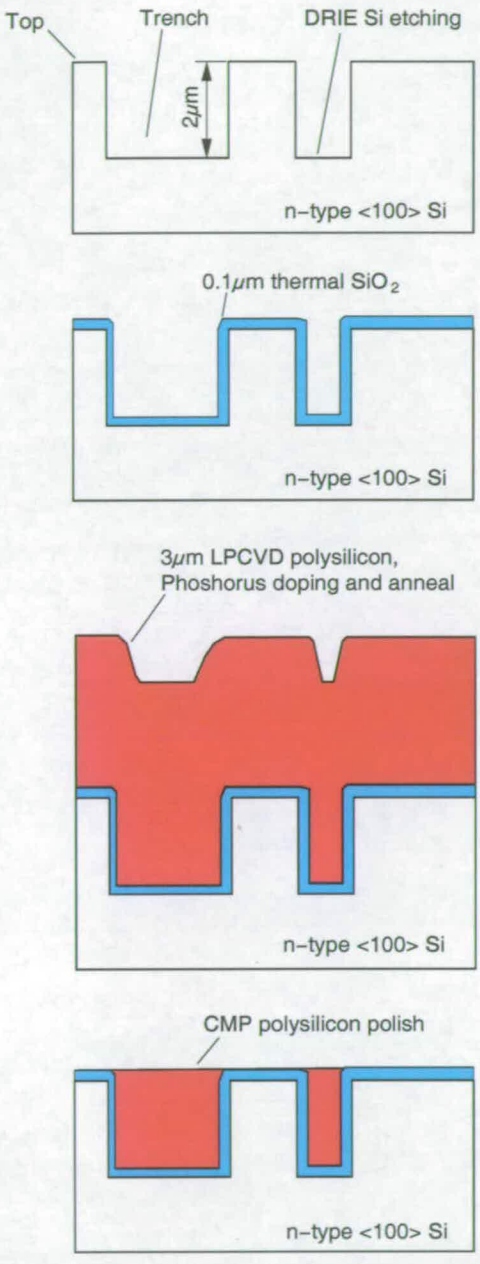

Figure 4.2. Process flow for CMP polysilicon polishing. Test wafers for CMP polysilicon polishing are prepared by DRIE etching the density pattern into the Si. The etched Si pattern simulates later the polishing of resonators with different dimensions and spacing between them. Sacrificial SiO_2 and polysilicon are deposited before CMP polishing.

rate over time. One challenge for the future would involve researching MEMS polishing recipes, where even thicker layers (>10μm) and therefore long polishing times are required.

The polysilicon thickness after polishing shows a centre-to-edge variation of 29.5% after polishing. The optimisation of the thickness uniformity across the wafer is not a priority for experiments carried out within this thesis. Of primary concern is the extraction of CMP polishing rates depending on the density pattern to provide a guideline for future MEMS test chip designers.

To provide this information to MEMS designers, six patterned test wafers are planarised for different times ranging from 1-6 minutes. Because the polysilicon polish is not uniform throughout the wafer, the layer thickness is measured on the four centre dies on each wafer. At these locations, the polysilicon thickness is assumed to be most uniform and a reliable conclusion could be drawn from these measurements without being influenced by possible thickness non-uniformity as seen across the whole Si wafer. Polysilicon thickness measurements are performed before and after CMP on top of the etched Si features to extract the polishing rate (Fig. 4.3). To extract the polishing rate, the polysilicon thickness is measured on each die for pattern densities ranging from 16% to 100%. It is not possible to obtain reliable thickness measurement data on top of smaller etched Si features, because of the large light spot size of the spectrophotometer.

After CMP, wafers with fully planarised polysilicon are diced into individual dies. These dies are submerged into a $NH_4F : CH_3COOH$ solution to expose the 0.1μm wide gap, which is defined by the width of sacrificial thermal SiO_2. Exposed gaps are observed using a Hitachi S 4500 SEM.

4.3 Results and Discussion

Fig. 4.4 presents the CMP polysilicon polishing rate on top of etched Si features as a function of pattern density. Data for longer polishing times (4-6minutes) was not included, because polysilicon was completely removed for low density features.

It is evident from Fig. 4.4, that the CMP removal rate is dependent on pattern density and time. The observed time dependent polysilicon polishing rate characteristic can be explained using Preston's law (see Eq. (2.30)). When deposited, the polysilicon

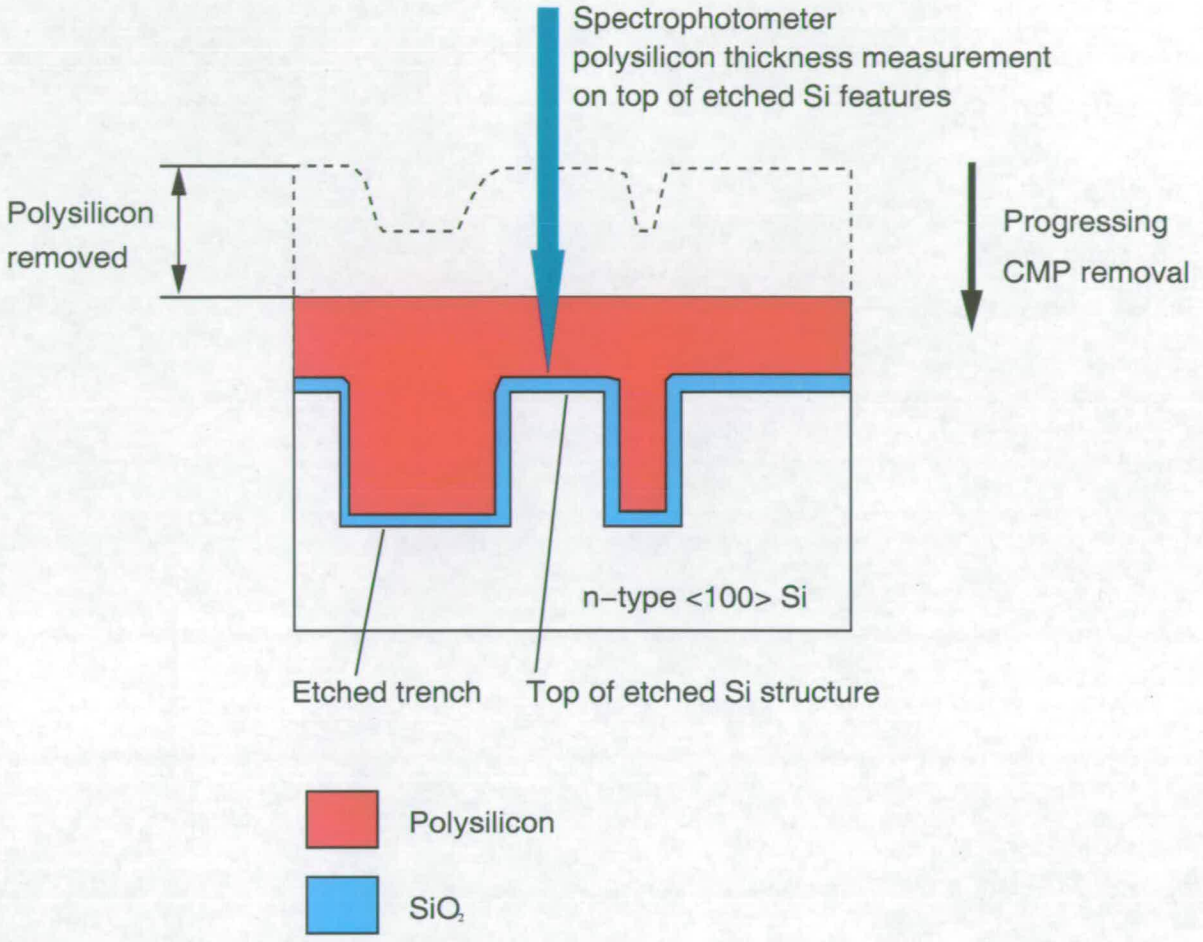

Figure 4.3. Extraction of the CMP polysilicon polishing rate. The CMP polishing rate is extracted for different pattern densities from the measured polysilicon thickness on top of etched Si feature and the polishing time. The CMP polysilicon polishing rate is the ratio of removed thickness and polishing time. Polysilicon thickness on top of the etched Si features is extracted from spectrophotometer measurements.

area contacting the polishing pad is small and as result of the characteristic surface topography. In this case, the pressure of the polishing pad is a high and polysilicon is removed at a high rate. Once the polysilicon is planarised and a uniform flat surface is achieved, the force per unit area decreases and consequently the polishing rate is reduced. Once, the polysilicon has been planarised in high density areas, the polishing rate gradually levels to the value close to those found for blanket deposited wafers.

The pattern density dependence of the polishing rate can also be explained by Preston's law. The polishing rate is dependent on the pressure the polishing pad imposes

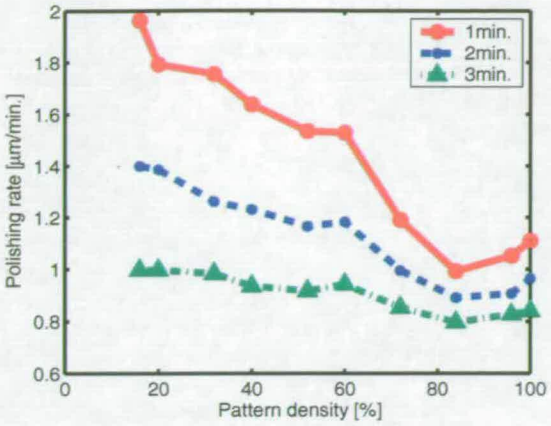

Figure 4.4. Polysilicon polishing rate as a function of pattern densities. Polysilicon polishing rate on top of etched Si features as a function of pattern density for different polishing times. The CMP removal rates decrease with progressing polishing times and increasing pattern density. Data for longer polishing times (4-6minutes) was not included into this graph, because polysilicon was completely removed for low density features.

onto the surface. Low density patterns have a small area and the polishing rate is high. With increasing density, the area of the etched Si features increases and the polishing rate consequently drops. Note, a similar pattern dependent removal rate is also experienced during DRIE etching [56], where a so called microloading effect removes silicon faster in large mask opening areas compared to smaller ones. This effect can also be greatly reduced and a etch uniformity improved by proper mask design [56].

After 3 minutes of CMP polishing, a wafer with fully planarised polysilicon was diced and individual dies etched in $NH_4F : CH_3COOH$ for 125 minutes. After etching, dies were cleaved and inspected using a Hitachi S 4500 SEM. Fig. 4.5 displays the removed SiO_2 in a 0.1μm wide gap.

Fig. 4.5 shows fully planarised polysilicon with an adjacent etched Si feature. Si and polysilicon are separated by a 0.1μm wide gap. The gap width itself varies with the vertical and horizontal orientation of the SiO_2. This variance is a result of the oxidation rate dependence with the crystallographic orientation of the Si substrate [97]. Note, this is not an issue for polysilicon resonators, since transducer gaps are defined by the SiO_2 width at the sidewalls alone. At these locations, the crystallographic orientation in polysilicon does not change and therefore the SiO_2 is most likely to be constant. The observed Si sidewall scalloping is a result of the DRIE BOSCH process that was used. This sidewall profile, however, is undesirable in polysilicon resonators,

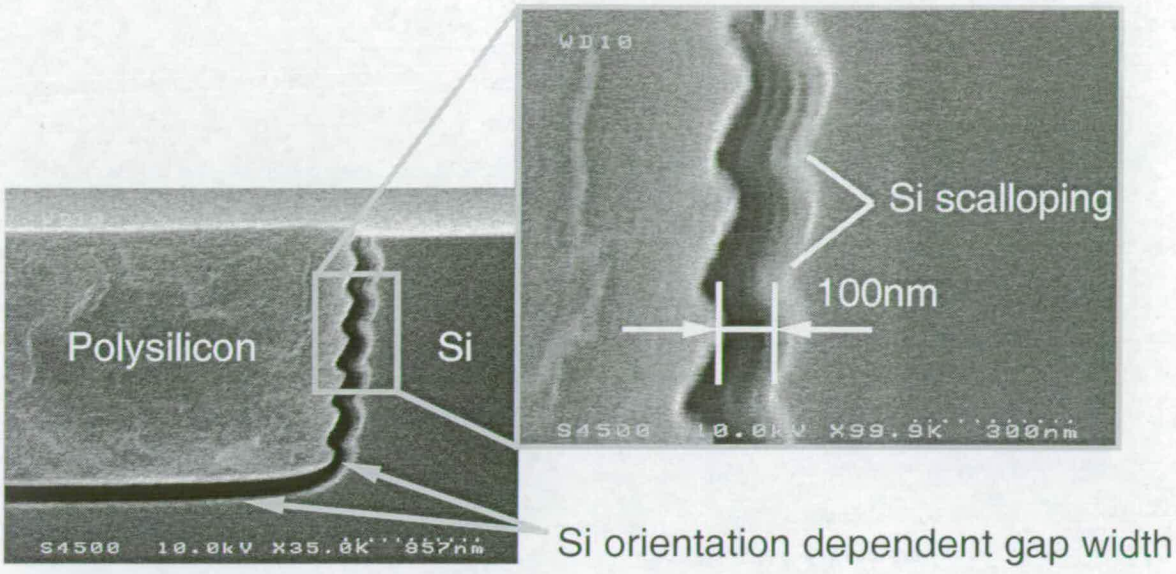

Figure 4.5. SEM image of planarised CMP test pattern with removed sacrificial SiO_2 in a 100nm wide gap. Planarised polysilicon is clearly visible. Sacrificial SiO_2 in the gap was etched for 125 minutes in $NH_4F : CH_3COOH$. Note, the non-uniform gap width. This is a result of the dependence of the oxidation rate onto the crystallographic orientation of the Si substrate. The Si sidewall profile shows scalloping, which is characteristic for a DRIE BOSCH process.

because it reduces the effective electrode-to-resonator area, which causes a decrease in electromechanical coupling. Recall from Eq. (2.19), a reduction in electromechanical coupling reduces the output current and increases the impedance of the resonator.

As the purpose was to demonstrate the CMP process, it should be noted that the DRIE etch was not optimised to minimise scalloping, or to achieve vertical sidewalls. For the development of planarised resonators devices a RIE, ion mill or a recently developed DRIE [75] process would ensure a scallop free sidewall.

4.4 Conclusions

In this chapter, a CMP test chip was used to examine the polysilicon polishing rate for different pattern densities. It was found, that the CMP polysilicon polishing rate is strongly dependent on the pattern density and polishing characteristics determined in semiconductor research are also valid for thick polysilicon layers [119]. These results suggest, that MEMS test chip designs should contain an equal pattern density to ensure

a uniform polishing rate across the wafer. One way to achieve this is to fill empty areas between resonator devices on the test chip design with CMP "dummy" structures to achieve a constant CMP removal rate and throughout the test chip.

This is a common techniques in semiconductor manufacturing to ensure a uniform polishing rate across the wafer [62]. An improved uniformity in polysilicon thickness across the wafer would reduce the amount of over-polishing and therefore possible dishing, processing time and cost. SEM images of planarised wafers indicate, that a dry etch process for thick polysilicon has to be developed to provide straight vertical sidewalks, which avoids the observed Si sidewall scalloping profile. Such a process ensures that electromechanical coupling is not affected by the dry etching of the resonator shape.

In conclusion, the CMP polishing experiments suggest, that MEMS test chips with a equal pattern density ensure an uniform CMP polysilicon removal rate across the sample. A uniform pattern density can be provided by CMP dummy structures.

Chapter 5

Fabrication of MEMS resonators

This chapter describes the layout and fabrication of micromechanical resonators to characterise FIB Pt and electrochemical Ag deposited tuning.

5.1 Introduction

Micro Electro Mechanical Systems (MEMS) resonator technology benefits from new frequency tuning methods, because these would bring performance improvements, cost reductions and power savings in future multi-band wireless transceivers. However, before these methods can fuel modern communication equipment with these advantages, the proposed frequency tuning methods have to be investigated for their suitability in modern transceivers, their characteristics studied, analysed and suggestions made for their improvement. One way to investigate the suitability of modern resonator frequency tuning methods is to use different test structures arranged on silicon chips. Test structures have been developed and extensively used in semiconductor and MEMS research to monitor and characterise fabrication processes or device behaviour. Information extracted from different test structures find application in areas ranging from process development, parameter extraction, yield analysis to material and process characterisation.

This chapter describes the design and fabrication of two test chips containing micromechanical cantilever beam and bridge resonators used to investigate the suitability of Focused Ion Beam (FIB) platinum (Pt) and electrochemical silver (Ag) deposited frequency tuning. Manufactured resonator structures from these test chips are physically characterised and presented. At the end of the chapter, results are summarised and a conclusion is made.

5.2 Materials and Methods

Two test chips, containing micromechanical cantilever beam and bridge resonators, have been designed to evaluate FIB Pt and electrochemical Ag deposited frequency tuning. The reason to use micromechanical resonators is threefold: (i) They are simple structures and mechanically well understood, (ii) easy to fabricate and (iii) sensitive to changes in deposited mass and stiffness [33]. These properties makes them ideal test structures to demonstrate and characterise the two proposed tuning methods. This section describes the design and the associated fabrication processes of these resonators.

5.2.1 First resonator test chip

The first test chip consists of three masks and is used to integrate an Ag deposition scheme with micromechanical bridge resonators for the purpose of frequency tuning (see Fig. 5.1). The Ag deposition scheme consists of a Ag loaded solid electrolyte, used as a transport medium for deposited Ag; an Ag anode to provide ions for the deposition process; and aluminium (Al) contacts to electrical connection and control of the tuning process.

Mask one of the test chip defines arrays of four bridge resonators, which are used to analyse Ag deposited frequency tuning (see Ch. 8). The bridges are available in two different widths of 15μm and 20μm and length their range from L=75μm to 200μm. The widths of resonators are larger than the laser spot size (5μm) of a vibrometer to ensure sufficient reflection during frequency measurements (Ch. 6 and Ch. 8). The lengths of bridges are designed to be long enough to generate resonant frequencies lower than provided by the signal generator ($0 \leq f \leq 15MHz$), which is used for the vibration actuation.

The other two masks are used to produce Al electrodes and an Ag anode. Note, the latter two are shadow masks and used after resonator fabrication to avoid the contamination of the Edinburgh silicon processing facilities with Ag. The production of the Al contacts and Ag anode is performed at Arizona State University, where there are Ag processing facilities available. To ensure electrical connection and packaging of the manufactured test chips, the size of Al contacts (2mm$\times$2mm and 9.5mm$\times$2.3mm) and Ag anode (8.5mm$\times$2mm) are chosen to be large enough to allow their attachment with wire bonds using silver epoxy glue in case of unsuccessful bonding.

The fabrication of the bridge arrays is shown in Fig. 5.2. Fabrication of the resonators starts with the thermal growth of 0.1μm thick adhesion SiO_2 layer on n-type $< 100 >$ Si wafers. Over the adhesion layer a 2.3μm thick Plasma Enhanced Chemical Vapour Deposition (PECVD) SiO_2 sacrificial spacer and 1μm Low Pressure Chemical Vapour Deposition (LPCVD) structural polysilicon layer is deposited. In order to reduce stress in the polysilicon, the wafers are annealed at 1100°C in N_2 for 1hour. The first mask is employed to photolithographically pattern the wafer and and Reactive Ion Etch (RIE) the polysilicon to form the bridge resonators. To form free standing bridge resonators, devices are released by wet chemical removal of the sacrificial SiO_2 using hydrofluoric acid (HF) and subsequently supercritical point dried using carbon dioxide (CO_2).

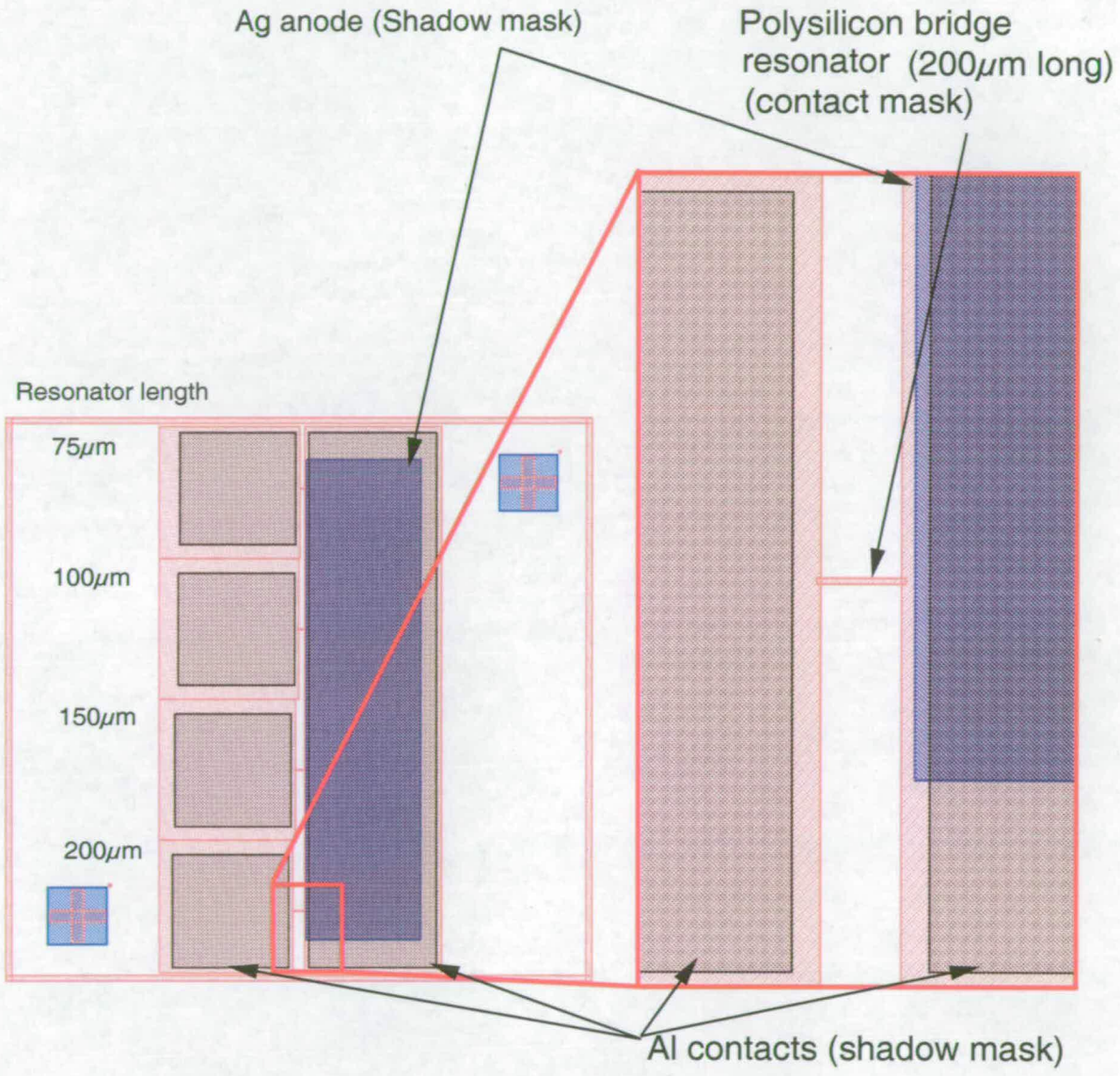

Figure 5.1. First test chip design for the characterisation of Ag deposited deposited frequency tuning. The figure shows the test chip design with three masking layers. The enlargement of the the designs clearly highlights the first mask defining the micromechanical bridge resonators, and the latter two realised as shadow masks to produce an Ag anode and Al contacts. Al contacts and Ag anode were chosen to be sufficient large to enable electrical connection by means of silver epoxy glue in case of unsuccessful wire bonding.

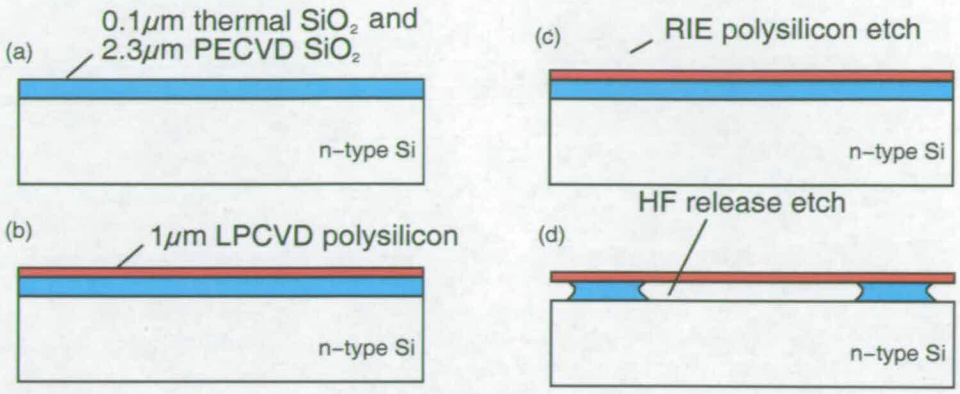

Figure 5.2. Resonator process flow for the first test chip. Process flows of micromechanical polysilicon resonators for electrochemical Ag deposited frequency tuning. Fabrication of free standing bridge resonators involves the deposition and selective etching of sacrificial SiO_2 and structural polysilicon.

After polysilicon resonator release, wafers are diced into individual chips and shipped to Arizona State University, where a combination of thin film evaporation and two shadow masks are used to integrate an Ag deposition tuning scheme with the manufactured polysilicon bridge resonators [26]. Fig. 5.3 summarises the integration process.

Note, no wet processing is used in subsequent processing steps to avoid damage and stiction of the released polysilicon bridge resonators. The released polysilicon bridge resonators are blanket deposited with a 80nm thick chalcogenide glass $Ge_{0.3}Se_{0.7}$ film using an Edwards evaporation system. This is followed by 15nm of Ag, which is photodiffused into the glass to form the solid-electrolyte (Fig. 5.3a-b). Photodissolution takes place using 405nm UV light at a power density of $3.9mW/cm^2$ for 20 minutes (Fig. 5.3c) on a Karl Suss mask aligner (see also Ch. 8). The Ag thickness is chosen to complete diffuse into the glass to avoid removal of excess Ag via wet chemical etching. Furthermore, the undercut of the bridge resonators ensures that the electrolyte on top of the resonators and on the silicon substrate are electrically isolated. A 50nm thick Ag anode and 500nm thick Al contacts are produced by a Edwards evaporator using the two designed shadow masks (Fig. 5.3d-e).

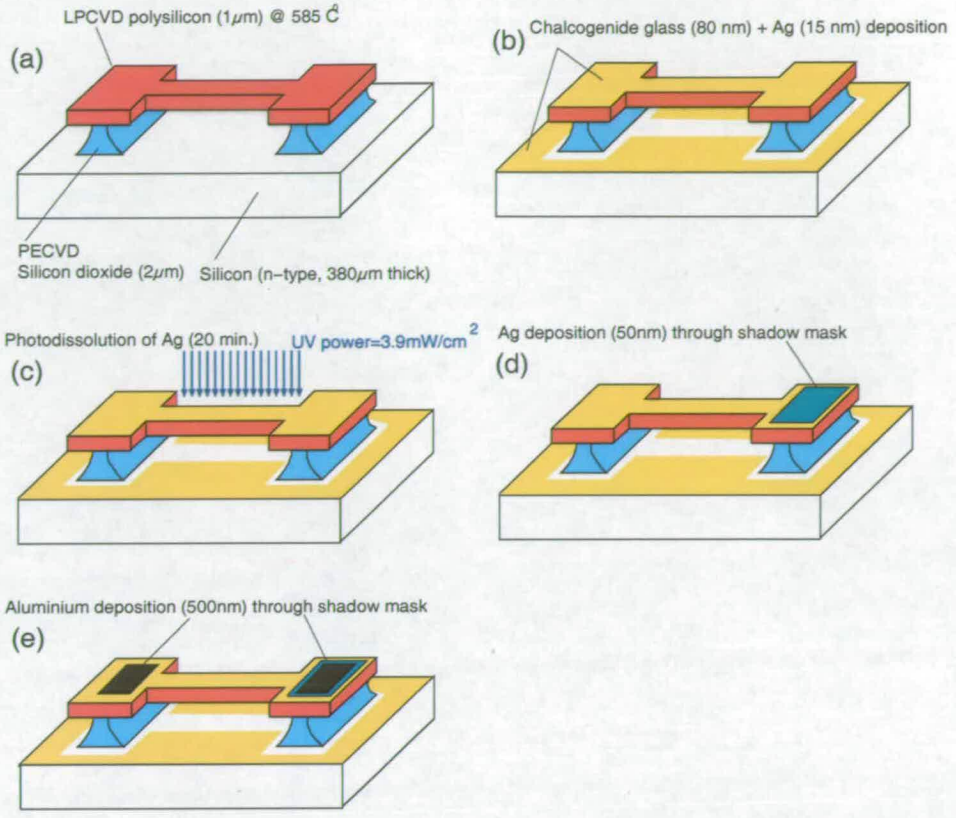

Figure 5.3. Integration process sequence for tunable silver deposit. The integration of the Ag deposition mechanism is performed after polysilicon bridge resonators fabrication. The integration of the Ag deposited tuning scheme involves the deposition of the solid electrolyte and the definition of the Ag anode and aluminium electrodes using two shadow masks.

5.2.2 Second resonator test chip

The second test chip contains one mask of six cantilever beam and bridge resonator arrays used for the analysis of FIB Pt deposited frequency tuning (Fig. 5.4). In addition, Fig. 5.4 shows single enlarged cantilever beam and bridge designs together with a 3 dimensional schematics describing the appearance of devices after fabrication. All resonators have a width of 15μm and lengths ranging from 25μm to 250μm [50]. The width of the resonators is designed to be larger than the spot size of the detection laser (5μm) in a vibrometer, which is used for frequency measurements (Ch. 6). The length of the resonators is determined by the frequency range ($0 \leq f \leq 15MHz$) of the function generator.

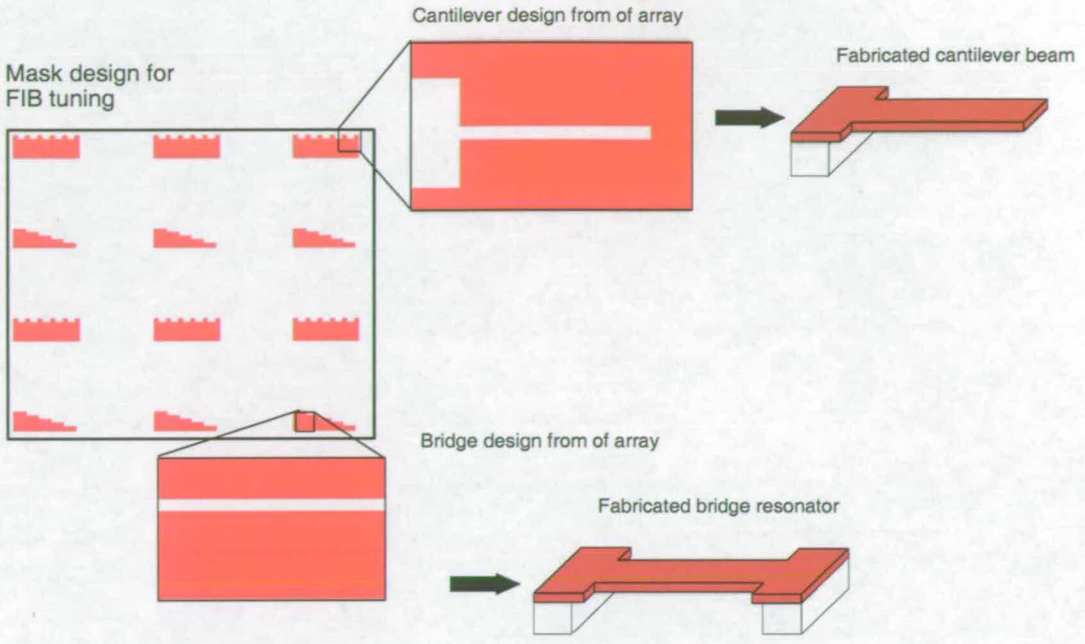

Figure 5.4. Test chip design for the characterisation of FIB platinum deposited frequency tuning. The figure shows the mask design of the second test chip with cantilever beam and bridge resonator arrays. The enlargement of the the design clearly shows examples of 200μm long bridges cantilever together with 3 dimensional schematics describing the appearance of resonators after fabrication.

The fabrication process of polysilicon beam resonators is outlined in Fig. 5.5. Processing of the second test chip starts with the thermal growth of 0.1μm thick SiO_2 on n-type $< 100 >$ Si wafers at 950°C. The thermal SiO_2 serves as an adhesion layer for the 2.3μm thick sacrificial PECVD SiO_2, which is subsequently deposited onto the wafers. The sacrificial SiO_2 is densified at 950°C in a N_2 environment for one hour. This is followed by the deposition of a 2.3μm thick polysilicon layer at 585°C, which serves as the structural material for the beam resonators. The polysilicon is then phosphorus doped using Solid Source Diffusion (SSD) at 1000°C in N_2 for 90 minutes.

An 0.5μm thick PECVD SiO_2 hard mask is deposited on the polysilicon and annealed at 1100°C in N_2 for 1 hour together with the polysilicon to relieve stress and activate dopants. The hard mask and polysilicon are etched using a combination of RIE and DRIE etching to form the resonators. Resonators are released by a wet etching in HF for 10 minutes and subsequently dried using critical point drying in liquid CO_2.

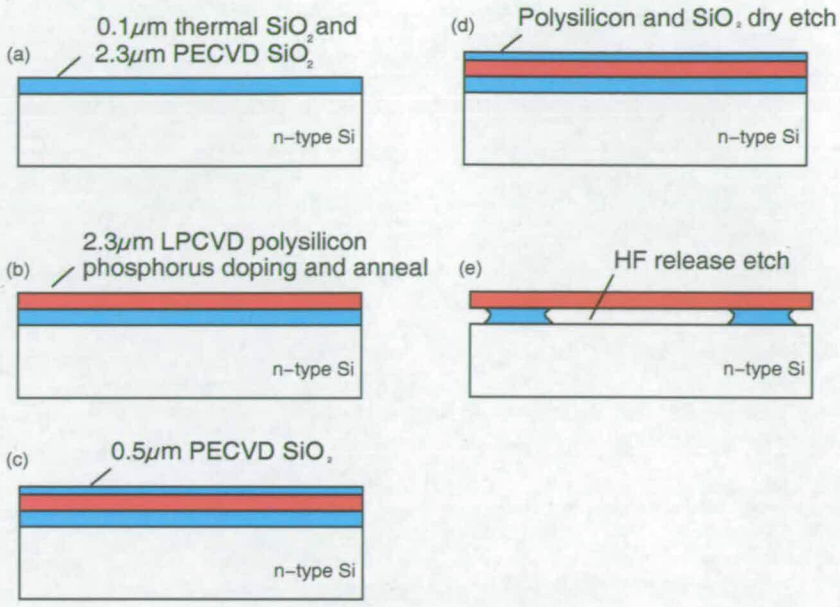

Figure 5.5. Resonator process flow for the second test chip. Process flow for micromechanical polysilicon resonators used for FIB Pt deposited frequency tuning. Resonators are fabricated using standard surface micromachining. This involves the deposition and etching of a sacrificial *SiO2* and polysilicon layer to form free standing cantilever and bridge resonators of various lengths.

5.3 Results and Discussion

Quantitative visual inspections on microfabricated beam and bridge resonators were performed using a SEM. For this purpose, samples were tilted to determine that all SiO_2 had cleared underneath the resonators. At the same time, resonators were analysed for possible out-of-plane bending. Note, because of the transparency of polysilicon under normal light, a standard light microscope was usually sufficient to observe any remaining SiO_2 underneath beam resonators. However, in the case of resonators being fabricated for FIB deposited tuning, the polysilicon was too thick to be transparent and had to be viewed under a SEM. SEM inspections were carried out for resonators made for FIB and Ag deposited tuning and are discussed below. In particular, to examine the quality of the integration of the Ag deposition scheme with bridge resonators, samples were viewed in a SEM and FIB both before and after integration.

5.3.1 Fabricated polysilicon bridge resonators from test chip one

Bridge resonators arrays were manufactured for Ag deposited tuning using the first test chip (Fig. 5.1). Fig. 5.6 and Fig. 5.7 both depict a $150\mu m \times 20\mu m \times 1\mu m$ microfabricated polysilicon bridge resonator from one of the microfabricated arrays both before and after integration of the Ag deposition scheme.

The polysilicon bridge resonator before integration is shown in Fig. 5.6. The bridge resonator is straight and does not show any buckling. This suggests low residual stress in the polysilicon. However, deflection and frequency measurements have to be performed to confirm these assumptions (Ch. 6).

Fig. 5.7 shows a $150\mu m \times 20\mu m \times 1\mu m$ polysilicon bridge resonator after the integration of an Ag deposition scheme. The misalignment of the Ag anode and Al cathode is clearly visible and covers the polysilicon bridge over several tens of microns. The observed misalignment is a result of the manual alignment of the shadow mask over the polysilicon bridge samples. Depending on the degree of the misalignment, the resonant frequency of bridges before Ag deposited tuning is influenced to different degrees.

Hence, it is clear the observed misalignment needs to be reduced to achieve reproduce able Ag deposited tuning with minimal influence on the Q-factor. One way to reduce the misalignment is is to use micromachined shadow masks with built in alignment capability [76]. This would avoid unwanted bridge coverage with Ag and Al and would not require additional cleanroom facilities.

Another way to substantially reduce the misalignment is to use standard photolithography to pattern and subsequently etching the Ag anode and Al contact. However, cleanroom facilities need to be available, which allow this post-processing and can tolerate Ag contamination.

In addition to the reduction in alignment issues, photolithographically patterning of the Ag anode and Al contacts increases yield, since device are not brought in direct contact with the masks during pattern definition. In contrast, pattern definition using shadow mask requires direct contact between resonators and mask, which has considerably affected the yield and only a small number of samples were available for Ag deposited tuning. However, shadow mask techniques seemed to sufficient to 1) prevent Ag contamination of the Edinburgh silicon processing lines and 2) demonstrate

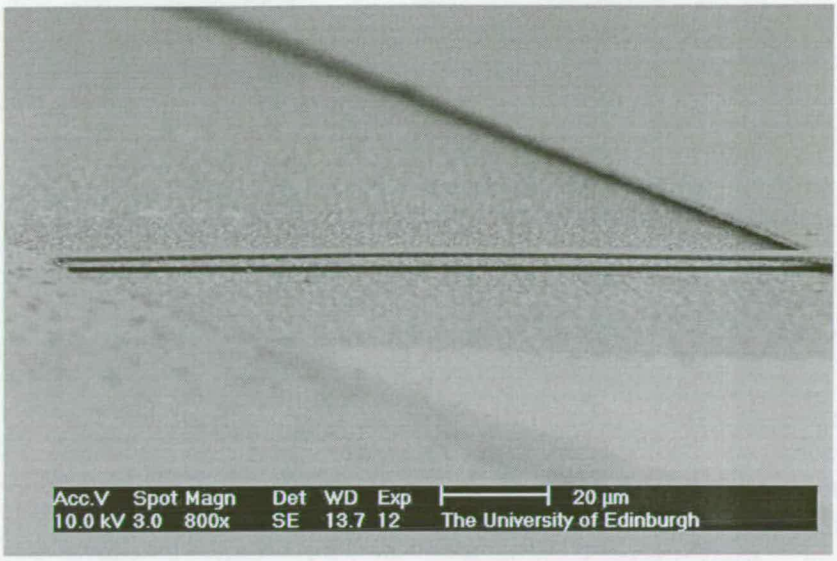

Figure 5.6. Polysilicon bridge resonator before integration of the Ag deposition scheme. SEM pictures of a released polysilicon beam ($150 \times 20 \times 1\mu$m). The depicted polysilicon bridge resonator appears to be straight, suggesting low residual stress. A SEM picture of the whole beam array could not be obtained due to the large sample size of 9.8mm×9.8mm.

Ag deposited tuning. Improvement on manufacture-ability and yield are subjects to further research.

5.3.2 Fabricated polysilicon beam resonators from test chip two

Micromechanical resonators fabricated from test chip two can be seen in Fig. 5.8. As can be observed, both polysilicon cantilevers and bridge resonators are straight and show no visible bending. This suggests low residual stress along the axis or through the polysilicon layer thickness. However, optical surface profiler and frequency measurements measurement have to be performed to explore stress in the polysilicon resonators further.

5.4 Conclusions

This chapter has reported on the design and manufacturing of polysilicon bridge and beam resonators from two test chips. The resonators are used in Ch. 7 and Ch. 8 for the characterisation of FIB and Ag deposited tuning. SEM and FIB images showed

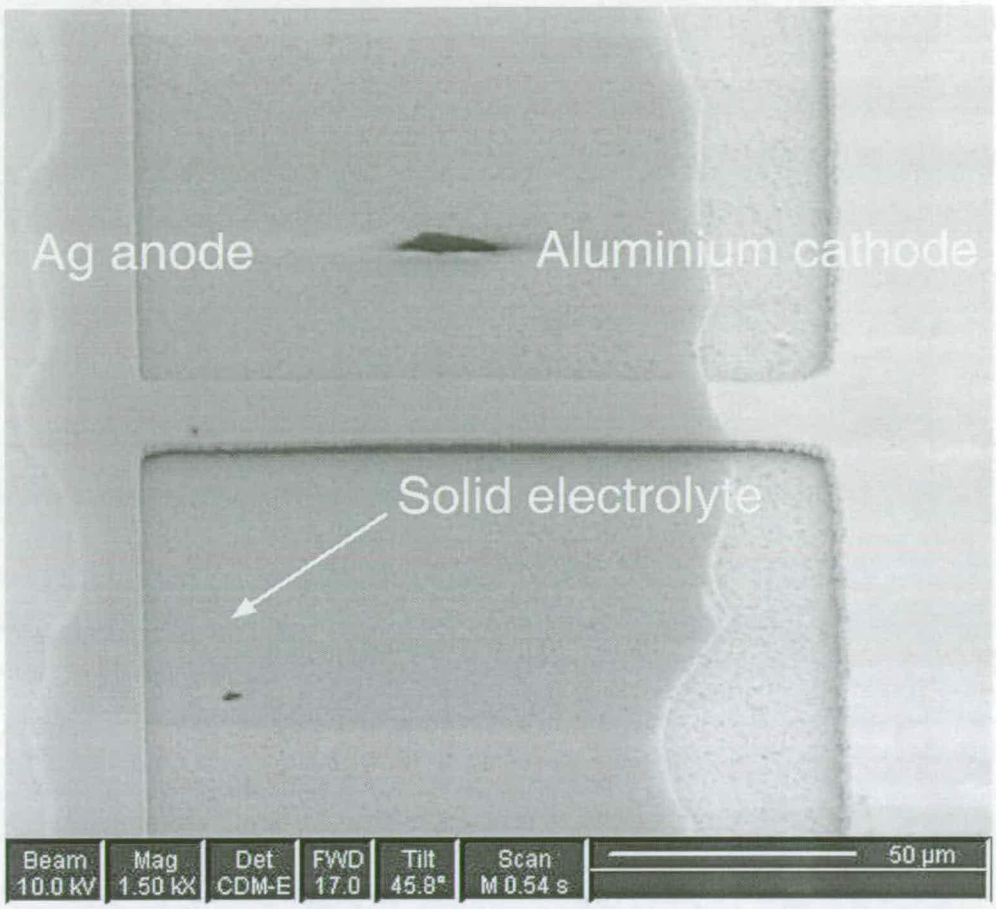

Figure 5.7. Polysilicon bridge resonator after integration of the Ag deposition scheme. This FIB image shows a 150μm×20μm×1μm polysilicon bridge resonator with integrated Ag deposited tuning scheme. The Ag deposited tuning scheme includes a 80nm thick blanket deposited solid electrolyte, a 50nm Ag anode and 500nm thick Al electrodes. Note the use of shadow masks caused misalignment of the Al cathode and Ag anode.

that resonators were fully released and show no visible bending. Small or no bending suggests low residual stress in the polysilicon. In addition, the use of shadow masks for the integration of an Ag deposition scheme in resonators from test chip one caused a reduction in yield and partial devices coverage with Ag and Al. The partial coverage is likely to cause a variability in mass frequency change between resonators and a reduction in the mechanical Q-factor. The former results in a reduction in tuning repeatability. However, frequency and deflection measurements have to be performed to analyse residual stress and the effect of misalignment on fabricated resonators.

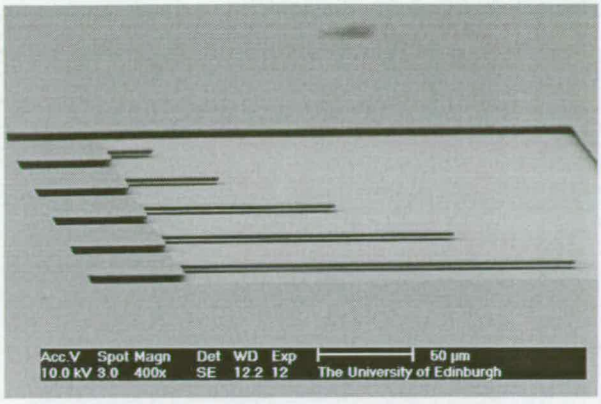

(a)

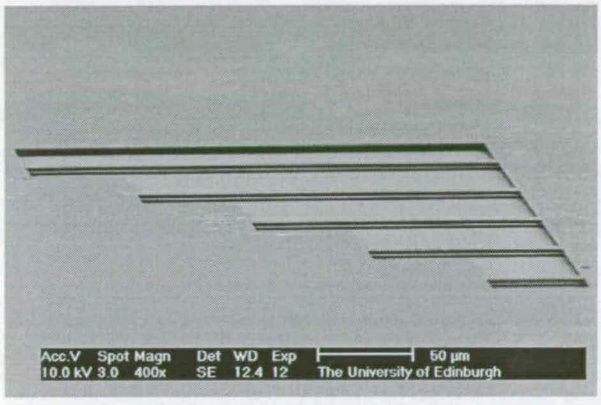

(b)

Figure 5.8. Arrays of polysilicon micromechanical beam resonators. SEM images of manufactured polysilicon micromechanical resonator beam arrays showing (a) cantilevers and (b) bridges.

In conclusion, the presented polysilicon surface micromachining process is capable to produce free standing and released beam and bridge resonators ready for the characterisation of FIB and Ag deposited tuning. The use of shadow masks to integrate an Ag deposition scheme into polysilicon bridge resonators reduces the yield and is most likely to decrease the tuning repeatability mechanical Q. However, frequency and deflections measurements have to be performed to fully analyse the manufactured resonators.

Chapter 6

Characterisation of micromachined MEMS resonators

This chapter describes the testing of micromachined polysilicon cantilever and bridge resonators. The chapter is divided into two parts. In part one, the optical characterisation workstation is described. In part two, this workstation is used to characterise polysilicon resonators fabricated from two test chip designs and experimental results are presented and discussed.

6.1 Introduction

Microfabrication related effects, such as variations in Young's modulus or biaxial stress, change the resonant frequency of polysilicon resonators by varying degrees. Analysing these effects is important to determine and optimise the quality of a fabrication process and to evaluate Finite Element Method (FEM) models, which describe the dynamic behaviour of manufactured resonators.

In this chapter, an optical workstation was used to extract biaxial stress and Young's modulus from deflection and frequency measurements on manufactured polysilicon resonators (Ch. 5). The analysis of these values helped to determine the quality of the polysilicon fabrication process and to evaluate FEM - models, which were used to describe the FIB and Ag deposited frequency tuning of manufactured polysilicon resonators (Ch. 7 and Ch. 8).

6.2 Optical workstation

The equipment used to analyse micromachined polysilicon cantilever and bridge resonators was an optical workstation [45]. The advantages of optical testing are the non-destructive character and the high signal to noise ratio of measured vibration signals.

The optical workstation is a combination of a Zygo surface profiler, a Polytech laser vibrometer and a Nd:YAG ablation laser (Fig. 6.1). Assembling these optical components into a workstation avoided the transfer of samples between different measurement sites and provided the user with various testing possibilities [34, 44]. For example, while a Zygo white light surface profiler was used to perform static measurements, a Polytech laser vibrometer was utilised for frequency measurements. To perform these measurements, the output of a Charge-Coupled Device (CCD) camera was used to move between different samples and focus onto the resonator surface.

A Zygo NewView 5020 white light interferometer was used to perform static deflection measurements on fabricated micromechanical cantilever and bridge resonators. To measure the deflection, a 10X Mirau objective was used, which gave a horizontal resolution of 1μm. During deflection measurement, the surface of each resonator was scanned and a picture returned with 640$\times$480 data points. The vertical resolution of these surface scans was less than 1nm over a 5mm scanning range [45].

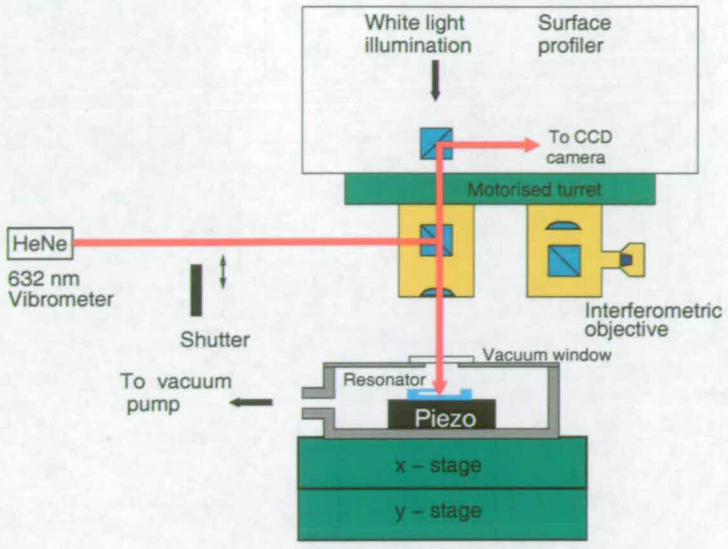

(a)

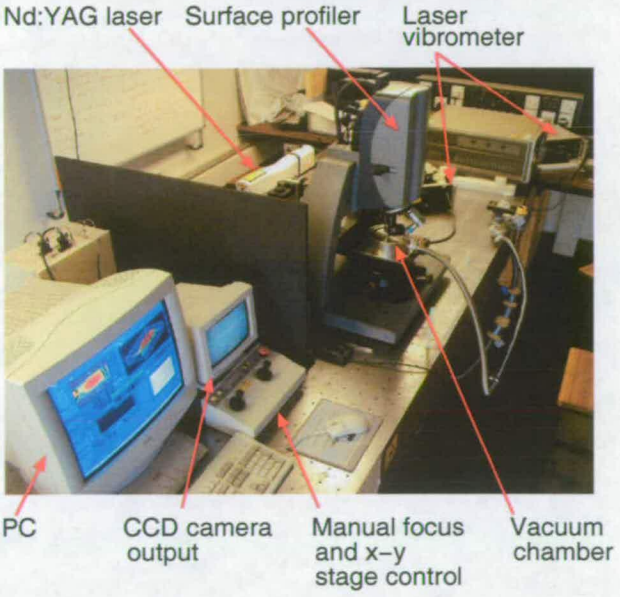

(b)

Figure 6.1. Schematic and photograph of an optical workstation. (a) A schematic of the workstation shows the Zygo surface profiler and the Polytech laser vibrometer. The Nd:YAG ablation laser is omitted from the schematic, because it was not used for any of the experiments in this thesis. However, for clarity the photograph in (b) shows all the main components of the workstation [45]. The output of a CCD camera was used to move between different devices and to bring the sample surface into focus for surface profiler and vibration measurements. Surface profiler and frequency data was stored on a designated PC. (Photograph courtesy of John Hedley, University of Newcastle, UK).

A Polytech HeNe laser vibrometer was used to measure the out of plane resonant frequency of vibrating polysilicon cantilevers and bridge resonators. To measure the resonant frequency of a vibrating resonator, a HeNe laser beam from a Polytech OFV 501 single mode optic fibre interferometer was split into a reference and measurement beam, shown in Fig. 6.2. The measurement beam was directed onto the surface of a moving object (a cantilever or bridge resonator), while the reference beam was passed through a frequency shifting Bragg cell. Both beams were combined at a beam splitter (BS3) and converted into an electrical output voltage, which was passed to a Polytech OVF 3000 RF signal processing unit. In the signal processing unit, an output signal was produced from the detected voltage, which was proportional to the velocity and displacement of the vibrating resonator. The output signal from the RF unit was fed into a dual channel 8bit ADC card to display the resonator frequency spectra in a Labview embedded spectrum analyser.

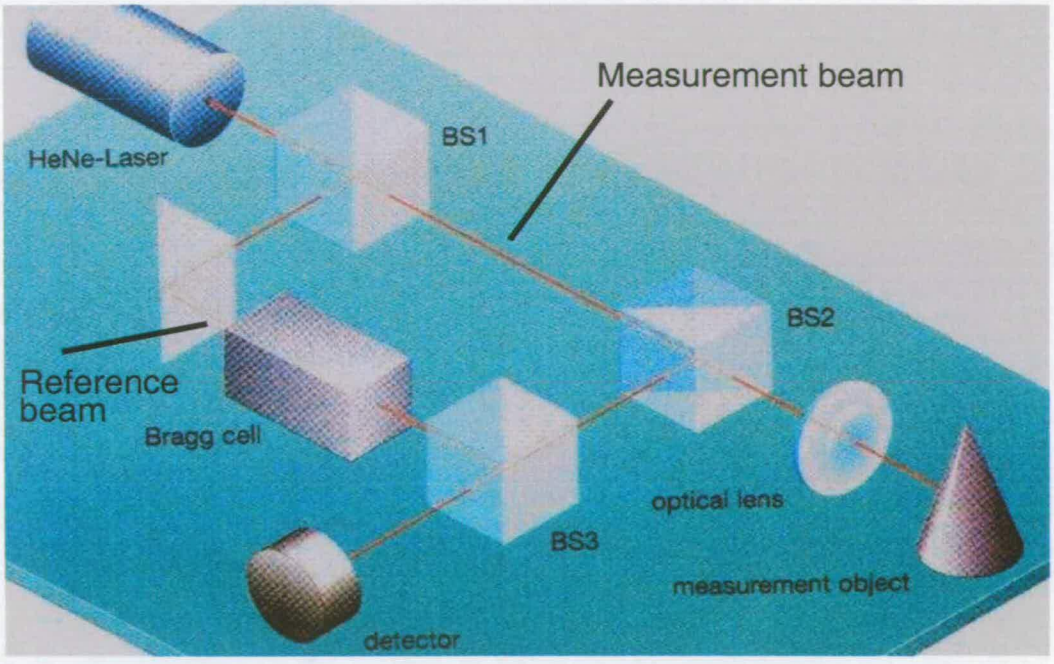

Figure 6.2. Schematic of a laser vibrometer measurement. During a vibrometer measurement, a HeNe laser beam was split into a reference beam and measurement beam. The resonant frequency was determined from the Doppler shift between these two beams [45]. (Picture courtesy of John Hedley, University of Newcastle, UK).

6.3 Characterisation of MEMS resonators

Polysilicon cantilever and bridge resonators, fabricated from two different test chip designs (Ch. 5), were glued to copper disks in preparation for static and dynamic characterisation. The characterisation of cantilever and bridge resonators involved:

- deflection measurements to determine residual stress
- resonant frequency measurements

A Zygo white light surface profiler was used for deflection measurements of individual or groups of cantilever and bridge resonators. The deflection was measured at the free end of cantilevers and middle of bridges with respect to a previously defined reference plane at the anchor region of the resonators.

In order to avoid air damping, frequency measurements on polysilicon resonators were performed in a vacuum with a constant pressure of 20μbar. For vibration actuation, resonator samples glued to copper disks were attached to a piezoelectric disk using wax (Apiezon Wax W100). The laser vibrometer was focused onto the surface of polysilicon cantilevers and bridge resonators to detect the resonance. Resonance was produced by applying an Alternating Current (AC) actuation voltage with a predefined frequency range to the piezoelectric block. The detected resonator vibration amplitude was displayed as a function of the scanned frequency in a Labview integrated spectrum analyser. The resonant frequency of a polysilicon cantilever or bridge resonator was extracted from these recorded frequency spectra and used in FEM simulations to determine the Young's modulus and biaxial stress of polysilicon.

6.3.1 Deflection measurements

This section reports on out-of-plane deflection measurements of micromachined polysilicon resonators manufactured from two test chips.

Resonator from test chip one

The deflection of undoped polysilicon bridge resonators is plotted as a function of length in Fig. 6.3(a). An example of a surface profile scan for a $200\mu\text{m}\times20\mu\text{m}\times1\mu\text{m}$ polysilicon bridge resonator is shown in Fig. 6.3(b).

The surface profile in Fig. 6.3(b) shows the polysilicon bridge with severe upward deflection (buckling). Buckling was observed on all manufactured bridges, which suggested biaxial compressive stress in the undoped polysilicon [31].

However, wafer curvature measurements found tensile biaxial stress for undoped polysilicon deposited at 585°C (Fig. B.4). In these experiments it was found that biaxial stress of undoped polysilicon was strongly dependent on the deposition temperature inside the furnace (Fig. B.4). During this work, the polysilicon furnace tube had to be replaced several times. It was noted at a later point in this project, that temperature sensors located at the perimeter of the tube were not accurately installed, which resulted in incorrect temperature readings. Inaccurate sensing caused a shift (ΔT=15°C) in deposition temperature and in biaxial stress from tensile to compressive.

The presence of compressive biaxial stress caused buckling, which was detected through the midpoint deflection of polysilicon bridge resonators (Fig. 6.3(a)). Fig. 6.3(a) shows the measured bridge midpoint deflection, which increased linearly with the resonator length. Standard mechanics literature, however, shows that the bridge midpoint deflection is inversely proportional to length in the transition from pre- to post-buckling [20, 37]. This discrepancy was a result of imperfections in the polysilicon, which is not accounted for in standard buckling models. Sources of imperfections include stress variations through the polysilicon film thickness, curvature of the wafer and slight changes in resonator cross section along the length. These imperfections produced the observed linear increase in midpoint deflection in the transition from the pre- to the post-buckling. The experimentally obtained linear relationship between midpoint deflection and bridge length agreed with the literature [31].

To show the presence of imperfections in the polysilicon layer, a surface profiler scan was taken at the anchor of a 150μm $\times$ 20μm $\times$ 1μm polysilicon bridge (Fig. 6.4). The surface profiler scan shows an anchor region deflection, which continuously increased over a distance of 18μm with a maximum value of 35nm. The distance of the detected deflection equaled an etch undercut, which originated from the wet chemical release etch of the underlying sacrificial PECVD SiO_2 layer.

The detected upward deflection of the anchor region suggested a tensile stress gradient through the polysilicon film thickness, which acted as an imperfection of the bridge resonators and caused a linear increase in midpoint deflection with length.

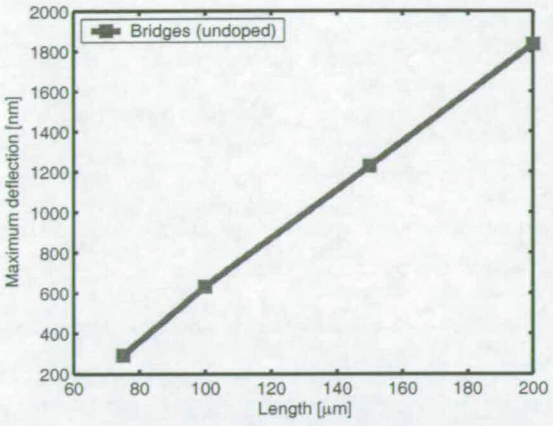

(a)

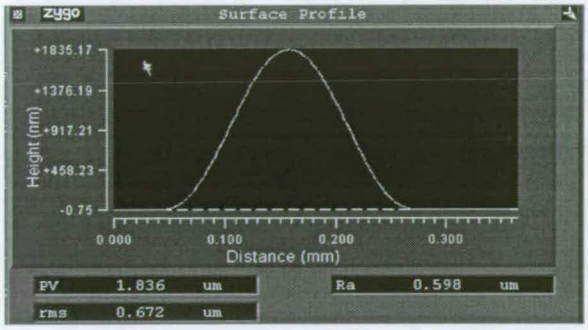

(b)

Figure 6.3. Measured bridge resonator midpoint deflection. (a) Measured resonator midpoint deflection as a function of length. (b) Surface profiler plot of a buckled $200\mu m \times 20\mu m \times 1\mu m$ polysilicon bridge resonator. The buckling suggested compressive biaxial stress in the polysilicon. The deflection of polysilicon bridge resonators decreased in a linear fashion with their length. Standard mechanical models describe an inverse rise in deflection with length $\frac{1}{L}$ in transition between pre-to post-buckling [20, 37]. The reason for this discrepancy was imperfections in the polysilicon, which produced the observed linear relationship between midpoint deflection and bridge length [31]. The presented linear relationship agreed with the one published elsewhere [31].

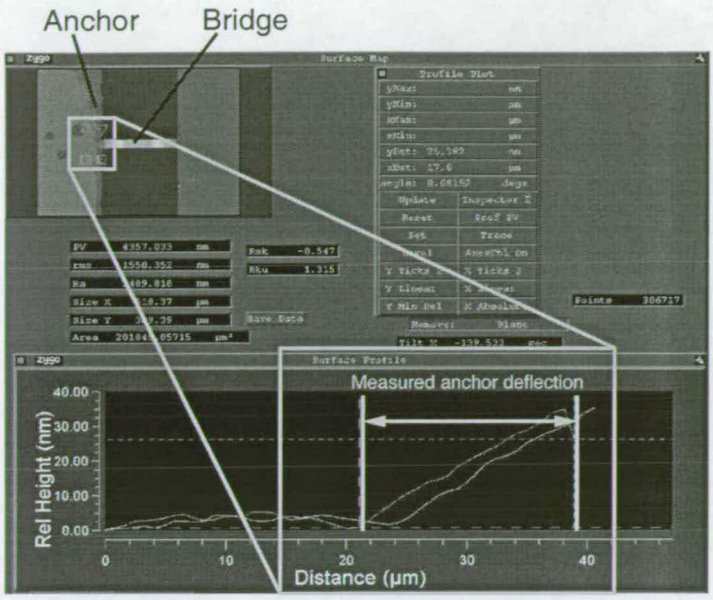

Figure 6.4. Measured polysilicon anchor deflection. The measured anchor deflection of a 150μm $\times$ 20μm $\times$ 1μm bridge resonator suggested a tensile stress gradient through the polysilicon film. The tensile stress gradient acted as an imperfection, which caused a linear increase in midpoint deflection with bridge resonator length. An etch undercut of 18μm$\pm$1μm was extracted from the deflection of the polysilicon anchor region.

Resonator from test chip two

Fig. 6.5 depicts the deflection of phosphorus doped polysilicon cantilever and bridge resonators as a function of their length. Included in the measurement data are surface scans of 200μm$\times$15μm$\times$2.3μm cantilever and bridge resonators.

Both cantilevers and bridges showed an upward deflection, which suggested a tensile stress gradient through the polysilicon layer. The stress gradient, $\sigma_{gradient}$, through the polysilicon layer relates to the measured tip deflection, $\delta_{cantilever}$, of a cantilever beam with length L and thickness t [32]:

$$\sigma_{gradient} = \frac{E_{poly} t \delta_{cantilever}}{L^2}. \tag{6.1}$$

The measured cantilever tip deflection changed in a linear fashion with length. However, Eq. (6.1) defines a quadratic relationship between tip deflection and beam length. This indicated a variation in $\sigma_{gradient}$ for different locations on the sample. To further investigate this variation, Eq. (6.1) and the measured tip deflections were used to determine an average tensile stress gradient of +2.7MPa$\pm$1MPa. The calculated variation

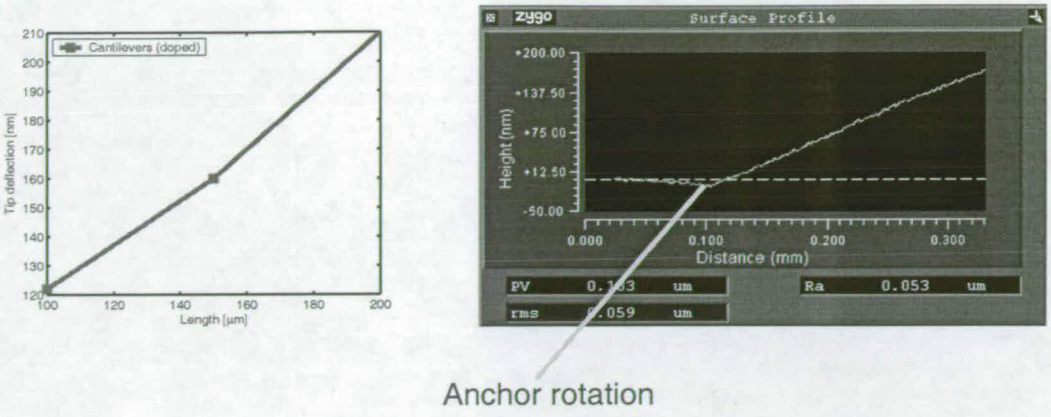

(a) Cantilevers

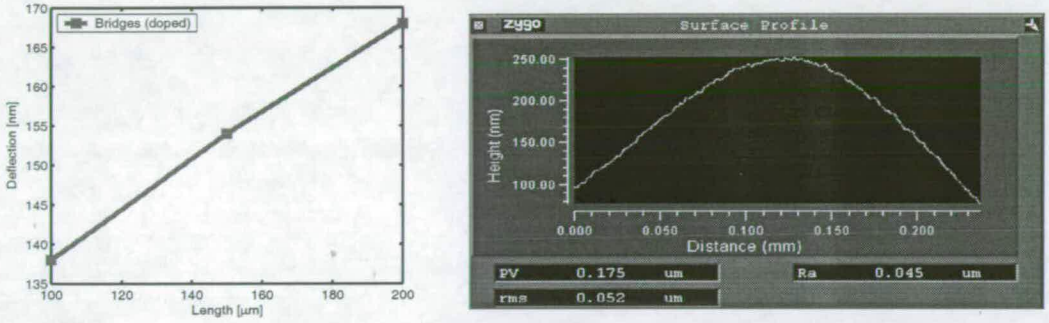

(b) Bridges

Figure 6.5. Measured resonator deflection. Deflection of phosphorus doped polysilicon (a) cantilevers and (b) bridges as a function of their length. The deflection was measured at the tip of cantilevers and middle section of bridges. The surface scans showed a slight upward deflection of a $200\mu m \times 15\mu m \times 2.3\mu m$ cantilever and bridge, suggesting a slight tensile stress gradient in the polysilicon layer. Note that the slight anchor rotation in (a) suggested compressive axial stress in the polysilicon [32].

in the stress gradient throughout the sample was the reason for the deviation from the quadratic relationship between tip deflection and cantilever beam length.

The slight rotation at the anchor of the cantilever beam (Fig. 6.5(a)), suggested a compressive axial stress in the polysilicon [32]. However, frequency measurements on bridge resonators needed to be performed to confirm these findings.

Bridges experienced a similar slight upward deflection to cantilevers, which confirmed the presence of a small tensile stress gradient through the polysilicon film thickness (Fig. 6.5(b)).

To further prove the existence of the stress gradient, deflection measurements were performed at the anchor region of a 150μm $\times$ 15μm $\times$ 1μm bridge resonator (Fig. 6.6). The deflection slope of the polysilicon anchor shown in Fig. 6.6 extended over a distance of 28μm with a maximum displacement of 55nm. The extent of this deflection indicated an etch undercut of 28μm$\pm$1μm and a slight tensile stress gradient through the polysilicon film.

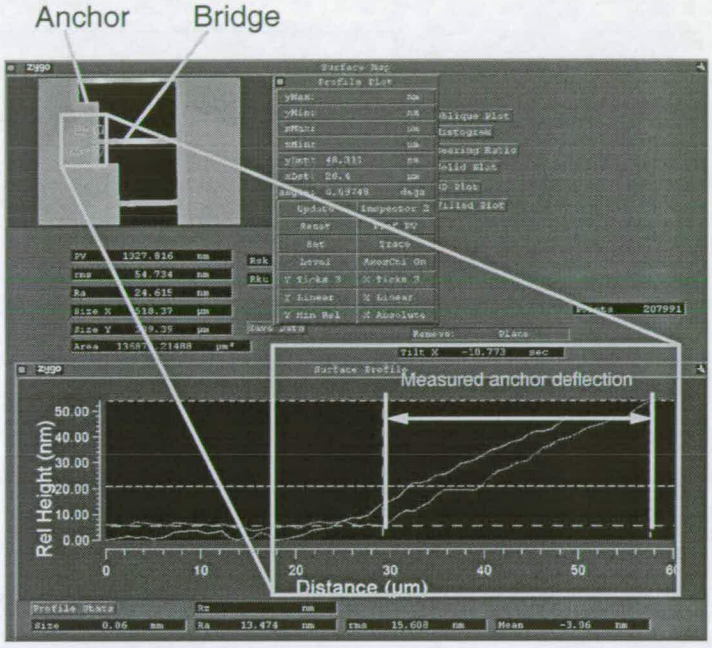

Figure 6.6. Measured polysilicon anchor deflection. The measured anchor deflection of a 150μm $\times$ 20μm $\times$ 1μm bridge resonator suggested a tensile stress gradient through the polysilicon film, which was previously explored in cantilevers displacement measurements. An etch undercut of 28μm$\pm$1μm was extracted from the extent of deflection of the polysilicon anchor region.

6.3.2 Frequency measurements

Resonators from test chip one

The measured resonant frequency of undoped polysilicon bridge resonators manufactured from the first test chip is presented in Fig. 6.7 along with results from FEM simulations. Results from FEM simulations were matched to experimental results to find polysilicon biaxial stress in the bridge resonators. To match FEM results with experimental data, a temperature gradient was applied between bottom and top side of the bridges to generate initial bridge buckling. Once the buckling agreed with measured bridge deflections, the biaxial stress was applied to the bridge resonators until their resonant frequencies matched those from the experiments. The simulations assumed an etch undercut of 18μm a polysilicon Young's modulus of 160GPa [74].

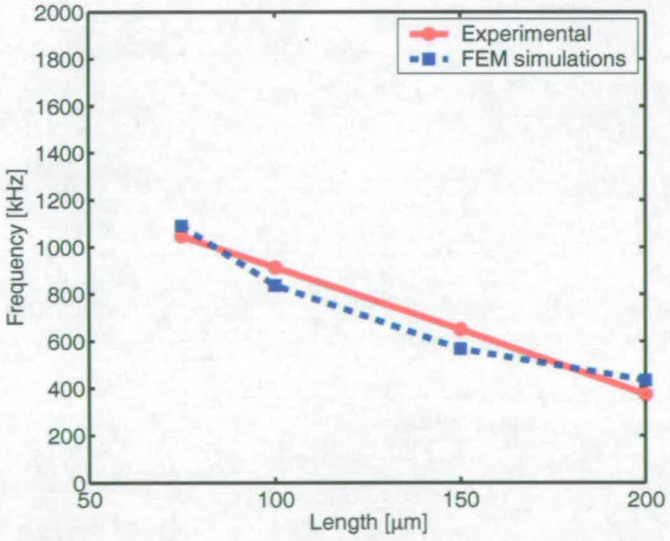

Figure 6.7. Resonant frequency as a function of bridge resonator length. The measured resonant frequency decreased linearly with bridge length (L). Results from FEM simulations deviated from the measurement data and predicted a fall in resonant frequency with a $\frac{1}{L}$ behaviour. This difference was believed to be a result of stress relief in glue, which was used to mount the resonator sample to the copper disk (Ch. 7). Softening and hardening of the glue during and after sample attachment caused stress in the polysilicon bridges, which altered their resonant frequency over time and caused the deviation between measurements and simulations.

The measured resonant frequency in Fig. 6.7 decreased linearly with rising bridge resonator length. In contrast, FEM simulation followed a $\frac{1}{L}$ relationship. The discrepancy between measurement and simulations was believed due to stress relief in glue, which was used to attach the polysilicon resonator sample to a copper carrier plate (Ch. 7). The stress relief in the glue caused a change in bridge resonant frequency and the observed difference to the FEM simulations. Despite the observed discrepancy, a compressive biaxial stress of 60MPa was extracted from FEM simulations and confirmed assumptions made during the deflections measurements. It should be noted at this point, that the influence of the stress relief in the glue on the bridge resonant frequency was observed at the very end of this project and a full investigation could not be performed due to the limited time available. The future work, which needs to be done is discussed in the concluding chapter of this thesis.

Resonators from test chip two

Fig. 6.8 presents the measured resonant frequency of phosphorus doped polysilicon cantilever and bridge resonators as a function of length (L) and compares them with results obtained from FEM simulations. FEM simulations were matched to experimental results in order to extract Young's modulus and biaxial stress in the phosphorus doped polysilicon. Note that FEM simulations included a measured etch undercut of 28μm for polysilicon cantilever and bridge resonators.

The measured and simulated resonant frequencies of cantilevers and bridges were in good agreement and decreased as expected with a $\frac{1}{L^2}$ relationship (Fig. 6.8).

FEM cantilever simulations were used to extract the Young's modulus, since their resonant frequencies were not affected by the biaxial stress. From these simulations, a Young's modulus of 135GPa for phosphorus doped polysilicon was extracted, which was slightly lower than that reported for undoped polysilicon [74]. The decrease in Young's modulus with the introduction of phosphorus has also been observed by other researchers [66]. However, a plausible explanation for the reduction in polysilicon Young's modulus with increasing phosphorus doping concentration has not been given [66].

Once the polysilicon Young's modulus was known, further FEM simulations were performed to extract polysilicon biaxial stress. Simulations found a compressive biaxial stress of 30MPa. The compressive stress in polysilicon confirmed observations made

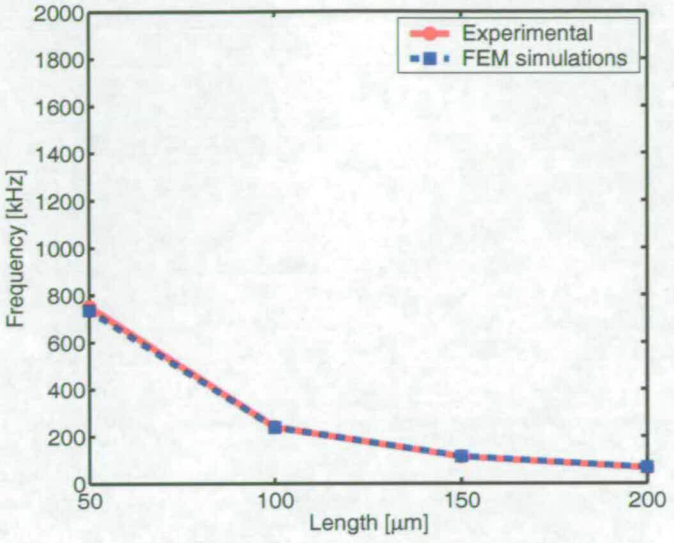

(a) Cantilevers

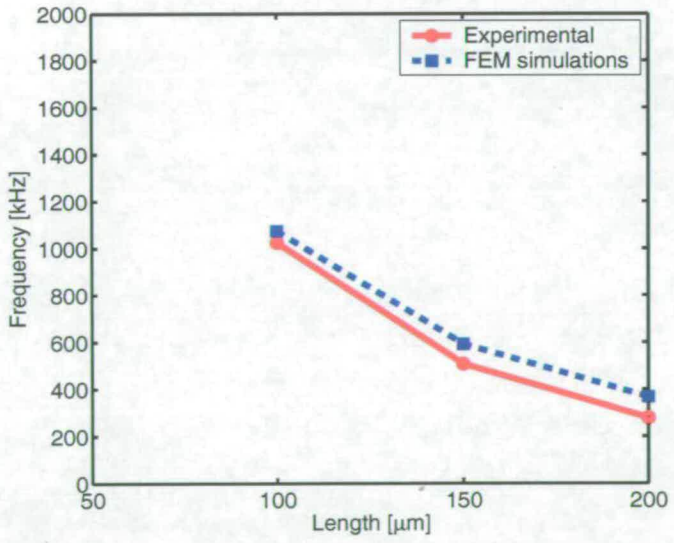

(b) Bridges

Figure 6.8. Resonant frequency as a function of resonator length. Measured and simulated resonant frequencies of phosphorus doped polysilicon (a) cantilevers and (b) bridges. FEM simulations were matched to experimental results to extract polysilicon Young's modulus and biaxial stress. Note that measured and simulated resonant frequencies decreased with the expected $\frac{1}{L^2}$ relationship.

during the deflection measurement in Sec. 6.3.1. The compressive biaxial stress in the polysilicon was a result of the phosphorus doping [91] (Appendix B).

Note, the maximum measured variation in resonant frequency for polysilicon cantilevers and bridges was 0.95% and 22%, respectively. As observed in case of polysilicon bridges from test chip one, the large frequency variation in bridges was believed to be a result of stress relief in glue used to attach the resonator sample to a copper carrier plate onto the piezoelectric block. The investigation of stress relaxation in mounting glue is future work.

6.4 Conclusions

This chapter has described the test equipment and the characterisation of micromachined polysilicon resonators fabricated from two test chips. The optical workstation used to perform all testing included a Zygo surface profiler to perform static deflection and a HeNe laser vibrometer to undertake frequency measurements on all polysilicon cantilever and bridge resonators.

Testing of polysilicon bridge resonators from the first test chip involved deflection and frequency measurements. Deflection measurements showed excessive buckling in the undoped polysilicon bridges and suggested a combination of a compressive biaxial and stress gradient. The presence of biaxial stress was confirmed by frequency measurements and FEM simulations. The measured resonant frequency deviated from FEM simulations, which was believed due to the effect of stress relief in glue. Despite the difference between measurements and simulations, a biaxial compressive stress of 60MPa was extracted. Note that measurement results were based on one sample only and the effect of glue stress relief was discovered at the very end of this project. Hence, a full investigation into the influenced of glue stress relief was not pursued due to the limited time and number of samples available. The investigation of the stress relief is future work.

Deflection measurements on polysilicon cantilevers and bridges fabricated from the second test chip did not show the excessive deflection seen for devices from the first test chip. An average tensile stress gradient as low as 3MPa was determined from cantilever tip deflection measurements, while FEM resonator simulations extracted a

Young's modulus of 135GPa and a compressive biaxial stress of 30MPa. Heavy phosphorus doping caused the compressive biaxial stress in the polysilicon. The development of compressive stress with increasing phosphorus doping was reported in the literature [91] and experimentally confirmed by curvature measurements on blanket deposited films (Appendix B). The value that was extracted for the Young's modulus was lower than values found for undoped polysilicon [74]. However, it has been reported elsewhere that phosphorus caused a reduction in Young's modulus [66].

In conclusion, compressive biaxial stress was found in polysilicon resonators from two test chips. Excessive compressive biaxial stress can significantly alter the resonant frequency of micromechanical resonators, which would make them unsuitable for filter and oscillator applications. Part of this PhD project involved the process optimisation of polysilicon deposition and biaxial stress. To reduce biaxial polysilicon stress, tensile undoped polysilicon was used and phosphorus introduced to make films more compressive. By balancing the phosphorus concentration in polysilicon, films with a biaxial stress as low as 5MPa were produced (Appendix B). In reality, however, some biaxial stress always remains in the polysilicon, which causes shifts in the resonant frequency of micromechanical resonators. Hence, a tuning method has to be available, which can modify the resonant frequency to accommodate biaxial stress.

Chapter 7

Characterisation of frequency tuning by FIB platinum deposition

This chapter characterises and demonstrates Focused Ion Beam (FIB) platinum (Pt) deposition for the purpose of frequency tuning of micromechanical SiC and polysilicon resonators. FEM simulations, analytical modelling and frequency measurements are used to analyse this tuning technique and results are presented and discussed.

7.1 Introduction

Fabrication of micromechanical resonators is accompanied by tolerances in the etch process, layer deposition and intrinsic stress. These fabrication related factors cause a variation of the resonant frequency. Depending on the magnitude of this variation, filters and oscillators may not be able to meet their designed target specifications. Tuning methods are used to rectify the situation by correcting the resonant frequency. Mainly passive frequency tuning methods are employed for high-Q RF filters, because of their superior accuracy compared to their active counterparts (Ch. 3). Current passive methods can make very accurate changes in resonant frequency, but device failure is always a possibility [1].

In recent years, Focused Ion Beam (FIB) has found a wide range of applications because it is capable of depositing and sputtering material in different sized volumes. The deposition and sputtering of different sized material volumes can alter resonant frequency over a wide range. This makes it an ideal technique for frequency tuning, because coarse and fine changes can be performed and the change only depends on the amount of sputtered or deposited material. Once FIB sputtering and deposition has been performed to cause a frequency change in a resonator, no additional energy is required to maintain this modification in resonant frequency, making the technology valuable for RF filter applications in low power transceivers, where battery power is limited.

Related research has shown that a FIB system can be used for frequency tuning. In existing work, tuning was achieved by sputtering the suspension of a comb drive resonator [122]. However, frequency tuning by FIB material deposition using platinum (Pt) has not been demonstrated to date. Therefore, it is of interest to characterise FIB Pt deposited frequency tuning of micromechanical resonators.

In this chapter, 3C silicon carbide (SiC) and polysilicon cantilever and bridge resonators from a second test chip (Ch. 5) are used to characterise FIB Pt deposited frequency tuning. FEM simulation and analytical modelling are used to predict and analyse FIB Pt deposited tuning. Simulation results are experimentally verified by depositing various amounts of Pt onto the resonators and parameters such as frequency change and Q-value are extracted.

7.2 Focused Ion Beam deposited frequency tuning

7.2.1 Focused Ion Beam

Focused Ion Beam (FIB) systems to enable high resolution deposition and sputtering emerged in the mid 1970's when the first working Liquid Metal Ion Sources (LMIS) appeared. These were initially intended for scanning ion microscopy and microcircuit fabrication, but soon found other applications ranging from Transmission Electron Microscope (TEM) sample preparation [38] to IC failure analysis [42] and resistless lithography [36]. Because of its precision and flexibility in machining and deposition, FIB also found applications in the field of MEMS for fabrication of thermal actuators [125], microaccelormeters [22] and sensors [10].

A FIB system incorporates a LMIS source as shown in Fig. 7.1 [113]. This source con-

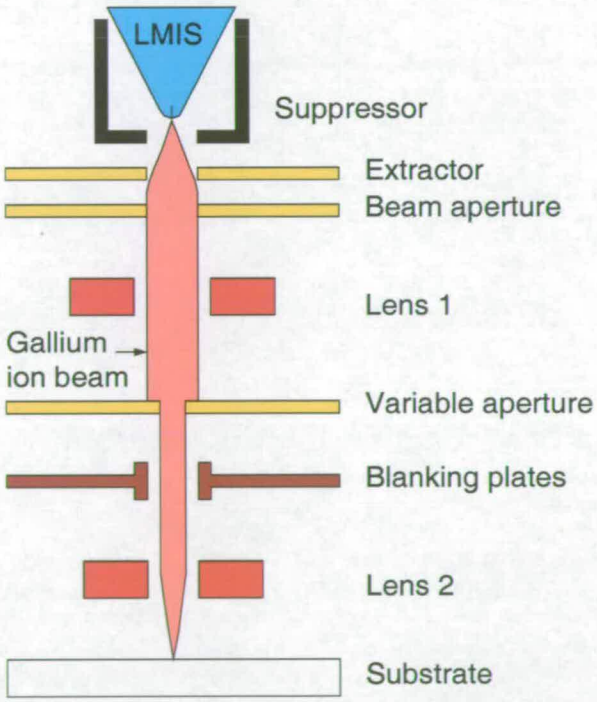

Figure 7.1. Schematic of a FIB system. The heart of FIB is a LMIS source, which provides heavy Ga^+ ions for imaging, sputtering and selective material deposition. The source is heated to cover a needle apex with liquid gallium. Ga^+ ions are extracted from the needle using field emission and accelerated to the sample surface using a high electric field [115].

sists of a needle connected to a reservoir of liquid metal such as gallium (Ga^+). Heavy

Ga^+ ions are produced from the source by field emission under the action of an electric field [98]. The extracted ions are then accelerated to the sample surface where they can be used for imaging purposes, high resolution sputtering or selective material deposition.

In the sputtering mode (Fig. 7.2), high energy Ga^+ hits the sample surface and removes material in the form of neutral atoms and secondary ions and electrons. Apart from material removal, the emitted ions or electrons can be detected to create an image of the scanned area.

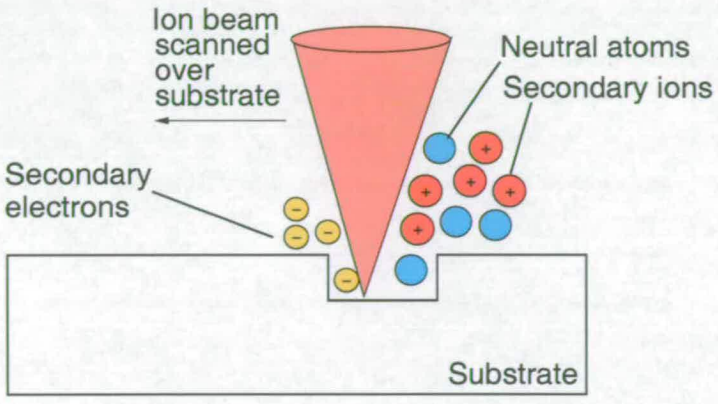

Figure 7.2. FIB material sputtering. High energy (30keV) Ga^+ ions remove secondary ions, electrons and atoms from the surface of the sample. The sputtered electrons and secondary ions can be used for imaging purposes utilising in-built detectors.

In the FIB platinum (Pt) deposition mode (Fig. 7.3), an organometallic precursor gas (trimethyl platinum) is delivered to the sample by a gas needle located 100μm above the target surface. Deposition only takes place if enough gas molecules are absorbed to the target surface and their binding energy is sufficiently large compared to the decomposition of the molecules. The incoming Ga^+ ions first break surface bonds of the resonator material and provide bonds for the precursor gas. Additional cross linking between neighbour surface bound molecules initialises the film growth. Under continuing Ga^+ ion bombardment, the organic component is separated from the Pt part and film growth proceeds [99]. Note, that it is possible to deposit other materials than Pt using FIB. Alternative materials are tungsten (W), silicon dioxide (SiO_2) and even magnetic materials [49].

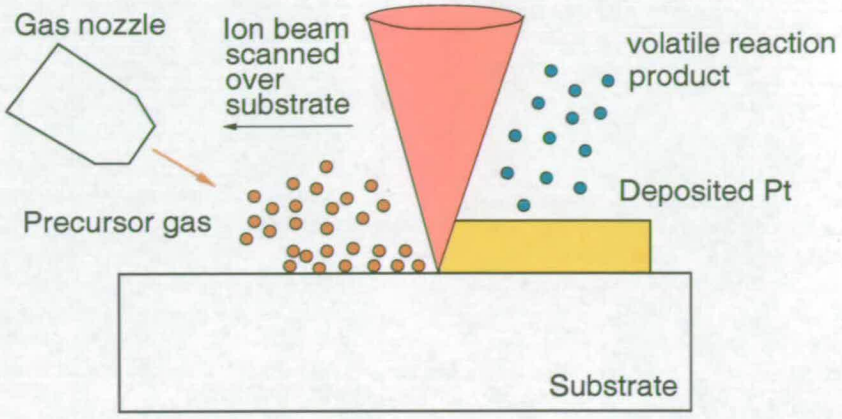

Figure 7.3. FIB platinum deposition. The energy of Ga^+ is utilised to break the surface bonds of the resonator material to enable the precursor gas absorption. Subsequently, the organometallic gas is decomposed under the influence of the Ga^+ ions, leaving Pt metal behind. The resulting volatile reaction products are pumped out of the FIB chamber.

7.2.2 Concept of Focused Ion Beam frequency tuning

Compared to sputtering [122], FIB Pt deposition [29] is an alternative way of tuning the resonant frequency of micromechanical resonators as shown in Fig. 7.4. In this case, the FIB deposited Pt alters the resonant frequency depending on the amount and location of the deposition along the the length of cantilevers and bridges. FIB Pt deposits close to the support of the resonators increase the equivalent stiffness and the resonant frequency. Pt deposits located away from the support of the resonator increase the equivalent mass of the device and therefore decrease the resonant frequency. In this work only the equivalent mass was altered by placing Pt in the middle of bridges and tips of cantilevers. An alteration of the equivalent stiffness is future work.

7.3 FIB deposited tuning of SiC and polysilicon resonators

FIB deposited frequency tuning has been characterised using (i) SiC and (ii) polysilicon cantilever and bridge resonators. Both types of resonators were manufactured from a second test chip design, which contained devices of different lengths (Sec. 5.2.2). Due to the small number of samples available, only one die of SiC and polysilicon resonators were used to perform FIB Pt deposited frequency tuning. One cantilever

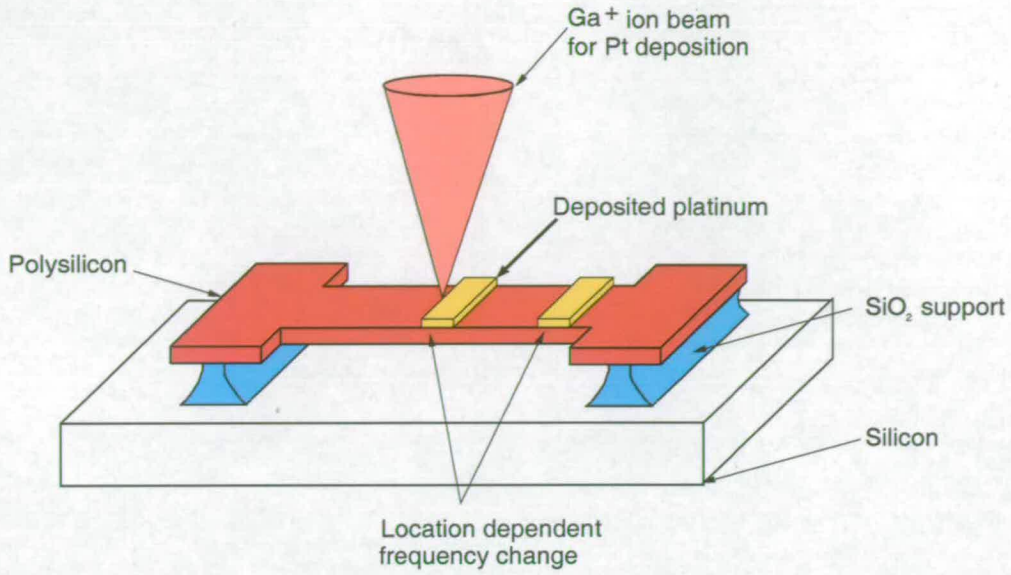

Figure 7.4. Frequency tuning of resonators by FIB Pt deposition. FIB deposition on flexural vibrating resonators causes a location dependent change of equivalent mass and stiffness along the device length. Pt deposits near the support of the device increase the equivalent stiffness and hence frequency. Deposits located in the centre of the resonator increase the equivalent mass and decrease the resonant frequency. In this work, the latter deposition strategy was used to decrease the resonant frequency of resonators. An alteration of the equivalent stiffness by Pt deposition is future work.

and bridge resonator of each length was not exposed to Ga^+ ions or deposited with Pt. These resonators served as "reference" resonators used to detect any changes in measurement condition, which would otherwise have been difficult to measure on Pt deposited devices.

SiC resonators ($200\mu m \times 15\ \mu m \times 2\mu m$) were used to demonstrate FIB deposited tuning by changing their equivalent mass. This "mass tuning effect" was achieved by selective Pt deposition on the tips of cantilevers and middle of bridges. The measured changes in resonant frequency were compared to polysilicon resonators ($200\mu m \times 15\ \mu m \times 2.3\mu m$), which were deposited with Pt at the same locations.

To predict and subsequently analyse the mass tuning effect, Finite Element Method (FEM) simulations and analytical modelling were used. Simulation results were experimentally verified by Pt deposition on SiC and polysilicon resonators. Before Pt deposition, resonators were attached to a copper plate to experimentally characterise them using an optical workstation (Ch. 6). The experimental characterisation before

and after Pt depositions included surface profiler and frequency measurements on SiC and polysilicon resonators using an optical workstation.

Surface profiler measurements were performed to measure the thickness of the deposited Pt. The measured Pt thickness was used to evaluate the FIB deposition process and to determine a deposition rate.

For the frequency measurements, resonator samples on copper carrier plates were attached to a piezoelectric disc and inertially actuated in a vacuum with a constant pressure of 20μbar. Their resonant peaks were detected and displayed using a laser vibrometer and a LabVieW integrated spectrum analyser. The change in resonant frequency was obtained by measuring the fundamental resonant frequency of each resonator before and after the Pt deposition process. From the recorded frequency spectra, the Q-factor was extracted using the bandwidth method as described in Chapter 2.

7.4 Characterisation of FIB Pt deposited tuning on SiC resonators

7.4.1 Modelling and Simulation

In order to evaluate the mass tuning, SiC resonators were first simulated using a FEM model, which predicted the change in resonant frequency due to the deposition of Pt material. The software employed for the FEM-analysis was Coventorware 2004. The resonators simulated were 200μm$\times$15μm$\times$2μm 3C SiC cantilevers and bridge resonators, which included an 7.5μm undercut at the attachment region of the resonators [50]. Details of the assigned boundary conditions, which were applied for the simulations are summarised in Fig. 7.5.

The analytical model developed in Sec. 2.3.2 was used to predict the frequency change as result of Pt deposition. The analytical model in contrast to the simulation did not include biaxial stress and an etch undercut in the attachment region. It also assumed that the vibrational mode shape did not change upon the deposition of the Pt material.

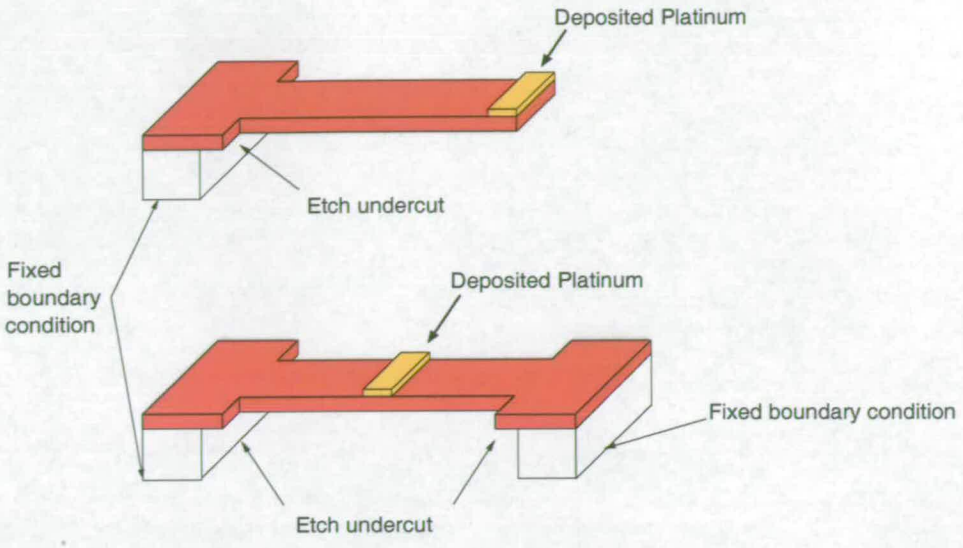

Figure 7.5. Assigned boundary conditions for the FEM simulation of FIB Pt deposited mass tuning. FIB Pt deposits were placed in the middle of bridges and tip of cantilevers to decrease the resonant frequency by increasing the Pt thickness. SiC resonators were resting on Si. An etch undercut of 7.5μm was included into the simulation model.

Physical material parameters employed for the modelling and simulations of FIB deposited resonator tuning are summarised in Table 7.1. Both the analytical model and

Property	3C SiC	Polysilicon	Platinum
Young's modulus, E $[GPa]$	400	135	168
Density, ρ $[kg \times m^{-3}]$	3,230	2,230	21,500
Poison ratio, η	0.22	0.226	0.377
Biaxial stress, σ $[MPa]$	400	-30	0

Table 7.1. Material properties used for the FEM simulation. Material properties of 3C SiC [50], [106], polysilicon (Ch. 5) and bulk Pt [54].

FEM simulations assumed an ideal rectangular cross section and a uniform resonator thickness. In order to evaluate the mass tuning effect, a Pt layer with a fixed 13×5μm surface area and a range of thicknesses from 0.3 to 3.1μm was placed on the tips of cantilevers and the middle sections of bridges.

Fig. 7.6 presents the simulated and analytically calculated frequency change of SiC cantilever and bridge resonators as a function of deposited Pt thickness. Modelling and simulation results presented were based on actual measured Pt thicknesses found on the resonators (Sec. 7.4.2).

Both analytical model and simulations were in good agreement and predicted a linear decrease in cantilever resonant frequency with increasing Pt thickness. The simulated and calculated maximum frequency changes were -21% and -22% for cantilevers, respectively. The linear decrease in resonant frequency with deposited Pt suggests an increase in equivalent mass of the cantilever resonators. Equivalent mass of cantilevers increased linearly with deposited Pt thickness $m_{Pt} \approx t_{pt}$ (Eq. (2.12)). Therefore, resonant frequency decreased linearly with further deposited Pt thickness.

As observed in the case of cantilevers, the resonant frequency of bridges decreased in a linear fashion with the deposited Pt thickness (Fig. 7.6(b)). Again, the decrease in frequency was a result of a growing equivalent mass m_{eq}, which has a linear relationship to thickness.

The maximum simulated and calculated frequency changes of SiC bridges were -19% and -16.6%, respectively. This discrepancy between simulation and calculation was due to a number of reasons. FEM simulations were performed with a limited number of elements (80,000) to keep computation times in a manageable time frame. The limited number of elements caused inaccuracies, which need to be taken into account when analytical model and FEM simulations are compared. Another factor contributing to the difference is the limited accuracy in eigenvalue extraction during the FEM modal analysis, which was observed by other researchers [35]. Discrepancies arose also from the analytical model, which omitted the present etch undercut and axial stress in the cantilevers and bridges.

7.4.2 FIB platinum deposition

A FEI FIB 200 workstation was employed to deposit Pt on 200μm$\times$15μm$\times$2μm 3C SiC cantilever and bridge resonators with an acceleration voltage of 30kV. For optimum Pt deposition, the FIB user's manual suggested a Ga^+ ion beam current density of $2pA\ \mu m^{-2}$ - $6pA\ \mu m^{-2}$ [19]. Pt was selectively deposited on a 13$\times$5μm surface area of the SiC resonators in thicknesses ranging between 0.3 and 3.1μm. In this work, a Ga^+ ion beam current density of 2pA μm^{-2} was used to deposit Pt. Fig. 7.7 shows deposited Pt on SiC cantilever and bridge resonators.

After FIB deposition onto the resonators, a white light surface profiler was used to measure the thickness of the Pt. From these measurements it was found that the Pt deposition rate specified in the FIB system differed from the measured one by up to

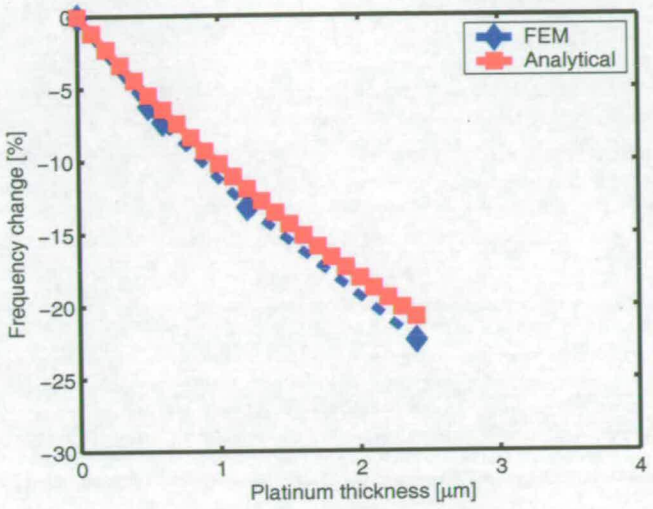

(a) SiC cantilevers

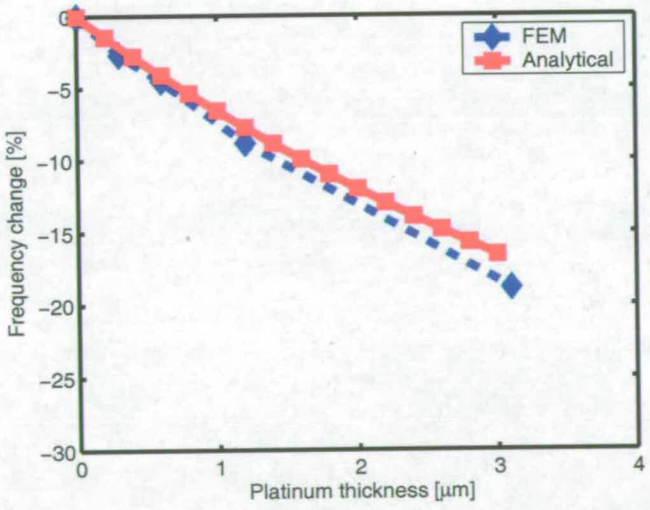

(b) SiC bridges

Figure 7.6. Simulated and analytically modelled frequency change of 3C SiC cantilever and bridge resonators as a function of deposited Pt thickness. Simulated and calculated frequency change of 200μm $\times$ 15μm $\times$ 2μm SiC (a) cantilevers and (b) bridges as a function of Pt thickness. Pt thicknesses used for simulations and analytical calculations are those measured in Sec. 7.4.2.

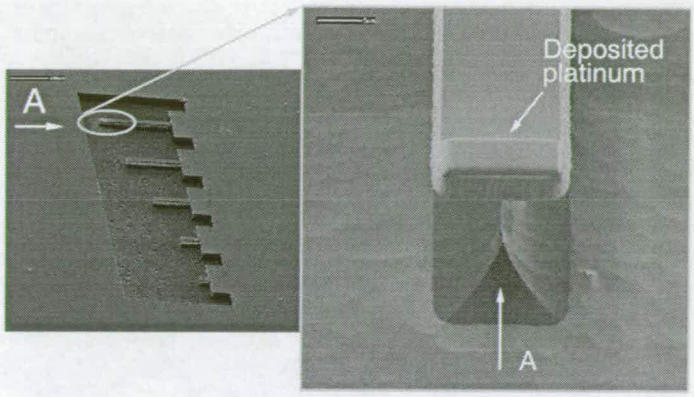

(a) SiC cantilever

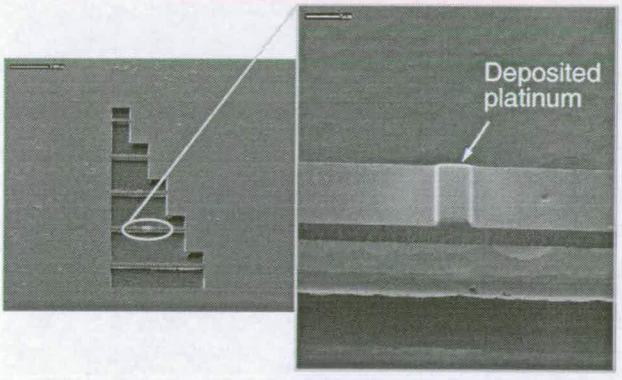

(b) SiC bridge

Figure 7.7. Selective Pt deposition on SiC resonators. The figures show an example of 1.2μm thick deposited Pt on a 13μm×5μm surface area at the tip of SiC cantilever and middle section of bridge resonators. The Pt deposited resonators were 200μm × 15 μm × 2μm in size.

40%. The observed deviation in deposition rate is a result of the widening of the FIB aperture, which resulted in a beam current of 190pA instead of the 150pA specified before deposition. Despite the observed off-set in deposited Pt thickness, an average Pt deposition rate of 0.12μm/min. was determined for SiC resonators, respectively. A variability in deposited thickness of ±20% causes a variability in frequency change by up to ±10% (Eq. (2.17)). Such a large variation in frequency is not acceptable for frequency tuning of sensors and filters. However, real time tuning is alternative where variation in deposited Pt thickness do not influence the desired frequency change in micromechanical resonators. Real time tuning entails the in-situ monitoring of the

resonant frequency during FIB deposition. This would eliminate the errors, since FIB deposited tuning can be controlled by constant monitoring of the resonant frequency. The implementation of such a tuning arrangement is future work.

7.4.3 FIB deposited tuning of SiC resonators

The measured change in resonant frequency as a function of the deposited Pt thickness for SiC resonators is presented in Fig. 7.8. It can be observed that resonant frequency of the cantilevers and bridges decreased with Pt thickness as predicted by previous analytical calculations and FEM simulations (Fig. 7.6). While the resonant frequency of cantilevers decreased linearly with the deposited Pt thickness, bridges abated in a non-linear fashion. The maximum measured change in resonant frequency was found to be -12% in the case of SiC cantilevers and bridges with a Pt thickness of 2.4μm and 3.1μm, respectively.

Initial simulation (Fig. 7.6) results differed markedly from the measurement data by up to 10%, because properties of bulk Pt and a nominal SiC thickness (2μm) were used as input data for both the FEM-analysis and analytical calculations. In order to match the simulations and calculations with the measurement data, the thickness of the SiC was determined using an ellipsometer (SOPRA SE-5). Measurements gave a material thickness of 2.5μm instead of the 2μm assumed for the previous analysis. After the resonator thickness was known, the value of bulk Pt density was changed from $\rho_1 = 21,500kg\ m^{-3}$ to $\rho_2 = 13,400kg\ m^{-3}$ to match simulation with measurement results (Fig. 7.8). The deviation of Pt mass density from its bulk value was explained by the enclosure of organic residues into the FIB deposited films. Resistivity measurements confirmed the presence of organometallic residues in FIB deposited Pt [115], which altered the structural composition and hence the mass density of Pt.

Fig. 7.8 includes the re-simulated and calculated frequency change using the modified SiC thickness and Pt density. Using these parameters, the maximum simulated and calculated frequency change for SiC cantilevers was -13.4%. For bridges, a maximum simulated and calculated frequency change was -11.3% and -10.9, respectively. The difference between FEM simulation and analytical modelling in cantilevers and bridges was due the number of factors highlighted in Sec. 7.4.1.

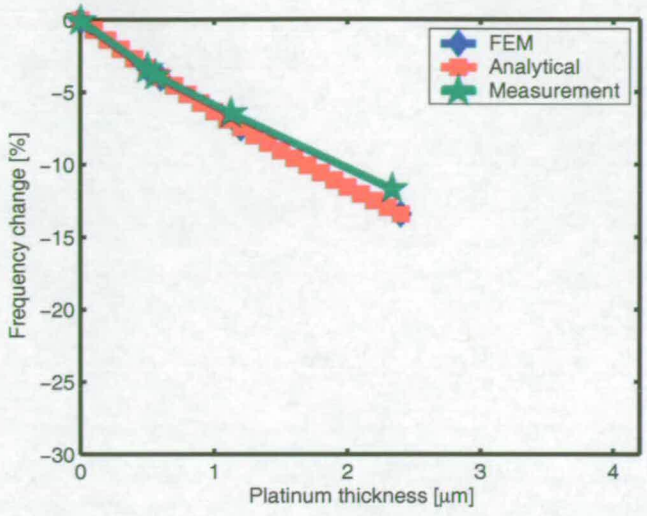

(a) SiC cantilevers

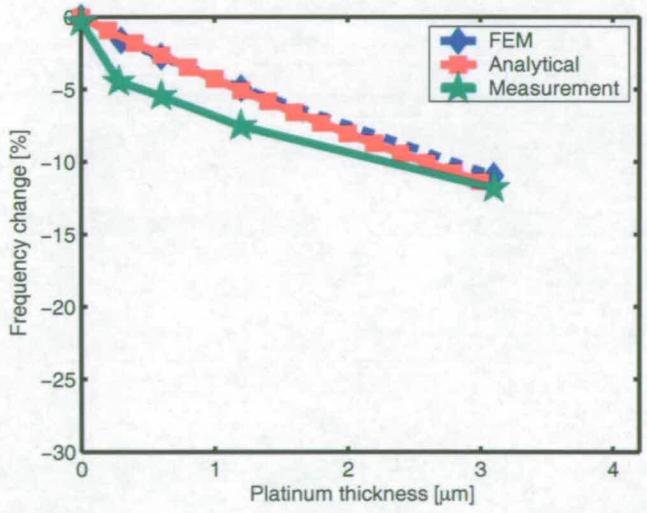

(b) SiC bridges

Figure 7.8. Measured, re-simulated and calculated resonant frequency change as a function of the deposited Pt thickness at the tip of SiC cantilevers and middle section of SiC bridges. Measured, re-simulated and analytically calculated resonant frequency change of $200\mu m \times 15\mu m \times 2.5\mu m$ SiC (a) cantilever and (b) bridges resonators as a function of deposited Pt thickness. To determine the change in resonant frequency, frequency measurements were performed before and after Pt deposition. One cantilever and bridge resonator was not deposited with Pt and acted as a "reference" to determine changes in measurement conditions. After the SiC thickness was measured, the value of the Pt mass density was decreased to match simulations and analytical calculations with measured frequency changes.

Measurement results for SiC cantilevers show the same linear decrease in resonant frequency with deposited Pt as observed for FEM simulations and analytical modelling (Fig. 7.8). The linear decrease in resonant frequency is caused by a rise in equivalent mass of the cantilever, which increases with the Pt thickness in a linear fashion. Measurements differed from FEM simulations and analytical calculations by 1.4% for a maximum deposited Pt thickness of 2.3μm. This discrepancy is explained by 1) the limited number of elements used for the FEM simulations and 2) assumptions made for the analytical model.

All carried out FEM simulations used a limited number of elements (30,000) to keep the computation times in a manageable time frame. This limitation obviously had an effect on the accuracy of the predicted resonant frequency. Additionally, the analytical model described the dynamic behaviour of the resonator as an ideal spring mass system with the deposited Pt being represented as an added point mass. The assumption of a point mass may have resulted in an overestimation in the added Pt mass and frequency change of SiC cantilevers.

FEM simulations and analytical calculations for SiC bridges showed in contrast to the measurement results a linear decrease in resonant frequency with deposited Pt thickness (Fig. 7.8(b)). Measurements differed from FEM simulations and calculations by up to 2.9% for the smallest and 1.1% for the largest Pt deposit. The reason for the observed discrepancy may be the cause of the variability in the measured bridge resonant frequency both before and after Pt deposition. The measured resonant frequency of bridges changed during the experiments due to stress relief in glue, which was used to attach the resonator samples to the copper carrier plate. This behaviour was observed in case of polysilicon bridges (Ch. 6).

7.4.4 Measurement issues

During the course of experiments it was noted that the resonant frequency of the reference cantilevers decreased between measurements taken before and after FIB Pt deposited tuning. The reason for the decrease in resonant frequency was the deposition of wax (Apiezon Wax W100), which was used to mount the copper carrier plate to the piezoelectric block to produce resonance. The wax was melted by placing a heated soldering iron on the copper plate. After the copper plate was attached to the piezoelectric block inside test chamber, the pressure was reduced until a working pressure

of 20μbar was reached. A consequence of the pressure reduction was a reduction in the boiling point of the soft wax. Wax vapourized inside the vacuum chamber and deposited itself once the pressure was increased after the end of each measurement session.

In order to calculate the amount of deposited wax m_{wax}, the measured change in resonant frequency Δf_0 was related to (Ch. 2):

$$m_{wax} = -\frac{2\Delta f_0 m_{eq}}{f_0} \tag{7.1}$$

In this way, the mass of the wax m_{wax} deposited was determined (Fig. 7.9).

Apart from a change in resonant frequency, one would also expect a change in the mechanical Q-factor of the resonator due to the increased damping produced in the deposited wax layer (Sec. 7.4.5).

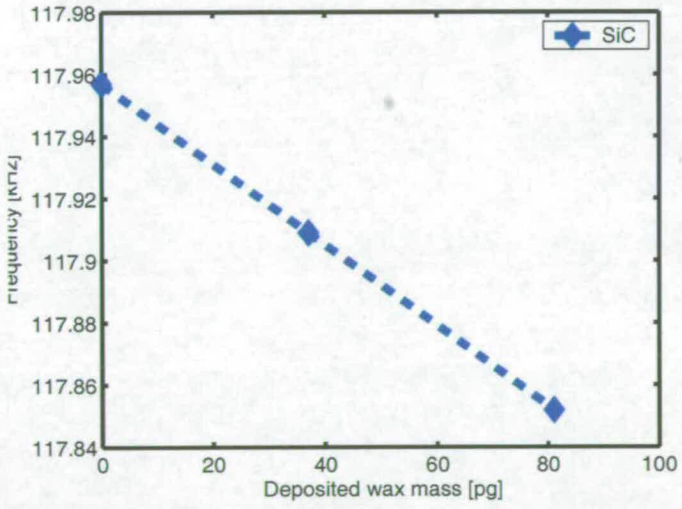

Figure 7.9. Measured resonant frequency as a function of deposited wax mass. The deposited wax mass m_{wax} was calculated from the measured change in resonant frequency of a 200μm×15μm×2.5μm SiC cantilever (Eq. (7.1)).

7.4.5 Q-factor of Pt deposited SiC resonators

Fig. 7.10 shows a measured frequency spectrum of a 200μm × 15μm × 2.5μm SiC cantilever resonator before and after 0.5μm thick Pt deposition. After Pt deposition, the Q-factor of the cantilever significantly decreased (74%) as a result of thermoelastic

damping in the deposited Pt [135]. That is, Pt was constantly compressed and expanded during the vibration movement of the resonator. The constant deformation of Pt was transformed into heat and dissipated into the environment, which degraded the Q-factor.

To research the impact of deposited Pt in detail, Q-factors before Q_{noPt} and after Q_{Pt} FIB deposition were extracted from measured frequency spectra and normalised using the relation Q_{Pt}/Q_{noPt}. Fig. 7.11 indicates that the normalised Q-factor of cantilever and bridges decreased sharply for the 0.5μm thick deposit and further increase of the Pt thickness caused only to a small reduction in the Q-factor. This behaviour was observed elsewhere for gold coated SiO_2 resonators [101] and it was proposed that the Q-factor was significantly influenced by thermoelastic damping occurring at the interface between the resonator and the deposit. In addition, it was found that deposited Pt layers on silicon reed resonators increased the internal friction and caused a reduction in the Q-factor [93]. It is therefore possible that the Q-factor after Pt deposition is influenced by thermoelastic damping at the interface between the SiC surface and the Pt and in the deposit itself. Hence, the Q-factor SiC resonators decreased rapidly with the deposition of thin films and levelled with thicker Pt films.

It was interesting to note that the Q-factor of the "reference" cantilever and bridge resonators without any deposited Pt decreased by up to 60% of their original value. In addition, the reference devices were not directly exposed to the Ga^+ ion beam at any time during the experiments. The reasons for the decrease are surface contamination and oxidation of the resonators, which have all been reported to cause a decrease in Q [139]. This confirms findings from the frequency measurements of reference cantilevers, where deposited wax caused a reduction in resonant frequency over time.

This suggests that the decline in the Q-factor of SiC was markedly influenced by surface contaminates (60%) such as vapourized wax and not by the deposited Pt. Both effects combined caused a maximum Q-factor decrease of up to 80% in cantilevers and 56% in bridges with 2.6μm and 3.1μm thick deposited Pt, respectively. The difference in Q-factor reduction between cantilevers and bridges is mainly due to the lower frequency resolution used during vibration measurements. This difference is clearly shown by the different sized error bars in Fig. 7.11.

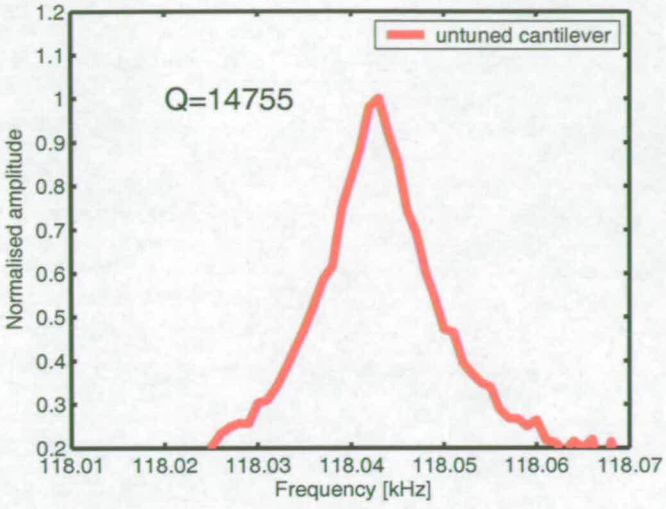

(a) Before Pt deposition

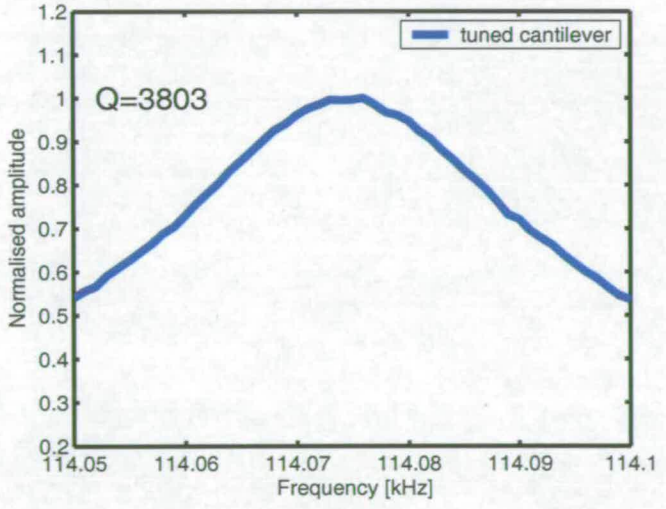

(b) After Pt deposition

Figure 7.10. Normalised amplitude of SiC cantilevers as a function of frequency before and after Pt deposition. Frequency spectrum of a SiC cantilever (a) before and (b) after the deposition of 0.5μm thick Pt. The Q-factor before and after Pt deposition was extracted from the displayed frequency spectra using the bandwidth method described in Chapter 2. The Q-factor of the SiC cantilever markedly decreased with the deposition of Pt. Thermoelastic damping in the deposited Pt caused irreversible energy dissipation during vibration, which decreased the Q-factor.

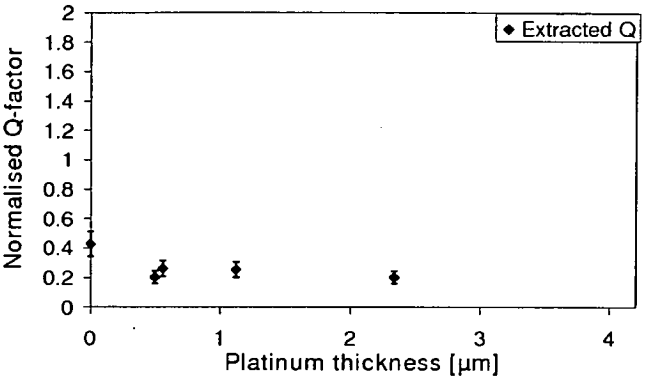

(a) SiC cantilevers

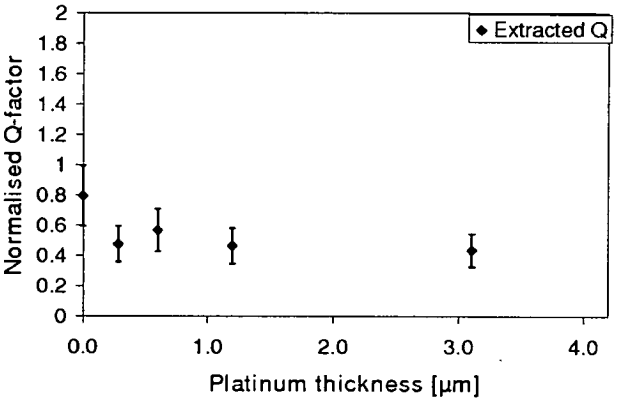

(b) SiC bridges

Figure 7.11. Normalised Q-factors of 200μm$\times$15μm$\times$2.5μm SiC cantilever and bridge resonators as a function of Pt thickness. Extracted Q-factors before Q_{noPt} and after Pt deposition Q_{Pt} were normalised (Q_{Pt}/Q_{noPt}) and plotted as a function of Pt thickness for SiC (a) cantilevers and (b) bridges. The strong decrease in normalised Q-factor of "reference" resonators indicated the presence of deposited wax. Deposited wax caused a strong decrease in Q compared to the deposited Pt.

7.5 Characterisation of FIB Pt deposited tuning on polysilicon resonators

Polysilicon cantilever and bridge resonators (200μm $\times$ 15μm $\times$ 2.3μm) were used to demonstrate the mass tuning effect and results compared to those for SiC resonators. Results from simulation and experiments are subsequently presented and discussed.

7.5.1 Modelling and Simulation

FEM simulations and an analytical model developed in Chapter 2 were employed to predict the frequency change of Pt deposited polysilicon cantilever and bridge resonators. Boundary condition and material properties listed in Sec. 7.4.1 were used to predict this frequency change. Both simulations and analytical modelling assumed a Pt mass density of 13,400kg m^{-3} and omitted structural and squeeze film damping. Simulations, in contrast to the analytical model, included biaxial polysilicon stress and an etch undercut of 28 μm at the attachment region of the resonators (Ch. 6).

In order to predict the tuning effect, a Pt layer with a 13 μm$\times$5 μm surface area and thicknesses ranging from 0.5 to 4.2 μm was placed on the tips of cantilevers and the middle sections of bridges. Fig. 7.12 shows the simulated and analytically calculated frequency change of polysilicon cantilever and bridges as a function of Pt thickness. The Pt thicknesses used for the modelling were those which were experimentally obtained from surface profiler measurements in Sec. 7.5.2.

FEM simulations and analytical modelling showed a similar trend in frequency change with the deposited Pt thickness as observed in SiC resonators. In the case of cantilevers, both the simulation and analytical model predicted a linear decrease in resonant frequency with progressing Pt thickness. Simulation and analytical modelling showed a maximum frequency change of -19.7% and -19.6% for a 2.6μm thick Pt deposit, respectively. Simulation and analytical model are in very good agreement.

In bridges, simulations and analytical calculations predicted a linear resonant frequency decrease with Pt thickness. A maximum frequency change of -17% and -15.3% was extracted from simulations and the analytical model for a Pt thickness of 4.2μm, respectively. The reason for the discrepancy between model and simulation was explained in Sec. 7.4.1.

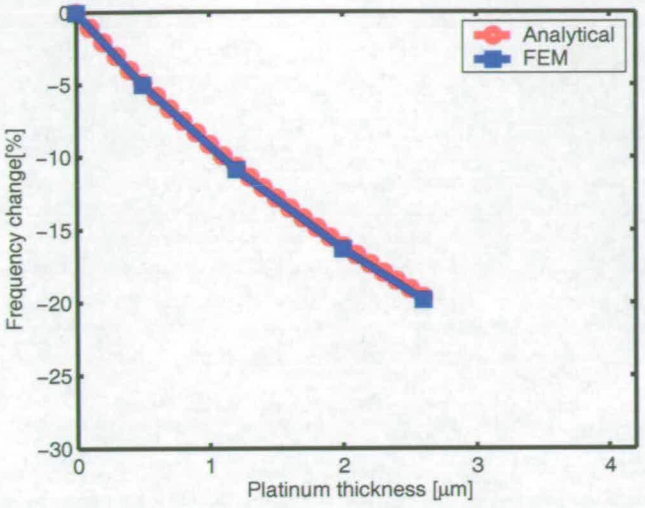

(a) Polysilicon cantilevers

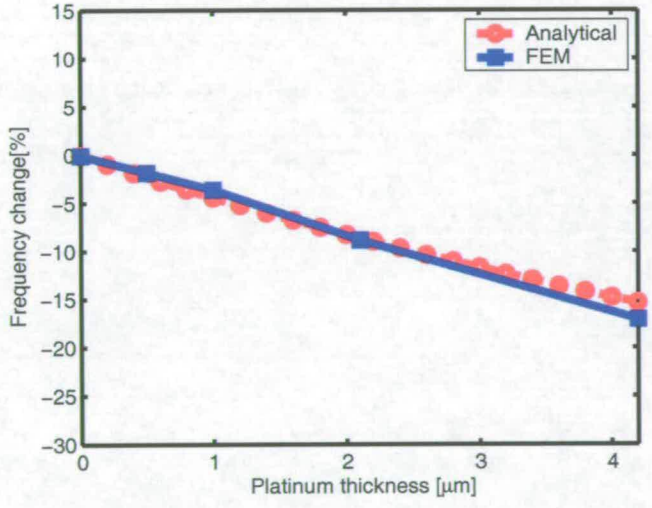

(b) Polysilicon bridges

Figure 7.12. Simulated and analytically modelled frequency change of polysilicon cantilever and bridge resonators as a function of deposited Pt thickness. Simulated and calculated frequency change for 200μm $\times$ 15μm $\times$ 2.3μm polysilicon (a) cantilevers and (b) bridges as a function of Pt thickness. Simulation and analytical model used the actual deposited Pt thicknesses from Sec. 7.5.2, a Pt mass density of 13,400$kg\ m^{-3}$ and omitted structural and squeeze film damping. In contrast to the analytical model, FEM simulations included an etch undercut of 28μm at the attachment region of polysilicon resonators.

7.5.2 FIB platinum deposition

A FEI FIB 200 workstation was used to deposit Pt in 13μm $\times$ 5μm sized patches at the tip of polysilicon cantilevers and the middle section of bridges with thicknesses ranging from 0.5 to 4.2μm. Fig. 7.13 shows Pt deposited on 200μm $\times$ 15μm $\times$ 2.3μm polysilicon cantilever and bridge resonators. After deposition, the Pt height was measured using a white light surface profilometer (Ch. 6) and a Pt deposition rate of 0.105μm/min. was determined. As observed on SiC resonators, Pt deposits on polysilicon devices were 57% thicker than intended to be due to the higher Ga $^+$ ion beam current. Pt was selectively deposited using a Ga^+ ion beam current density of around 2pA μm^{-2} and an acceleration voltage of 30kV.

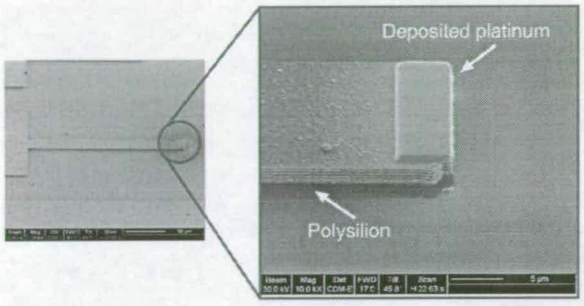

(a) Polysilicon cantilever

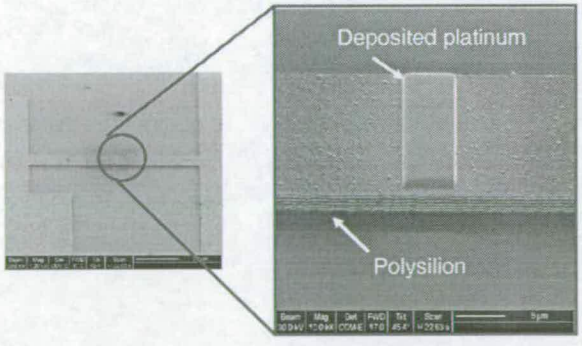

(b) Polysilicon bridge

Figure 7.13. Selective Pt deposition on polysilicon resonators. Selective deposition of 1μm thick Pt on a 13μm $\times$ 5μm section on polysilicon (a) cantilever and (b) bridge resonators. Pt was deposited with a Ga^+ beam current density of 2pA μm^{-2} and an acceleration voltage of 30kV.

7.5.3 FIB deposited frequency tuning

The measured resonant frequency change as a function of Pt thickness for polysilicon cantilever and bridge resonators is shown in Fig. 7.14. As predicted by previous simulation and modelling (Fig. 7.12), the measured resonant frequency of cantilevers decreased in a linear fashion with the deposited Pt thickness (Fig. 7.14). The observed linear decrease in frequency with Pt thickness was a result of an increase in equivalent mass, which rose constantly with the deposited Pt thickness.

Measurements determined a maximum change in resonant frequency of -15.6% for 2.6μm thick Pt, which differed by more than 4% from the results obtained from previous simulations and analytical modelling (Fig. 7.12). The reason for this discrepancy between measurements and simulations was a smaller Pt mass density than assumed for the FEM analysis and analytical calculations. The Pt mass density was changed from ρ=13,400$kg\ m^{-3}$ to 9,900 $kg\ m^{-3}$ to match FEM simulations and analytical results with the measurements. The variability in Pt mass density over time may be explained by the variability in the Ga^+ ion beam current, which caused thicker Pt deposits than expected (see Sec. 7.5.2). A variable Ga^+ beam current density caused a variability in deposited Pt thickness and composition.

Fig. 7.14 includes re-simulated and analytical calculated frequency changes obtained using the modified Pt mass density. Using the modified Pt mass density, FEM simulations and analytical calculations predicted a maximum frequency change of -15.6% and -15.5% for a Pt thickness of 2.6μm, which were in very good agreement with the measurement results.

Despite the difference in deposited Pt mass, polysilicon cantilevers showed a slightly larger frequency change than their SiC counterparts. The reason for the different frequency change was the lower equivalent mass of polysilicon devices compared to SiC resonators. Resonators with a lower equivalent mass show a higher change in frequency as indicated by Eq. (2.17) in Chapter 2.

7.5.4 Measurement issues

As observed in the case of SiC, the resonant frequency of the polysilicon "reference" cantilever changed between measurements taken before and after FIB Pt deposition as a result of deposited wax (Fig. 7.15).

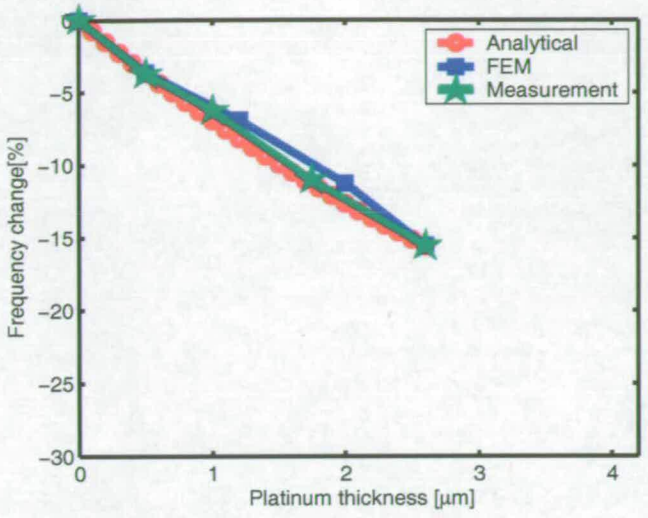

(a) Polysilicon cantilevers

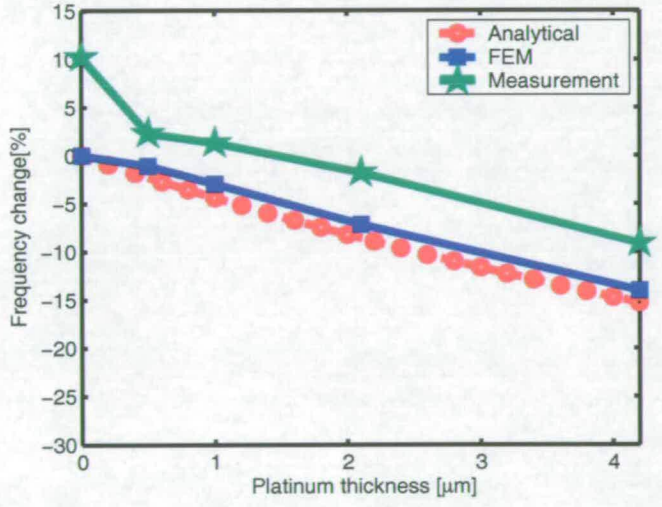

(b) Polysilicon bridges

Figure 7.14. Measured, re-simulated and calculated resonant frequency change as a function of Pt thickness for polysilicon cantilevers and bridges. Measured resonant frequency change of 200μm $\times$ 15μm $\times$ 2.3μm polysilicon (a) cantilevers and (b) bridges as a function of deposited Pt thickness. To determine the change in resonant frequency, frequency measurements were performed before and after Pt deposition. One cantilever and bridge resonator was not deposited with Pt and acted as a "reference" to determine changes in measurement conditions. The Pt mass density was altered from ρ=13,400$kg\ m^{-3}$ to 9,900$kg\ m^{-3}$ to match simulations and calculations with measurement results.

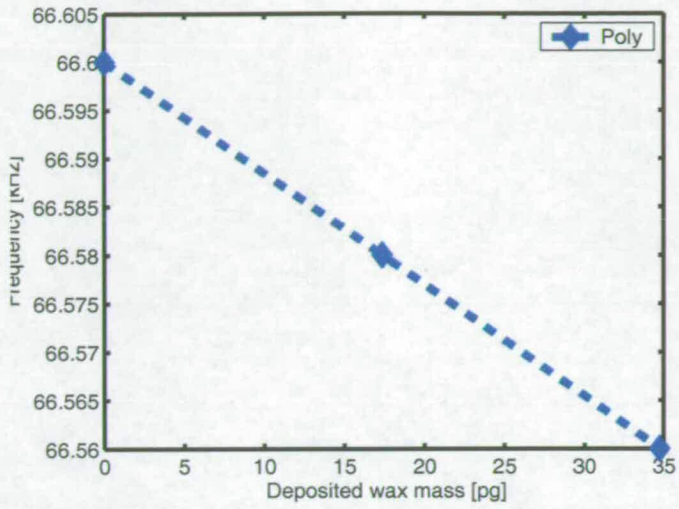

Figure 7.15. Measured resonant frequency as a function of deposited wax mass. Measured resonant frequency of a 200μm×15μm×2.3μm polysilicon cantilever as a function of deposited wax mass. The deposited wax mass was calculated from the measured frequency change of the polysilicon cantilever using Eq. (7.1).

Frequency measurements before and after Pt deposition showed a strong variation in bridge resonant frequencies. The reason for the observed variations was believed to be due to stress relief in the epoxy glue, which altered the polysilicon bridge resonant frequency and markedly influenced the results on Pt deposited tuning (Ch. 6). For example, the resonant frequency of the "reference" polysilicon bridge resonator changed by +10.1% between measurements taken before and after Pt deposited tuning of the remaining devices (Fig. 7.14). This variation was most likely due to the stress relief in the glue, which was used to mount the resonator samples on copper carrier plates. The variation in measured frequency caused the non-linear behaviour in Pt deposited polysilicon bridges and the deviation from linear relationship predicated by FEM simulations and analytical calculations (Fig. 7.14). The same trend in frequency change was observed in case of SiC bridge resonator tuning (Fig. 7.8), which was explained by a variation in detected bridge resonant frequency. However, further work is required to confirm these findings.

7.5.5 Q-factor of Pt deposited resonators

Fig. 7.16 shows the measured frequency spectrum of a 200μm $\times$ 15μm $\times$ 2.3μm polysilicon cantilever before and after 0.5μm thick Pt deposition. In comparison to SiC resonators, devices made from polysilicon have a significant lower Q-factor, both before and after Pt deposition. The reason for the difference in the Q-factor lies in the structure of these two materials. Polysilicon has a polycrystalline structure, while SiC is a perfect single crystal. Thermoelastic damping in perfect single crystal is smaller than in polycrystalline films [117]. Hence, Q-factors in single crystal SiC were higher than in polysilicon resonators.

The Q-factor of the polysilicon cantilever beam significantly decreased (52%) as a result of thermoelastic damping in the deposited wax and 0.5μm thick deposited Pt (Fig. 7.16). In contrast, a SiC cantilever with the same deposited Pt showed a 74% decrease in the Q-factor (Fig. 7.10). The reason for the observed discrepancy was the resolution of the detected frequency. Frequency measurements on polysilicon resonators were performed with a 20Hz resolution, while SiC cantilevers were measured with 1Hz resolution. The high resolution measurements on SiC cantilever were obtained with great difficulty due to the large amount of data involved and stretched the available computer technology to its limits. Hence, a lower frequency resolution was used for the frequency recordings for polysilicon resonators.

To investigate the influence of the deposited wax and Pt in detail, normalised Q-factors of polysilicon cantilevers and bridges Q_{noPt}/Q_{Pt} were plotted as a function of Pt thickness in Fig. 7.17.

The Q-factor of the polysilicon "reference" cantilever and bridge resonators decreased by 50% over time, although these had not been deposited with Pt or were directly exposed to FIB Ga^+ ions at any time. This decrease is comparable with the one found in case of SiC counterparts, confirming the influence of deposited wax on the Q-factor.

The Q-factor of the remaining polysilicon cantilever and bridge resonators decreased further with deposited Pt thickness similar as found for their SiC counterparts. Thicker Pt deposits produced more thermoelastic damping and decreased the Q-factor further [135]. The maximum decrease in Q was 58% for cantilevers with a Pt thickness of 2.6μm. Compared to the characteristics discussed so far, the Q-factor of the polysilicon reference bridge resonator seems to have increased (Fig. 7.17(b)). This discrepancy is

due to the variability in the measured resonant frequency (Sec. 7.5.3), which obviously has an influence on the extracted Q-factor (Sec. 2.3.3). However, despite the strong deviation seen for polysilicon bridges, the Q-factor declines under the influence of increasing thermoelastic damping due to thicker deposited Pt.

The data of extracted Q-factors from polysilicon and SiC resonators suggested that most of the damping was caused by the deposited wax contamination and not by the Pt. From Fig. 7.11 Fig. 7.17, it can be shown that the deposited Pt only decreased the Q-factor by 8% and 12% in polysilicon and SiC cantilevers, respectively.

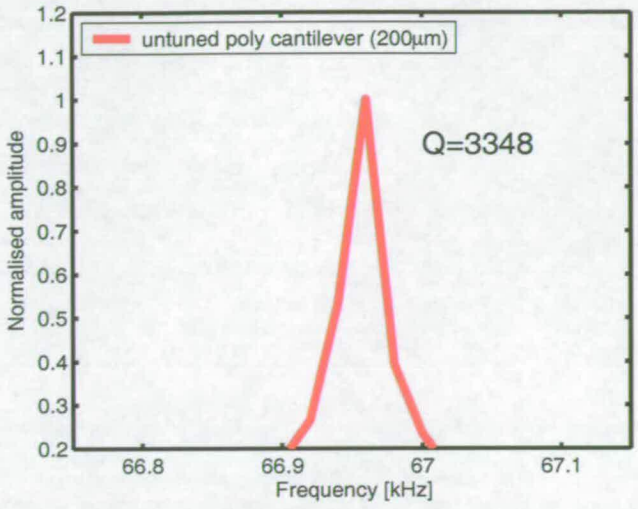

(a) Before Pt deposition

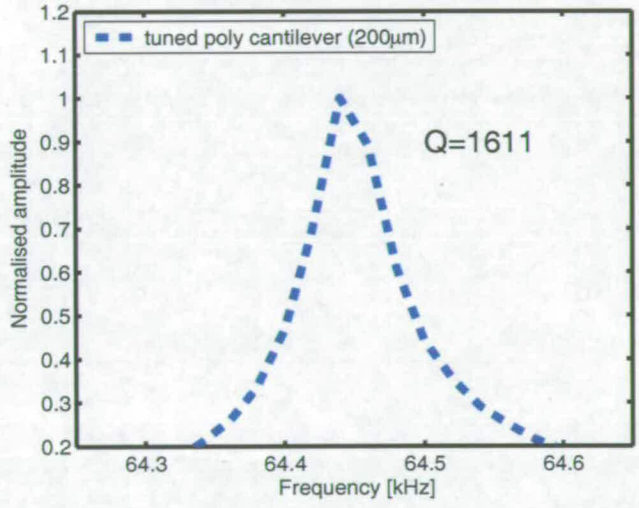

(b) After Pt deposition

Figure 7.16. Normalised amplitude of a polysilicon cantilever as a function of frequency before and after Pt deposition. Frequency spectrum of a 200μm×15μm×2.3μm polysilicon cantilever (a) before and (b) after 0.5μm thick Pt deposition. The Q-factor before and after Pt deposition was extracted from the displayed frequency spectra using the bandwidth method described in Chapter 2. The Q-factor of the polysilicon cantilever markedly decreased with the deposition of Pt. Thermoelastic damping in the deposited Pt caused irreversible energy dissipation during vibration, which decreased the Q-factor.

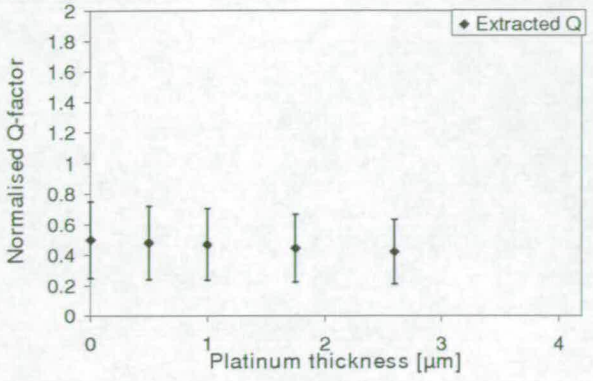

(a) Polysilicon cantilevers

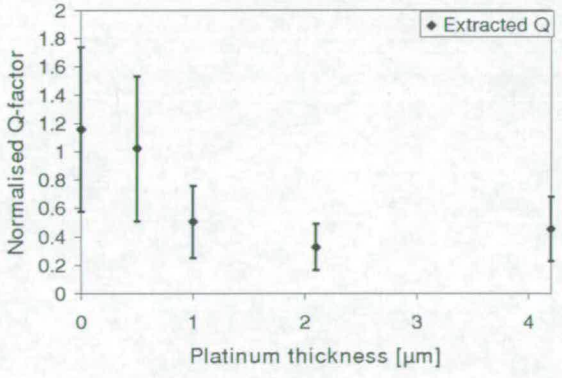

(b) Polysilicon bridges

Figure 7.17. Normalised Q-factor of 200μm $\times$ 15μm $\times$ 2.3μm polysilicon cantilever and bridge resonators as a function of Pt thickness. The normalised Q-factors of cantilever and bridges were extracted from measured frequency spectra before (Q_{noPt}) and after (Q_{Pt}) Pt deposition. The extracted Q-factors were normalised and plotted as a function of Pt thickness for polysilicon (a) cantilevers and (b) bridges. The decrease in normalised Q-factor of "reference" resonators indicated the presence of deposited wax. Deposited wax caused a strong decrease in Q compared to the deposited Pt. A lower frequency resolution and errors related to stress relief in the glue caused a strong variability in case of bridges. Despite the shown variability in bridge data a trend of decreasing Q values with deposited Pt thickness is still existent.

7.6 Conclusions

In this chapter, a novel FIB Pt deposition scheme has been demonstrated and characterised for the purpose of frequency tuning of micromechanical resonators. Resonant frequency tuning was achieved by selective FIB Pt deposition on flexural vibrated cantilever and bridge resonators. The resonant frequency of these devices was decreased by placing Pt at the tips of cantilevers and the middle sections of bridge resonators.

FEM simulations and analytical modelling were first performed to predict frequency changes in cantilever and bridge resonators. To verify the simulation results and to demonstrate the FIB Pt deposited frequency tuning, the equivalent mass of cantilevers and bridges was changed. A change in equivalent mass was achieved by the deposition of Pt on the tips of cantilevers and middle section of bridges. This so called "mass tuning" effect decreased the resonant frequency of SiC and polysilicon cantilevers and bridges less than predicated by simulations and calculations. The discrepancy between theory and measurements was due to the variability in the deposited Pt mass density. A variation in Pt mass density would cause a variability in deposited frequency tuning. In practise, this is not an issue, since frequency tuning can be performed in real time.

Despite the observed variability in the deposited Pt mass density, polysilicon resonators showed a stronger decrease in resonant frequency than their SiC counterparts. The slight difference was attributed to the lower equivalent mass of polysilicon resonators compared to their SiC counterparts.

The Q-factor of SiC and polysilicon resonators decreased over time in a linear fashion due to damping in deposited surface contaminants and Pt. The source of surface contamination was the deposited wax on the resonators, which decreased the resonant frequency of SiC and polysilicon cantilever reference structures. The wax markedly decreased the Q-factor of resonators compared to the FIB deposited Pt. Thin Pt deposits showed a stronger impact on the Q-factor than thicker ones, indicating that most thermoelastic damping occurs at the interface between resonator surface and deposit [101]. It should be noted at this point, that the extracted Q-factor of polysilicon bridges was directly related to the detected variability in recorded frequency. However, despite the strong deviation seen for polysilicon bridges, the Q-factor declines under the influence of increasing thermoelastic damping due to thicker deposited Pt.

Compared to other tuning methods [16, 1], FIB Pt deposition produced a decrease in resonant frequency of micromechanical resonators without causing device failure. This

considerably increases device yield and reduces cost, which removes one of the stepping stones preventing micromechanical resonators from being employed in low cost wireless transceivers. In addition, once Pt is deposited, no additional energy or a high tuning voltage [6] is required to maintain the modified resonant frequency. Tuning methods that require little or no energy to hold the modified resonant frequency are important to low power wireless transceivers, because of their limited battery power.

A strong decrease in SiC resonators Q-factors of up to 74% is not acceptable for RF filters in future wireless transceivers architectures (Ch. 2). However, the observed Q-factor decrease was mainly due to surface contamination in the form of deposited wax. Surface contamination can be easily reduced by vacuum encapsulation or covering resonators with a glass cap. This would considerably reduce the amount of surface contamination and maintain a higher Q-factor.

In conclusion, FIB Pt deposition provides frequency tuning for micromechanical resonators without using high voltages or causing any device failure.

Chapter 8

Characterisation of frequency tuning by silver deposition

This chapter describes an electrochemical Ag deposition scheme for adjusting the resonant frequency of polysilicon bridge resonators. Different test structures are used to analyse the Ag deposition scheme and results are discussed.

8.1 Introduction

In the previous chapter, FIB platinum deposition was presented as a method for tuning micromechanical resonators without any device failure [29]. Although this method offers advantages over currently available tuning, the cost effectiveness as a high volume manufacturing technique has yet to be confirmed.

In contrast, a solid state electrochemical silver (Ag) deposition scheme has the ability to electrically control Ag deposition on many micromechanical resonators [26]. This makes it a cost effective in-situ tuning method in a high volume manufacturing environment, enabling real time bidirectional frequency changes of micromechanical resonators. The key element for Ag deposited tuning is a solid electrolyte. Evaporated as a blanket layer, the solid electrolyte provides a medium for the transport and deposition of Ag. In order to evaluate the suitability of this tuning method to micromechanical resonators, the solid electrolyte and Ag deposition need characterisation.

This chapter reports the results of using different test structures to extract material properties of the solid electrolyte and to characterise Ag deposited tuning. In this work, the extracted material parameters were used to construct an analytical model to describe the deposited tuning of polysilicon resonators. Experimental and simulation results are discussed and conclusions drawn.

8.2 Material system and Ag deposited frequency tuning

This section briefly explains the production of the solid electrolyte material system and gives a detailed description of the Ag deposited tuning concept.

8.2.1 Production of solid electrolytes

The electrolyte capable of ion transport and subsequent electrodeposition was formed in a two step process at room temperature via evaporation of 80nm $Ge_{0.3}Se_{0.7}$ base glass followed by a thin 15nm Ag layer. This thickness combination allowed complete dissolution of the Ag layer into the base glass layer and avoided metal remaining on the surface of the base glass. The thin and optically transparent Ag layer was diffused into the base glass layer by photodissolution as shown in Fig. 8.1. Photodissolution of Ag was performed using a 405nm ultraviolet light (UV) source with a power density of $3.9mW/cm^2$ for a time of 20 minutes. Photodissolution enabled Ag ions to be

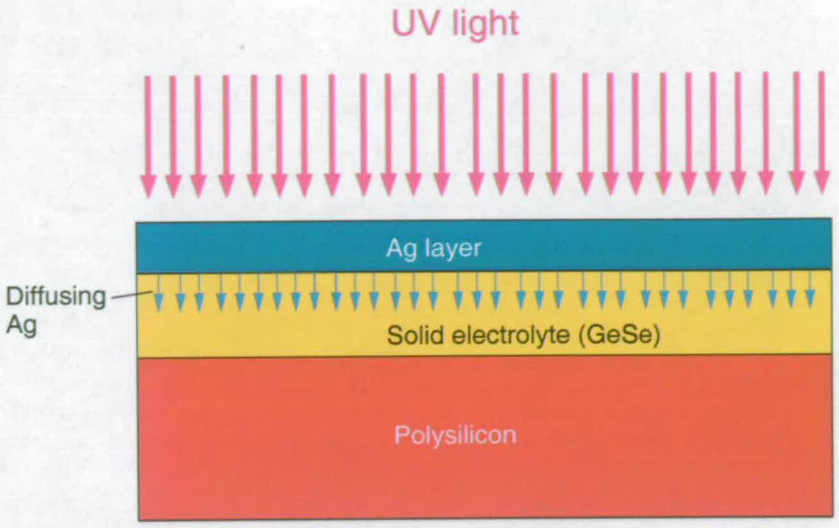

Figure 8.1. Schematic representation of the photodissolution process of Ag and GeSe. The thin evaporated Ag layer diffused into the glass base layer to form the solid electrolyte. The energy for the diffusion was provided by the UV light source during photodissolution. The photodissolution process provided the base glass layer with Ag ions, necessary to perform electrodeposited frequency tuning.

weakly held in negatively charged chalcogen sites and created a solid electrolyte with a substantial mole fraction of the superionic phase Ag_2Se and a Ge-rich dielectric like backbone. Ag was used in this work for the photodissolution and deposited frequency tuning. Copper (Cu) is also suitable for electrodeposited tuning, however, Ag was the only material available.

8.2.2 Ag deposited frequency tuning concept

Once integrated with micromechanical bridge resonators, the Ag loaded solid electrolyte was employed to tune their resonant frequency by a combination of Ag migration and electrodeposition [26]. Ag ion movement in this blanket deposited ternary $Ag_{0.1}\,(Ge_{0.3}Se_{0.7})_{0.9}$ system was induced by a DC electric field between an oxidizable Ag anode and an inert cathode as shown in Fig. 8.2. This particular electrolyte composition was chosen over other combinations, because it was shown to produce the most uniform electrodeposited Ag films [78]. The applied electric field caused Ag ion migration in the electrolyte towards the Al cathode, where they were reduced into a metallic state to form an Ag electrodeposit. The movement caused a decrease of Ag ions in the solid-electrolyte and left negative charged chalcogenide centres behind. The vacated

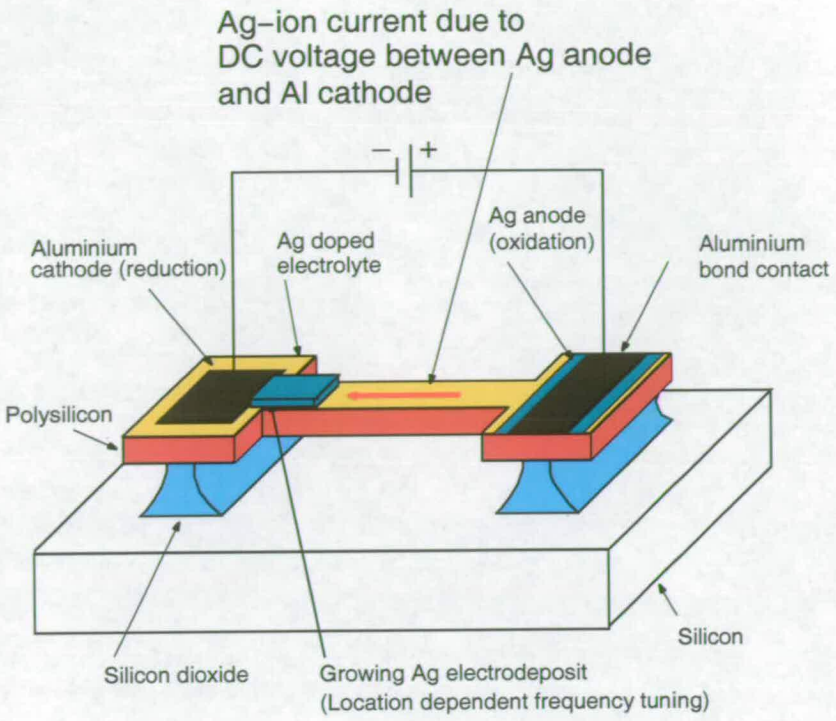

Figure 8.2. Schematic of a polysilicon bridge resonator with integrated solid electrolyte, Ag anode and aluminium (Al) contacts. Application of a DC voltage between an Ag anode and an Al cathode resulted in an Ag ion current. Ag ions were provided by an anode via oxidation and deposited at the cathode through reduction. The location of Ag on the resonator affected the direction of frequency change. Initially, Ag deposited at the cathode increased the equivalent stiffness and therefore the resonant frequency of the bridge resonator. The resonant frequency decreased with further Ag coverage due to the rise in equivalent mass of the bridge resonator.

negative sites were filled with fresh Ag ions coming from neighbouring sites and from an oxidizable Ag anode, which provided the ions for the deposition. This resulted in an Ag ion current flow in the electrolyte from the anode to the cathode. Therefore, there was a net redistribution of Ag ions from the anode into the solid-electrolyte. Once the Ag electrodeposit was formed, it became the source of electrons and further reduction of Ag ions occurred. This allowed the Ag deposit to extend along the surface of the bridge resonator towards the anode [61].

The Ag movement changed the resonant frequency depending on the location of the electrodeposit along the length of the bridge resonator. Ag deposits near the anchor caused an increase in equivalent stiffness and in resonant frequency. The resonant

frequency decreased with further Ag deposition towards the centre of the bridge due to a rise in equivalent mass.

8.3 Materials and Methods

The solid electrolyte ($Ag_{0.1}$ $(Ge_{0.3}Se_{0.7})_{0.9}$) performed an important role in Ag deposited tuning and both its electrical and mechanical material parameters had to be known to investigate and model the change in resonant frequency of micromechanical bridge resonators.

During electrodeposition the total current passing through these electrolyte systems consists of an Ag ion carrying Faraday i_F and a so called electron "leakage" i_{leak} component. In order to characterise and analytically model Ag electrodeposited frequency tuning, the electrical resistivity in both situations has to be known. Faraday's law applies in this system and the i_F passed through the solid electrolyte is proportional to the deposited Ag mass m_{Ag} ($i_F \propto m_{Ag}$). Since i_F can not be measured directly, the volume of deposited Ag is a measure of i_F and consequently of a so called Faraday "resistivity". To extract the Faraday current and resistivity, polysilicon bridge test resonators (Sec. 8.4.3) were deposited with Ag. The volume and mass of the deposited Ag was determined from SEM imaging. Once the deposited Ag mass m_{Ag} was known, the Faraday current and resistivity was determined. The second current passing through the dielectric part of the solid electrolyte is an electron carrying "leakage" component. In this situation, the corresponding "leakage" resistivity gives an indication of layer composition, the amount of Ag ions in the solid electrolyte electrolyte and the rate of electrodeposition. For example, a high "leakage" resistivity indicates a low number of Ag ions and a small electrodeposition rate, while a low "leakage" resistivity represents a high number of Ag ions and results in a large electrodeposition rate. A first test chip design containing Greek cross test structures was used to extract the "leakage" resistivity of the solid electrolyte from sheet resistance measurements.

After the electrical characterisation had been performed, a second test chip design (Sec. 5.2.2), containing polysilicon cantilever beam resonators, was used to extract mechanical properties of the solid electrolyte. These properties included mass density $\rho_{electro}$ and Young's modulus $E_{electro}$. Both parameters had to be known to model the Ag deposited tuning of polysilicon bridge resonators.

After the material properties of the solid electrolyte were extracted, a test chip design containing polysilicon bridge resonators with an integrated Ag deposition scheme (Sec. 5.2.1) was used to characterise frequency tuning.

The first two test chips were used to extract electrical and mechanical material properties of the solid electrolyte. Their design, fabrication and operation are described below.

8.3.1 Test chip for electrical characterisation

The first test chip contained microelectronic Greek cross test structures to extract the electric "leakage" resistivity ζ_{leak} of the solid electrolyte $Ag_{0.1}\ (Ge_{0.3}Se_{0.7})_{0.9}$ [25]. In order to extract the "leakage" resistivity, the sheet resistance R_s of the solid electrolyte was measured using the Greek crosses. The theory and the procedure to measure the sheet resistance on a Greek cross is described in Appendix A. One important requirement for the sheet resistance measurements was that the solid electrolyte layer was uniform in layer thickness and homogeneous in composition.

Knowing the sheet resistance R_s and thickness $t_{electro}$ of the *homogeneous* solid electrolyte, one can derive the resistivity $\zeta_{electro}$ using the relationship:

$$\zeta_{electro} = R_s\, t_{electro} \quad [\Omega m]. \tag{8.1}$$

The following describes the Greek cross test chip design, which consisted of two masks. The test chip is shown in Fig. 8.3. The first mask of the test chip contained Greek cross test structures with arm lengths of 120μm and arm widths ranging from 1-20μm. The second mask layer provided 100μm$\times$100μm metal pads for probing Greek crosses during the sheet resistance measurements of the solid electrolyte.

Standard fabrication of Greek crosses usually involves the blanket deposition of silicon dioxide (SiO_2) and the conducting film to be evaluated. The conductive film is patterned to form the Greek crosses and the sheet resistance is measured as outlined in Appendix A. This fabrication technique could not be applied to the solid-electrolyte used in this thesis, because it contained Ag and was therefore not compatible with CMOS fabrication. To overcome this problem, suspended Greek cross test structures (see Fig. 8.4) were developed and used to determine the sheet resistance of blanket deposited solid electrolyte $Ag_{0.1}\ (Ge_{0.3}Se_{0.7})_{0.9}$. The suspended Greek crosses were made

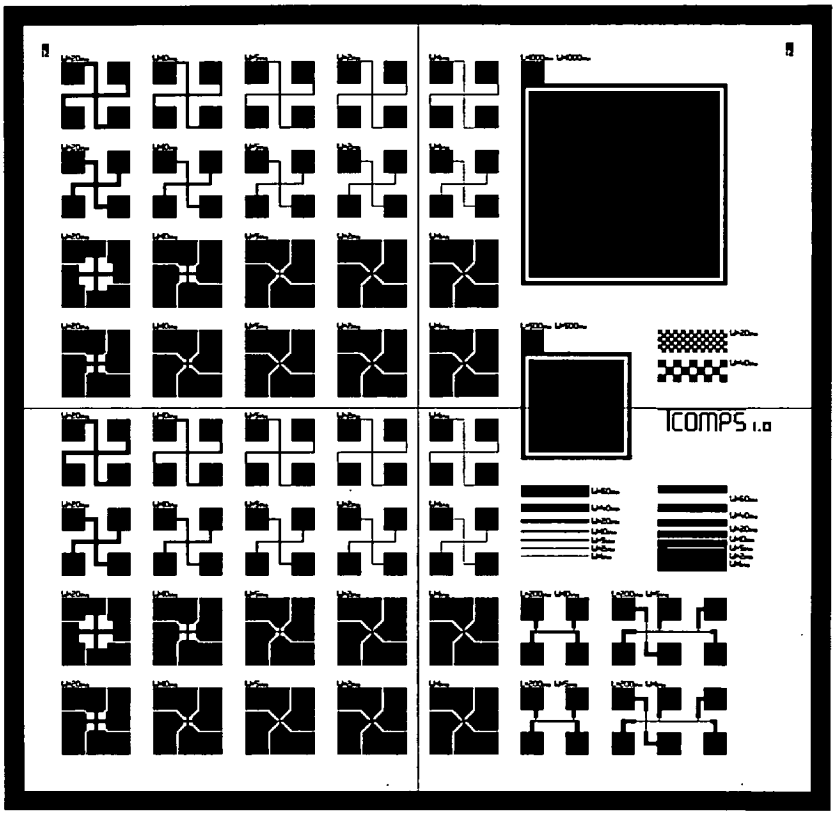

Figure 8.3. Layout of the first test chip containing Greek cross test structures for the characterisation of the solid-electrolyte. The test chip contained two masks. The first mask defined Greek crosses with an arm length of 120μm and and width ranging from 1-20μm. The second mask defined 100μm$\times$100μm metal pads to allow electrical probing during the sheet resistance measurement.

from polysilicon with a silicon nitride cap, which automatically patterned the device and at the same time served as the carrier for the solid electrolyte to be characterised. This novel test structure was further developed by other researchers to characterise Joule heating, which is associated with the sheet resistance measurement of low resistivity conducting metal films [41]. However, in case of the solid electrolyte, Joule heating [28, 27] was not an issue, because of its high resistivity.

The following describes the fabrication of the Greek cross test chip. The fabrication process for the Greek crosses started with the growth of 0.1μm wet thermal silicon dioxide (SiO_2) at 950°C and subsequent deposition of a 2.3μm thick sacrificial Plasma Enhanced Chemical Vapour Deposition (PECVD) SiO_2 layer on $\langle 100 \rangle$ n-type silicon wafers (Fig. 8.5). Both SiO_2 layers acted as sacrificial layers for the suspended Greek crosses. The thermal SiO_2 avoided any adhesion problems of the PECVD layer to the

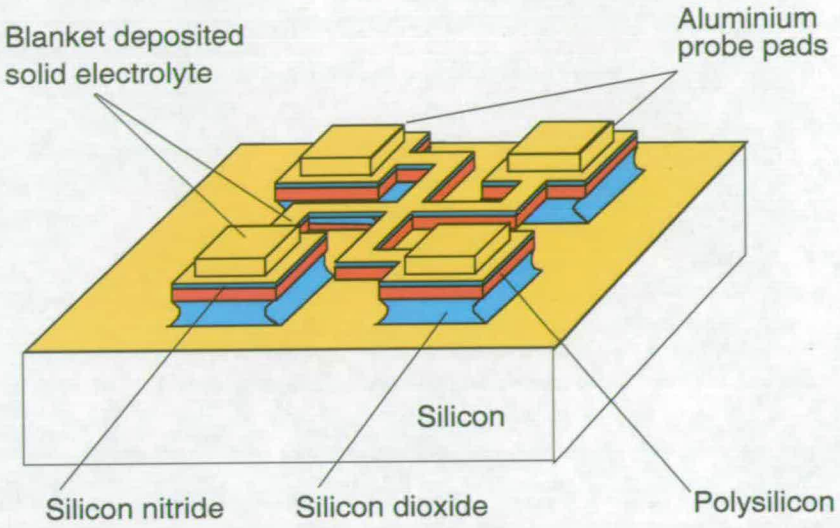

Figure 8.4. Suspended Greek cross test structure. The suspended Greek cross consisted of polysilicon and a silicon nitride gap, which automatically patterned the device and at the same time served as the carrier for the solid electrolyte to be characterised. Thick aluminium (Al) metal pads allowed easy multiple probing of thin deposited solid electrode.

Si substrate. This was followed by the deposition of 1μm thick LPCVD polysilicon at 600°C, which served as mechanical support for the film being evaluated. To prevent the polysilicon making electrical contact with the material to be assessed, a 0.1μm LPCVD Si_3N_4 layer was deposited at nominal 800°C. These two layers were then patterned using a combination of Reactive Ion Etching (RIE) and Deep Reactive Ion Etching (DRIE) to form the arms of the test structures and the probe areas. A 1.5μm thick aluminium (Al) layer was deposited with 2kW power using a Balzers sputter system and patterned employing wet chemical etch using phosphoric acid at 45°C to form contact pads for probing on the Si_3N_4-polysilicon probe areas. The test structures were released from the Si-substrate by removing SiO_2 under the arms of the crosses and around the probe areas using a $NH_4F : CH_3COOH$ solution and subsequent critical point drying in liquid carbon dioxide (CO_2). Note that the undercut created by the wet etch of the SiO_2 ensured that the electrolyte on top of the test structures was isolated from the solid electrolyte on the substrate surface. Fig. 8.6 shows a Greek cross test structure with Al pads after the release etch step.

As a precaution the sidewalls of the arms of the test structures were covered with a 5nm thick polymer to reduce the risk of surface currents using the polysilicon as a parasitic path. The polymer (C_4F_8) deposition was carried using the passivation cycle

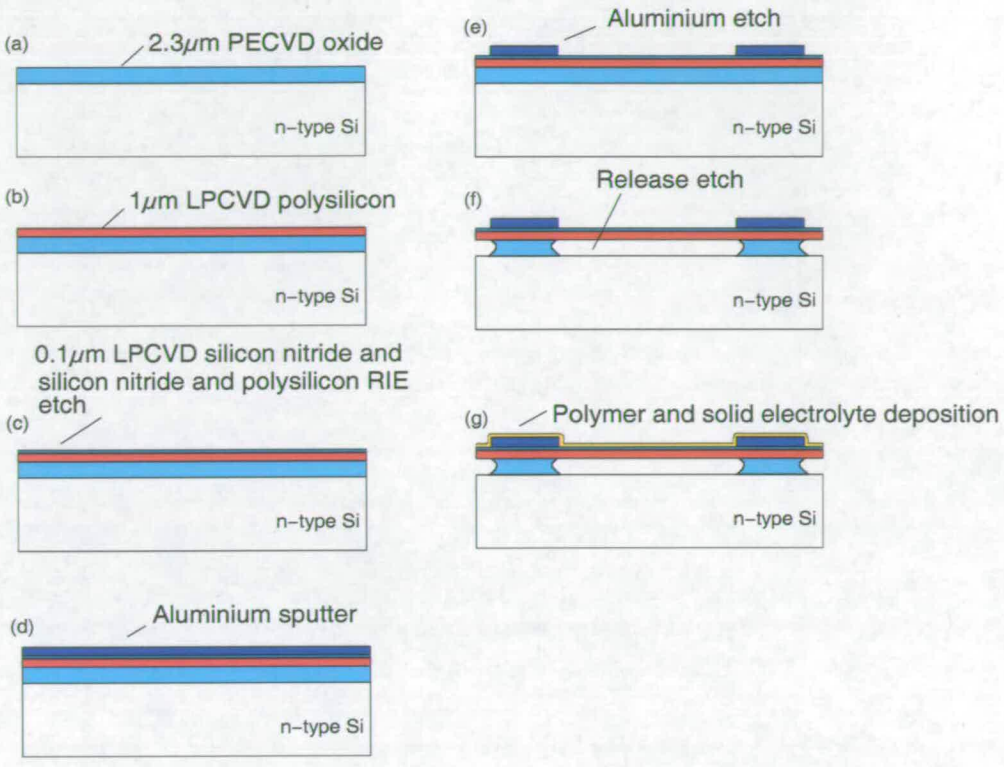

Figure 8.5. Fabrication process for the first test chip. The manufacturing process involved the deposition and etching of sacrificial SiO_2, polysilicon and Si_3N_4 and Al to form the suspended Greek crosses with thick Al probe pads.

of a Bosch process in a STS DRIE etcher at 300W for 12s. The polymer on top of the test structures was removed by 15 minutes of argon milling in a Balzers sputter system.

At this stage, the platform was ready to characterise the $Ag_{0.1}\,(Ge_{0.3}Se_{0.7})_{0.9}$ film. Before Greek crosses were used to measure the sheet resistance of $Ag_{0.1}\,(Ge_{0.3}Se_{0.7})_{0.9}$, gold and copper layers were utilised to demonstrate the performance of the Greek crosses. After successful demonstration of the proposed test structures [25], the solid electrolyte was deposited onto the Greek crosses. The deposition process involved the evaporation of 80nm thick chalcogenide glass ($Ge_{0.3}Se_{0.7}$) and a 15nm thick Ag film onto the Greek crosses. To form the solid electrolyte, Ag was driven into the chalcogenide glass layer via photodissolution using a 405nm Ultra Violet (UV) light source and a power density of $3.9mW/cm^2$ for 20 minutes on a Karl Suss mask aligner. The dissolution process provided the required solid electrolyte with Ag ions [77]. After the samples were covered with the $Ag_{0.1}\,(Ge_{0.3}Se_{0.7})_{0.9}$, sheet resistance measurements were performed [24].

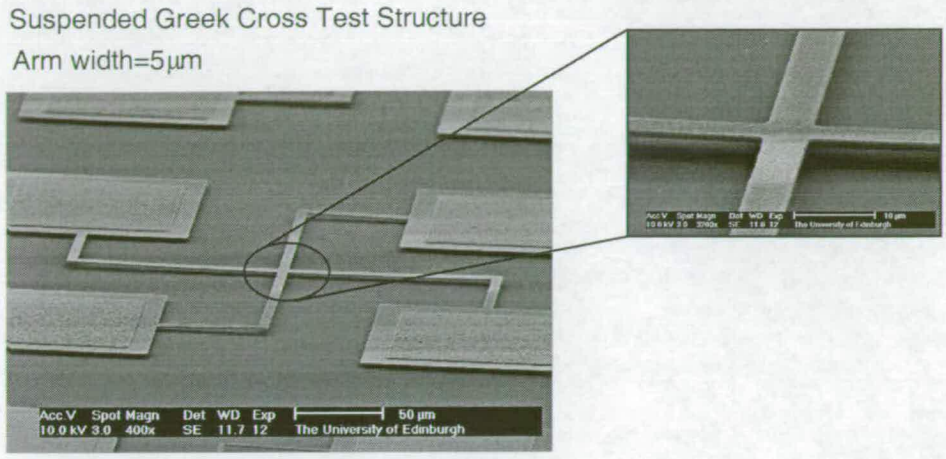

Figure 8.6. SEM image of a Greek cross test structure with 5μm arm width including Al probe pads. The inset shows the suspended heart of the Greek cross, the location where the sheet resistance of blanket deposited films was extracted.

8.3.2 Test chip for mechanical characterisation

Three dies of polysilicon cantilevers, fabricated from a second test chip (Sec. 5.2.2), were used to extract the mass density $\rho_{electro}$ and Young's modulus $E_{electro}$ of the solid electrolyte. Polysilicon bridge resonators were not included in the analysis due to the large error associated with the resonant frequency measurements reported in Chapter 6. To extract $\rho_{electro}$ and $E_{electro}$, two cantilever dies were covered with a relatively thin (20nm) and thick (80nm) solid electrolyte and the resonant frequency was measured both before and after deposition. A third die was not covered with the solid electrolyte and served as a reference sample.

The thin film (20nm) was used to extract $\rho_{electro}$. The deposited film ($t_{electro\ (thin)}$) was relatively thin compared to the thickness (t) of the cantilever beam ($t \gg t_{electro\ (thin)}$). In this case it was assumed that the location of the neutral beam axis remained unchanged after solid electrolyte deposition. Therefore, the change in cantilever resonant frequency was assumed to be a result of a change in equivalent mass alone. FEM simulations were used to match the measured change in resonant frequency by alteration of the solid electrolyte mass density. When simulated and measured shifts in resonant frequency matched, $\rho_{electro}$ was found.

The thick film (80nm) was used to determine $E_{electro}$. In contrast to the thin electrolyte, the location of the neutral axis changed with deposition of thick film. Assuming the same mass density between these two films, $E_{electro}$ was extracted by matching the

measured change in resonant frequency with FEM simulations. To ensure an identical mass density $\rho_{electro}$ between these two films, 15nm and 4nm of Ag was driven into the thick (80nm) and thin (20nm) solid electrolyte layers via UV photodissolution using a Karl Suss Mask aligner with a power density of $3.9mW/cm^2$ for 20 minutes.

The resonant frequencies of all three cantilever beam samples were determined under vacuum (p=20μbar) using laser vibrometer measurements as described in Chapter 6. The solid electrolyte was assumed to be stress free. This assumption was reasonable, because the solid electrolyte was deposited at room temperature inside an evaporator.

8.4 Results and Discussion

This section presents and discusses results from the characterisation of the solid electrolyte and the demonstration of Ag deposited tuning using manufactured and prepared bridge resonator test structures.

8.4.1 Characterisation of the solid electrolyte

Electrical solid electrolyte characterisation

The $Ag_{0.1}\ (Ge_{0.3}Se_{0.7})_{0.9}$ deposited on manufactured suspended Greek crosses was electrically characterised using a HP4156B semiconductor parameter analyser and a manual probe station. During all measurements the substrate was allowed to float electrically. Before sheet resistance measurements were made, the isolation of the measurement platform was tested by attempting to force a DC current of 1nA with a voltage compliance of 40V between a probe pad and the surrounding Si substrate. This determined that the Greek crosses provided sufficient isolation from the measurement currents entering the surrounding substrate from the probe areas. Sheet resistance was determined by forcing a 10nA DC current through the $Ag_{0.1}\ (Ge_{0.3}Se_{0.7})_{0.9}$ layer and calculated using equation Eq. (A.13). The resistivity of the evaporated films was calculated using equation Eq. (8.1).

Fig. 8.7 presents the measured sheet resistance for 80nm thick $Ag_{0.1}\ (Ge_{0.3}Se_{0.7})_{0.9}$ as a function of the Greek cross arm width and measurement time. Fig. 8.7(a) indicates that the measured sheet resistance of $Ag_{0.1}\ (Ge_{0.3}Se_{0.7})_{0.9}$ was variable with the arm width. This suggested that the film was not homogeneous in composition and/or of nonuniform thickness across the test chip.

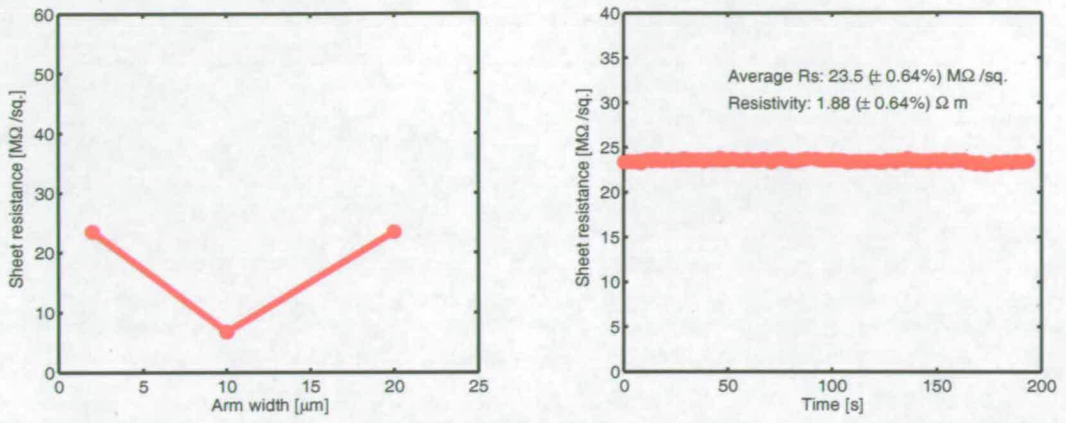

(a) (b)

Figure 8.7. Measured sheet resistance for an 80nm thick solid electrolyte using Greek crosses. The graphs show the measured sheet resistance (a) as a function of Greek cross arm width for 80nm thick blanket deposited $Ag_{0.1}\,(Ge_{0.3}Se_{0.7})_{0.9}$ and (b) as a function of measurement time for a 2μm wide Greek cross test structure.

The extracted "leakage" resistivity from the Greek cross sheet resistance measurements ranged from 0.53 to $1.88\Omega m$ for $Ag_{0.1}\,(Ge_{0.3}Se_{0.7})_{0.9}$. These values agreed with the ones published in [78]. The high resistivity of $Ag_{0.1}\,(Ge_{0.3}Se_{0.7})_{0.9}$ was a result of the low number of Ag ions in this relatively thick film compared to thinner films characterised elsewhere [24, 78].

Fig. 8.7(b) shows the measured sheet resistance as a function of measurement time. The depicted data suggested that Greek crosses showed little change in measured sheet resistance over the considered measurement time. Therefore, possible Ag electrodeposition at the metal probe pads did not electrically alter the heart of the cross from where the sheet resistance was extracted. Greek cross test structures were therefore the better choice to measure sheet resistance compared to bridges where diffusion/ion migration at the contact pads altered the solid electrolyte resistance with time [138, 24].

Sheet resistance measurements on $Ag_{0.1}\,(Ge_{0.3}Se_{0.7})_{0.9}$ showed that the solid electrolyte was non-uniform in thickness and composition. The extracted resistivity changed by 255% across the sample, which was related to structural composition and Ag ion content of the solid electrolyte. The large variation in resistivity (number of Ag ions in the solid electrolyte) affected the the rate of Ag electrodeposition. This suggested that Ag

deposited tuning was subject to large variation as a result of the variability in the solid electrolyte film composition.

Mechanical solid electrolyte characterisation

Fig. 8.8 shows the extracted solid electrolyte mass density $\rho_{electro}$ as a function of cantilever beam length. The mass density $\rho_{electro}$ varied for different cantilever beam lengths and was therefore dependent on the location of the die. This location dependent variation in density suggested that the solid electrolyte had a non-homogeneous composition across the sample. Hence, non-homogeneous composition caused the measured variation in $\rho_{electro}$ of $\pm 15\%$. From all measurements an average mass density of $\rho_{electro} = 6,500 kg\ m^{-3}$ was extracted (Fig. 8.8).

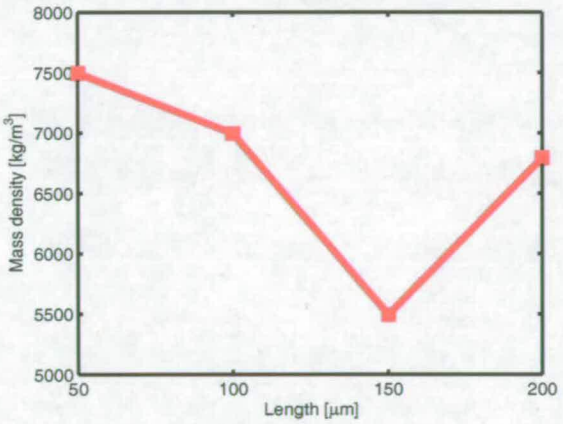

Figure 8.8. Solid electrolyte mass density as a function of resonator length. Extracted mass density of a 20nm thick $Ag_{0.1}\,(Ge_{0.3}Se_{0.7})_{0.9}$ solid electrolyte film as a function of cantilever beam length. The extraction of the mass density was performed using frequency measurements on polysilicon beam resonators and FEM simulations. The mass density was found by matching simulated resonant frequencies with measured ones.

This result was slightly lower than expected. Calculations, assuming the solid electrolyte volume consisting of 60% Ge_2Se_3 and 40% Ag_2Se, found a mass density value of $\rho_{electro} = 8,500 kg\ m^{-3}$ [60]. This discrepancy again suggested a variability in solid electrolyte composition.

The $E_{electro}$ was extracted from FEM simulations and is shown as a function of the resonator length for 80nm thick $Ag_{0.1}\,(Ge_{0.3}Se_{0.7})_{0.9}$ in Fig. 8.9. An average Young's modulus of $E_{electro}$=20 GPa was extracted from the FEM simulations. The average extracted

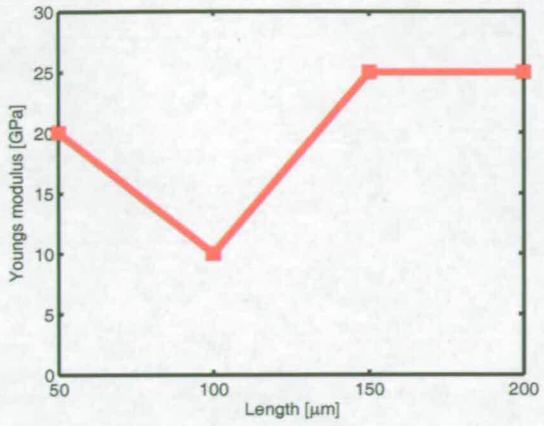

Figure 8.9. Solid electrolyte Young's modulus as a function of cantilever beam length. The Young's modulus of a 80nm thick $Ag_{0.1}\,(Ge_{0.3}Se_{0.7})_{0.9}$ was extracted by matching FEM simulations with experimentally determined resonant frequencies of blanket deposited cantilevers. The Young's modulus was found by matching simulated cantilever resonant frequencies with measurement data.

$E_{electro}$ agreed well with values found in the literature for chalcogenide glass films containing $Ge - Se$ components being 21 GPa [114]. $E_{electro}$ changed of up to $\pm 50\%$ for the resonator length available, indicating a non-homogeneous composition across the sample. Again, as observed in case of $\rho_{electro}$, a strong variation in $E_{electro}$ indicates a non-homogeneous electrolyte composition, which needs to be optimised to ensure Ag deposited tuning with a high repeatability in frequency tuning.

8.4.2 Electrochemical Ag deposited tuning - a model

Ag deposited tuning of micromechanical polysilicon resonators is a process, which combines (i) electrochemical Ag deposition and (ii) mechanical vibration. To analytically model Ag deposited tuning, the theory of Ag electrodeposition and mechanical vibration had to be considered. This section describes in two parts the development of such a model, which predicted Ag deposited tuning of bridge resonators. In part one, a model for electrodeposition of Ag is derived on the basis of experimentally determined Faraday resistivity. Part two uses the developed electrodeposition model and vibrational theory (Ch. 2) to describe Ag deposited frequency tuning of bridge resonators.

Electrodeposition

To model Ag electrodeposition, the solid electrolyte, which covered the surface of bridge resonator and electrically connected the Ag anode with the Al cathode had to be considered (Fig. 8.10). An equivalent circuit was developed, which described the solid electrolyte electrically [146]. Fig. 8.10(b) depicts an adapted version of the equivalent electrical circuit, which electrically describes the solid electrolyte on the polysilicon bridge resonator.

The solid electrolyte between the Ag anode and cathode was described by a number of variable and constant resistances. These resistances were formed by the Ag ion conducting solid electrolyte R_F, the Ag deposit R_{Ag} and a cathode double layer R_p. The resistance of the solid electrolyte and of the Ag deposit varied with progressing electrodeposition from the cathode to the Ag anode, while the resistance across the 10nm wide double layer remained constant [60]. The cathode double layer resistance is in the order of $2.1 \times 10^8 \Omega cm^{-2}$ [146].

This double layer at the cathode was located inside the solid electrolyte, where negatively charged electrons faced positive Ag ions (Fig. 8.10(a)). Electrochemical reduction between these two layers and subsequent Ag deposition only occurred, when the potential difference across the cathode double layer was above 250mV [60]. However, Ag electrodeposition in case of blanket deposited bridge resonators required considerably higher voltages as result of the comparatively large electrolyte R_F and Ag deposit (R_{Ag}) resistances, which were in series with R_p.

Faraday's law of electrolysis applies in the these solid electrolyte systems and determined the mass of material deposited m_{Ag}, which was proportional to the amount of charge C supplied by the external electrical circuitry. The electric charge supplied by the external circuit is defined by:

$$C = \int_0^t i_F(t)dt \tag{8.2}$$

where t is the total deposition time and i_F the Faraday current. The charge required to deposit a given mass of material can be written as

$$C = n(Ag)F \tag{8.3}$$

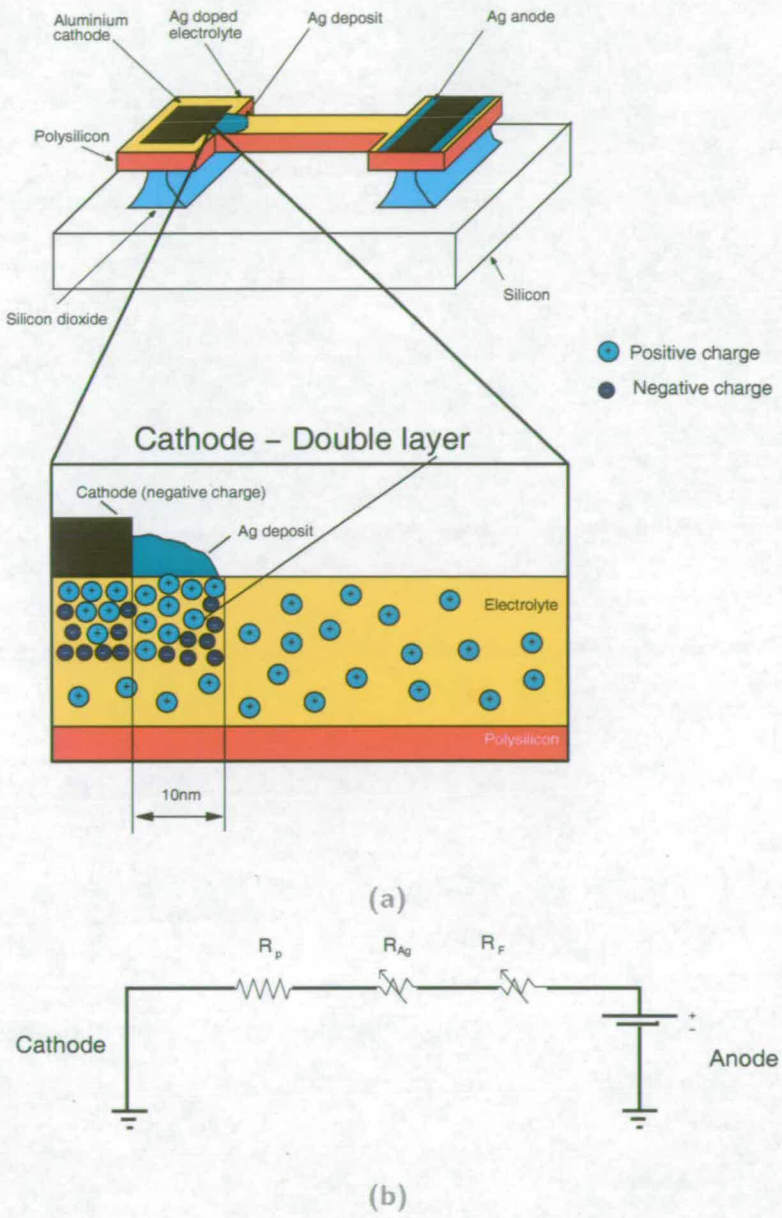

Figure 8.10. Physical and electrical representation of the Ag deposition scheme. (a) Polysilicon bridge resonator covered with solid electrolyte. The magnified cathode-solid electrolyte region shows the 10nm wide cathode double layer, which consists of an accumulation of positively charged Ag ions and negatively charged electrons. (b) Equivalent electrical circuit describing the Ag deposition scheme. The circuit consists of a series connection of the Ag ion carrying solid electrolyte R_F, Ag deposit R_{Ag} and cathode double layer R_p resistance.

where $n(Ag)$ are the moles of Ag ions contributing to the electrodeposit and F=96,486 C/mol is the Faraday constant [131]. Since one Ag ion combined with one electron to form atomic Ag, the deposited mass m_{Ag} can be expressed as follows,

$$m_{Ag} = \frac{i_F dt \Lambda_{Ag}}{F} \tag{8.4}$$

The constant $\Lambda_{Ag} = 107.9\ g \times mol^{-1}$ is the molar mass of atomic Ag. Therefore, the deposited Ag mass can be calculated for a given Faraday current and time using Eq. (8.4).

Including the applied electrical voltage U and the total time dependent series resistance $R_t(t)$ between the Ag anode and the Al cathode, one can write Eq. (8.4) as

$$m_{Ag} = \frac{U dt \Lambda_{ag}}{R_t(t) F}. \tag{8.5}$$

The time dependent total series resistance $R(t)_{total}$ between the Ag anode and the Al cathode was given by:

$$R(t)_{total} = R_F(t) + R_{Ag}(t) + R_p. \tag{8.6}$$

The time dependent resistance of the solid electrolyte $R_F(t)$ was calculated from the so called Faraday "resistivity" ζ_F. In practise, the Faraday current i_F and "resistivity" through the electrolyte are unknown. One way of finding the Faraday current is to perform Ag deposition tests (Sec. 8.4.3) and subsequently measure the total volume of the electrodeposits V_{Ag} using SEM imaging. The deposited Ag mass m_{Ag} per unit time ($dt = 1s$) can then be related to the measured total volume V_{Ag} and deposition time t

$$\frac{m_{Ag}}{dt} = \rho_{Ag} \frac{V_{Ag}}{t} \tag{8.7}$$

where ρ_{Ag}=10,490$kg\ m^{-3}$ [145] is the mass density of bulk Ag. Equation (8.4) can be rewritten to determine the Faraday current

$$i_F = \frac{F m_{Ag}}{\Lambda_{Ag} dt} \tag{8.8}$$

From the Faraday current i_F, a corresponding "resistivity" of the electrolyte can be found for an applied electrical voltage U

$$\zeta_F = \frac{U\ A_e}{i_F\ L} \tag{8.9}$$

A time dependent Faraday resistance was calculated from this extracted "resistivity" value using

$$R_F(t) = \frac{\zeta_F \Delta L_{electro}}{t_{electro} w_{electro}} \tag{8.10}$$

where $t_{electro}$ and $w_{electro} = w$ were the thickness and width of the solid electrolyte. The length $\Delta L_{electro}$ of the solid electrolyte contributing to the overall $R_F(t)$ decreased with the progressing length of the Ag deposit L_{Ag}. Initially, the length of the electrolyte was equal to that of the polysilicon bridge L. With expanding Ag deposition, $\Delta L_{electro}$ became

$$\Delta L_{electro} = L - L_{Ag}. \tag{8.11}$$

The length of the progressing Ag deposit L_{Ag} was given by:

$$L_{Ag} = v_{Ag} t \tag{8.12}$$

where v_{Ag} was the velocity of the progressing Ag deposit. The velocity was determined by $v_{Ag} = L_b / t_{short}$, where t_{short} was the measured time from the start of deposition until the Ag anode and Al cathode were electrically shorted by the Ag electrodeposit. The electrical short between the Ag anode and Al cathode was experimentally determined using a ammeter during deposited frequency tuning experiments.

The resistance of the Ag deposit was determined by:

$$R_{Ag}(t) = \frac{\zeta_{Ag} L_{Ag}}{w_{Ag} t_{Ag}} \tag{8.13}$$

where $\zeta_{Ag} = 1.59 \times 10^{-8} \Omega\, m$ [145], $w_{Ag} = w$ and t_{Ag} were the bulk resistivity, thickness and width of the Ag deposit.

Using Equation (8.5) and Eq. (8.6), the deposited Ag mass on a blanket solid electrolyte deposited 200μm$\times$20μm$\times$1μm polysilicon bridge resonator was calculated and is presented as a function of time for a 2V DC bias (Fig. 8.11). For the calculations a 80nm thick blanket deposited solid electrolyte was assumed.

Fig. 8.11 shows a nonlinear increase in deposited Ag mass with time for a 2V DC bias. The non-linear increase in Ag mass with time was a result of the Ag deposit extending along the polysilicon bridge resonator. While the Ag deposit progressed with time along the length of the bridge resonator, the overall series resistance by the external circuitry continuously decreased. A smaller series resistance produced a higher electrical current and therefore more deposited Ag mass with time.

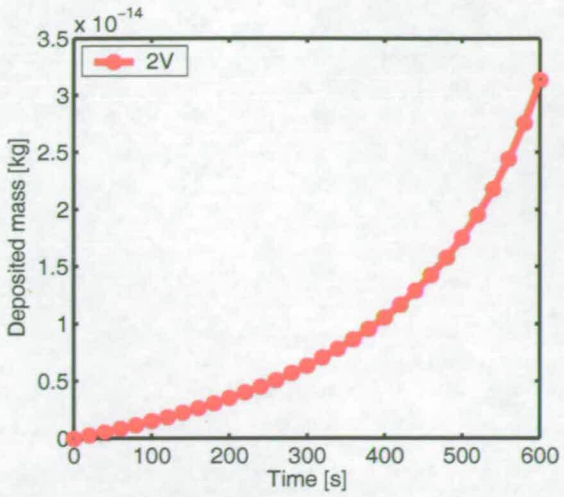

Figure 8.11. Deposited Ag mass as a function of deposition time for a 2V DC bias. For the calculation a 80nm thick blanket deposited solid electrolyte on a 200μm$\times$20μm$\times$1μm polysilicon bridge resonator was assumed.

Frequency tuning

During Ag deposition, both the equivalent mass me_{eq} and stiffness ke_{eq} of a solid electrolyte covered polysilicon bridge resonator with perfectly clamped anchors changed constantly. The change in me_{eq} and ke_{eq} caused Ag deposited frequency tuning. To model Ag deposited tuning, the analysis presented in Sec. 2.3.2 was used.

The equivalent mass me_{eq} of a electrolyte covered polysilicon bridge is:

$$me_{eq} = \rho_{poly} wt \int_0^L (X(x))^2 \, dx + \rho_{electro} wt_{electro} \int_0^L (X(x))^2 \, dx \tag{8.14}$$

where ρ_{poly}=2,230kgm^{-3} and $\rho_{electro}$=6,500kgm^{-3} (Sec. 8.4.1) are the mass densities of polysilicon and the solid electrolyte. The equivalent stiffness of the electrolyte covered polysilicon bridge resonator is:

$$ke_{eq} = \hat{E}_{poly} I_{poly} \int_0^L \left(\frac{d^2X(x)}{dx^2} \right)^2 dx + \hat{E}_{electro} I_e \int_0^L \left(\frac{d^2X(x)}{dx^2} \right)^2 dx \tag{8.15}$$

where E_{poly}=160GPa, I_{poly}, $E_{electro}$=21GPa (Sec. 8.4.1) and I_e are the Young's modulus and second moment of area of the polysilicon bridge and the solid electrolyte layer. The second moment of area are:

$$I_{poly} = \frac{wt^3}{12} \tag{8.16}$$

$$I_e = \frac{wt_{electro}^3}{12} \tag{8.17}$$

The presence of the solid electrolyte and Ag deposition caused a shift in the neutral axis of the bridge. Based on the discussions in Sec. 2.3.2, the new location of the neutral axis was calculated by transforming the cross section of the composite bridge resonator by multiplying the widths of the electrolyte and Ag with the following modular ratios $mr_{electro} = \frac{E_{electro}}{E}$ and $mr_{Ag} = \frac{E_{Ag}}{E}$ (Fig. 8.12). The following Young's modulus values were used: $E = 160GPa$, $E_{electro} = 20GPa$ and $E_{Ag} = 83GPa$ ([145]).

The new neutral axis was calculated by:

$$\acute{Z} = \frac{w_{Ag}t_{Ag}\left(t + t_{electro} + t_{Ag}/2\right) + w_{electro}t_{electro}\left(t + t_{electro}/2\right) + wt\left(t/2\right)}{\left(w_{Ag}t_{Ag}\right) + \left(w_{electro}t_{electro}\right) + \left(tw\right)}. \tag{8.18}$$

The second moment of area of the deposited Ag layer was:

$$I_{Ag} = \frac{1}{12}(w)(t_{Ag})^3 + (A_{Ag})(t + t_{electro} + \frac{t_{Ag}}{2} - \acute{Z})^2 \tag{8.19}$$

where A_{Ag} was the cross sectional area of the Ag deposit.

The frequency f_{Ag} of a polysilicon bridge resonator covered with solid electrolyte and progressing Ag deposits was modelled by [34]:

$$f_{Ag} = \frac{1}{2\,\pi}\sqrt{\frac{ke_{eq} + \Delta k}{me_{eq} + \Delta m}}. \tag{8.20}$$

where Δk and Δm was the change in equivalent stiffness and mass produced by the deposited Ag. The change in equivalent mass Δm is calculated as follows:

$$\Delta m = \rho_{Ag} w t_{Ag} \int_0^{L_{Ag}} \left(X(x)\right)^2 dx \tag{8.21}$$

where $\rho_{Ag} = 10,490\ kg\ m^{-3}$ [145] was the mass density of the Ag deposit.

The change in equivalent stiffness Δk was calculated

$$\Delta k = \hat{E}_{Ag} I_{Ag} \int_0^{L_{Ag}} \left(\frac{d^2X(x)}{dx^2}\right)^2 dx \tag{8.22}$$

where $\hat{E}_{Ag}$ was the effective Young's modulus of the Ag deposit (Ch. 2).

The frequency change was calculated from:

$$\Delta f = \frac{f_{Ag} - f_0}{f_0}. \tag{8.23}$$

Fig. 8.13 shows the change in resonant frequency as a function of time for 2V Ag deposition along a $200\mu m \times 20\mu m \times 1\mu m$ polysilicon bridge resonator. The analytical calculation assumed a continuously progressing blanket deposited $0.5\mu m$ thick Ag deposit,

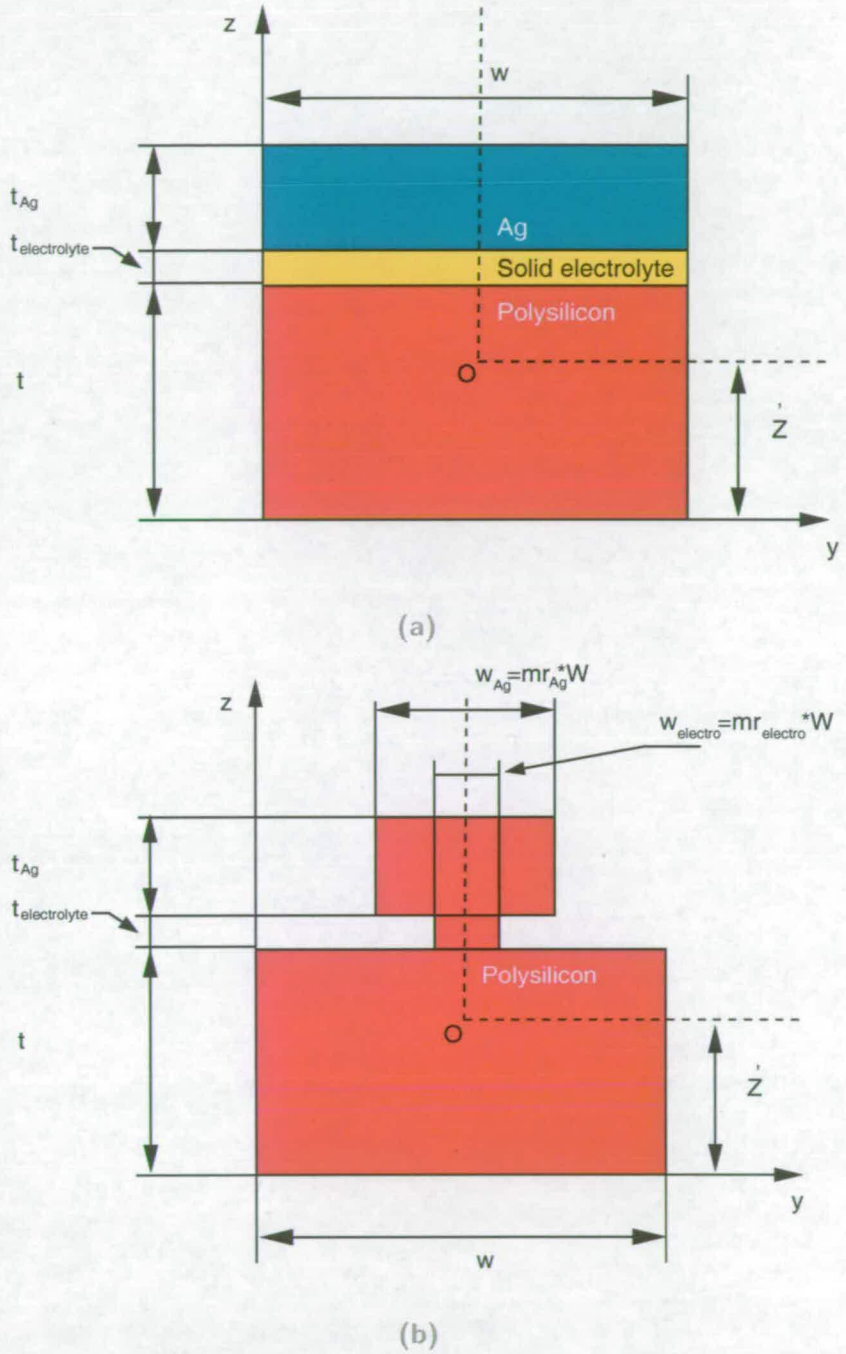

Figure 8.12. Cross section of polysilicon bridge resonator covered with solid electrolyte and Ag. (a) Cross section of composite bridge. (b) cross section of bridge after applying the transformed section method Sec. 2.3.2. To transform the cross sections of the solid electrolyte and Ag deposit, their widths were multiplied with the modular ratios.

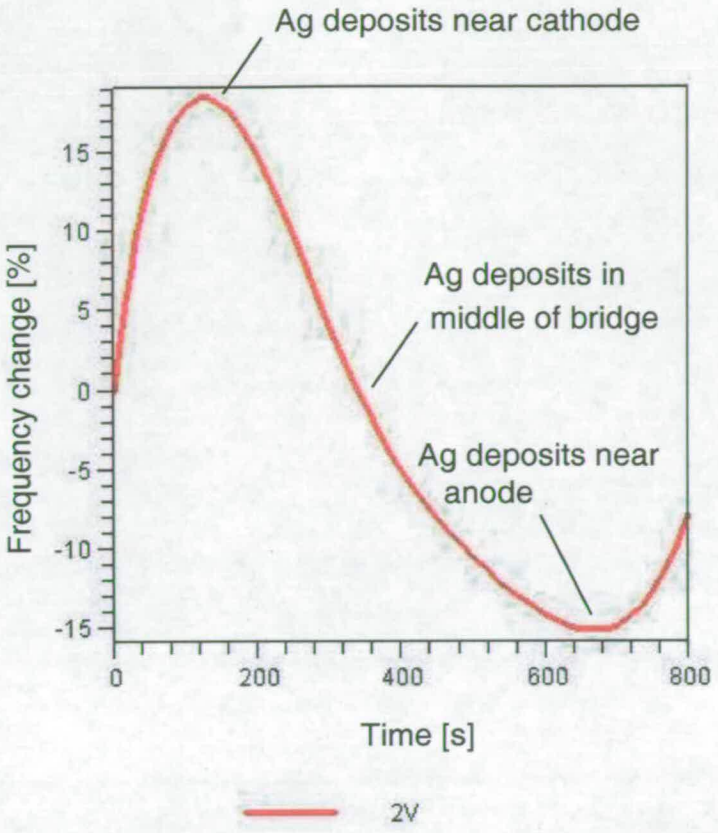

Figure 8.13. Change in resonant frequency as a function of time. Calculated change in resonant frequency as a function of time for a DC bias of 2V. The calculation assumed a 0.5μm thick blanket deposited Ag deposit, progressing from the cathode towards the Ag anode of the bridge resonator. The progressing Ag deposit caused a time and location dependent frequency change. The deposited Ag located near the cathode and Ag anode end of the bridge increased the equivalent stiffness and resonant frequency of the bridge. Ag deposits passing through the middle section of the bridge increase the equivalent mass, which consequently reduced the resonant frequency.

moving from the cathode to the Ag anode end of the bridge resonator. Ag deposits at the cathode initially increased the equivalent stiffness and resonant frequency. As the Ag deposits move further towards the middle of the bridge, the resonant frequency decreased as a result of the rising equivalent mass. The equivalent stiffness and resonant frequency increased again as the Ag deposit approached the Ag anode. Fig. 8.13 clearly identified a time dependent and therefore location dependent tuning behaviour.

8.4.3 Characterisation of Ag deposited tuning scheme

After the integration of the Ag deposition scheme (Sec. 5.2.1), polysilicon bridge resonators were gold wire bonded in a 28 pin DIP and attached to a piezo disk for vibration measurements. To analyse the Ag deposited tuning, the resonant frequency of polysilicon bridge resonators was measured before and after Ag deposition. Ag deposition was produced by applying a DC voltage between the Ag anode and Al cathode of polysilicon bridges. Cathodes of neighbouring bridges were set to the Ag anode potential, to ensure that only one device at a time was deposited with Ag.

The characterisation of the Ag tuning scheme was based on the test of two bonded packages, tested with 2V and 3V. The Ag growth along the polysilicon bridge resonators was detected using surface profiler and frequency measurements. Full bridge coverage was detected through the measurement of the electrical short between Ag anode and Al cathode. Subsequent SEM and FIB imaging was used for characterisation of the Ag deposits.

Preliminary results

Initial tests of the Ag deposition mechanism on the first bonded package involved the application of 3V for 16 minutes between the anode and cathode of polysilicon bridge resonators. This resulted in the transport of Ag ions and subsequent deposition on the polysilicon bridges. Ag deposition on the two shorter structures (Fig. 8.14) caused a -8% and -10% reduction in resonant frequency. The two longer 150μm and 200μm polysilicon bridges showed tuning of -1.2% and +6.2%, respectively. This inconsistency was attributed to the variation in deposited Ag thickness along the length of long polysilicon bridges (Fig. 8.15). Thick Ag deposits near the cathode of the long bridge resonators increased their equivalent stiffness and resonant frequency. In contrast, a more uniform Ag deposition along short bridge resonators increased the equivalent mass and therefore caused a reduction of resonant frequency.

It was not possible to measure the deposited Ag thickness with an optical surface profiler, because Ag electrodeposits had a high surface roughness, which was too high to provide sufficient reflection for the measurement.

Preliminary results suggested that the application of a DC bias voltage between the anode and the cathode provided sufficient Ag ions for electrodeposition and subsequent frequency tuning of micromechanical polysilicon resonators. The deposited Ag

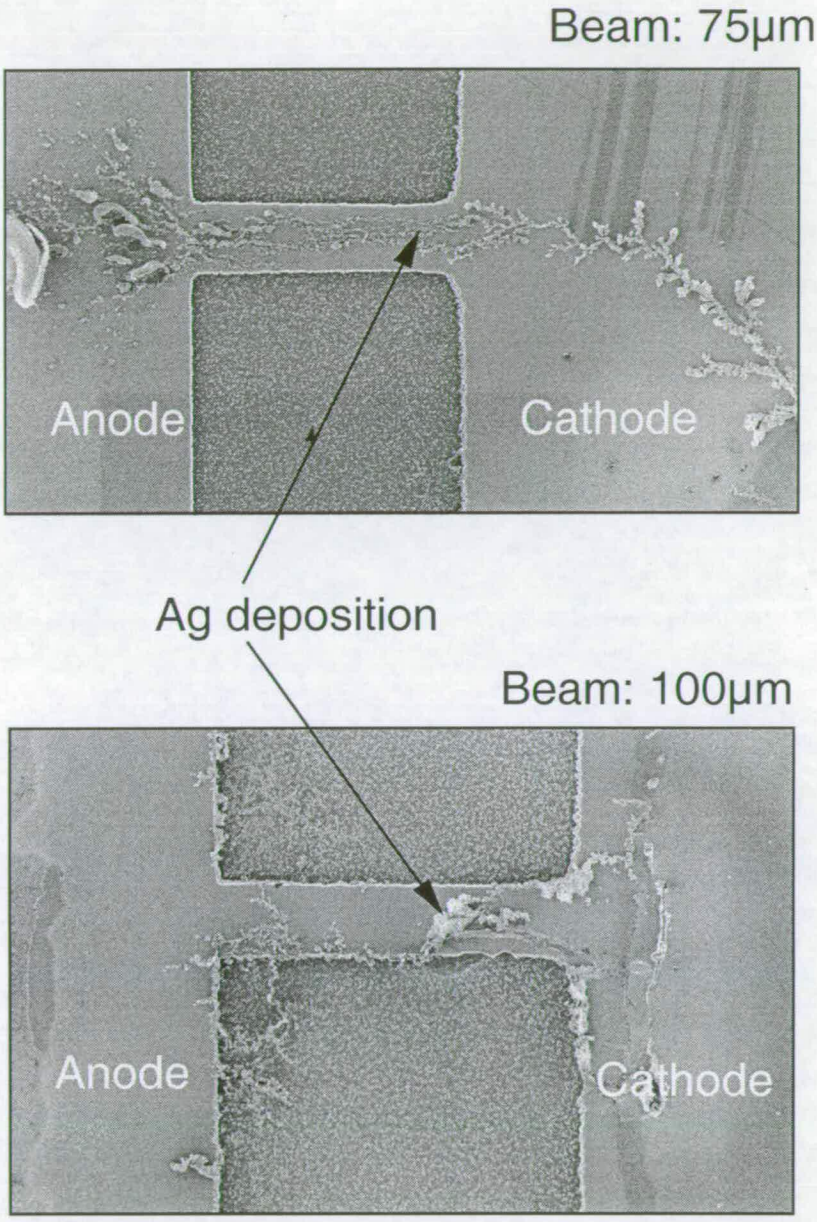

Figure 8.14. FIB images of Ag-deposited polysilicon bridge resonators. Ag deposited $75\mu m \times 20\mu m \times 1\mu m$ and $100\mu m \times 20\mu m \times 1\mu m$ polysilicon bridge resonators with -8% and -10% frequency change, respectively. Ag deposition was performed with 3V for a 16 minute period. The Ag growth was dendritic and connected Ag anode with Al cathode. Ag deposits on the shortest bridge were evenly distributed across the length of the bridge, while Ag deposits for the $100\mu m$ were concentrated in the middle of the resonator. Both cases caused an increase in equivalent stiffness and reduction in resonant frequency.

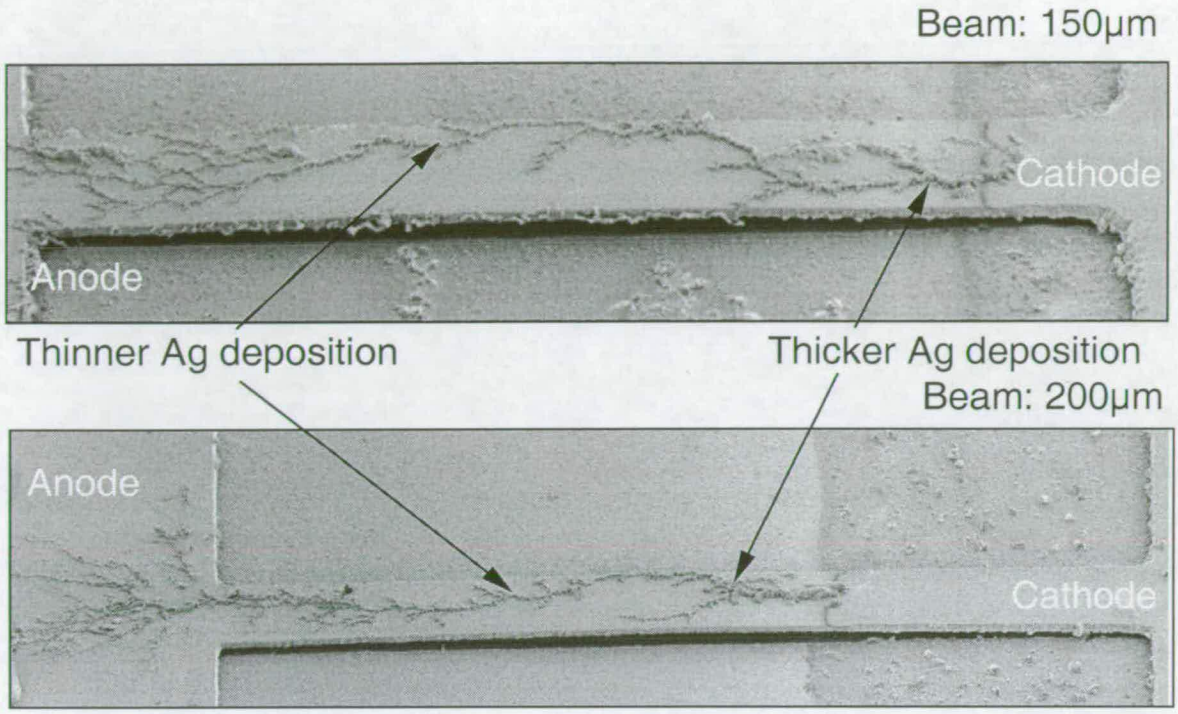

Figure 8.15. Polysilicon bridge resonators with with misaligned Al cathodes. Measured frequency changes were -1% for 150μm$\times$20μm$\times$1μm and +6% for 200μm$\times$20μm$\times$1μm long polysilicon bridge resonators after 16 minutes using a 3V DC bias. More dendritic deposited Ag deposition near the cathode and anode caused an increase in equivalent stiffness and resonant frequency.

thickness was non-uniform across the polysilicon bridges and caused a variation in detected frequency change between tested devices.

Forms of Ag deposits

During the tuning of polysilicon bridge resonators, three different forms of Ag deposits were observed. These Ag deposits were (i) dendritic, (ii) stringy and (iii) hillock shaped. The majority of samples showed dendritic Ag deposition (Fig. 8.15). Dendritic Ag deposits were non-uniform in thickness and irregular in shape along the length of individual resonators as well as between different devices on the same chip. The variation in Ag deposition thickness between different bridge samples and along individual devices reduced the repeatability of the detected frequency change and made it difficult to predict tuning. The difference in deposited Ag thickness was a result of the variability in solid electrolyte resistivity as shown in Sec. 8.4.1.

The second form of Ag deposition was the stringy pattern as shown in Fig. 8.16. These Ag patterns grew over several hundred microns along the sidewalls of scratches. In these samples, the scratches in the solid electrolyte were produced during the removal of the shadow masks used for the Ag anode and Al contact definition as described in Sec. 5.3.1. As can be observed in Fig. 8.16, Ag deposits perfectly aligned to the orientation of the scratch.

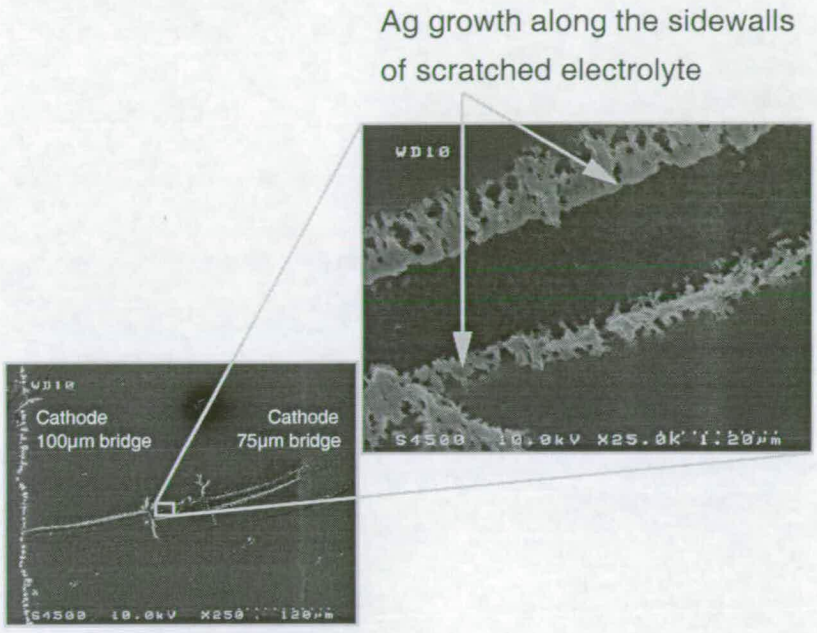

Figure 8.16. Ag deposits as stringy patterns using 2V DC bias. The SEM image shows Ag deposits perfectly aligned to the orientation of the scratch in the solid electrolyte. Scratches in the solid electrolyte were produced during the removal of metal shadow masks, which were used to produce the Ag anode and Al cathodes.

Ag deposition on solid electrolytes was influenced by the Ag ion supply, electric field and surface area. The scratched areas had a higher field and a bigger surface area (and higher free volume) compared to the blanket deposited solid electrolyte. Therefore, Ag deposition was enhanced in the scratched areas compared to areas with no surface damage. Lithographic patterning of the solid electrolytes into stripes or trenches provides the possibility of ensuring guided and more uniform Ag deposition onto polysilicon bridges. However, further research is required to characterise Ag deposition in patterned solid electrolytes (Ch. 9).

A third form of Ag deposition was hillock shaped as shown in Fig. 8.17. The two hillock shaped Ag deposits were concentrated at the interface between solid electrolyte

and Al cathode and were several micron in diameter. Ag deposition tended to proceed into the height rather in the lateral direction as in the case for dendritic patterns. It is well known that the Ag ion concentration and the base glass composition influence the form of electrodeposits [110, 78]. Hence, the observed deviation from the dendritic Ag growth pattern suggested a variation in Ag ion concentration and/or a variation in the base glass composition and confirms results made during the characterisation of the solid electrolyte (Sec. 8.4.1).

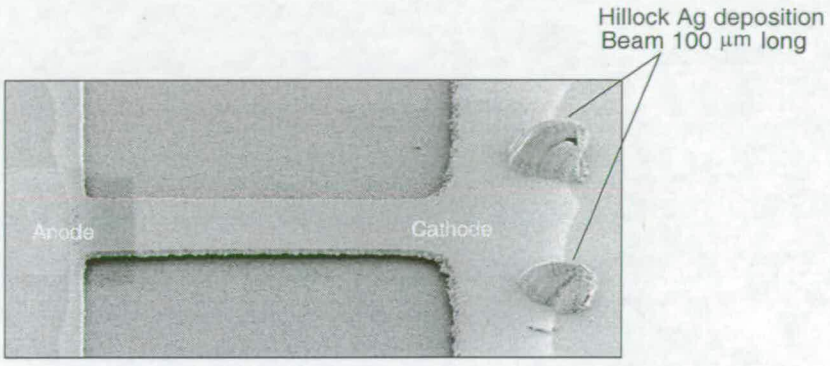

Figure 8.17. Ag deposited in hillock shapes using 2V bias for 70 minutes. The SEM image shows hillock Ag deposits forming at the interface between solid electrolyte and Al cathode located at the attachment region of the bridge resonator. The deviation in Ag electrodeposition from dendritic patterns suggested a variation in solid electrolyte composition and Ag ion concentration.

Ag deposited frequency tuning

After Ag deposited tuning was demonstrated successfully, further characterisation of this technique was performed on a $200\mu m \times 20\mu m \times 1\mu m$ polysilicon bridge resonator using 2V for 36 minutes (see Fig. 8.18). Before Ag deposited tuning started, frequency measurements of the polysilicon bridge showed a 7% difference in resonant frequency compared to the long bridge shown in Fig. 8.15. The reason for the discrepancy was the misalignment of the shadow mask, which was differed between these two resonators and contributed to the initial frequency variability.

Despite the observed variability, the use of a 2 DC bias resulted in an Ag deposition pattern onto the resonator, which was less dendritic than in the case of Ag deposited tuning using 3V (Fig. 8.15). The difference in the Ag deposition pattern between these two samples was explained by the variation in Ag ion concentration in their solid electrolytes. According to [110], deposition patterns of metal electrodeposits are influenced

by the metal ion concentration in the electrolyte. Recall that the Greek cross measurements extracted a variation in "leakage" resistivity and concluded a variation in sample composition even for devices on the same test sample. Furthermore, it was found by the author elsewhere [24], that the conduction in these solid electrolyte systems was influenced by the level of Ag ion concentration. The observed variation in Ag deposition pattern was therefore a result of different Ag ion concentration between these two samples.

These Ag deposition patterns started to form at the cathode of the polysilicon bridge once the 2V DC bias was applied between Ag anode and Al cathode. The measured electron current through the electrolyte during deposition was 100nA, providing frequency tuning with an impressive power consumption of 200nW. As a consequence of the Ag deposition process, the resonant frequency of the polysilicon bridge started to increase Fig. 8.18(b). The increase was a result of the increased equivalent stiffness. Equivalent stiffness is a function of location with maxima at both anchor sites and minimum in the middle of the polysilicon bridge [6]. Hence, Ag deposition near the anchors increased the equivalent stiffness and caused a rise in resonant frequency.

When time progressed, more electrodepositions occurred and the Ag thickness at the cathode increased. A thicker Ag electrodeposit further increased the equivalent stiffness and the resonant frequency of the polysilicon bridge rose to a maximum value of +10.7%. Once the Ag deposition pattern started to move along and towards the Ag anode, the equivalent mass of the bridge increased and frequency dropped. The equivalent mass is a function of length, with a minimum at the centre and two maxima at the anchor points of the bridge [6]. Further deposition increased the equivalent mass and reduced the resonant frequency to a minimum value of -6.3% for full bridge coverage with Ag.

The resonant frequency of polysilicon bridge resonators drifted during the measurement on average by +77 Hz$\times$minute^{-1} (+0.025% of the untuned resonant frequency). This drift was a result of heating of the polysilicon bridge over time. The heat was supplied by the vibrometer laser, which increased the temperature in the deposited polysilicon bridge and caused biaxial stress between the deposited Ag and the underlying polysilicon. Biaxial stress caused further bridge buckling and an increase in resonant frequency with time.

Analytically modelling presented in Sec. 8.4.2 deviated from the experimentally determined frequency change shown in Fig. 8.18(b). The reason for the large difference

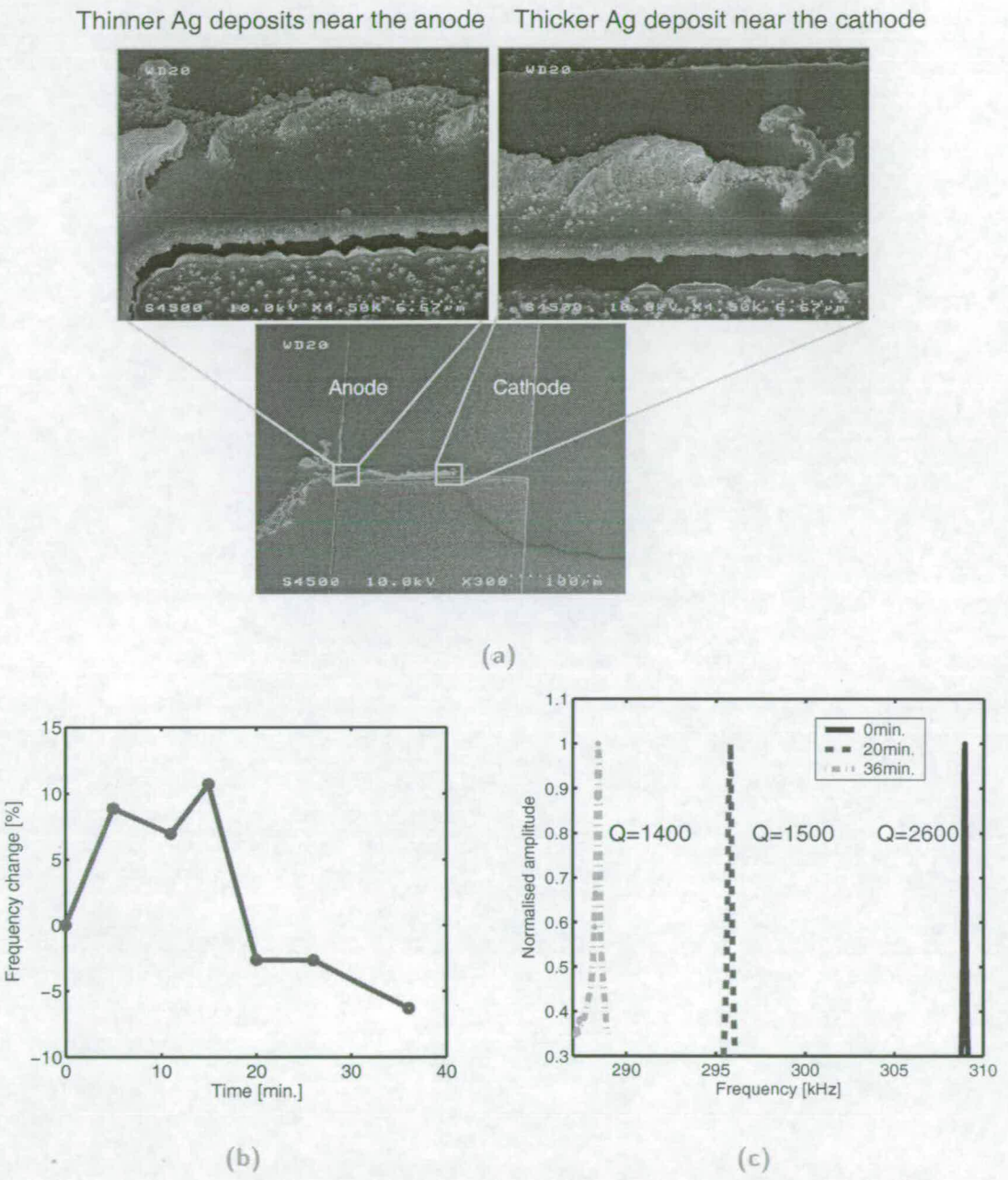

Figure 8.18. Ag deposited frequency tuning of a polysilicon bridge with 2V DC bias for 36 minutes. Ag deposited tuning of a 200μm×20μm×1μm was performed in vacuum under a constant pressure of 20μbar using 2V for 36 minutes. (a) SEM image of Ag deposited polysilicon bridge resonator with misaligned cathode. The enlarged pictures illustrated the non-uniform thickness in deposited Ag along the bridge resonator. (b) Resonant frequency as a function of time and (c) Measured frequency spectra during different stages of Ag deposited tuning.

in resonant frequency change between between modelling and experimental results was the non-uniform Ag deposition on polysilicon bridge resonators (Fig. 8.18(a)). The analytical model assumed a constant deposited Ag thickness (0.5μm) along the polysilicon bridge. In reality however, Ag was being deposited non-uniformly across the polysilicon resonator. Therefore, the measured frequency experienced an initial increase in frequency as predicated by the analytical model, but did not show a repeated rise in frequency near the Ag anode of the bridge resonator.

Apart from the resonant frequency, the Q-factor of tuned polysilicon bridge resonators was extracted from the measured frequency spectra as shown in Fig. 8.18(c). The extracted Q-factor reduced from an initial value of 2,600 to 1,400 after 36 minutes of tuning. This 46% decrease in the Q-factor was a result of deposited Ag, increasing the thermoelastic damping and degrading the Q-factor as the tuning progressed. However, these results are based on one sample and further experiments have to be performed to confirm these findings.

The Q-factor reduced further with the progressing Ag along the bridge resonator as a result of more thermoelastic damping occurring in the growing Ag deposit Fig. 8.18(c). As more Ag was deposited onto the polysilicon bridge resonator, the Q-reduction became stronger. This confirms findings for FIB Pt deposited tuning, where the deposition of Pt caused a decrease in Q. However, compared to the FIB Pt tuning, the Q-reduction observed for Ag deposited tuning was more severe. The reason for the difference was that more thermoelastic damping occurred in the deposited Ag than in FIB Pt.

8.5 Conclusions

In this chapter, an Ag deposition scheme was characterised for the purpose of frequency tuning of flexural vibrating polysilicon bridge resonators. The medium used to transport and enable Ag deposition on the polysilicon bridge resonators was a blanket evaporated Ag loaded solid electrolyte. Ag ion migration was simply induced by a DC voltage between an oxidizable Ag-anode and an Al cathode. Once Ag ions arrived at the negatively charged Al cathode, a reduction of Ag and subsequent deposition occurred. Deposited Ag altered the equivalent stiffness and mass of the polysilicon bridge and consequently modified the resonant frequency.

The characterisation of the Ag deposited tuning scheme involved the analysis of the (i) solid electrolyte and (ii) Ag deposition and (iii) tuning. The characterisation of the solid electrolyte revealed a non-homogeneous structural composition, which caused a variation in electrical resistivity, mass density and Young's modulus. A direct effect of a strong variation in resistivity was a strong variability in thickness and shape of deposited Ag. This variability in Ag deposition made accurate predictions of Ag deposited tuning difficult. However, analytical modelling was able to predict the trend of Ag deposited tuning.

The characterisation of Ag deposition found Ag with non-uniform thickness and irregular shapes. Most interesting was the observation of Ag growth along scratches in the electrolyte. This means it may be possibly to pholithograhically pattern the solid electrolyte in future. Patterned solid electrolyte would reduce the amount of solid electrolyte on the resonator, which would considerably reduce damping and increase the Q-factor. Photolithographic patterning would also reduce partial resonator coverage with Ag and Al, mainly a result of the coarse alignment of shadow masks used to integrate the Ag deposition scheme with MEMS resonators. Coverage of bridge resonators with Ag and Al due to misalignment caused a variability in resonant frequency by 7%.

The analysis of Ag deposited tuning found a dynamically in-situ, location dependent and bidirectional frequency change in polysilicon bridges (-6.3% to +10.7%) with an impressive 200 nW of power consumption. The mechanical Q-factor decreased with progressing Ag.

From the current characterisation work carried out it can be concluded that the Ag deposition scheme is not immediately applicable to micromechanical filters and oscillators. The observed frequency variability and substantial Q-factor reduction (46%) would degrade the performance of micromechanical resonator in oscillators and bandpass filters, which then do not meet the bandwidth and noise requirements in wireless transceivers.

The use of shadow masks needs to be engineered to reduce misalignment, frequency variability and damping. Other tuning methods by comparison showed no or some reduction in Q [1, 16]. However, data on tuning repeatability was not reported by other researchers. To improve the repeatability in Ag deposited tuning, the structural composition of the solid electrolyte must be improved to produce layers with a uniform resistivity. Further, the performance of the tuning scheme would greatly benefit from

the photolithographic patterning of the Al contacts and Ag anode to avoid misalignment errors. A consequence of better alignment is that partial resonator coverage with Ag and Al would not be an issue any longer and the frequency variability is reduced. This would make this technology applicable to filters and oscillators to perform the needed low power dynamic in-situ frequency tuning. The Q-factor of a resonator is further increased if the solid electrolyte on the polysilicon bridge is lithographically patterned or even omitted using alternative tuning arrangements. One arrangement is the deposition of Ag on the anchors of the resonator, which has been proposed by other researcher, but so far (to the authors knowledge) not been practically demonstrated [72].

It should be noted at this point that the solid electrolyte and the Ag deposition at Arizona State University used a non-optimised thermal evaporation type process that was inherently non-uniform with significant variation from run to run. In addition, the shadow mask alignment was extremely difficult and coarse and could be easily improved to reduce the degree of misalignment. Hence, many of the issues arising from the work reported in this chapter can be be significantly reduced by relatively simple means.

In conclusion, the presented Ag deposited tuning method needs substantial performance improvement in terms of electrolyte composition, repeatability and Q-factor. However, the concept of Ag deposited tuning is worth pursuing, because the presented technology provides low power, dynamic in-situ frequency tuning of MEMS resonators.

Chapter 9

Conclusions and Future work

This chapter summarises and reviews the results of this thesis. Major conclusions are made and future work is addressed.

9.1 Conclusions

This thesis has evaluated technologies to provide low cost high yield fabrication and low power non-destructive tuning of micromechanical resonators. It has presented characterisation results of a CMP based polishing process and deposition methods for FIB Pt and electrochemical Ag frequency tuning. This chapter briefly addresses the conclusions of the results presented, discusses the implications of this research for future low power communication equipment and suggests future work.

9.1.1 Characterisation of a CMP based polishing process

Chapter 4 demonstrated and characterised a novel CMP based polishing process to simplify resonator fabrication and reduce device impedance. The characterisation of this process involved CMP polishing experiments, which found that relatively thick polysilicon can be successfully polished with a sufficiently high removal rate. This was important, because MEMS in contrast to semiconductor manufacturing, uses thicker layers to produce devices with the required performance. The CMP removal characteristics in this work agreed with those found for semiconductor processing [119]. That is, the CMP removal rate is strongly dependent on the pattern density present on the test wafers. From these results the conclusion was made, that a uniform CMP polishing rate and a sufficiently high device yield is achieved for MEMS test chip designs, which have an equal pattern density.

After CMP polysilicon polishing tests were completed, wet chemical removal of 100nm thick sacrificial gap SiO_2 was performed to investigate the DRIE sidewall profile of the planarised silicon test structures. SEM images showed a sidewall profile with scalloping. Scalloping reduces the effective total electrode-to-resonator area in micromechanical resonators and therefore increases their impedance. Further, it increases the surface roughness and is likely to have an impact on the Q-factor of fabricated resonators. A solution to the problem is hydrogen annealing of the resonator structures after DRIE etching, which smoothes the surface of Si structures [65]. Hydrogen annealing is a available in standard LPCVD reactors and can be combined with one of the stress annealing steps within the resonator fabrication flow. Another alternative is to use a recently developed scallop free DRIE process [75].

The CMP resonator fabrication process, which has been presented, is not limited to one polishing step and can be extended. For example, a first CMP stage can be used to reduce the roughness of the resonator surface and a second one to planarise the electrodes. The advantage of the first polishing stage is a reduction in resonator surface roughness, which reduces internal damping and increases the Q-factor. Apart from the fabrication of resonators, CMP can also be employed to produce multilayer MEMS structures, micromirrors [116] and was lately used for MEMS and CMOS integration [68].

9.1.2 Fabrication and characterisation of MEMS resonators

Chapter 5 and Chapter 6 demonstrated the successful fabrication of polysilicon micromechanical cantilever and bridge test resonators, which were used for the characterisation of Focused Ion Beam (FIB) platinum (Pt) (see Ch. 7) and electrochemical silver (Ag) (see Ch. 8) deposited frequency tuning. These resonators were first characterised using SEM, frequency and deflection measurements before they were employed for tuning. SEM images and frequency measurements showed that these fabricated test resonators were fully released and functional. The analysis of frequency measurements with FEM simulations found biaxial stress in the polysilicon resonators. Sources of the stress were a change in polysilicon deposition temperature and heavy phosphorus doping. The latter reduced the Young's modulus of polysilicon test resonators and confirmed findings made by other researchers [66].

The reason to minimise biaxial stress in polysilicon is to prevent buckling, which in extreme cases can result in permanent attachment of the resonators to the underlying substrate. This would considerably reduce device yield and increase cost. In this work, biaxial stress was reduced by the optimisation of the polysilicon deposition process (Appendix B). Low stress polysilicon resonators produced from a second test chip showed little or no buckling, which was achieved using a tensile polysilicon film to start with and subsequent phosphorus doping. In principle, biaxial stress can be further reduced by matching the phosphorus doping concentration in the polysilicon to the desired biaxial stress (Appendix B).

During the frequency measurements it was found, that the measured resonant frequencies of polysilicon resonators changed with time. A possible cause of this frequency variation was stress relief in glue, which was used to attach the resonator sample to a

copper carrier plate. This effect was discovered at the very end of this project and is future work.

9.1.3 Characterisation of frequency tuning by FIB platinum deposition

Chapter 7 successfully demonstrated and characterised FIB Pt deposited tuning of micromechanical 3C SiC and polysilicon cantilever beam and bridge test resonators. Note, that Pt deposited tuning was performed on resonators with typical resonant frequencies in the kHz range as opposed to MHz and GHz, which are used in wireless low power transceivers. These rather low frequency resonators were chosen for three reasons: (i) these devices are relatively quickly to fabricate, (ii): they are simple test structures and relatively easy to analyse and (iii) their low resonant frequency reduces the requirements on measurement equipment to demonstrate and characterise the technology of selective Pt deposited tuning.

Selective Pt deposition at tips of polysilicon and 3C SiC cantilevers and middle sections of bridge resonators changed the resonant frequency by up to -15.6% as a result of an increase in equivalent mass. FEM simulations and analytical modelling predicted and explained this so called "mass tuning" effect. Theoretically Pt deposition can also be used to increase the equivalent stiffness and consequently the resonant frequency of test resonators. This so called "stiffness tuning" effect is future work.

Compared to other tuning methods, such as laser trimming [1], relatively large frequency changes were achieved without causing any device failure. The latter characteristic of this tuning method is essential, because it increases the yield and reduces cost of fabricated micromechanical resonators. In addition, the wide tuning range is beneficial in cases of biaxial stress in bridge resonators (Ch. 6), to compensate for the large changes in resonant frequency.

Surface profiler scans found tuned resonators with up to 57% thicker Pt deposits than expected. The reason for this discrepancy was the widening of the FIB beam aperture, which resulted in a higher FIB Ga^+ ion beam current and thicker deposits. Despite thicker Pt deposits, the measured change in resonant frequency was lower than predicted by FEM simulations and analytical modelling. The reason for the difference in tuning was a lower mass density of the FIB deposited Pt compared to the bulk value,

which was used for the initial calculations. The difference in mass density was explained by enclosure of organometallic material inside the deposited platinum and a variation in Ga^+ ion beam current density. The former not only changes physical but also electrical properties of the deposited films [115]. The large variation in deposited FIB Pt thickness over the life time of the FIB machine makes accurate tuning of RF filters difficult and needs to be avoided. However, this is no longer an issue, when the resonant frequency is tuned in real time (see Sec. 9.2.3).

Far more critical than a variation in deposited Pt thickness was a reduction in the Q-factor (74%) of SiC and polysilicon resonators over time due to thermoelastic damping in deposited surface contaminants and Pt. The source of surface contamination was deposited wax, which was used to mount resonator samples onto a piezoelectric disk for vibration actuation. The presence of deposited of wax was evident through a reduction in resonant frequency of SiC and polysilicon reference cantilevers after each measurement session. It was found that the deposited wax markedly decreased the Q-factor (60%) of resonators compared to the FIB deposited Pt. In any case, a strong reduction in the Q-factor of micromechanical resonators after FIB Pt deposited tuning is not acceptable, because it severely influences the frequency selectivity of RF filters and consequently degrades the signal quality in wireless transceivers (Ch. 2).

It should be be noted at this point, that the deposited wax is not not a fundamental issue of this tuning technology and can be easily avoided by resonator vacuum packaging after FIB tuning and electrostatic vibration actuation and sensing. The latter would also reduce the observed variability in measured bridge resonant frequency and Q-factor. This variability, as observed in Chapter 6, was believed to be a result of stress relief in glue, which was used to attach resonator samples to a copper carrier plates in order to perform vibration measurements. Deposited wax is no longer an issue for electrostatic actuated resonators, since a piezoelectric disk is not required to perform frequency measurements.

Characteristics of FIB Pt tuned bridge resonators presented in this thesis are already sufficient for Low Frequency (LF) filters and reference oscillators in wristwatches, where devices with lower resonant frequencies and moderate Q-factors are used [143, 89]. Other areas of interest for FIB Pt deposition include frequency tuning and calibration of gyroscopes and ultra-sensitive mass sensors [35, 10].

9.1.4 Characterisation of frequency tuning by silver deposition

Chapter 8 successfully demonstrated low power and real time electrochemical deposited tuning of micromechanical polysilicon bridge resonators. This Ag deposited tuning technology was demonstrated on simple low frequency test resonators for reasons highlighted in the previous section. Frequency measurements before and after Ag deposition found location dependent bidirectional tuning (-10% to +10.7%).

The trend of this location dependent tuning process was analysed and predicted by analytical modelling. Experimental results and analytical modelling did not match, because of the non-uniform deposited Ag thickness along bridge resonators and compressive biaxial stress in the polysilicon (Ch. 6), which was not accounted for in the model. However, analytical modelling gave a valuable insight into the dynamic behaviour of the Ag deposited resonators.

Relatively long times of up to 36 minutes were required to achieve full Ag coverage of polysilicon bridge resonators using a 2V DC bias. This is not a fundamental problem of the tuning technology, since a higher Ag concentration in the solid electrolyte and larger DC bias voltages enable the deposition of more Ag in a shorter time [110]. Ag deposition tests need to be performed with different DC bias and solid electrolyte configurations to find an optimum for Ag deposited tuning of micromechanical resonators (see Sec. 9.2.4).

The integration of the Ag deposition scheme with polysilicon resonators using shadow masks needs improvement. Shadow masks were used in this work to prevent contamination of the University of Edinburgh micromachining facilities with Ag. The manual alignment of these metal masks caused partial coverage of the resonators with Ag anodes and Al contacts. This resulted in a frequency variability of 7% between different resonators after shadow mask alignment. The detected variability in resonant frequency needs to avoided to ensure that all resonators in a filter or oscillator deliver the same performance. Misalignment and frequency variability can be prevented using photolithographic patterning and subsequent etching to define the Ag anode and Al contacts. This eliminates the overlay of the resonator with Ag and Al and increases the repeatability of Ag deposited tuning. An immediate improvement is achieved using DRIE micromachined shadow masks [76].

Ag deposition was observed along scratches in the solid electrolyte, which opens the possibility of applying standard photolithography and subsequent etching to define

lines of electrolyte on the resonator structure or alternatively on its supports. Photolithographic patterning reduces or even eliminates the amount of electrolyte on the bridge resonators and decreases thermoelastic damping. Lower damping translates into a higher Q-factor for the resonators.

Ag deposition along defined lines of solid electrolyte increases the repeatability for Ag deposited tuning. The placement of solid electrolyte lines and subsequent Ag deposition along these lines is particularly attractive on the anchor regions of the bridge resonator. In this case, no solid electrolyte or Ag is being deposited on the resonator structure itself, which further reduces the damping and maintains a higher Q-factor. This would help to prevent the strong decreases in the Q-factor by more than 46% that was observed on polysilicon bridge resonators after Ag deposition. Such a decrease is not acceptable for RF filters or oscillators, which require a high Q-factor to provide power saving and robustness against interferences in wireless communication equipment.

The repeatability of the Ag deposited tuning can be further improved by the optimisation of the solid electrolyte composition. Electrical and mechanical measurements on test structures found that the solid electrolyte shows a strong variability in its mechanical and electrical properties, which both contribute to the low repeatability of Ag deposited tuning that was observed in deposition tests and tuning experiments. In this work, only a small number of samples were tuned with different DC bias voltages and therefore no final conclusion can be made about the influence of the non-homogeneous electrolyte composition on the Ag deposited tuning. In any case, RF filters require a tuning scheme with a high repeatability and hence electrolyte composition needs substantial improvement.

The impact of this technology, once optimised in terms of Q-factor and electrolyte composition, to the field of micromechanical resonator research and society is tremendous. This method is the first published (to the authors knowledge), which offers real time low power (200nW as opposed to 10mW) frequency tuning of micromechanical resonators using low voltages (<5V) [51]. This makes this method particular attractive to low power electronics with limited battery capacity such as mobile phones and wristwatches. In addition, it also offers the opportunity to tune the resonant frequency in response to changes in ambient temperature and pressure throughout the lifetime of the resonator, using substantially less power than any other method published. At the

same time, this method makes power consuming methods such micro oven control or thermal tuning methods redundant [88].

This technology is not only bound to micromechanical resonator frequency correction, it can also find application in sensors to detect the level of Ultra Violet (UV) exposure of photoresist inside a wafer scanner. Remember that the solid electrolyte is doped with Ag by means of UV photodissolution and its resistance changes depending on the UV level. Solid electrolyte incorporated in these sensors would allow the UV exposure of photoresist to be measured during photolithography without the need for time consuming experiments.

9.2 Future work

In the course of the fabrication and tuning of micromechanical resonators, this research has identified many items that need further investigation. These are described in the following sections.

9.2.1 Characterisation of a CMP based polishing process

Part of this PhD project was to decrease the impedance of capacitive actuated resonators using the presented CMP polishing based process and novel device designs. Various novel resonator and filter designs were included in a test chip layout and were presented in Appendix C. Due to time constraints, the designed test chip was not fabricated as part of this work. Hence, fabrication and testing is planned for future work.

One of the critical paths during fabrication of these resonators is the wet chemical removal of the nanometer thick SiO_2 in the transducer gaps. The thinner the gap width between the transducer electrodes and resonators, the slower is the etch process to remove the nanometer wide sacrificial SiO_2. Etching at alleviated temperatures and the use of agitation might help to reduce the time required to remove the SiO_2 in nanometer scale capacitive gaps.

An alternative approach is to use internal electrostatic actuation by filling the transducer gaps with high-k dielectrics (eg. TiO_2) as shown in Fig. 9.1. These dielectrics have a higher permittivity than air and therefore decrease the impedance substantially [7]. This would make wet chemical etching of nanometer thin gaps redundant,

simplify fabrication and therefore reduce cost. In addition, unwanted collection of particles inside the transducer gaps would not be an issue and resonators are less affected by mechanical shock [70]. However, CMP polishing and selectivity between polysilicon and those dielectrics would have to be characterised.

Using either air or dielectric filled transducer gaps, process recipes for the DRIE etch process need to be optimised to reduce the resonator sidewall scalloping. Straight sidewalls are required in capacitive transducer gaps to maximise the resonator-to-electrode area and to provide resonators with low impedances. An alternative way to reduce scalloping is to combine standard DRIE etching and subsequent hydrogen annealing to smoothen the sidewall roughness [65]. Both methods are available in standard semiconductor processing facilities. Another alternative is to use a scallop free DRIE process [75].

9.2.2 Fabrication and characterisation of MEMS resonators

Biaxial stress in polysilicon MEMS resonators has room for further reduction. Biaxial stress in doped polysilicon can be minimised by a reduction in phosphorus concentration, while in undoped polysilicon resonators stress can be further reduced by a change in deposition temperature (Fig. B.4). A decrease in biaxial stress causes smaller frequency changes and buckling in polysilicon bridge resonators.

In this work, the measured resonant frequency of polysilicon bridge resonators was subject to large variations believed to be due to stress relief in glue, which was used to attach the resonator samples to a copper carrier plate. However, this effect was discovered at the very end of this PhD project and needs further investigation. To analyse this effect, one sample of polysilicon bridge resonators is glued to an aluminium and another to a copper carrier plate. Both plates are heated using a soldering iron and the resonant frequency of bridges is recorded over time. The use of different carrier plate materials with distinct thermal expansion coefficients will determine whether the plate material or the glue causes the observed frequency variations over time. In case experiments confirm glue being the cause for the observed frequency variations, further experiments can be carried out with hot and cool carrier plates to quantify the effect of stress relief in the glue.

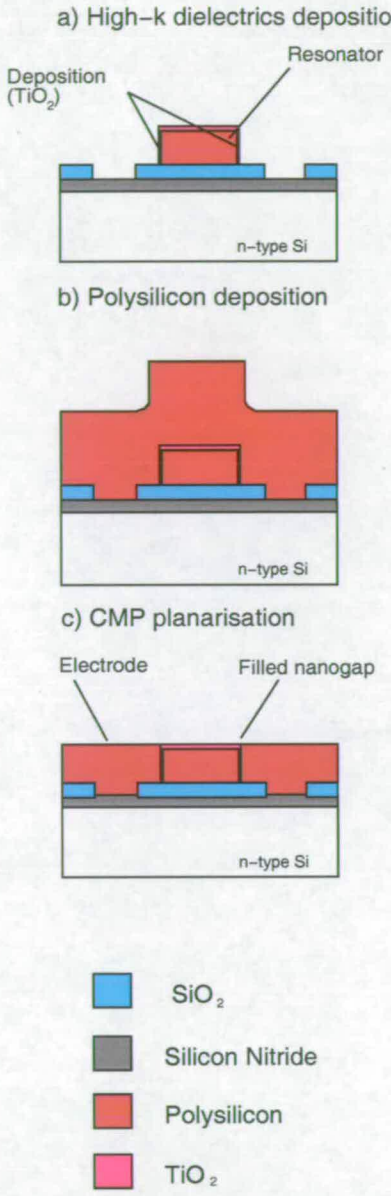

Figure 9.1. CMP fabrication of MEMS resonators with internal electrostatic actuation. High-k dielectrics have a higher permittivity than air and substantially increase the electromechanical coupling in capacitive transducer gaps with the effect of lowering the resonator impedances. The application of these high-k dielectrics in ultra thin transducer gaps dramatically reduces the impedance of micromechanical resonators. This makes the wet chemical etching of sacrificial material in nanometer gaps redundant, simplifies fabrication and reduces cost.

9.2.3 Characterisation of frequency tuning by FIB platinum deposition

In Chapter 7 it was found, that deposited Pt located at tips of cantilevers and middle section of bridges caused an increase in their equivalent mass and consequently reduced their resonant frequencies. Frequency tuning produced by an alteration of equivalent stiffness has not been demonstrated yet and is future work. To demonstrate this "stiffness tuning" effect, Pt is selectively deposited at the clamped end of cantilevers and bridges. Deposited Pt at these locations increases the equivalent stiffness and frequency of resonators. FIB Pt deposition on the anchors would provide another way of FIB tuning and should be exploited [72]. Special attention should be paid to the FIB tuning of resonators using smaller Pt amounts. These Pt deposits cause smaller changes in frequency and improve the tuning accuracy, which is required for RF filters with bandwidths as small as 0.06% [84]. The advantage of smaller Pt volumes is less thermoelastic damping, which preserves a high resonator Q-factor. As an alternative, tungsten (W) should be considered for FIB deposited tuning of micromechanical resonators. Tungsten has a higher Young's modulus and density than Pt. Therefore, smaller amounts of W compared to Pt would be required to achieve the the same change in resonant frequency. This would reduce the FIB deposition time and operation costs.

Once Pt or W is deposited, the influence of the temperature on the tuned resonant frequency needs to be characterised. This is essential, when FIB Pt or W tuned resonators are used as RF filters or oscillators inside wireless transceivers. These devices require a stable resonant frequency with temperature. However, drift of resonant frequency with temperature is not an issue thanks to developed compensation schemes developed by other researchers [48]. In addition, the long term stability (aging) of this FIB tuning method needs to be characterised.

The possibility of Pt and W being deposited on both ends of bridges rather than in the centre of the bridge should be investigated to further reduce damping. This would enable a symmetrical rather than an asymmetrical loading of the resonator during vibration and has, in the case of laser trimming, preserved the Q-factor [1].

To transfer the presented FIB tuning method to frequencies found in wireless transceivers, high-Q capacitive transduced disk resonators need to be used (Fig. 9.2). These resonators, when employed in RF filters or oscillators require frequency tuning with an accuracy of up to 0.03% [84]. To make such accurate changes in frequency real time

tuning is required. Real time tuning entails FIB selective Pt/W deposition during resonator actuation (Fig. 9.2). The resonant frequency is constantly monitored through a network analyser and Pt/W is deposited until devices operate at their desired resonant frequency. This would reduce excessive FIB Ga^+ ion exposure of the resonators, improve the accuracy of FIB deposited tuning and reduce the impact on the Q-factor. The observed variation in deposited Pt thickness would no longer be an issue.

9.2.4 Characterisation of frequency tuning by silver deposition

One of the consequences of the research work carried out on the electrochemical Ag deposited tuning scheme is that the composition of the solid electrolyte needs improvement. A homogeneous solid electrolyte composition ensures equal Ag deposition for a given DC voltage on all beam resonators. This is a basic requirement for resonators used as filters in transceivers, where a specified tuning characteristic has to be ensured. Another requirement is low damping and a high-Q-factor of trimmed devices. Hence, the influence of the solid electrolyte and Ag deposits on the Q-factor of resonators requires further investigation. Once the solid electrolyte is homogeneous in its composition, the electrodeposition can be characterised in dependence of voltage, Ag ion content and surface roughness of the underlying polysilicon.

The stability of Ag tuned resonators needs investigation in dependence of temperature. A low temperature coefficient in micromechanical resonators is required to ensure a stable resonant frequency despite changes in ambient temperature [48]. The change in resonant frequency with temperature is not an issue in Ag deposited resonators, since any change in frequency can be corrected by additional depositions throughout the lifetime of the device. This is one of the most attractive properties of this technology and should be further exploited.

Further improvement can be achieved by the photolithographic patterning of the solid electrolyte, Ag anode and Al contacts. Patterning reduces the misalignment of Ag anode and Al contacts and therefore increases the repeatability of frequency tuning. Electrodeposition tests along patterned solid electrolyte lines are of interest, since they reduce the amount of solid electrolyte on the bridge resonators and provide guidance for the deposited Ag. Additionally, Ag deposition onto resonator anchors should be

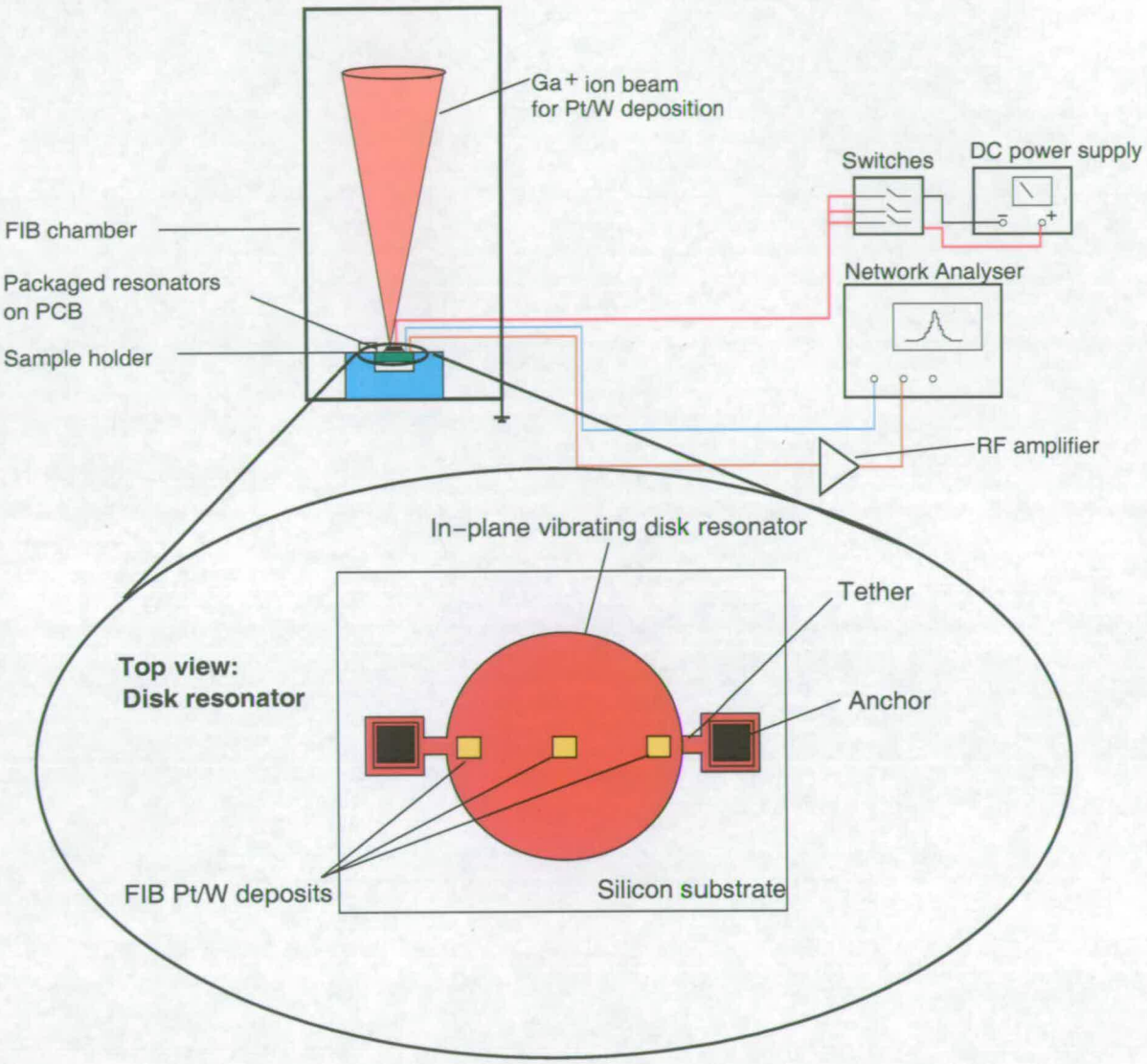

Figure 9.2. Real time FIB Pt/W deposited frequency tuning. Pt or W is selectively deposited onto high-Q in-plane vibrating micromechanical disk resonators during actuation. This improves the accuracy of achievable frequency changes and avoids possible frequency variability, arising from from a variation in FIB deposition rate over time. Note, input and output electrodes located at the perimeter of the disk resonator are omitted from the schematic for clarity.

explored as an alternative way of tuning [72]. Once the Ag deposition scheme is optimised in terms of Q-factor and repeatability, Ag deposited tuning can be transfered to resonators with higher operating frequencies, such as disks. Fig. 9.3 shows a possible example of Ag deposited tuning of disk resonators along photolithographically patterned solid electrolyte.

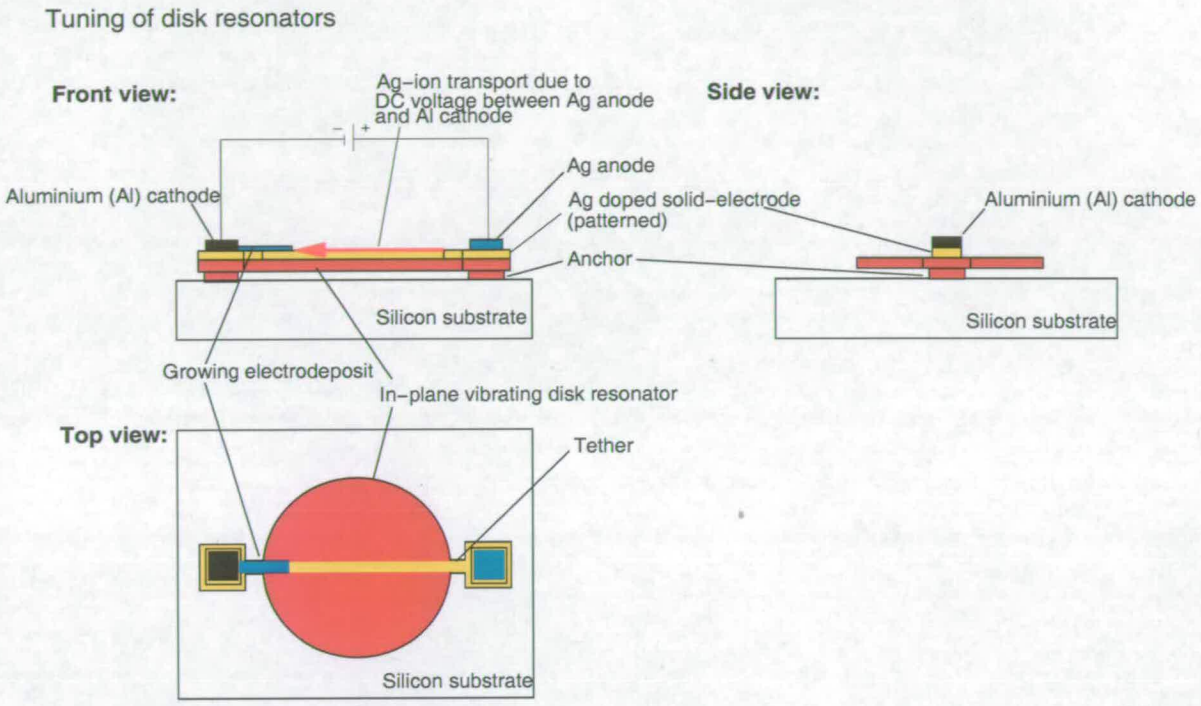

Figure 9.3. Possible arrangement for Ag deposited tuning of a micromechanical disk resonator. Photolithographically patterned and etched Ag anode, Al contacts and solid electrolyte provide repeatable frequency tuning. Ag deposits form at the Al cathode and progress along the patterned solid electrolyte onto an in-plane vibrating micromechanical disk resonator, altering the resonant frequency with time. Note, input and output electrodes located at the perimeter of the disk resonator are omitted from the schematic for clarity.

In theory, Ag electrodeposition is reversible. This has not been demonstrated yet and is another field of interest for further research. The reversibility could become useful if the frequency were to change after initial tuning as a result of changes in ambient humidity or temperature. This would substantially improve the long term stability of resonators. Resonator lifetime is another field of interest, which needs to be investigated before this technology is mature enough to be used in communication systems.

9.3 Final conclusions

The work presented in this thesis has demonstrated a CMP based polishing process, FIB Pt and electrochemical Ag deposition to provide a fabrication and tuning platform for micromechanical resonators. Previously, the applicability of micromechanical resonators as filters and oscillators in wireless communication equipment was hindered by their relatively high fabrication cost and impedance. In addition, available post-fabrication tuning methods were often accurate enough to cause the required frequency changes, but tended to cause the resonator devices failure and used relatively high power and tuning voltages. In contrast, a CMP polysilicon polishing demonstrated a low cost fabrication platform for micromechanical resonators with a reduced number of processing steps. In comparison to a recently published CMP method [100], the polishing process presented in this work increases the device yield by including a polishing stop layer, and tends not to cause transducer gap widening as a result of photoresist tapering, which can severely increase device impedance.

FIB Pt and electrochemical Ag deposition provided frequency tuning of micromechanical resonators without any device failure and with considerably lower power consumption than any other previously demonstrated methods. This increases the yield of fabricated resonators, reduces the power consumption and cost of future wireless communication equipment.

The study of the two tuning methods using micromechanical beam resonators gave a valuable insight into their characteristics, provided a basis for further research and helped to provide useful technologies for future communication equipment.

Appendix A

Measurement methods and equipment

This part of the thesis describes different measurement methods and equipment used for the development and charcaterisation of a polysilicon surface micromachining processes and Ag deposited tuning.

A.1 Measurement methods for fabrication processes

This section reviews physical, optical and mechnaical measurements methods used for the charcaterisation of a polysilicon surface micromachining and CMP planarisation process.

A.1.1 Physical measurements

One of the simplest physical measurements involves the patterning and subsequent etching of a thin film to be measured. The film thickness is then measured by moving a needle stylus over the generated steps (see Fig. A.1).

Commercially available stylus profiler can measure step heights down to 10nm. More advanced instrumentation such as Atomic Force Microscope (AFM) can detect step heights down to 1Å [9]. These instruments can not only the thickness of a film, but also surface roughness and grain sizes. AFM measurements are obtained by the measurement of the force on a sharp tip created by the proximity to the surface of the sample. When the stylus is moved it follows the surface contours of a sample. This enables to create a surface map of a small area of a deposited film or substrate.

Other physical measurement techniques for measuring the film thickness include Scanning Electron Microscope (SEM) or high resolution Transmission Electron Microscope (TEM) cross-sectional images. In case of the SEM, a beam of electrons is accelerated and focused onto the sample surface using electrostatic and magnetic lenses (Fig. A.2). The incoming electrons provide energy for electrons in the sample, allowing them to be emitted from the surface. The image is obtained from these so called secondary electrons, which are collected by a detector. If the incoming beam is rastered in the XY direction, an image from the the region of interest can be obtained [90].

The TEM, detects electrons passing through the sample. The image from a TEM comes from the transmitted electrons after they pass through the sample and impinge on a phosphor screen [97]. Feature sizes down to the 0.2 nm can be extracted using the cross sectional techniques. However, time consuming sample preparation makes this technique only suited for small number of specimen and is therefore notused in a production environment.

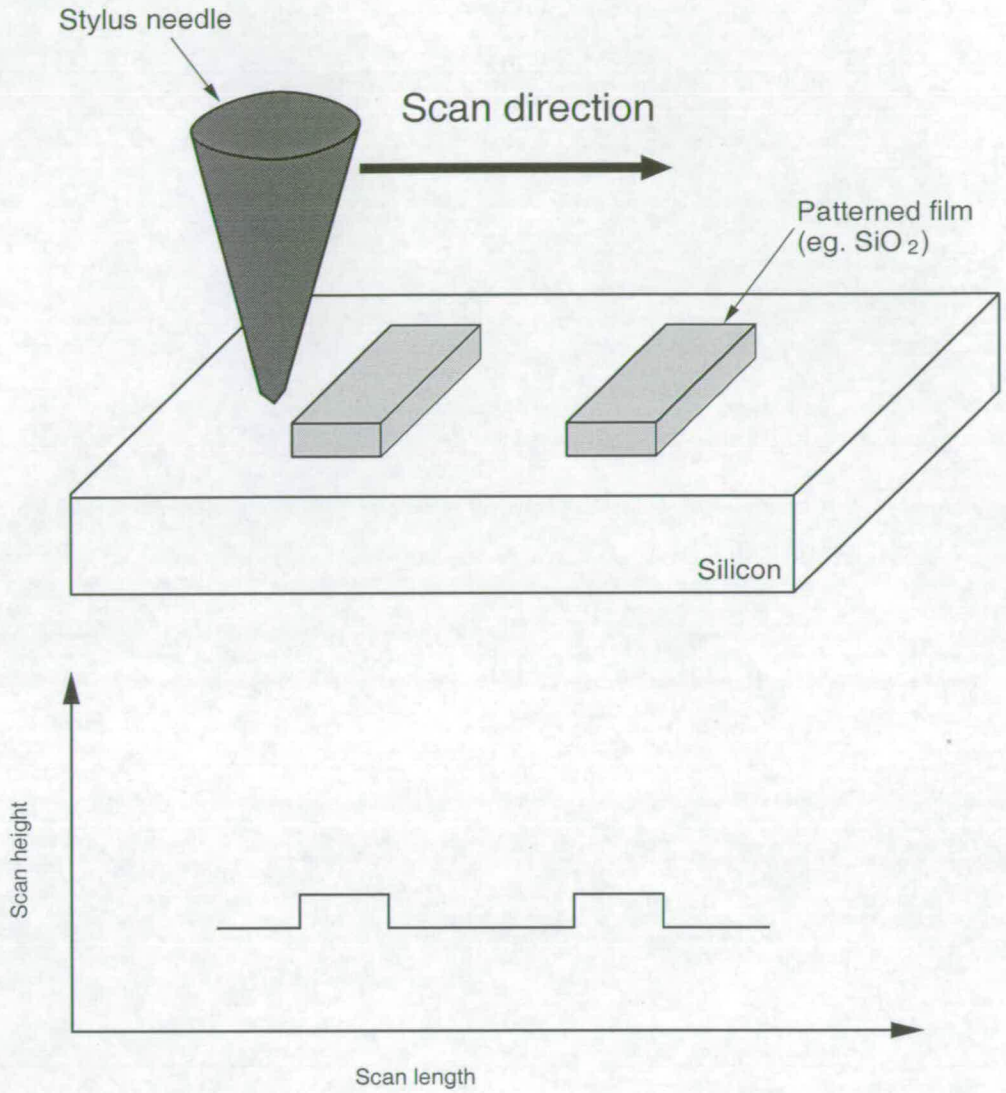

Figure A.1. Principle of a stylus profiler. Measurement of film thickness by scanning a needle stylus over a generated film pattern.

A.1.2 Optical measurements

Optical measurement techniques are widely used to measure film thicknesses and lateral dimensions. One of the simplest ways to measure the film thickness of LPCVD silicon dioxide (SiO_2), silicon nitride (Si_3N_4) and polycrystalline silicon films on a reflective substrate is by the human eye under flourescensic daylight using colour charts. This technique is based on the principle that if white light is used to illuminate a thin transparent dielectric film on a reflective substrate, destructive interference will occur

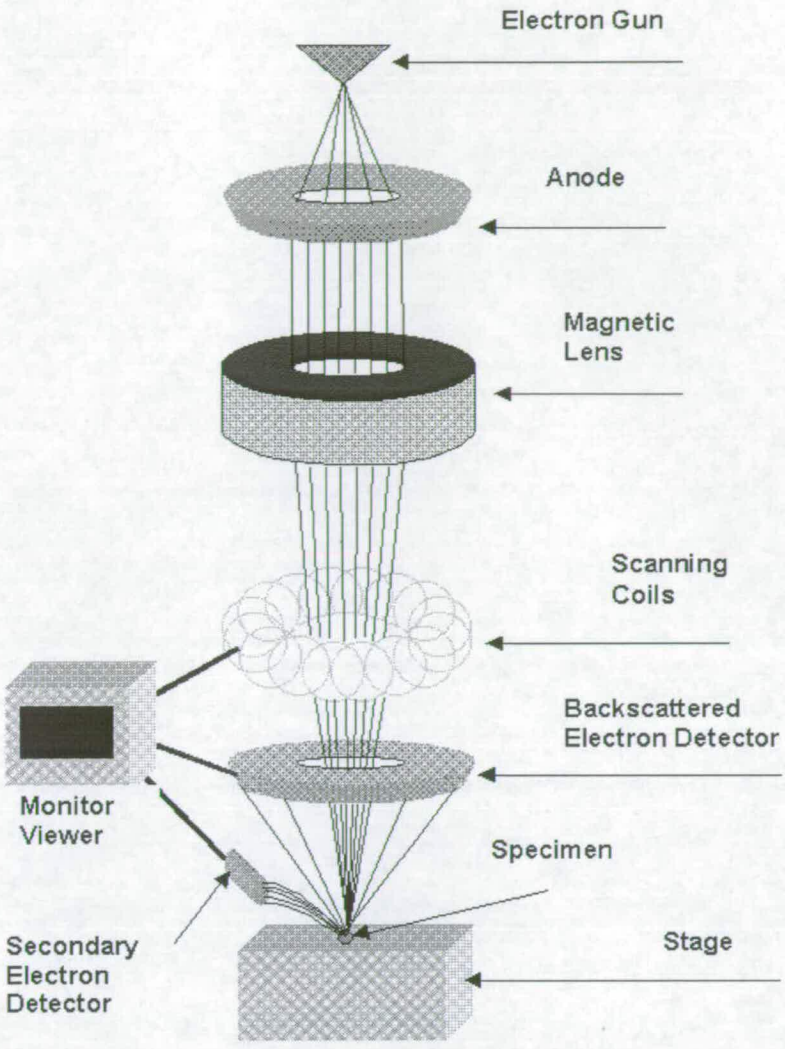

Figure A.2. Schematic of a Scanning Electron Microscope (SEM). A high energy electron beam is accelerated and focused onto the sample. An image is obtained from the collected secondary electrons emitted by the high energy electron beam. (Picture courtesy: Rensselaer Polytechnic Institute (RPI) [107])

for some wavelengths in the reflected light, giving it a characteristic colour. The observed colours repeat every 200nm for Si_3N_4 and every 300nm for SiO_2. The human eye is remarkably good in distinguishing colour and an estimate of thickness within 10-20nm can be made using these charts. However, SiO_2 below 500nm has no colour and other instrumentation has to be employed to measure the thicknesses of thinner dielectric films.

One method to measure the thickness thin films is to use a spectrophotometer. A spectrophotometere illuminates a transparent dielectric film, deposited on a reflective surface, with monochromatic light of a single wavelength λ at an angle ϕ (Fig. A.3) [97].

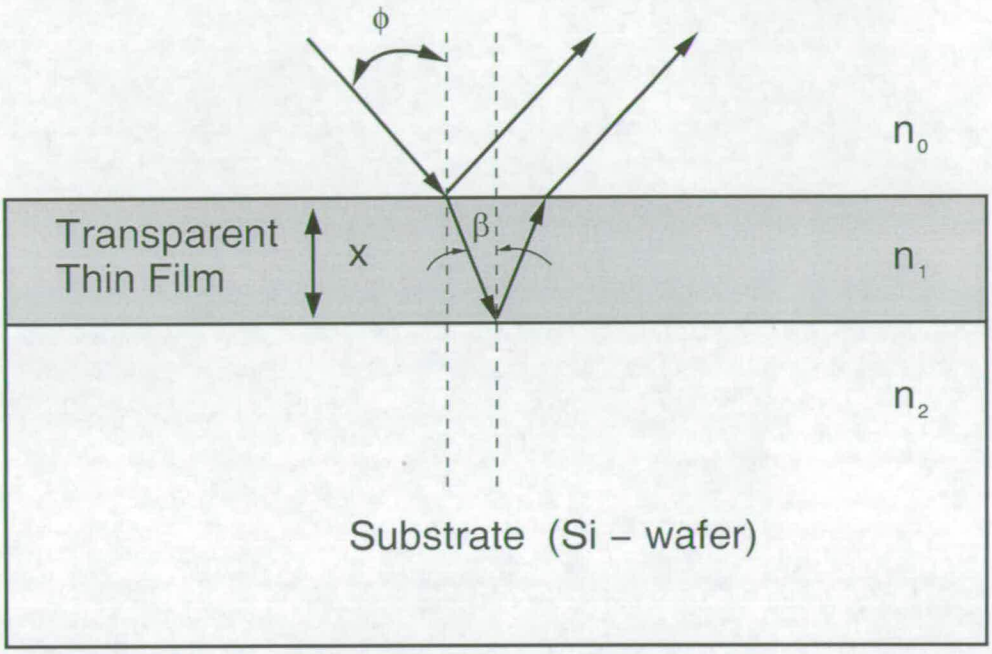

Figure A.3. Measurement of transparent dielectric films using a spectrophotometer. Light reflection from a sample with a transparent thin film on its surface. n_0 is the index of refraction of air (1.0), n_1 is the index of refraction of thin dielectric film and n_2 is the index of refraction of the substrate. ϕ is the angle of the incident light, β is the angle of the reflecting light at the bottom interface.

Reflection of the light occurs at the top and bottom layer of the film to be measured and return to two light waves. For some wavelengths λ, these two reflected waves are in phase andadd; for other λ, destructive interference occurs. The reflected intensities forms maxima and minima as λ is varied. Maxima and minima occur for example in photoresist at values of λ given by:

$$\lambda_{min,max} = \frac{2n_1 x_0 \cos\beta}{m}, \tag{A.1}$$

where

$$\beta = \sin^{-1}\left[\frac{n_0 \sin\phi}{n_1}\right] \tag{A.2}$$

and $m = 1, 2, 3...$ for maxima and $1/2, 3/2, 5/2, ...$ for minima. In practise, λ is swept with at a constant ϕ. The dielectric film thickness can then be determined by fitting the reflected light intensityto Eq. (A.1).

One condition to use this technique is that the refractive index of the dielectric film must be known. This techniques works reliable for film thicknesses greater than a few tens of nm. For thinner films it is difficult to detect the first interefence minimum unless very short wavelength are used.

For thinner layers, as in gate oxides ($<$ 10nm) in Metal Oxide Semiconductor (MOS) structures, the n_1 varies with process conditions and the thickness can not be determined precisely. In this case, ellipsometry is the better alternative to measure the film thickness. An ellipsometer uses polarised light measures the change in polarisation of the reflected light from the dielectric/substrate surface. The change in polarisation depends on the film thickness and index of refraction. Conditions for the measurements is that the film is transparent for wavelengths being used and the properties of the substrate are known. Ellipsometry is very versatile and is able to measure stacks of several layers with different dielectric properties. Commercial available ellipsometer are able to measure thickness down to 1nm.

A.1.3 Mechanical measurements

While physical and optical measurements can extract information about film thickness and make estimations about the qualitative film composition, mechanical measurements are employed to determine elastic film properties such as Young's modulus, density and stress. These parameters have an influence on the resonant frequency and of micromechanical resonators. The knowledge of elastic parameters is important to the MEMS designer in order to accurately predict the device behaviour of resonators. Excessive residual stress in movable micromechanical devices produces strong bending, which can cause failure of resonators. Therefore, stress has to be tailored to produce micromechanical resonators with a predictable device behaviour.

Stress in thin films can be divided into extrinsic and intrinsic. Extrinsic stress is caused by thermal mismatch due to different expansions coefficient between two layers during a change in temperature. Intrinsic stresses are generated during the film composition process [73]. Young's modulus and density are effected during the film deposition process. In most cases these parameters are extracted from test structures and methods,

which are refered as mechanical measurements. Mechanical measurements involve test structures and can be divided into static and dynamic tests. One of the simplest static tests is the disk method Fig. A.4.

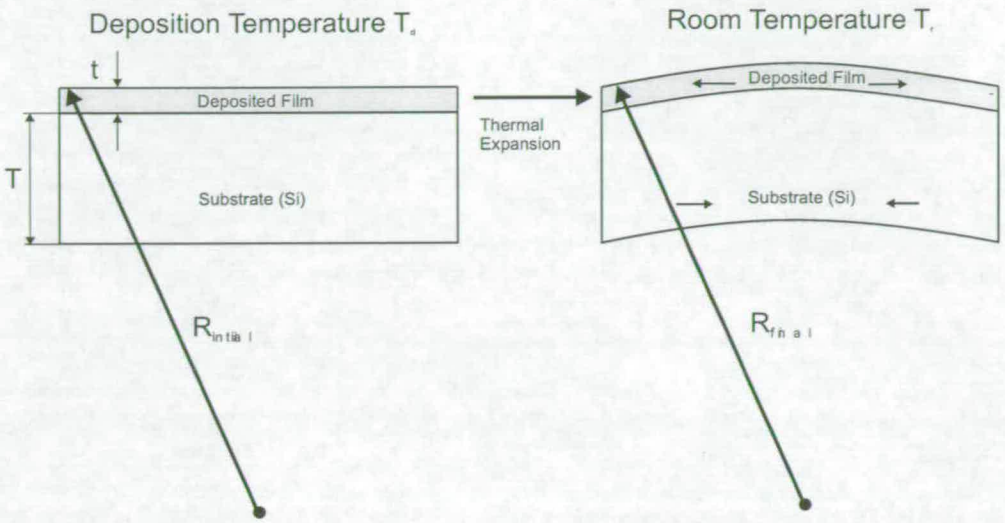

Figure A.4. Disk method. Measurement of wafer curvature R before and after deposition. Any change in R is attributed to biaxial thermal stress σ_{th} in thin films.

The disk method is based on the measurement of the deflection in the centre of the disk substrate (silicon wafer) before and after film deposition. Since any change in wafer curvature is attributed to the stress in the deposited film, stress can be calculated by measuring these changes. Stress in thin films can be found by employing the Stoney equation, relating film stress to substrate curvature [120]:

$$\sigma_{th} = \frac{1}{R} \frac{E}{(1-\nu)} \frac{T^2}{t} \tag{A.3}$$

where $1/R = 1/R_{final} - 1/R_{initial}$ is the radius of curvature of the bent silicon wafer. In practise the wafer curvature is measured before $R_{initial}$ and after R_{final} film deposition, since the wafer substrate is not flat to start with. The biaxial modulus of the silicon substrate is given by $\frac{E}{(1-\nu)}$, where E is the Young's modulus and ν the Poisson's ratio. The parameters T and t are thicknesses of the substrate and the film, respectively. Wafer curvature can be measured using a surface stylus profiler scanning across the entire wafer diameter. These measurement can only give a measure of the global stress in the film.

In order to extract intrinsic stress locally in films, micromachined test structures have to be used. Examples of these are strain gauges, spirals, fixed-fixed beams and cantilevers. Clamped-clamped beams with increasing length can be used to determine the critical buckling load and hence deduce the residual compressive stress in polycrystalline silicon films [40]. The buckling strain for clamped-clamped beams is given by:

$$\epsilon_c = \frac{F_a}{AE} = \frac{\pi^2 h^2}{3L_c^2} \tag{A.4}$$

where F_a is the axial force acting on the beam cross section A, E the Young's modulus h the thickness of the beam. Buckling of simply supported or clamped beams is only a function of the beam geometry and not material parameters.

Cantilever beams can be used to determine the stress gradient in a thin layer such as Low Pressure Chemical Vapour Deposition (LPCVD) polycrystalline silicon. The stress gradient $\sigma_{gradient}$ of a thin film can be extracted from the cantilever tip deflection $\delta_{cantilever}$ [32].

$$\sigma_{gradient} = \frac{Et\delta_{cantilever}}{L^2} \tag{A.5}$$

where E, t and L are the Young's modulus, thickness and length of the cantilever.

Apart from measuring stress, cantilevers and bridges can also be used to determine elastic properties of thin layers such as Young's modulus and Poisson's ratio [95], [132]. One common method is the so called resonant method. The resonant method is based on the fact that the resonant frequency of a resonator (cantilever or bridge) depends on device dimensions as well as on elastic properties of the resonator material such as the Young's modulus. Therefore resonant frequency is a mean to deduce the elastic properties of thin films. Other parameters such as density can also be derived from measurement of resonant frequency. This a very powerful method, since it is not destructive and can give information about the stress distribution across the die.

According to the vibration analysis of a Euler-Bernoulli beam model, the Young's modulus E and the n-th natural frequency of the bending beam vibration $(f_B)_n$ of a cantilever has the following relationship [129]:

$$E = \frac{48\pi^2 \rho L^4 (f_B)_n^2}{(\beta_n L)^4 h^2} \tag{A.6}$$

where ρ is the density, L and h the length and thickness of the cantilever, respectively. The parameter $(\beta_n\ L)$ is the constant associated with the $n-th$ flexural mode of the beam and is $\beta_1\ L\ =\ 1.875$ for the first flexural mode. Resonant frequencies can for example be measured using a optical workstation as described in Sec. 6.2.

A.2 Electrical characterisation methods

Electrical measurements are used in semiconductor research extensively, because they are non-destructive and do not require time consuming sample preparations. They extract parameters such as resistivity, capacitance, and so on. The measurement of resistivity for example provides information about the quality of the film composition and fabrication process. It also give an insight into doping levels of polysilicon, which has an effect on the oxidation rate [53]. Resistivity is an essential parameter for the MEMS engineer to make realistic device analysis possible. Resistivity of a bulk of material defines the relationship between the electric field ε and the current density J [97]

$$\zeta = \frac{\varepsilon}{J} \tag{A.7}$$

given in Ωm. Resistivity can be thought of as a resistance that would be measured between the sides of a cube (Fig. A.5). Note, that the resistivity does not depend on the size of the bulk material. If instead of a cube, the resistance were measured between the shallow edges of a square with depth x_j, the resistance would be bigger and would measure

$$R = \frac{\zeta}{x_j} \tag{A.8}$$

and is given in $\Omega/\square$. This resistance is refered as sheet resistance and identical for any square of material.

One of the most common methods of measuring the sheet resistance with the four point probe as illustrated in Fig. A.6. In order to measure the sheet resistance with the four point probe, current is forced between the outer two electrode and voltage sensed between the two inner ones. If the electrode spacing s is much smaller than the layer/wafer thickness t, then the sheet resistance can be written as follows [112]:

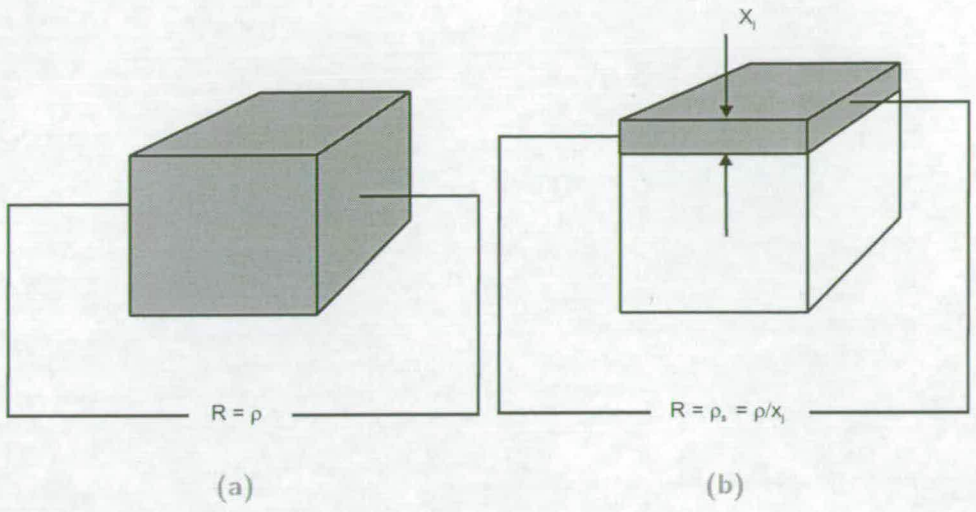

Figure A.5. Resistivity in bulk and sheet materials. Relationship between resistivity and sheet resistance. (a) Definition of bulk resistivity and (b) Definition of sheet resistance.

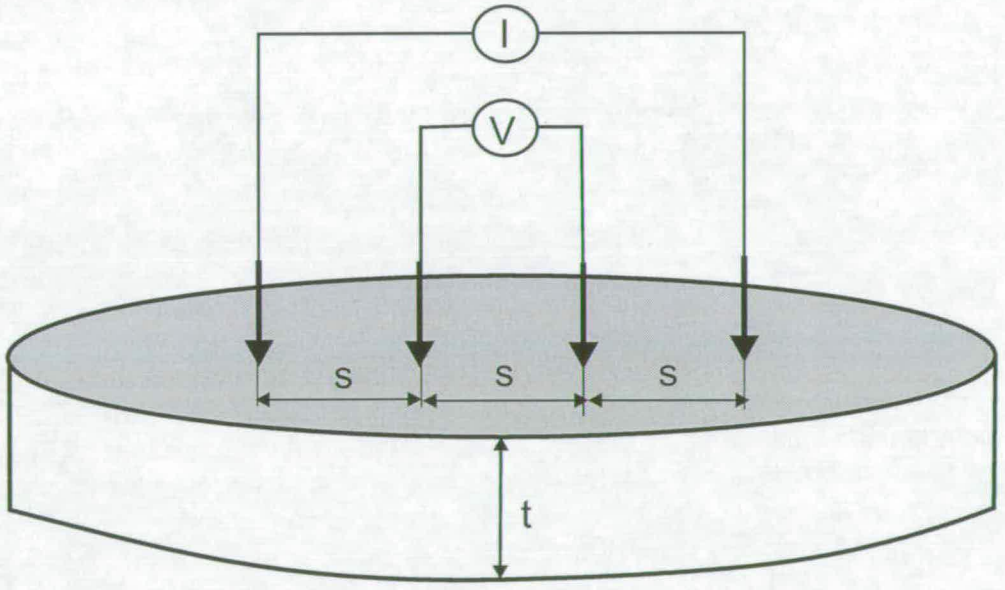

Figure A.6. Four point probe for sheet resistance measurement. During a four point probe measurement current is forced between the outer two electrodes and voltage measured between the inner two electrodes.

$$R_s = \frac{\zeta}{x_j} = \frac{\pi}{ln(2)} \frac{V}{I} = 4.532 \frac{V}{I} \tag{A.9}$$

and is given in $\Omega/\square$. In case of patterned structures, Greek cross test structure as shown in Fig. A.7 are used to extract the sheet resistance and resistivity of a conductive layer.

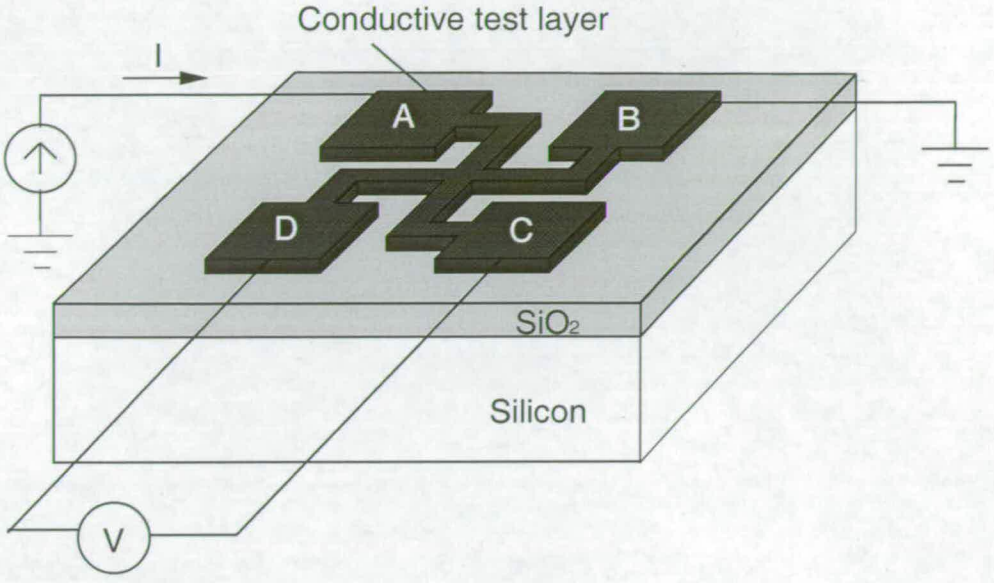

Figure A.7. Measurement of sheet resistance using a Greek cross test structure. Current is forced between pad A and B and voltage measured between pad C and D. Sheet resistance is determined using Eq. (A.13)

The sheet resistance is extracted at the heart of the cross and an accuracy of better than 0.1 % can be achieved [137]. The sheet resistance is determined by forcing a current from pad A to B and measuring the potential difference across D and C. After that the current is reversed and the potential V_{DC} is measured and the resistance extracted [13]:

$$R_{0^\circ} = \frac{V_{DC} - V_{CD}}{I_{AB} - I_{BA}}. \tag{A.10}$$

The current is then forced between B and C and the process repeated.

$$R_{90^\circ} = \frac{V_{AD} - V_{DA}}{I_{BC} - I_{CB}} \tag{A.11}$$

The average resistance of these two measurements is then calculated:

$$R = \frac{R_{0^\circ} + R_{90^\circ}}{2} \tag{A.12}$$

and the sheet resistance derived:

$$R_s = f\left(\frac{\pi R}{ln(2)}\right) \quad [\Omega/\square]. \tag{A.13}$$

where f is a correction factor related to the geometrical asymmetry of the sheet resistor. The measurement assumes layers, which are *homogeneous* in composition and uniform in film thickness, setting f to 1.

The measurement of sheet resistance gives an insight into the resistivity of the film and its composition across the die. It is therefore a measure for the quality of a thin film with a high accuracy.

Appendix B

Process development for polysilicon surface micromachining

This part of the thesis describes the process characterisation of a polysilicon surface microimachining process. Results on polysilicon layer deposition, stress optimisation and silicon dioxide etching are presented and discussed.

B.1 Introduction

Standard polysilicon surface micromachining was employed to manufacture test structures for the characterisation of FIB and Ag deposited frequency tuning. The main components of such a process (see Ch. 2) are:

- Polysilicon layer deposition and
- sacrificial layer etching.

To fabricate resonators with a high device yield, process characteristics and the interaction of the above individual processing steps must be understood.

B.2 Characterisation of polysilicon deposoition

Polysilicon is used as a structural material for the majority of structures in this thesis. Its deposition process conditions obviously influence biaxial film stress σ_{poly} and the layer thickness t across the wafer. These parameters influence the resonant frequency of micromechnaical resonators as shown in Ch. 2 and therefore have to be characterised and controlled.

The LPCVD polysilicon deposition process was investigated in terms of (i) layer thickness uniformity and (ii) biaxial film stress. Both quanities influence the resonant freqeuncy of resonators. A high polysilicon thickness uniformity and low axial stress are required to reduce strong variations in resonant frequency and excessive bending, which can severly reduce device yield. Hence, both quanities have to be characterised before MEMS resonators can be produced and used for FIB and Ag deposited tuning.

To charcaterise and optimise polysilicon thickness uniformity and biaxial stress, five 76mm n-type $< 100 >$ Si test wafers with 0.1μm thick thermal SiO_2 were used for each polysilicon deposition. All depositions were carried out for 100minutes. The test wafers were placed in slot 11 to 15 of a 25 wafer boat and were sandwiched between two sets of 2×5 dummy wafers to ensure homogenous silane SiH_4 flow for the test wafers.

Both the charcaterisation of the deposition uniformity and biaxial stress required accurate and reproducable thickness measurements. The averegae deposited polysilicon thcikness was determined from five points (center, top, bottom, left, right) on the wafer

using a spectrophotometer (Fig. B.1). The polysilicon thickness uniformity was calaclulated from the difference in layer thickness between center and the avergae of the four remaining values (top, bottom, left and right).

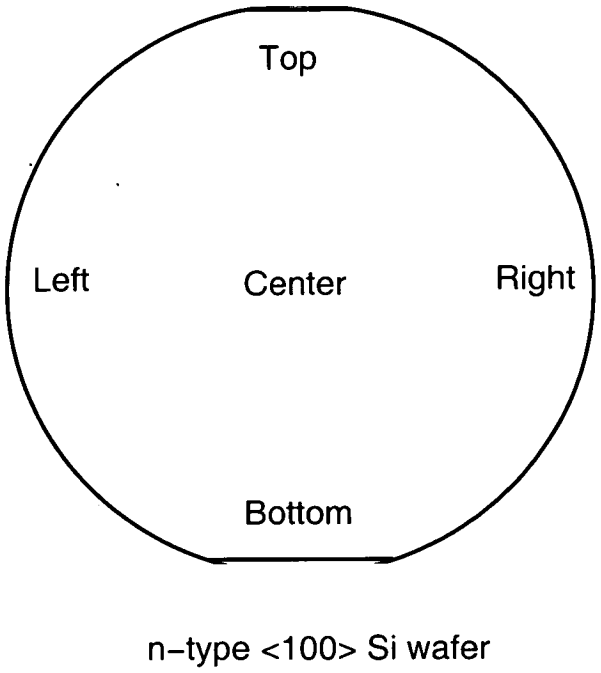

Figure B.1. Schematic of a 76mm Si wafer with five measurement points. The thickness was measured for each of the five points. From these measurements the average deposition thickness and the uniformity was extracted.

B.2.1 Polysilicon thickness uniformity

The polysilicon thickness uniformity was charcaterised for SiH_4 flows ranging from 20 sccm to 60 sccm (sccm = standard cubic centimeters per minute) at a nominal deposition temperature of 600°C. Fig. B.2 shows the center to edge thickness variation (uniformity) and deposition rate as a function of silane SiH_4 gas flow. The polysilicon thickness uniformity improved with decreasing SiH_4 gas flow. Lower gas flow caused less turbulent flow in the furnace tube and improved thickness uniformity. However, a reduced gas flow reduced the deposition rate at the same time. A flow rate of 30sccm was chosen as compromise between thickness uniformity and deposition rate.

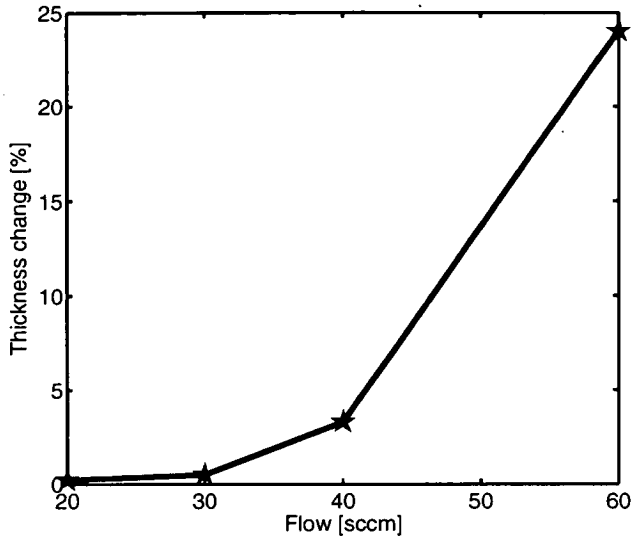

(a)

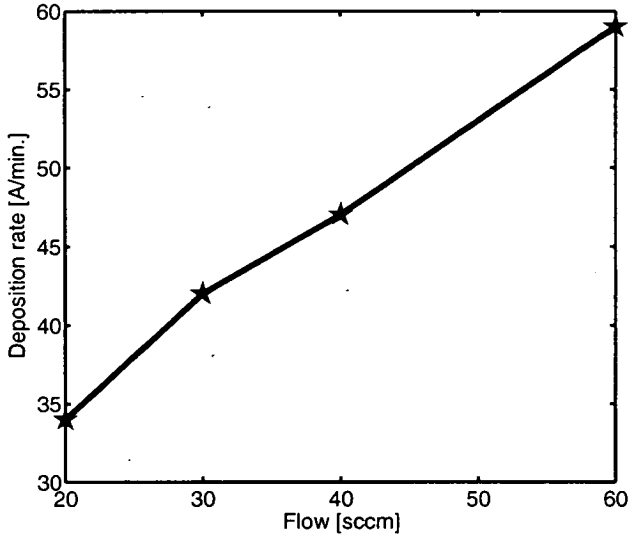

(b)

Figure B.2. Uniformity and deposition rate of polysilicon on 76mm n-type Si wafers. (a) Thickness variation from center to edge and (b) Average deposition rate on the wafer as a function of the SiH_4 flow rate.

B.2.2 Biaxial polysilicon stress

The polysilicon deposition rate and the biaxial stress were determined as function of deposition temperature ranging from 570°C to 620°C for a gas flow of 30sccm. The polysilicon layer thickness was measured at five points on each test wafer using a spectrophotometer.

For the stress measurements, the radius curvature was measured across the whole Si subtstrate using a Dektak surface profiler (see Fig. B.3). This process was repeated by rotating the wafer by 90° and scanning the surface profiler across the entire diameter of the Si substrate. The average radius was calculated from these two measuered radii as $R = (R_1 + R_2)/2$.

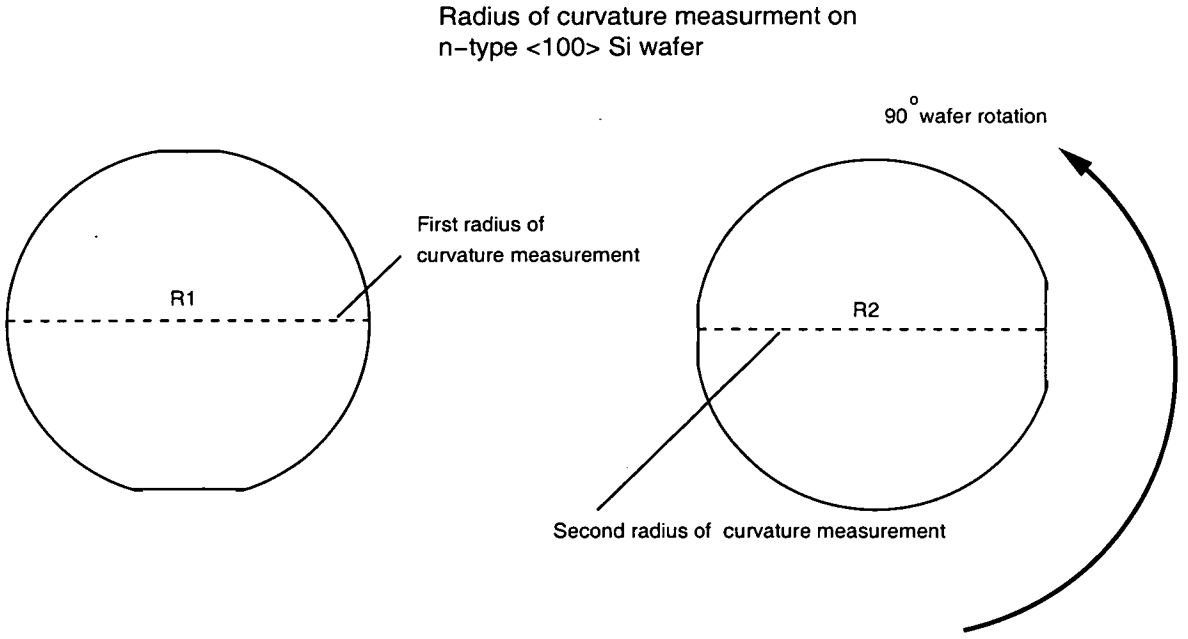

Figure B.3. Radius of curvature measurments on a 76mm Si wafer. The average radius of curvature was determined from two surface scans across the entire 76mm Si substrate. For the biaxial film stress calculations, the radius of curvature was determined in the described way before and after polysilicon removal on the backside of the wafer. The Stoney equation was used to extract the biaxial stress from the measured polysilicon film thickness and wafer curvature.

In order to calaculate the biaxial polysilicon stress, the average radius of curvature was measured in the decribed manner before $R_{initial}$ and after R_{final} polysilicon removal on

the backside of the wafer. Polysilcon was removed on the back of the wafer using RIE etching.

The measured polysilicon thickness t_f and the radii of curvature $R_{initial}$ and R_{final} were inserted into the Stoney equation [120] to determine the biaxial polysilicon film stress σ_0:

$$\sigma_0 = \left(\frac{1}{R_{final}} - \frac{1}{R_{initial}} \right) \frac{E_{Si}}{(1 - \nu_{Si})} \frac{T_s^2}{t_f}. \tag{B.1}$$

Where T_s, E_{Si} and ν_{Si} are the wafer thickness, the Young's modulus and the Poisson ratio of the Si substrate, repectively.

The measured deposition rate and biaxial stress of undoped polysilicon is shown as a function of the deposition temperature in Fig. B.4.

The polysilicon deposition rate increased with rising temperature because more energy was provided for the decomposition of SiH_4. Biaxial stress in polysilicon follows a change from compressive (570-580°C) to tensile (580-590°C) and back to compressive stress (590-620°C) (Fig. B.4). Compressive stress was due to the competitive grain growth and tensile stress due to the amorphous-to crystalline transformation during deposition [73].

Next, the influence of phosphorus doping on biaxial polysilicn stress was investigated. In doing so, wafers were covered with 1μm thick tensile stressed polysilicon, which was deposited at 585°C and subsequently doped for various times with phosphorus via Solid Source Diffusion (SSD) at 1000°C. In order to activate dopants and promote grain growth, wafers were annealed in N_2 at 1100°C for one hour. After annealing, the sheet resistance of the polysilicon was measured using a four point probe (Appendix A). The biaxial stress in the doped polysilicon was determined as described as above.

Fig. B.5 shows the biaxial stress as a function of sheet resistance. Biaxial stress changed from tensile to compressive with descreasing sheet resistance and therefore increasing phosphorus concentration. Phosphorus has a larger lattice constant than silicon and therefore promotes compressive stress [91].

In conclusion, in order to ensure low biaxial stress in doped polysilicon microstrucrtures, films should be deposited at 585°C, doped with phosphorus for 70-90 minutes and subsequentelly annealed at 1100°C.

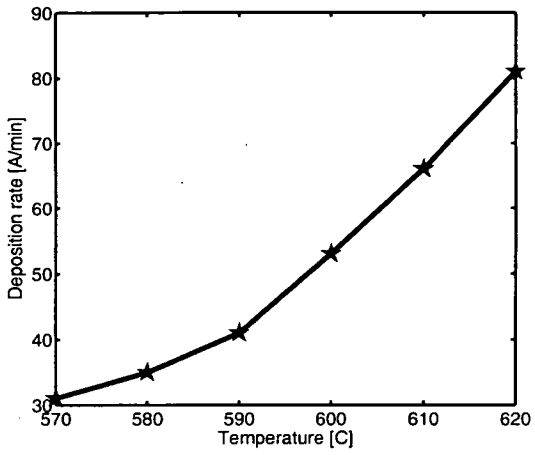

(a)

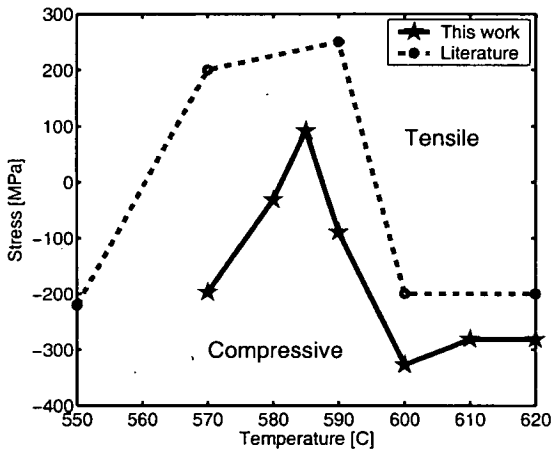

(b)

Figure B.4. Deposition rate and biaxial stress of polysilicon. (a) Deposition rate as a function of temperature. (b) Measured biaxial stress as a function of deposition temperature in comparision to values found in the literature [148]. Biaxial stress was determined using wafer curvature measurements on a surface profiler profiler and the Stoney equation.

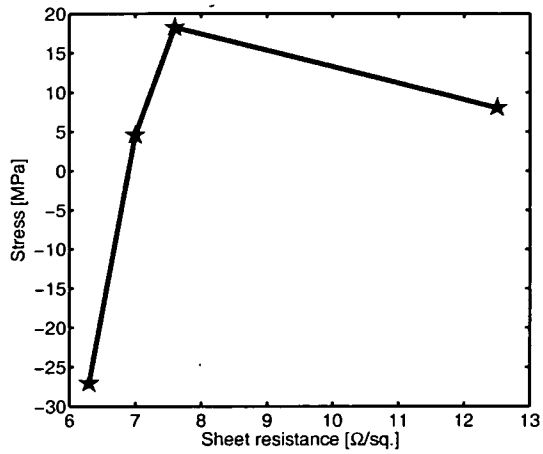

Figure B.5. Biaxial stress of phosphorus doped polysilicon. Biaxial stress as a function sheet resistance.

B.2.3 Sacrificial layer etching

Sacrificial SiO_2 layer etching was used to produce free standing micromechanical test structures. During this so called release etch in hydroflouric acid (HF), a high selectivity between SiO_2 and resonator Al metallisation is important to provide electrically control of micromachined devices. Polysilicon is hardly attacked by HF and therefore has a sufficient high selectivity to SiO_2 [14]. However, the selectivity between Al metallisation and SiO_2 in 10:1 HF is only 11:1 [147], too low to provide intact electrical contacts after long release etches. Hence, a high selectivity between SiO_2 and Al is needed.

To characterise the selectivity between SiO_2 and Al, micromechanical polysilicon resonators with Al electrodes fabricated for Ag deposited frequency tuning (Sec. 5.2.1) were submerged in various oxide etch solutions. The selectivity was extracted by measuring the SiO_2 undercut with an optical microscope and Al thickness with a Dekatk surface profilometer both before and after etching. This approach is accurate and easy to perform within the process environment and enables both Al and SiO_2 to be measured on the same structure.

B.2.4 Sacrificial layer etching

Resonators with Al metallisation were placed in various acids such as (i) 49% HF, (ii) BHF (4:1), (iii) BHF(4:1):CH_3COOH (4:1), (iv) NH_4F : CH_3COOH (10:9) and Silox glass etch. Samples were etched in daylight. The SiO_2 removal rate was determined by measuring the undercut of the polysilicon bridges in a Vickers Microscope (polysilicon is transparent under normal light) and divided the amount of SiO_2 removed by the etch time. Al thicknesss was measured before and after etching using a surface profiler. The Al etch rate was determined by the ratio of Al removed to the etch time. The SiO_2-Al is the ratio of the etch rate of Si_2 to Al. In table B.1. the selectivity for various acids have been summarised.

Etchant	SiO_2:Al Selectivity
HF (49%)	13:1
BHF (4:1)	12:1
BHF (4:1):$CH_3COOH(4:1)$	15:1
NH_4F:CH_3COOH (10:9)	24:1
Silox glass etch	18:1

Table B.1. Experimental measured SiO_2-Al selectivity using different flourine based acids.

An examples of a resonator with Al metallisation after a 10minute etch in HF (49%) is shown in Fig. B.6. After the etch the Al electrodes are partly or fully dissolved.

Fig. B.7 shows a microscope pictures of Al elctrodes etched in NH_4F:CH_3COOH for 160minutes. As can be observed, the electrodes are fully intact and seem not to be affected by the acid.

In conclusion, the intact Al metallisation is provided after long release etches using NH_4F:CH_3COOH.

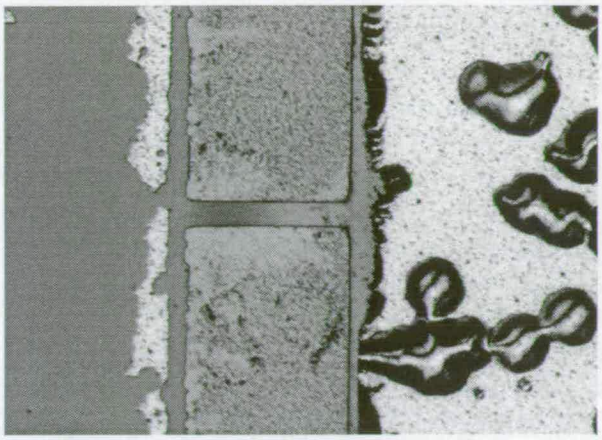

Figure B.6. Microscope picture in 200X magnification of 1μm thick Al electrodes after a 10 minutes etch in 49% HF. This microscope picture clearly shows the effect of standard 49% HF on Al metallisation during a release etch.

Figure B.7. Microscope picture in 200X magnification of 1μm thick Al electrodes after 160 minutes of etch in $NH_4F : CH_3COOH$. $NH_4F : CH_3COOH$ clearly increases the ecth selectivity between SiO_2 and Al and provides intact electrical contacts even after long release etches.

Appendix C

CMP test chip

This part of the thesis describes the design of CMP a test chip consisting of of different micromechanical resonators and filters.

C.1 CMP test chip design and components

C.1.1 Test chip design

A test chip has been designed to demonstrate a CMP planarisation fabrication for micromechanical polysilicon resonators with submicron transducer gaps (see Fig. C.1). The test chip is 9.8mm^2 in size and can be divided into four main parts:

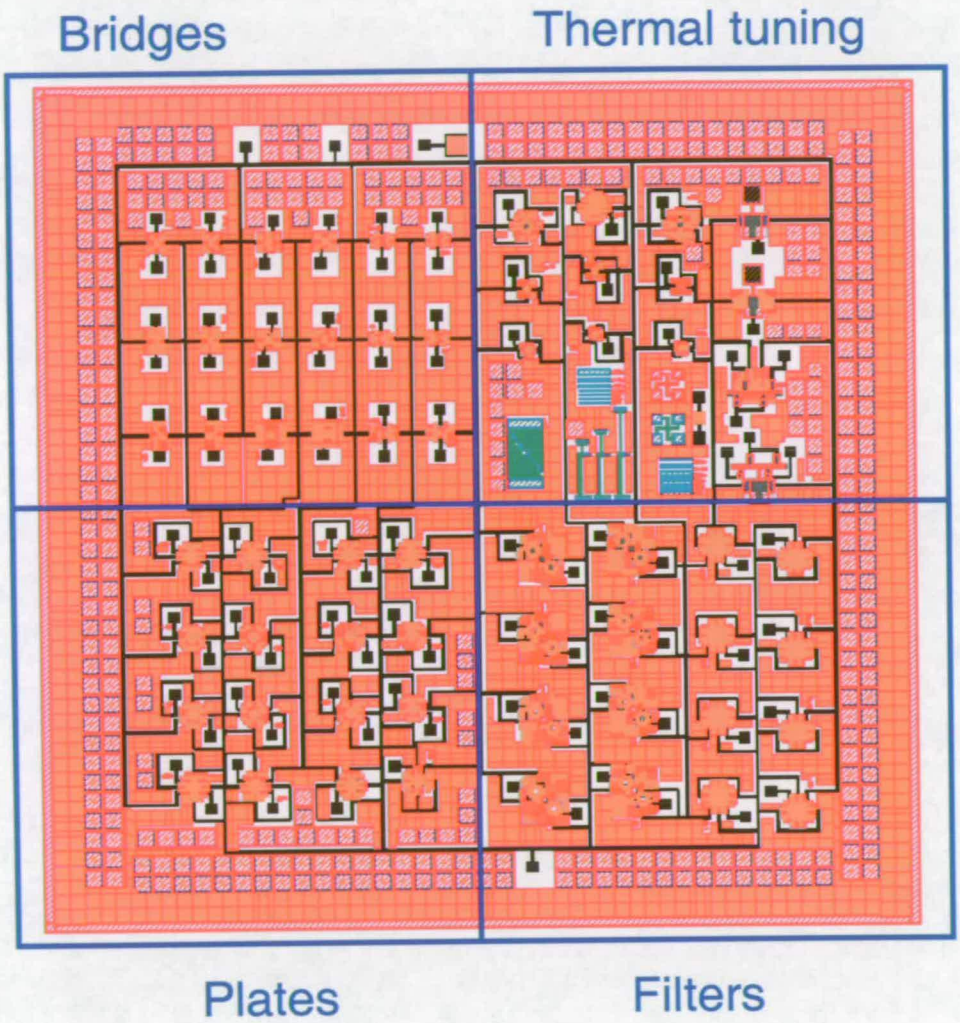

Figure C.1. CMP test chip design. The CMP test chip consists of four sections including test structures and various designs of micromechanical structures such as bridges, plates and filters.

1. Test Structures and thermal tuning structures
2. Micromechanical bridge/beam resonators

3. Micromechanical plate resonators

4. Micromechanical filters

Square shaped CMP buffer structures 50-100μm^2 in size were placed at the edge and inside the test chip to ensure a global and local uniform CMP polishing rate. To ensure a globally uniform CMP removal rate, buffer structures were located at the edge of the chip. Buffer structures were placed inside the chip between individual devices ensure a uniform CMP removal rate locally on each individual test chip.

Bonding pads 100μm^2 in size were placed at the edge of the chip to provide electrical contact to the devices. These bonding pads were allocated for different purposes such as measurement calibration (open, short and 50Ω) and signal routing (ground and input and output ports). Input and output were placed at opposite end of the test to reduce the effect of possible cross signal coupling. The design consists of seven masks from which fife are light and two are dark field.

C.1.2 Test chip components

This section presents some components of the CMP test chip design, which are located on the four main sections of the test chip.

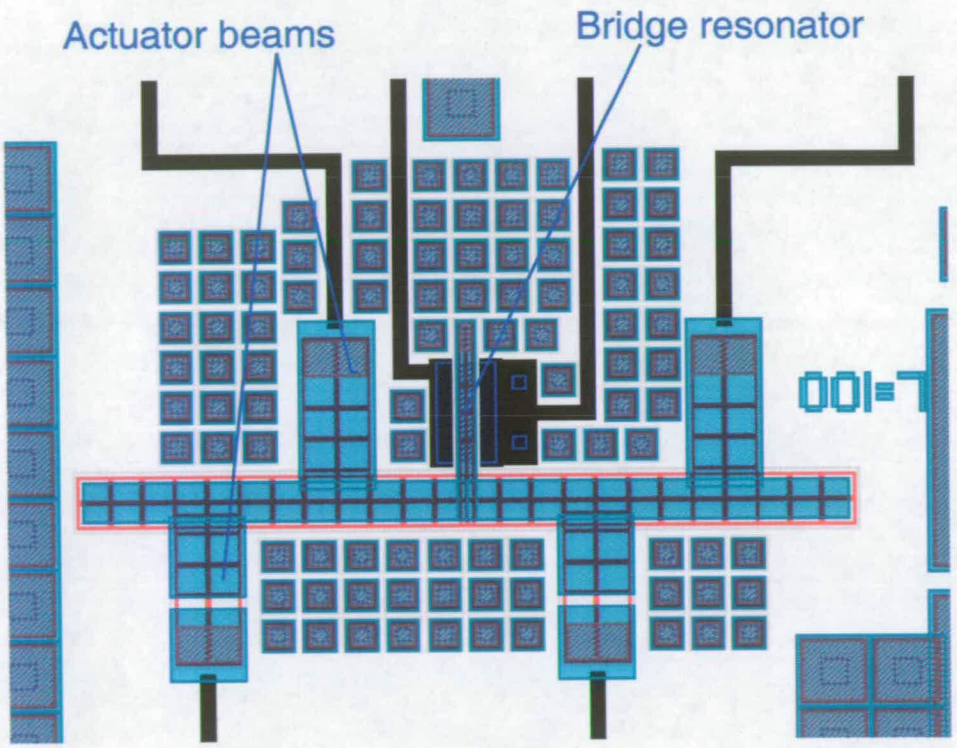

Figure C.2. Layout of a thermal frequency tuning mechanism. Jouling heating in the wide actuator beams causes compressive strain, which is transfered into a moment. The moment is transfered onto the bridge resonator, which is either compressed or expanded dependent on the arrangement of the actuator beams.

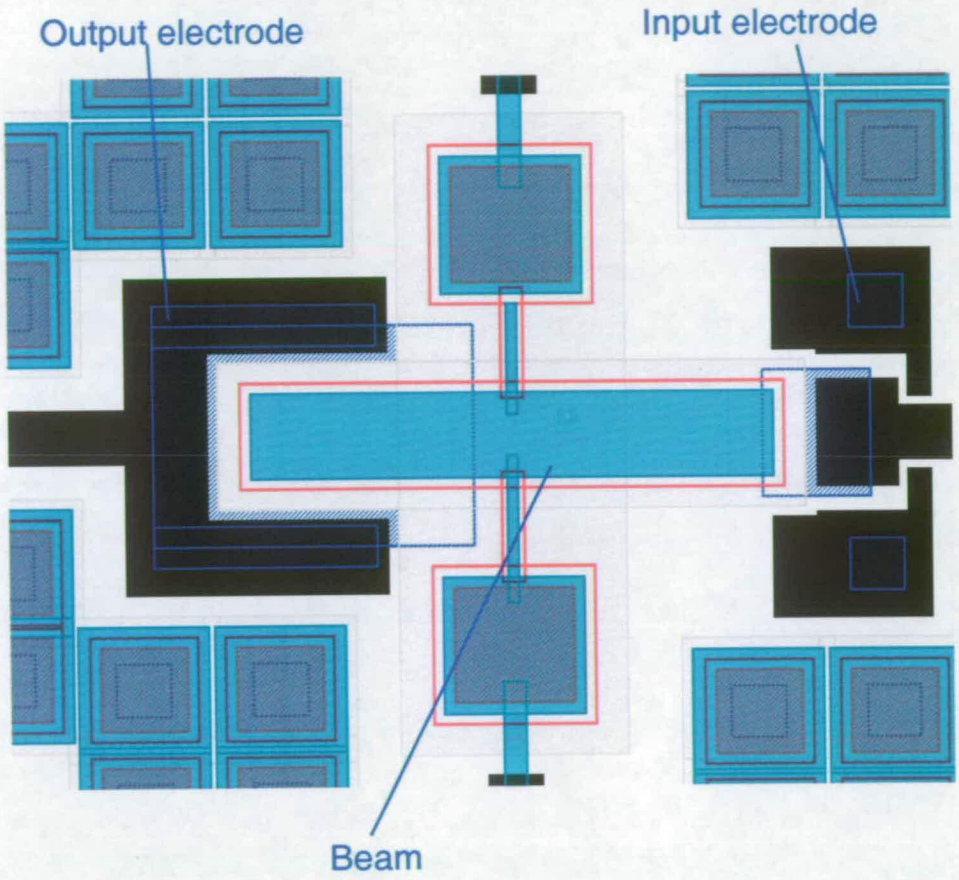

Figure C.3. Layout of a micromechanical beam resonator. Example of an extensional vibrating beam resonator designed with enlarged output electrode to increase the detected motional current.

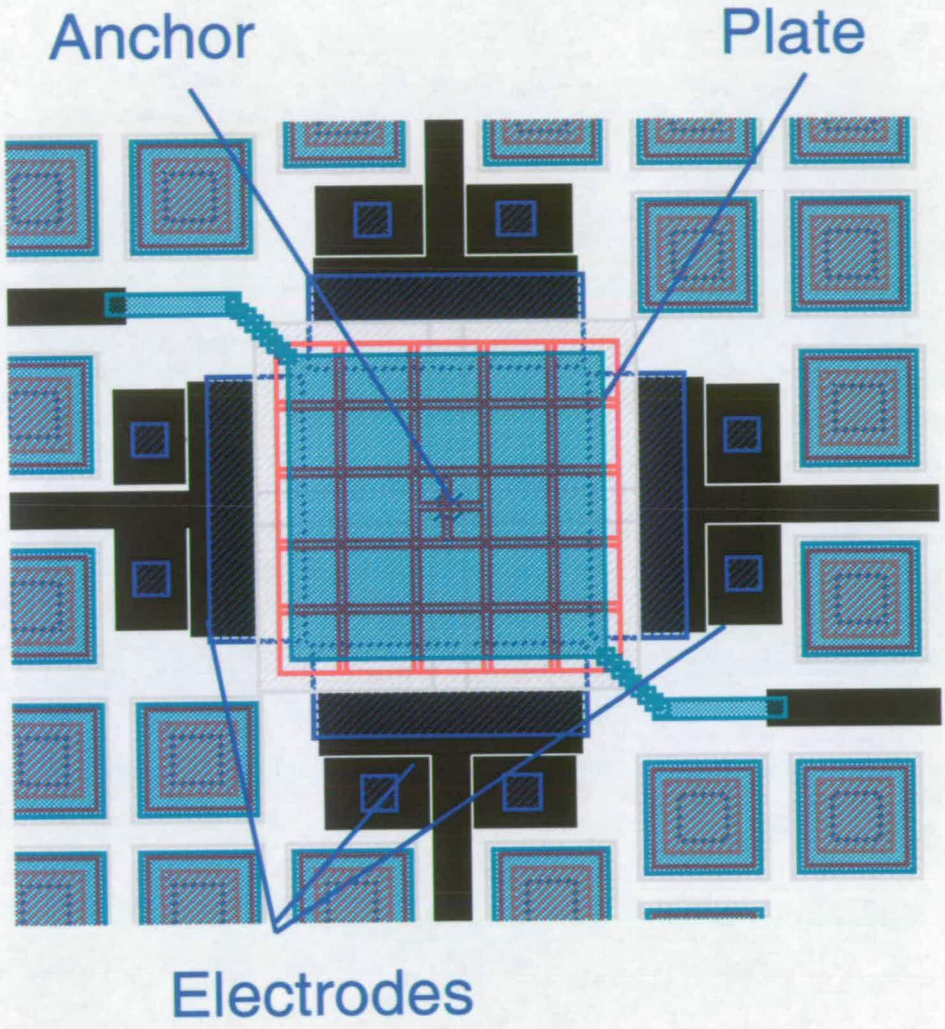

Figure C.4. Layout of a micromechanical plate resonator. Example of an extensional vibrating plate resonator.

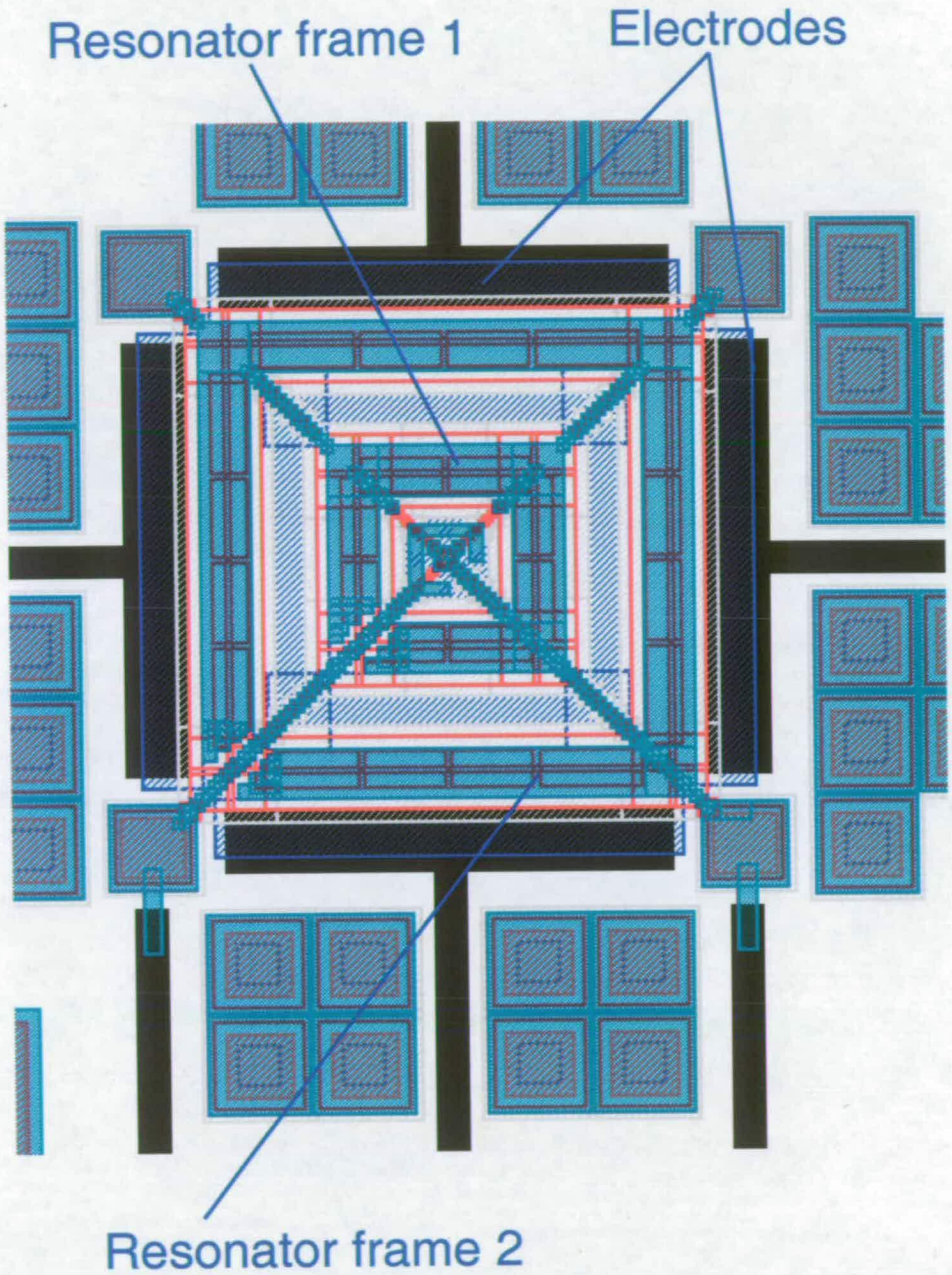

Figure C.5. Layout of a micromechanical filter. Example of an filter structure consisting of two frame resonators.

References

[1] Mohamed A. Abdelmoneum, Mustafa M. Demirci, Yu-Wei Lin, and Clark T.-C Nguyen. Location-dependent frequency tuning of vibrating micromechanical resonators via laser trimming. In *2004 IEEE Int. Ultrasonics, Ferroelectrics, and Frequency Control Joint 50th Anniversary Conf.*, pages 272–279, USA, 2004.

[2] S G Adams, F M Bertsch, K A Shaw, P G Hartwell, F C Moon, and N C MacDonald. Capacitance based tunable resonators. *J. Micromech. Microeng.*, 8:15–23, 1998.

[3] Scott G Adams, Fred M Bertsch, Kevin A Shaw, and Noel C MacDonald. Independent tuning of linear and nonlinear stiffness coefficient. *Journal of Microelectromechanical Systems*, 7(2):172–180, 1998.

[4] Yongchul Ahn, Henry Guckel, and J. David Zook. Capacitive microbeam resonator design. *Journal of Micromechanics and Microengineering*, 11:70–80, 2001.

[5] AMICON. The european network of excellence on RF MEMS and RF microsystems, 2005. (http://www.amicom.info/).

[6] Frank D. Bannon III, John R. Clark, and Clark T.-C. Nguyen. High-Q HF Microeletromechanical Filters. *IEEE Journal of Solid-State Circuits*, 35(4):512–526, 2000.

[7] Sunil Bhave and Roger T. Howe. Internal electrostatic transduction for bulk-mode MEMS resonators. In *Solid State Sensor, Actuator and Microsystems Workshop, Hilton Head Island*, pages 59–60, June 2004.

[8] Dubravka Bilić. *Micromachined Resonators*. PhD thesis, University of California at Berkeley, Department of Electrical Engineering and Computer Sciences, March 2001.

[9] G. Binning, C.F. Quate, and Ch. Gerber. Atomic force microscope. *Physical Review Letters*, 56(9):930–933, 1986.

[10] B. Boonliang, P.D. Prewett, M.C.L. Ward, and P.T. Docker. NEMS mass sensor by focused ion beam fabrication. In *Technical Proceedings of the 2005 NSTI Nanotechnology Conference and Trade Show*, pages 416–419, USA, May 2005.

[11] Siebe Bouwstra and Bert Geijselaers. On the resonance frequencies of microbridges. In *IEEE Transducers 1991*, pages 538–542, June 1991.

[12] Elliott R. Brown. RF-MEMS swicthes for reconfigurable integrated circuits. *IEEE Transactions on Microwave Theory and techniques*, 46(11):1868–1880, 1998.

[13] Martin G. Buehler and W. Robert Thurber. An Experimental Study of Various Cross Sheet Resistor Test Structures. *J. Electrochem. Soc.: Solid-State Science and Technology*, 125(4):650–654, 1978.

[14] J. Bühler, F. P. Steiner, and H. Baltes. Silicon dioxide sacrificial layer etching in surface micromachining. *Journal of Micromechanics and Microengineering*, 7:R1–R13, 1997.

[15] James M. Bustillo, Roger T. Howe, and Richard S. Muller. Surface micromachining for microelectromechanical systems. *Journal of Microelectromechanical Systems*, 86(8):1552–1574, 1998.

[16] Mu Chiao and Liwei Lin. Post-packaging tuning of microresonators by pulsed laser deposition. In *Int. Conference on Solid-State Sensors and Actuators-Transducers'2003*, pages 1820–1823, USA, 2003.

[17] Christopher L. Chua, David K. Fork, Koenraad Van Schuylenbergh, and Jeng-Ping Lu. Out-of-plane high-Q inductors on low-resistance silicon. *Journal of Microelectromechnaical Systems*, 12(6):989–995, 2003.

[18] Ray W. Clough and Joseph Penzien. *Dynamics of Structures*. McGraw-Hill Inc., New York, 2nd edition, 1993.

[19] FEI Company. Fib 200 series workstation user's guide, 1994.

[20] Stephen H. Crandall and Norman C. Dahl. *An Introduction to the Mechanics of Solids*. McGraw-Hill, New York, Second edition, 1972.

[21] Gerald W. Dahlmann, Eric M. Yeatman, Paul Young, Ian D. Robertson, and Stepan Lucyszyn. Fabrication, RF characteristics and mechanical stability of self-assembled 3D microwave inductors. *Sensors and Actuators*, A(97-98):215–220, 2002.

[22] Jürgen H. Daniel, David F. Moore, and John F. Walker. Focused ion beam and silicon-on-insulator-a novel approach to MEMS. *Smart Mater. Struct.*, 9:284–290, 2000.

[23] M.U. Demirci and C.T.-C. Nguyen. A low imedeance VHF micromechanical filter using coupled-array composite resonators. In *Technical Digest of IEEE Transducers'05*, pages 2131–2134, June 2005.

[24] S. Enderling, C.L. Brown III, S. Smith, M.H. Dicks, J.T.M. Stevenson, M. Mitkova, M.N. Kozicki, and A.J. Walton. Sheet resistance measurement of non-standard cleanroom materials using suspended Greek cross test structures. *IEEE Transactions on Semiconductor Manufacturing*, 19(1):2–9, 2006.

[25] S. Enderling, C.L. Brown III, S.Smith, M.H. Dicks, J.T.M. Stevenson, A.W.S. Ross, M.Mitkova, M.N. Kozicki, and A.J. Walton. Suspended Greek cross test structures for measuring the sheet resistance of non-standard cleanroom materials. In *Proc. 18th International Conference on Microelectronic Test Structures*, pages 1–4, Leuven, Belgium, 2005.

[26] S. Enderling, C.L.Brown III, M. Balakrishnan, J. Hedley, J.T.M. Stevenson, S.Bond, C.C. Dunare, A.J. Harris, J.S. Burdess, M. Mitkova, M.N. Kozicki, and A.J. Walton. Integration of a novel electrochemical tuning scheme with MEMS surface micromachined resonators. In *Proc. 18th IEEE Int. Conf. on Micro Electro Mechanical Systems*, pages 159–162, Miami, USA, 2005.

[27] S. Enderling, M.H. Dicks, S.Smith, J.T.M. Stevenson, and A.J. Walton. Thermal Design Considerations for Greek Cross Test Structures. In *Proc. 16th International Conference on Microelectronic Test Structures*, pages 8–13, Monterey, USA, 2003.

[28] S. Enderling, M.H. Dicks, S.Smith, J.T.M. Stevenson, and A.J. Walton. Design Rules to Minimize the Effect of Joule Heating in Greek Cross Test Structures. *IEEE Transactions on Semiconductor Manufacturing*, 17(2):84–90, 2004.

[29] S. Enderling, L. Jiang, A.W.S. Ross, S. Bond, J. Hedley, A.J. Harris, J.S. Burdess, R. Cheung, C.A. Zorman, M. Mehregany, and A.J. Walton. MEMS resonator tuning using focused ion beam platinum deposition. In *Technical Proceedings of the 2004 Nanotechnology Conference and Trade Show*, volume 3, pages 421–424, Boston, USA, 2004.

[30] V. Ermolov, H. Nieminen, K. Nybergh, T. Ryhänen, and S. Silanto. Microsystem Technologies for Mobile Communication Products. In *Surface Mount Technology International*, pages 710–717, 2001.

[31] W Fang and J A Wickert. Post buckling of micromachined beams. *J. Micromech. Microeng.*, 4:116–122, 1994.

[32] W Fang and J A Wickert. Determining mean and gradient residual stress in thin films using micromachined cantilevers. *J. Micromech. Microeng.*, 6:301–309, 1996.

[33] E. Forsén, G. Abadal, S.G. Nilsson, J. Verd, R. Sandberg, W. Svendsen, J. Teva, F.Pereź-Murano, J. Figueras, F. Campabadal, L. Montelius abd N. Barniol, and A. Boisen. Fully integrated nanoresonator system with attogram/Hz mass resolution. In *IEEE Int. Micro Electro Mechanical Systems Conference*, pages 867–870, USA, Jan. 2005.

[34] B. J. Gallacher, J. Hedley, J .S. Burdess, and A. J. Harris. Frequency tuning of silicon micromechanical cantilevers by laser ablation. In *Technical Proceedings of the 2003 Nanotechnology Conference and Trade Show*, volume 1, pages 478–481, USA, February 2003.

[35] Barry J. Gallacher. *The Design, Fabrication and Testing of a Multi-Axis vibrating ring gyroscope.* PhD thesis, University of Newcastle upon Tyne, Department of Mechanical, Materials and Manufacturing Engineering, August 2002.

[36] Kenji Gamo and Susumu Namba. Microfabrication using Focused Ion Beams. *Microelectronic Engineering*, 11:403–408, 1990.

[37] James M. Gere and Stephen P. Timoshenko. *Mechanics of Materials.* Chapman and Hall, London, Glasgow, New York, Tokyo, Melbourne, Madras, Third edition, 1991.

[38] L.A. Giannuzzi and F.A. Stevie. A review of focused ion beam milling techniques for TEM specimen preparation. *Micron*, 30(3):197–204, 1999.

[39] Charles K. Goldsmith, Zhimin Yao, Susan Eshelman, and David Denniston. Performance of Low-Loss RF MEMS Capacitive Switches. *IEEE Microwave and Guided Wave Letters*, 8(8):269–271, 1998.

[40] H. Guckel, T. Randazzo, and D.W. Burns. A simple technique for the determination of mechanical strain in thin films with applications to polysilicon. *Journal of Applied Physics*, 57(5):1671–1675, 1985.

[41] Tomoyuki Harada, Kota Ito, Tadashi Shibata, and Yoshio Mita. A bulk knife-edged as-deposition self-patterning structure for Greek cross and organic thin film transistors. In *The 2006 Int. Conf. on Microelectronic Test Structures*, pages 149–154, March 2006.

[42] L.R. Harriott, A Wagner, and F. Fritz. Integrated cicruit repair using focused ion beam milling. *Journal of Vacuum Science and Technology B*, 4(1):181–184, 1985.

[43] K.F. Harsh, B. Su, W. Zhang, V.M. Bright, and Y.C.Lee. The realization and design consideration of flip-chip integrated tunable capacitor. *Sensors and Actuators*, A(80):108–118, 2000.

[44] John Hedley, Jim S. Burdess, Alun J. Harris, and Barry J. Gallacher. Device characterization at the wafer level via optical actuation and detection. In *Technical Proceedings of the 2004 NSTI Nanotechnology Conference and Trade Show, Volume 1*, pages 394–397, Boston, USA, 2004.

[45] John Hedley, Jim S. Burdess, Alun J. Harris, Barry J. Gallacher, Calum J. McNeil, Peter J. Cumpson, and Stefan Enderling. An optical 'workstation' for characterization and modification of MEMS. In *Poceedings of SPIE 5458*, pages 244–252, Strasbourg, France, 2004.

[46] Roger T. Howe and Richard S. Muller. Resonant-Microbridge Vapor Sensor. *IEEE Transactions on Electron Devices*, ED-33(4):499–506, 1986.

[47] R.T. Howe and R.S. Muller. Polycrystalline Silicon Micromechanical Beams. *Journal Electrochemical Society*, 130(6):1420–1423, 1983.

[48] Wan-Thai Hsu and Clark T.-C. Nguyen. Stiffness-compensated temperature insensitive micromechanical resonators. In *IEEE MEMS 2002*, pages 731–734, USA, January 2002.

[49] Changbae Hyun, Alfred K H Lee, and Alex de Lozanne. Focused Ion Beam deposition of $Co_{71}Cr_{17}Pt_{12}$. *Nanotechnology*, 17:921–925, 2006.

[50] Liudi Jiang, R. Cheung, M. Hassan, A.J. Harris, J.S. Burdess, C.A. Zorman, and M. Mehregany. Fabrication of sic micro-electro-mechanical systems (MEMS) using one-step dry etching. *Vacuum Science and Technology B*, 21(6):2998–3001, 2003.

[51] Daphne Joachim and Liwei Lin. Characterization of selective polysilicon deposition for MEMS resonator tuning. *IEEE Journal of Microelectromechanical Systems*, 12(2):193–200, 2003.

[52] R.A. Johnson. *Mechanical Filters in Electronics*. New York: Wiley, New York, 1983.

[53] Ted Kamins. *Polycristalline Silicon for Integrated Cicuits Applications*. Kluwer Academic Publishers, Norwell, USA, 1988.

[54] G.W.C. Kaye and T.H. Laby. *Tables of Physical and Chemical Constants and some Mathematical Functions*. Longman Inc., Longman Inc., London and New York, 15th edition, 1986.

[55] Bongsang Kim, Rob N. Candler, Matthew Hopcroft, Manu Agarwal, Woo-Tae Park, and Thomas W. Kenny. Frequency stability of wafer-scale encapsulated MEMS resonators. In *The 13th Int. Conf. on Solid-State Sensors, Actuators and Microsystems*, pages 1965–1968, Korea, June 2005.

[56] Erno H. Klaassen, Kurt Peterson, J. Mark Noworolski, John Logan, Nadim I. Maluf, Joe Brown, Christopher Storment, Wendell McCulley, and Gregory T.A. Kovacs. Silicon fusion bonding and deep reactive ion etching: a new technology for microstructures. *Sensors and Actuators A*, 52:132–139, 1996.

[57] M. Koskenvuori, T. Mattila, A. Härä, J. Kiihamäki, I. Tittonen, A. Oja, and H. Seppä. Long-term stability of single-crystal silicon microresonators. *Sensors and Actuators A*, 115(1):23–27, 2004.

[58] Gregory T. A. Kovacs, Nadim I. Maluf, and Kurt E. Peterson. Bulk micromachining of silicon. *Journal of Microelectromechanical Systems*, 86(8):1536–1551, 1998.

[59] M. N. Kozicki, M. Mitkova, and J. P. Aberouette. Nanostructure of solid electrolytes and surface electrodeposits. *Physica E Low-Dimensional Systems and Nanostructures*, 19:161–166, July 2003.

[60] M.N. Kozicki, 2004. (Private communication).

[61] M.N. Kozicki, C.L. Brown III, M. Mitkova, S. Enderling, J. Hedley, and A.J. Walton. Application of Mass Transport in Solid Electrolyte Films in Tunable Microelectromechanical Resonators. In *Technical Proceedings of the 2005 NSTI Nanotechnology Conference and Trade Show*, pages 447–450, Anaheim, CA, USA, 2005.

[62] Brian Lee, Duane S. Boning, Dale L. Heitherington, and David J. Stein. Using smart dummy fill and selective reverse etchback for pattern density equalization. In *Proc. CMP-MIC*, pages 255–258, Santa Clara, USA, 2000.

[63] Choon-Sup Lee and Chul-Hi Han. A novel sub-micron gap fabrication technology using chemical-mechanical polishing (CMP):application to lateral field emission device (FED). *Sensors and Actuators*, A(97-98):739–743, 2002.

[64] Ki Bang Lee, Liwei Lin, and Young-Ho Cho. A frequency-tunable microactuator with a varied comb-width profile. In *IEEE 17th Int Conf. on Micro Electro Mechanical Systems*, pages 257–260, Netherlands, 2004.

[65] Ming-Chang M. Lee, Jin Yao, and Ming C. Wu. Silicon profile transformation and sidewall roughness reduction using hydrogen annealing. In *18th IEEE Int. Conf. on Micro Electro Mechanical Systems*, pages 596–599, Jan 2005.

[66] Sangwoo Lee, Vhangho Cho, Jongpal Kim, Sangjun Park, Sangwoo Yi, Jonjun Kim, and Dong il Cho. The effects of post-deposition processes on polysilicon Young's modulus. *Journal of Micromechanics and Microengineering*, 8:330–337, 1998.

[67] Sheng-Shian Li, Yu-Wei Lin, Yuan Xie, Zeying Ren, and Clark T.-C. Nguyen. Micromechanical hollow-disk ring resonators. In *17th Int. Conf. on Microelectromechanical Systems 2004*, pages 821–824, Netherlands, Jan. 2004.

[68] H. Lin, A.J. Walton, C.C. Dunare, J.T.M. Stevenson, A.M. Gundlach, S. Smith, and A.S. Bunting. Test structures for the characterisation of MEMS and CMOS integration technology. In *The 2006 Int. Conf. on Microelectronic Test Structures*, pages 143–148, March 2006.

[69] Y.-W. Lin, S. Lee, S.-S. Li, Y. Xie, Z. Ren, and C.T.-C. Nguyen. 60-MHz wine glass micromechanical disk reference oscillator. In *2004 IEEE Int. Solid-State Circuits Conf.*, pages 322–323, Feb. 2004.

[70] Yu-Wei Lin, Sheng-Shian Li, Yuan Xie, Zeying Ren, and Clark T.-C. Nguyen. Vibrating micromechanical resonators with solid dielectric capacitive transducer gaps. In *Proceedings, Joint IEEE Int. Frequency Control/Precision Time & Time Interval Symposium*, pages 128–134, August 2005.

[71] S. Lucyszyn. Review of radio frequency microelectromechnaical systems technology. *IEE Proc.-Sci. Meas. Technol.*, 151(2):93–102, 2004.

[72] Qing Ma, Peng Cheng, and Valluri Rao. Resonator frequency correction by modifying support structures, 2003. (US Patent: 20030001694).

[73] Marc Madou. *Fundamentals of microfabrication*. CRC Press LLC, Boca Rota, London, New York, Washington, D.C., second edition, 2002.

[74] D Maier-Schneider, A Köprülülü, S Ballhausen Holm, and E Obermeier. Elastic properties and microstructure of LPCVD polysilicon films. *J Micromech. Microeng.*, 6:436–446, 1996.

[75] Yoshio Mita, Masakazu Sugiyama, Masanori Kubota, Frederic Marty, Tarik Bououina, and Tadashi Shibata. Aspect ratio dependent scalloping attenuation in DRIE and an application to low-loss fiber-optical switches. In *The 19th International Conf. on Micro Electro Mechanical Systems (MEMS 2006)*, pages 114–117, 2006.

[76] Yoshio Mita, Agnés Tixer, Satoshi Oshima, Makoto Mita, Jean-Philippe Gouy, and Hiroyuki Fujita. A silicon shadow mask with unlimited patterns and a mechanical alignment structure by Al-delay masking process. *IEEJ Transactions on Sensors and Micromachines*, 120(7):357–362, 2000.

[77] M. Mitkova and M.N. Kozicki. Silver incorporation in Ge-Se glasses used in programmable metallization cell devices. *J. of Non-Crystalline Solids*, 299-302:1023–1027, 2002.

[78] M. Mitkova, M.N. Kozicki, and J. P. Aberouette. Morphology of electrochemically grown silver deposits on silver-saturated Ge-Se thin films. *J. of Non-Crystalline Solids*, 326-327:425–429, 2003.

[79] H.C. Nathanson and R.A. Wickstrom. A Resonant-Gate Silicon Surface Transistor with High-Q Band-Pass Properties. *Applied Physics Letters*, 7(4):84–86, 1965.

[80] Clark T.-C. Nguyen. Frequency-Selective MEMS for Miniaturized Communication Devices. In *1998 IEEE Aerospace Conference*, volume 1, pages 445–460, Colorado, March 1998.

[81] Clark T.-C. Nguyen. Micromachining technologies for miniaturized communication devices. In *Proceedings of the SPIE: Micromachining and Microfabrication*, pages 24–38, Santa Clara, USA, September 1998.

[82] Clark T.-C. Nguyen. Micromechanical filters for miniaturized low-power communications. In *Proceedings of the SPIE: Smart Structures and Materials (Smart Electronics and MEMS)*, Newport Beach, California, March 1999.

[83] Clark T.-C. Nguyen. Vibrating RF MEMS for Next Generation Wireless Applications. In *2004 IEEE Custom Integrated Circuits Conf.*, pages 257–264, Orlando, USA, October 2004.

[84] Clark T.-C. Nguyen. Vibrating RF-MEMS for next generation wireless applications. In *2004 IEEE Custom Integrated Circuits Conf.*, pages 257–264, October 2004.

[85] Clark T.-C. Nguyen. RF MEMS in wireless Architectures. In *Proceedings of the 42 nd Design Automation Conference*, pages 416–420, USA, June 2005.

[86] Clark T.-C. Nguyen. Vibrating RF MEMS technology: fuel for an integrated micromechanical circuit revolution? In *Transducers'05*, pages 243–246, Korea, June 2005.

[87] Clark T.-C. Nguyen and Roger T. Howe. An Integrated CMOS Micromechanical Resonator High-Q Oscillator. *IEEE Journal of Solid-State Circuits*, 34(4):440–455, 1999.

[88] Clark Tu-Cuong Nguyen. *Micromechanical Signal Processors*. PhD thesis, University of California at Berkeley, Department of Electrical Engineering and Computer Sciences, December 1994.

[89] NIST. Q-factors in quartz crystal oscillators, 2005. (http://tf.nist.gov/general/enc-q.htm).

[90] C.W. Oatley. *The Scanning Electron Microscope.* Cambridge at the University Press, Cambridge, 1972.

[91] M. Orpana and A.O. Korhonen. Control of residual stress of polyslicon thin films by heavy doping in surface micromachning. In *Int. Conference on Solid-State Sensors and Actuators-Transducers'91*, pages 957–960, USA, 1991.

[92] J.Y. Park, Y.J. Yee, H.J. Nam, and J.U. Bu. Micromachined RF MEMS tunable capacitors using piezoelectric actuation. In *Proc. IEEE MTT-S Symposium*, pages 2111–2114, May 2001.

[93] V. Pelosin, K. F. Badawi, and V. Branger. Internal friction and its thermal evolution measured on very thin platinum films. *Applied Physics Letters*, 66(6):691–693, 1995.

[94] Andrew Pember, Jim Smith, and Henri Kemhadjian. Study of the effect of boron doping on the aging of micromachined silicon cantilevers. *Applied Physics Letters*, 66(5):577–579, 1995.

[95] Kurt E. Petersen and C.R. Guarnieri. Young's modulus measurements of thin films using micromechanics. *Journal of Applied Physics*, 50(11):6761–6766, 1979.

[96] G. Piazza, P.J. Stephanou, J.M. Porter, M.B.J. Wijesundara, and A.P. Pisano. Low motional resistance ring-shaped contour-mode aluminium nitride piezoelectric micromechanical resonators for UHF applications. In *18th IEEE Int. Conf. on Micro Electro Mechanical Systems*, pages 20–23, Jan. 2005.

[97] James D. Plummer, Michael D. Deal, and Peter B. Griffin. *Silicon VLSI Technology.* Prentice Hall, Inc., Upper Saddle River, New Jersey, 2000.

[98] P.D. Prewett. Focused ion beams-microfabrication methods and applications. *Vacuum*, 44(3/4):345–351, 1993.

[99] P.D. Prewett and G.L.R. Mair. *Focused Ion Beams from Liquid Metal Ion Sources.* John Wiley and & Sons Inc., New York, Chichester, Toronto, Brisbane, Singapore, First edition, 1991.

[100] Emmanuel P. Quévy, Sunil A. Bhave, Hideki Takeuchi, Tsu-Jae King, and Roger T. Howe. Poly-SiGe high frequency resonantors based on lithographic definition of nano-gap lateral transducers. In *Hilton Head 2004*, pages 360–363, Hilton Head Island, 2004.

[101] A Boisen R Sandberg, K Molhave and W Svendsen. Effect of gold coating on the q-factor of a resonant cantilever. *J. Micromech. Microeng.*, 15:2249–2253, 2005.

[102] Gabriel M. Rebeiz. *RFMEMS Theory, Design, and Technology.* John Wiley & Sons, New Jersey, 2003.

[103] Todd Remtema and Liwei Lin. Active frequency tuning for micro resonators by localized thermal stressing effects. *Sensors and Actuators*, A(91):326–332, 2001.

[104] Steve Reyntjens and Robert Puers. A review of focused ion beam applications in microsystem technology. *J. Micromech. Microeng.*, 11:287–300, 2001.

[105] M.L. Roukes. Nanoelectromechanical Systems. In *Technical Digest of the 2000 Solid-State Sensor and Actuator Workshop*, pages 367–376, Hilton Head Island, USA, July 2000.

[106] S. Roy, A.K. McIlwain, R.G.DeAnna, A.J. Fleischman, C.A. Zorman R.K. Burla, and M. Mehregany. SiC Resonant Devices for High Q and High Temperature Applications. In *Solid-State Sensor and Actuator Workshop*, pages 22–25, Hilton Head Island, South Carolina, June 2000.

[107] Rennsselaer Polytechnic Institute (RPI). Better electron microscopes, 2006. (http://www.rpi.edu/).

[108] R. Ruby and R. Merchant. Micromachined Thin Film Bulk Acoustic Resonators. In *1994 IEEE Int. Frequency Control Symposium*, pages 135–138, Boston, USA, June 1994.

[109] Hector J. De Los Santos. *Introduction to Microelectromechanical (MEM) Microwave Systems*. Artech House, Boston,London, 1999.

[110] Yasuji Sawada, A. Dougherty, and J. P. Gollub. Dendritic and fractal growth in electrolytic metal deposits. *Physical Review Letters*, 56(12):1260–1263, 1986.

[111] D. Saya, L. Nicu, M. Guirardel, Y. Tauran, and C. Bergaud. Mechanical effect of gold nanoparticles labeling used for biochemical sensor applications: A multimode analysis by means of SiNx micromechanical cantilever and bridge mass detectors. *Review of Scientific Instruments*, 75(9):3010–3015, 2004.

[112] Dieter K. Schroder. *Semiconductor Material and Device and Characterization*. John Wiley & Sons, Inc., New York, 1990.

[113] R.L. Seliger, J.W. Ward, V. Wang, and R.L. Kubena. A high-intensity scanning ion probe with submicrometer spot size. *Applied Physics Letters*, 34(5):310–312, 1979.

[114] T.N. Shchurova and N.D. Savchenko. Correlation between mechanical parameters for amorphous chalcogenide films. *Journal of Optoelectronics and Advanced Materials*, 3(2):491–498, 2001.

[115] Stewart Smith, Anthony J. Walton, Sue Bond, Alan W.S. Ross, J. Tom M. Stevenson, and Alan. M. Gundlach. Electrical characterization of platinum deposited by Focused Ion Beam. *IEEE Transactions on Semiconductor Manufacturing*, 16(2):199–206, 2003.

[116] Jeffry J. Sniegowski. Chemical-mechanical polishing: enhancing the manufacturability of MEMS. In *Proceedings of the SPIE - The Int. Soc. for Optical Eng.*, volume 2879, pages 104–115, 1995.

[117] G. Stemme. Resonant silicon sensors. *Journal of Micromechanics and Microengineering*, 1:113–125, 1991.

[118] Brian S. Stine, Dennis O. Ouma, Rajesh R. Divecha, Duane S. Boning, and James E. Chung. CMP characterisation mask set - chip documentation. Technical report, Massachusetts Institute of Technology, 1997.

[119] Brian S. Stine, Dennis O. Ouma, Rajesh R. Divecha, Duane S. Boning, James E. Chung, Dale L. Hetherington, C. Randy Harwood, O. Samuuel Nakagawa, and Soo-Young Oh. Rapid characterization and modeling of pattern-dependent variation in chemical-mechanical polishing. *IEEE Transactions on Semiconductor Manufacturing*, 11(1):129–140, 1998.

[120] G. G. Stoney. The tension of their metallic film deposited by electrolysis. *Proc.Royal Society London*, A82:172, 1909.

[121] Richard R.A. Syms. Electrothermal frequency tuning of folded and coupled vibrating micromechanical resonators. *Journal of Microelectromechanical Systems*, 7(2):164–171, 1998.

[122] R.R.A. Syms and D.F. Moore. Focused ion beam tuning of in-plane vibrating micromechanical resonators. *Electronics Letters*, 35(15):1277–1278, 1999.

[123] William C. Tang, Tu-Cuong H. Nguyen, and Roger T. Howe. Laterally Driven Polysilicon Resonant Microstrcutures. *Sensors and Actuators A*, 20:25–32, 1989.

[124] Discera Microcommunication Technologies. Micromachined resonator on a us cent coin, 2005. (http://www.discera.com).

[125] J. Teng and P.D. Prewett. Focused ion beam fabrication of thermally actuated bimorph cantilevers. *Sensors and Actuators*, A(123-124):608–613, 2005.

[126] H A C Tilmans. A fully-packaged electromagnetic microrelay. In *Proc. IEEE Int. Conf. on Micro Electro Mechanical Systems*, pages 25–30, Jan. 1999.

[127] Harrie A C Tilmans, Walter De Raedt, and Eric Beyne. MEMS for wireless communications:'from RF-MEMS components to RF-MEMS-SiP. *J. Micromech. Microeng.*, 13:S139–S163, 2003.

[128] Harrie A.C. Tilmans, Miko Elwenspoek, and Jan H.J. Fluitman. Micro resonant force gauges. *Sensors and Actuators A*, 30:35–53, 1992.

[129] S. Timoshenko and D.H. Young. *Vibration Problems in Engineering*. D. van Nostrand Company, Inc., Toronto, New York, London, Third edition, 1955.

[130] Stephen P. Timoshenko. *Theory of Plates and Shells*. McGraw-Hill, New York, Second edition, 1959.

[131] Ben Tromans, David Provert, and Fred Essex. *The Canning Handbook - Surface finishing technology*. W. Canning plc., London, New York, first edition, 1982.

[132] Hsin-Chang Tsai and Weileun Fang. Determining the poisson's ratio of thin film materials using resonant method. *Sensors and Actuators*, A(103):377–383, 2003.

[133] Korea University. Schematic of CMP polishing, 2005. (http://ceramics.korea.ac.kr/cmp.htm).

[134] Vijay K. Varadan, K.J. Vinoy, and K.A. Jose. *RFMEMS and their Applications*. John Wiley & Sons Ltd., West Sussex, England, 1st edition, 2003.

[135] Srikar Vengallatore. Analysis of thermoelastic damping in laminated composite micromechanical beam resonators. *J. Micromech. Microeng.*, 15:2398–2404, 2005.

[136] Lebrecht von Trotha, Georg Mörsch, Peter Wolters, and Gerfried Zwicker. Advanced MEMS Fabrication using CMP. In *Semiconductor International*, volume 8/1/2004, 2004.

[137] A.J. Walton. Microelectronic test structures. In *Semicon 1997*, Geneva, Switzerland, 1997.

[138] A.J. Walton and N.G. Burrow. Structure for isolating the effect of conductor diffusion in thick film resistors. In *Proceedings 5th European Hybrid Microelectronics Conference*, pages 399–405, 1985.

[139] Dong F Wang, Takahito Ono, and Masayoshi Esashi. Thermal treatments and gas absorption influences on nanomechanics of ultra-thin silicon resonators for ultamate sensing. *Nanotechnology*, 15:1851–1854, 2004.

[140] Jing Wang, James E. Butler, Tatyana Feygelson, and Clark T.-C. Nguyen. 1.51-GHz nanocrystalline diamond micromechanical disk resonator with material-mismatched isolating support. In *17th Int. Conf. on Microelectromechanical Systems 2004*, pages 641–644, Netherlands, Jan. 2004.

[141] Jing Wang, Zeying Ren, and Clark T.-C. Nguyen. 1.156-GHz Self aligned vibrating Micromechnaical Disk resonator. *IEEE Transaction on Ultrasonics, Ferroelectrics, and Frequency Control*, 51(12):1607–1628, 2004.

[142] Kun Wang, Wan Thai Hsu Ark-Chew Wong, and Clark T.-C. Nguyen. Frequency Trimming and Q-Factor Enhancement of Micromechanical Resonators via Localized Annealing. In *1997 International Conference on Solid-State Sensors and Actuators*, pages 109–112, Illinois, USA, June 1997.

[143] Kun Wang and Clark T.-C. Nguyen. High-Order Micromechanical Electronic Filters. In *Int. Micro Electro Mechanical System Workshop*, pages 25–30, Japan, Jan. 1997.

[144] Y. Wang, Z. Li, D.T. McCormick, and N.C. Tien. A micromachined RF microrelay with electrothermal actuation. *Sensors and Actuators*, A(103):231–236, 2003.

[145] Robert C. Weast. *Handbook of Chemistry and Physics*. CRC Press, Cleveland, Ohio, 56th edition, 1975.

[146] W.C. West, K. Sieradzki, B. Kardynal, and M.N. Kozicki. Equivalent circuit of the $Ag|As_{0.24}S_{0.36}Ag_{0.40}|Ag$ system prepared by photodissolution of Ag. *J. Electrochem. Soc.*, 145(9):2971–2974, 1998.

[147] Kirt R. Williams, Kishan Gupta, and Matthew Wasilik. Etch rates for micromachining processing - part II. *IEEE Journal of Microelectromechanical Systems*, 12(6):761–777, 2003.

[148] Jie Yang, Harold Kahn, An-Qiang He, Stephen M. Phillips, and Arthur Heuer. A new technique for producing large-area a-deposited zero-stress LPCVD polysilicon films: The multipoly process. *IEEE Journal of Microlectromechanical Systems*, 9(4):485–494, 2000.

[149] T. Yang, K.L. Ekinci, X.M.H. Huang, L.M. Schiavone, and M.L. Roukes. Monocrystalline silicon carbide nanoelectromechanical systems. *Applied Physics Letters*, 78(2):162–164, 2001.

[150] J. Jason Yao. RF MEMS from a device perspective. *Journal of Micromechanics and Microengineering*, 10:9–38, 2000.

[151] J.J. Yao and N.C. MacDonald. A micronachined, single-crystal silicon, tunable resonator. *Journal of Micromechanics and Microengineering*, 6:257–264, 1996.

[152] J.J. Yao, S. Park, and J. DeNatale. High tuning-ratio MEMS based tunable capactitors for RF communication applications. In *Proc. of Solid-State Sensors and Actuators Workshop*, pages 124–127, June 1998.

[153] A.A. Yasseen, N.J. Mourlas, and M. Mehregany. Chemical-mechanical polishing for polysilicon surface micromachining. *Journal of the Electrochemical Society*, 144(1):237–242, 1997.

[154] Kevin Y. Yasumura, Timothy D. Stowe, Eugene M. Chow, Timothy Pfafman, Thomas W. Kenny, Barry C. Stipe, and Daniel Rugar. Quality Factors in Micron- and Submicron- Thick Cantilevers. *Journal of Microelectromechanical Systems*, 9(1):117–125, 2000.

[155] Yook Kong Yong and John R. Vig. Resonator surface contamination - a cause of freqeuncy fluctations? *IEEE Transactions on Ultrasonics, Ferroelectrics, and Frequency Control*, 36(4):452–458, 1989.

[156] Hongyu Yu, Wei PAng, Hao Zhang, and Eun Sok Kim. Film bulk acoustic resonator at 4.4GHz with ultra low temperature coefficient of resonant frequency. In *18th IEEE Int. Conf. on Micro Electro Mechanical Systems*, pages 28–31, Jan 2005.

[157] C. Patrick Yue and S. Simon Wong. On-chip spiral inductors with patterned ground shields for si-based RFIC's. *IEEE Journal of Solid-State Circuits*, 33(5):743–752, 1998.

[158] Parshuram B. Zantye, Ashok Kumar, and A.K. Sikder. Chemical mechanical planarization for microelectronics applications. *Material and Science and Engineering*, R45:89–220, 2004.